Estimating Wind Velocities in Atmospheric Mountain Waves Using Sailplane Flight Data

Ni Zhang

Department of Electrical and Computer Engineering

A thesis presented for the degree of
Doctor of Philosophy

University of Canterbury
Christchurch, New Zealand
October 2012

To my loving parents

Contents

Abstract

Atmospheric mountain waves form in the lee of mountainous terrain under appropriate conditions of the vertical structure of wind speed and atmospheric stability. Trapped lee waves can extend hundreds of kilometers downwind from the mountain range, and they can extend tens of kilometers vertically into the stratosphere. Mountain waves are of importance in meteorology as they affect the general circulation of the atmosphere, can influence the vertical structure of wind speed and temperature fields, produce turbulence and downdrafts that can be an aviation hazard, and affect the vertical transport of aerosols and trace gasses, and ozone concentration.

Sailplane pilots make extensive use of mountain lee waves as a source of energy with which to climb. There are many sailplane wave flights conducted every year throughout the world and they frequently cover large distances and reach high altitudes. Modern sailplanes frequently carry flight recorders that record their position at regular intervals during the flight. There is therefore potential to use this recorded data to determine the 3D wind velocity at positions on the sailplane flight path. This would provide an additional source of information on mountain waves to supplement other measurement techniques that might be useful for studies on mountain waves. The recorded data are limited however, and determination of wind velocities is not straightforward.

This thesis is concerned with the development and application of techniques to determine the vector wind field in atmospheric mountain waves using the limited flight data collected during sailplane flights. A detailed study is made of the characteristics, uniqueness, and sensitivity to errors in the data, of the problem of estimating the wind velocities from limited flight data consisting of ground velocities, possibly supplemented by air speed or heading data. A heuristic algorithm is developed for estimating 3D wind velocities in mountain waves from ground velocity and air speed data, and the algorithm is applied to flight data collected during "Perlan Project" flights. The problem is then posed as a statistical estimation problem and maximum likelihood and maximum *a posteriori* estimators are developed for a variety of different kinds of flight data. These estimators are tested on simulated flight data and data from Perlan Project flights.

Acknowledgements

I would like to express my gratitude to my supervisor Prof. Rick Millane. Without his constant guidance and encouragement, this thesis would not have been possible. My special thanks also go to my co-supervisor Dr. Allan McInnes and Dr. Peter Smith. They have provided valuable suggestions for the research. I am also grateful to Prof Phil Bones and Dr Steve Weddell for their advice and encouragement. I am grateful to the NZ Tertiary Education Commission for award of Top Achiever Doctoral scholarship.

I would like to extend my appreciation to Einar Enevoldson, formally of NASA Dryden Flight Research Centre and Jim Murray of NASA Dryden Flight Research Centre. Einar and Jim provided the flight data described in Chapter 3 and have been the source of much useful information and advice. NASA Dryden also provided support in terms of instrumentation for these flights as well as helping with some publication costs. Dr. Elizabeth Austin also provided advice and encouragement. Einar also piloted, together with Steve Fossett, the flights described in Chapter 3. The Perlan Project flights were supported financially by Steve before his untimely death in 2007.

Many thanks to my colleagues and friends in the Computational Imaging Group and the rest of the Department for their assistance and companionship, especially Victor Lo, David Wojtas, Bing Wu, Bahar Dar, Yu-An Chen, Michael Hwang and Tri Pham Minh. Thanks to my supportive flatmates and friends Maung Shein, Brian Peng, Ysabel Legaspi, Tiffany Su, and Nancy Xu.

Last but not least, it is my parents who have supported me the most throughout my upbringing and education. To my mother Li Kun and father Zhang Yongsheng, I cannot thank you enough.

Preface

This thesis is concerned with the development and application of techniques to use limited flight data collected during sailplane flights to determine the vector wind field in atmospheric mountain waves. The thesis can be divided into three topics. (1) A study of the characteristics, uniqueness and sensitivity to errors in the data, of the problem of estimating the wind velocities from limited flight data. (2) A heuristic method for determining 3D wind velocities from ground velocity and airspeed data, and application to data from sailplane wave flights. (3) Statistical estimation of wind velocities from a number of different kinds of limited flight data using maximum likelihood and maximum *a posteriori* estimation, and application to simulated and actual flight data. Review material is presented in Chapter 1, and original work is presented in Chapters 2-7.

Some of the work presented here builds on work developed by some of the author's predecessors. The bulk of this prior work is described in [1]. This includes the following: Approximately 25% of the work presented in Section 2.2.2. The basic ideas of Section 4.1 and 4.2, although the author has refined these ideas and their implementation and coding. Approximately 20% of the results presented in Section 4.3.1.

Chapter 1 contains a review of background material including relevant atmospheric physics, lee waves, sailplane aerodynamics and flight behavior, and inverse problems.

Chapter 2 contains an analysis of uniqueness and sensitivity of determining wind velocities from flight data consisting of ground velocity with airspeed or heading, or ground velocity alone.

Chapter 3 summarises the four flights for which experimental data is used in the thesis.

Chapter 4 describes a heuristic method of estimating the 3D wind velocities from ground velocity and airspeed data. The method is applied to the above four flights.

Chapter 5 describes methods used to generate simulated flight data.

Chapter 6 describes the application of maximum likelihood estimation to the problem of estimating wind velocities from ground velocity with airspeed or heading data. The methods are applied to simulated data and to actual flight data.

Chapter 7 considers the problem of wind velocity estimation when only ground velocity data are available. Suitable prior models for the airspeed and heading are considered. Maximum *a posteriori* estimators are developed. These estimators are applied to simulated and actual flight data.

A summary of key results from this thesis and suggestions for future research are given in Chapter 8.

Aspects of the work presented in this thesis have been published and presented. They are listed here in order of presentation.

Zhang, N., Millane, R.P., Hunter, A.J., (2009) Estimating 3D wind fields in mountain waves using sailplane flight data. Auckland, New Zealand: New Zealand Marine Science Society and Meteorological Society Joint Conference, 2-4 September 2009.

Zhang, N., Millane, R.P. and Hunter, A.J. (2010) Estimating wind velocity from limited aircraft flight data. Wuhan, China: 2010 2nd International Conference on Industrial Mechatronics and Automation (ICIMA), 30-31 May 2010. In Proceedings 626-629.

Zhang, N., Millane, R.P. and Hunter, A.J. (2010) In situ determination of wind fields from sailplane flight data. San Diego, CA, USA: In "Image Reconstruction from Incomplete Data VI," P.J. Bones, M.A. Fiddy and R.P. Millane (Eds.), Proc. SPIE, Vol. 7800, 78000A/1-6, 2010.

Millane, R.P., Stirling, G.D., Brown, R.G., Zhang, N., Lo, V.L., Enevoldson, E. and Murray, J.E. (2010) Estimating Wind Velocities in Mountain Lee Waves Using Sailplane Flight Data. Journal of Atmospheric and Oceanic Technology 27(1): 147-158.

Zhang, N., Millane, R.P., Enevoldson, E. and Murray, J.E. (2010) Measuring 3D Wind Fields in Mountain Waves Using Sailplane Flight Data. Szeged, Hungary: XXX OSTIV Congress, 28 July 4 August 2010.

Zhang, N., Millane, R.P., Enevoldson, E. and Murray, J.E. (2010) Measuring 3D Wind Fields in Mountain Waves Using Sailplane Flight Data. Technical Soaring 36(2): 57-66.

Zhang, N., Millane, R.P., Hunter, A.J., Enevoldson, E. and Murray, J.E. (2011) Estimating wind velocities from limited sailplane flight data. Dallas, Texas: 13th International Association of Science and Technology for Development (IASTED) International Conference on Image and Signal Processing, 14-16 Dec 2011. In Proc. IASTED Signal and Image Processing 2011, 109-114.

Zhang, N., Millane, R.P., Enevoldson, E. and Murray, J.E. (2012) Determining wind fields in mountain waves using sailplane flight data. San Diego, CA, USA: In "Image Reconstruction from Incomplete Data VII," P.J. Bones, M.A. Fiddy and R.P. Millane (Eds.), Proc. SPIE, Vol. 8500, 85000S/1-9, 2012.

Zhang, N., Millane, R.P., Enevoldson, E. and Murray, J.E. (2012) Estimating wind velocities from limited sailplane flight data. Texas USA: XXXI OSTIV Congress, 8-15 August 2012.

Zhang, N., Millane, R.P., Enevoldson, E. and Murray, J.E. (2012) Mountain wave 3D wind fields from sailplane flight data. Wellington, New Zealand: New Zealand Meteorological Society Annual Conference, 19-20 November 2012.

Chapter 1

Introduction

1.1 The Atmosphere

The state of the atmosphere is defined by the fundamental parameters temperature, density, pressure and humidity. Dry air behaves almost as an ideal gas, which is governed by the ideal gas law

$$PV = nRT, \tag{1.1}$$

where P is the pressure, V is the volume of gas, n is the number of moles of gas, $R = 8.31432\ JK^{-1}mol^{-1}$ is the universal gas constant, and T is the absolute temperature.

1.1.1 Pressure and temperature versus altitude

Standard atmosphere models are defined using a representative vertical distribution of atmospheric parameters. These standard conditions are the basis for most aircraft performance data, and are used for calibration of aircraft flight instruments. A commonly-used model is the International Standard Atmosphere (ISA), which defines a standard atmospheric pressure of 1013.2 millibars and a temperature of 288°K (15°C) at sea level [2]. According to the temperature change with increasing altitude, the earth's atmosphere is divided into 4 layers, namely the troposphere, stratosphere, mesosphere and thermosphere. The boundaries between the layers are called the tropopause, stratopause, and mesopause. The standard atmosphere model assumes a dry atmosphere for which the ideal gas law and hydrostatic equation apply. The pressure, temperature, density, and speed of sound profiles for the standard atmosphere model are shown in Fig. 1.1. The pressure and density decrease exponentially with altitude, however the temperature can decrease, increase with altitude or stay constant in different layers. Most weather phenomena occur in the troposphere since this layer contains most of the water vapor and clouds. The lower part of the troposphere interacts with the land and sea surface, and produces thermals, mountain waves and sea-breeze fronts. Sailplanes are usually flown in the troposphere, and have also been flown into the lower stratosphere with lift provided by mountain waves.

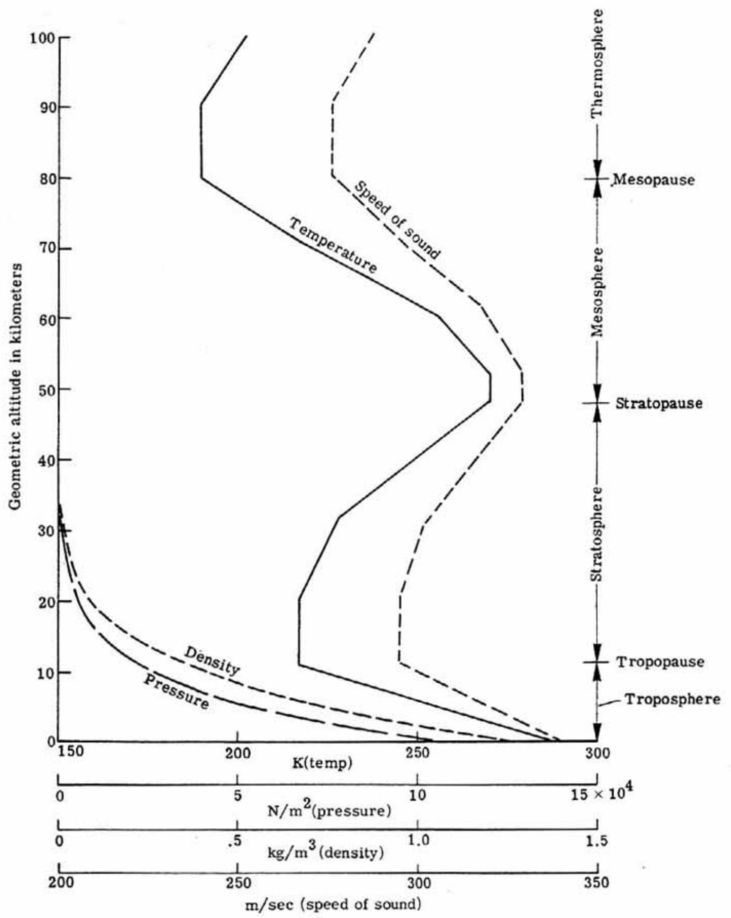

Figure 1.1 US standard atmosphere model: temperature, pressure, density and speed of sound versus altitude [2].

The relationships between temperature, density and pressure in the atmosphere are derived as follows. Consider a small column of air with unit horizontal cross-section area as shown in Fig. 1.2 between height z and $z+dz$. The pressure exerted on the bottom and the top of the air column surface is $P+dP$ and P, respectively. The mass of the air between z and $z+dz$ in the column of air is $dm=\rho dz$ where ρ is the density of the air. The force on the column due to gravity is $gdm=g\rho dz$ where g is the acceleration due to gravity. At hydrostatic equilibrium, the force acting on the air column due to the pressure difference $dP=P(z+dz)-P(z)$ is equal and opposite to the force due to gravity, i.e. $dP=-g\rho dz$. This gives the hydrostatic equation

$$\frac{dP}{dz}=-g\rho. \tag{1.2}$$

The air density is given by

$$\rho=\frac{nm_0}{V}, \tag{1.3}$$

where $m_0=0.02896$ kg/mol is the mean molar mass of air and V is the volume. Using the

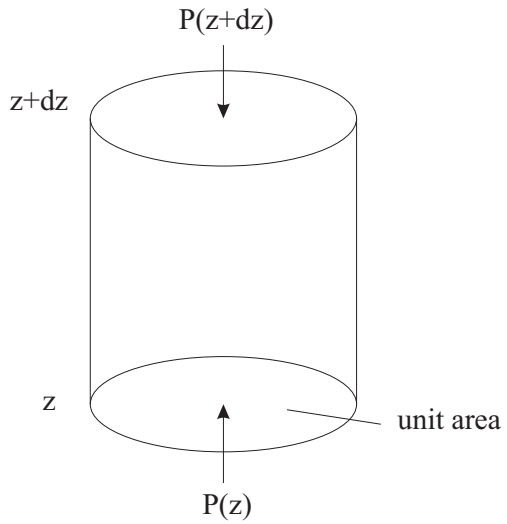

Figure 1.2 A column of air between height z and $z + dz$ with unit horizontal cross-sectional area.

ideal gas law (1.1) and (1.3) gives

$$P = \rho R_d T, \tag{1.4}$$

where $R_d = R/m_0 = 287.053$ Jkg^{-1}K^{-1} is the specific gas constant for dry air, i.e. the gas constant normalised by the molar mass of dry air. Substituting (1.4) into (1.2) gives

$$\frac{dP}{dz} = -\frac{gP}{R_d T}. \tag{1.5}$$

The lapse rate $\Gamma(z)$ is defined as the rate of change of temperature with altitude, i.e.

$$\Gamma(z) = \frac{dT}{dz}. \tag{1.6}$$

Consider first the case when the temperature is constant, i.e. $\Gamma(z) = 0$, and $T = T_0$, where T_0 is the temperature at a reference altitude z_0. This applies in the lower stratosphere between an altitude of about 11 and 20 km. From (1.5),

$$\frac{dP}{P} = -\frac{g}{R_d}\frac{dz}{T_0}, \tag{1.7}$$

and integrating both sides gives

$$\log\left(\frac{P}{P_0}\right) = -\frac{g}{R_d T_0}(z - z_0), \tag{1.8}$$

where P_0 is the pressure at altitude z_0. The pressure therefore decreases exponentially with altitude, i.e.

$$P = P_0 \exp\left(-\frac{g}{R_d T_0}(z - z_0)\right). \tag{1.9}$$

Consider now the case where the temperature changes linearly with altitude, i.e. Γ is constant and non-zero, and $dT = \Gamma dz$. Substitution into (1.5) gives

$$\frac{dP}{P} = -\frac{g}{R_d \Gamma}\frac{dT}{T}. \tag{1.10}$$

Integrating (1.10) gives

$$\log\left(\frac{P}{P_0}\right) = -\frac{g}{R_d\Gamma}\log\left(\frac{T}{T_0}\right), \tag{1.11}$$

where P_0 is the pressure at altitude z_0, so that

$$\frac{P}{P_0} = \left(\frac{T}{T_0}\right)^{\alpha}, \tag{1.12}$$

where $\alpha = -g/R_d\Gamma$. The temperature is given by $T = T_0 + \Gamma(z - z_0)$ so that

$$P = P_0\left(1 + (z - z_0)\frac{\Gamma}{T_0}\right)^{\alpha}, \tag{1.13}$$

which gives the pressure as a function of altitude. Taking z_0 as the altitude at sea level and defining z_1 as altitude above sea level, then

$$P = P_0\left(1 + \frac{\Gamma z_1}{T_0}\right)^{\alpha}. \tag{1.14}$$

1.1.2 Moisture in the atmosphere

The air density is affected by the amount of water vapor in the air. This is because the molecular weight of water vapor (18.0153 g/mol) is lower than that of the majority of the gases in the air (predominately nitrogen at 28.0134 g/mol and oxygen at 31.9989 g/mol). The amount of water vapor that air can sustain is affected by the temperature. Warm air can hold more moisture than dry air. The (mass) mixing ratio, r, is defined as the mass of water vapor contained in a unit mass of air, and can also be written in terms of partial pressures as

$$r = \frac{\varepsilon e}{P}, \tag{1.15}$$

where ε is the ratio of specific gas constant of dry air to that of water vapor, $\varepsilon = R_d/R_v = 0.622$, R_v is the specific gas constant for water vapor, and e is the partial pressure of the water vapor. The subscripts v and d denote water vapor and dry air, respectively. Air is said to be saturated when the liquid water and vapor contained in the air are at equilibrium at a certain temperature. The partial pressure of water vapor at saturation at temperature T is denoted $e_s(T)$. The mixing ratio at saturation r_s is then

$$r_s = \frac{\varepsilon e_s(T)}{P}. \tag{1.16}$$

The energy per unit mass required to change a substance from one state to another is called the latent heat L. At the transition from liquid water to water vapor the amount of heat absorbed per unit mass of water is called the latent heat of vaporization, L_v. The variation of the partial pressure of water vapor in saturated air e_s with respect to temperature is given by the Clausius-Clapeyron equation [3]

$$\frac{de_s}{dT} = \frac{L_v}{TdV}, \tag{1.17}$$

where dV is the increase of volume as a unit mass of water changes from liquid to vapor. Since the volume of the water vapor is much greater than that of the liquid, dV is approximately equal to the volume of water vapor per unit mass V_v. Using the ideal gas law, for unit mass of water vapor,

$$dV = V_v = \frac{1}{\rho_v} = \frac{R_v T}{e_s}, \tag{1.18}$$

where ρ_v is the density of water vapor and T is the temperature at the phase transition. Substituting (1.18) in (1.17) gives

$$\frac{de_s}{dT} = \frac{L_v e_s}{R_v T^2} \tag{1.19}$$

which is an alternative form of the Clausius-Clapeyron equation with volume eliminated.

Another important measure of the moisture content of air is the relative humidity (RH), defined as the ratio of the partial pressure of water vapor in the air to that of water vapor in saturated air, i.e.

$$RH = \frac{e}{e_s} = \frac{r}{r_s}. \tag{1.20}$$

Dry air has a RH of 0% and saturated air a RH of 100%.

1.1.3 Adiabatic lapse rate

The effects of vertical movement of air in the atmosphere are conveniently analysed using the concept of an "air parcel." An air parcel can be imagined as a small mass of air whose passage through the environment can be traced. It is influenced by the environment but does not influence the environment. The pressure in the parcel is equal to that of the environment but its temperature, density, etc. may differ from the environment. Vertical movement of an air parcel with no heat transfer between the air parcel and the ambient atmosphere, is called an adiabatic process. Assuming dry or unsaturated air, the dry adiabatic lapse rate is derived as follows.

Consider an air parcel of unit mass rising adiabatically from height z to $z + dz$. The work performed on the air parcel is, using (1.2),

$$dW = VdP = -gdz. \tag{1.21}$$

The change in the enthalpy, the total energy, of the air parcel dH is given by

$$dH = c_p dT = c_p \Gamma(z) dz, \tag{1.22}$$

where c_p is the specific heat capacity of air at constant pressure, $c_p = 1.0 \times 10^3$ Jkg^{-1}K^{-1}. For an adiabatic process, $dH = dW$ so that from (1.21) and (1.22),

$$\Gamma_d(z) = -\frac{g}{c_p}, \tag{1.23}$$

i.e. Γ_d is constant (independent of altitude) and $\Gamma_d = -9.8$ K/km. The negative sign is expected since as the air rises, it expands and cools. This applies to moist unsaturated air also since the moisture content gives little change to the specific heat. The relationships between pressure, temperature and altitude for Γ constant derived in Section 1.1.1 are therefore of particular importance. If the troposphere were in perfect adiabatic equilibrium then the lapse rate would be Γ_d. However, the adiabatic equilibrium is imperfect (i.e. conduction effects are present), the troposphere tends to be more isothermal, and the typical, or environmental, lapse rate Γ is about -5 K/km [4].

For saturated air, the lapse rate decreases (i.e. is less negative) since condensation of water vapor (as the temperature decreases) releases latent heat that warms the air as it rises. When a saturated air parcel rices, the heat released to the parcel due to condensation per unit mass of air is [3]

$$dQ = -L_v dr_s. \tag{1.24}$$

The total heat transferred to the rising air parcel is then

$$c_p dT + g dz + L_v dr_s = 0. \tag{1.25}$$

Taking the logarithm of (1.16) and differentiating gives

$$\frac{dr_s}{r_s} = \frac{de_s}{e_s} - \frac{dP}{P}. \tag{1.26}$$

Using (1.5) and (1.19) and substituting in the RHS of (1.26) gives

$$\frac{dr_s}{r_s} = \frac{L_v dT}{R_v T^2} + \frac{g dz}{R_d T}. \tag{1.27}$$

Substituting for dr_s from (1.27) into (1.25) gives

$$\left(c_p + \frac{L_v^2 r_s}{R_v T^2}\right) dT + g\left(1 + \frac{L_v r_s}{R_d T}\right) dz = 0, \tag{1.28}$$

and the saturated adiabatic lapse rate is given by

$$\Gamma_s = \frac{dT}{dz} = \left(-\frac{g}{c_p}\right) \frac{(1 + (L_v r_s)/(R_d T))}{(1 + (L_v^2 r_s)/(c_p R_v T^2))}. \tag{1.29}$$

As r_s is a function of temperature and pressure, Γ_s is also a function of temperature and pressure and can be written in the form $\Gamma_s = \Gamma_d f(T, P)$ and $f(T, P) < 1$. Since the temperature and pressure depend on altitude, Γ_s generally varies with altitude. Γ_s is typically -4 K/km near the surface, and -(6-7) K/km in the middle of the troposphere [4]. At high altitudes where the air is colder and holds less water vapor, Γ_s nearly equals Γ_d. Note that if the latent heat L_v were zero then Γ_s would equal Γ_d as expected. Γ_s is dependent on temperature in such a way that the lower the temperature, the less moisture the air holds and the closer Γ_s is to Γ_d. When a moist air parcel rises, it cools dry adiabatically following the dry adiabat with a constant potential temperature until it reaches a RH of 100% (this is called the lifting condensation level (LCL)) and it then follows the saturated adiabat with any further lifting.

1.1.4 Potential temperature

Potential temperature θ is a quantity related to temperature that is defined to remove the effects of dry adiabatic temperature changes. By definition, θ is the temperature that an air parcel at pressure P would acquire if adiabatically brought to a standard reference pressure or altitude.

The potential temperature as as a function of altitude is then simply

$$\theta(z) = T(z) - \Gamma_d z, \tag{1.30}$$

where the reference altitude is at $z = 0$. If the reference pressure is denoted P_0, then using (1.12) and (1.23) shows that the potential temperature can be written in terms of pressure as

$$\theta(P) = T(P) \left(\frac{P_0}{P} \right)^{R_d/c_p}. \tag{1.31}$$

For an adiabatically displaced air parcel the potential temperature is constant, i.e. $d\theta/dz = 0$.

1.1.5 Virtual temperature and virtual potential temperature

A virtual temperature T_v is defined to include the buoyant effect of water vapor and liquid water in the air. Virtual temperature is the temperature dry air must have to have a density equal to the density of moist air at the same pressure. Since water vapor is less dense than dry air, moist unsaturated air is more buoyant than dry air at the same temperature. Therefore, the virtual temperature of unsaturated moist air is always greater than the actual air temperature. The density of liquid water is greater than that of dry air, thus cloudy (saturated) air is less buoyant than cloud-free air at the same temperature. The ideal gas law (1.4) can be written for moist air in terms of virtual temperature as

$$P = \rho R_d T_v. \tag{1.32}$$

The pressure is given by

$$P = P_d + e, \tag{1.33}$$

where P_d denotes the partial pressure of the dry air and

$$\rho = \rho_d + \rho_v = \frac{P_d}{R_d T} + \frac{e}{R_v T} = \frac{P - e}{R_d T} + \frac{e}{R_v T}. \tag{1.34}$$

Substituting (1.34) into (1.32) and using (1.15) gives

$$P = \left(\frac{\varepsilon e}{r} - e + \varepsilon e\right)\frac{T_v}{T} = \frac{\varepsilon e}{r}, \tag{1.35}$$

and simplifying gives

$$\frac{T_v}{T} = \left(1 - \left(\frac{1}{\varepsilon} - 1\right) r\right)^{-1}, \tag{1.36}$$

and expanding to first order in r and substituting $\varepsilon = 0.622$ gives

$$T_v = T\left(1 + \left(\frac{1}{\varepsilon} - 1\right) r\right) = T(1 + 0.61r). \tag{1.37}$$

For saturated air, the liquid water contained in the air due to condensation needs to be taken into consideration, and the virtual temperature is given by

$$T_v = T(1 + 0.61 r_s - r_L), \tag{1.38}$$

where r_L is the mixing ratio of liquid water. In the same context, the virtual potential temperature for moist air is given by

$$\theta_v = \theta(1 + 0.61r), \tag{1.39}$$

and for saturated air by

$$\theta_v = \theta(1 + 0.61 r_s - r_L). \tag{1.40}$$

1.1.6 Stability of the atmosphere

Stability is a measure of the gravitational resistance of the atmosphere to vertical displacements. A region of the atmosphere is said to be statically stable if a vertically-displaced air parcel in this region tends to return to its equilibrium position. The restoring force that brings the air parcel back to equilibrium is a buoyancy force and is a result of the difference in density between the air parcel and the air into which it moves. The stability depends on the difference between the adiabatic and environmental lapse rates. This can be seen in Fig. 1.3 by considering an air parcel at the cross-over point. If $\Gamma < \Gamma_d$, then a parcel displaced upwards is colder and therefore heavier than the surroundings and has a tendency to fall back to its original position and the atmosphere is statically stable. A parcel displaced downwards will be lighter and will also tend to return to its original position. If $\Gamma > \Gamma_d$ the environmental temperature falls more rapidly with height than the dry adia-

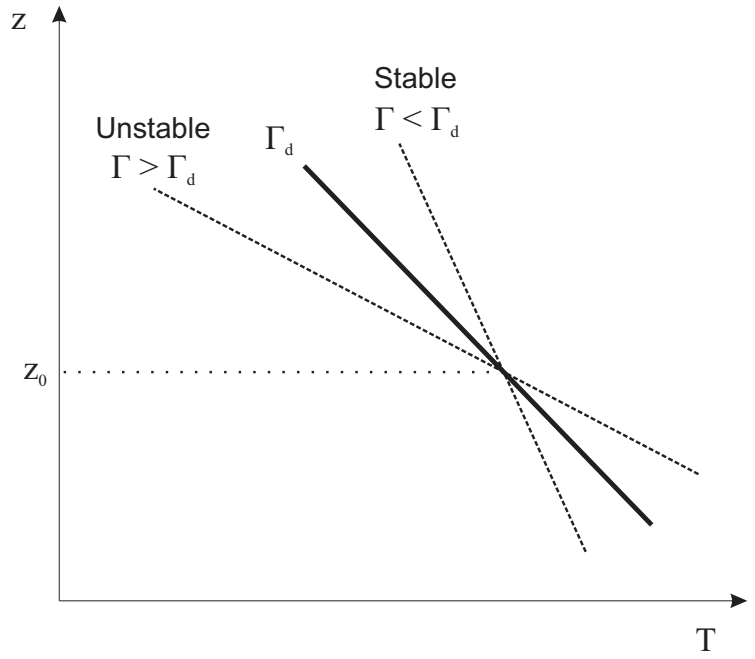

Figure 1.3 Illustration of stability of the atmosphere using the temperature profile. The dashed lines indicate environmental lapse rates, and the solid line indicates the dry adiabatic lapse rate.

batic lapse rate and a parcel displaced upwards is lighter than the surroundings and will continue to rise, and the atmosphere is statically unstable. If $\Gamma = \Gamma_d$ the atmosphere is said to be neutrally stable. For saturated air the same applies with Γ_d replaced by Γ_s. If $\Gamma_s < \Gamma < \Gamma_d$, a saturated parcel is unstable and an unsaturated parcel is stable, and the atmosphere is sometimes called conditionally stable.

In a stability stable region, the restoring force causes the air parcel to oscillate about the rest position and eventually back to the equilibrium. Consider an air parcel with volume V in a statically stable environment originally at the equilibrium height z_0 with density ρ_0, displaced by a small increment in height dz. The density of the environment is a function of altitude, $\rho(z)$. The buoyancy force is equal to the weight of air displaced by the air parcel, given by

$$F = -gVd\rho = -kdz, \tag{1.41}$$

where $d\rho = \rho(z) - \rho_0$, the difference between the density of the air parcel and the environment, and $k = gVd\rho/dz$. The negative sign is a result of, for example, if $d\rho$ is positive then the air parcel is denser ('heavier') than the environment and the restoring force is down (-ve z). Since the restoring force is proportional to, and is the opposite direction to (assuming that $d\rho/dz$ is positive), the displacement, the air parcel is a simple harmonic oscillator with spring constant k. Newton's third law for the air parcel is then

$$-kdz = \rho_0 V \frac{d^2(dz)}{dt^2}. \tag{1.42}$$

Denoting the displacement of the air parcel by z_ρ, (1.42) becomes

$$\frac{d^2 z_\rho}{dt^2} + \left(\frac{k}{\rho_0 V}\right) z_\rho = 0 \tag{1.43}$$

which has solution

$$z_\rho(t) = A\cos(\omega_0 t + \phi), \tag{1.44}$$

where A is the amplitude, ϕ is a phase shift, and ω_0 is the natural frequency of the harmonic motion given by

$$\omega_0 = \left(\frac{k}{\rho_0 V}\right)^{1/2} = \left(\frac{g}{\rho_0}\frac{d\rho(z)}{dz}\right)^{1/2}. \tag{1.45}$$

In meteorology, ω_0 is called the buoyancy, or Brunt-Väisälä frequency, and is equal to about 0.01 s^{-1} for average tropospheric conditions [5]. In meteorology, the buoyancy frequency is usually denoted N, but the notation ω_0 will be used here to emphasize that it is a natural frequency of the system. It can also be shown that the buoyancy frequency is related to the potential temperature by [6]

$$\omega_0^2 = \frac{g}{\theta}\frac{d\theta}{dz}. \tag{1.46}$$

For saturated air, the same applies with the potential temperature replaced by the virtual potential temperature.

The static stability, denoted S, of a region of the atmosphere is defined by

$$S = \omega_0^2. \tag{1.47}$$

If ω_0 is real then $S > 0$ and the atmosphere is statically stable. If ω_0 is imaginary, the solution to (1.43) has exponential growth, $S < 0$ and the region is unstable.

Static stability depends on the difference between the environmental and adiabatic lapse rates, and can be quantified as follows. The density difference $d\rho$ in the above analysis has two components, one due to the change in density of the air parcel as it rises (assumed dry adiabatically) and one due to the change in the density of the environment with altitude. Consider an unsaturated air parcel originally at height z_0, with values of temperature T_0, pressure P_0 and density ρ_0 all equal to its surroundings. If the parcel is adiabatically displaced to $z_1 = z_0 + dz$, its temperature is increased to $T_{p1} = T_0 + \Gamma_d dz$. The temperature of the environment at z_1 is $T_{e1} = T_0 + \Gamma dz$ where Γ is the environmental lapse rate. The pressures inside and outside the parcel at z_1 are equal, i.e. $P_{e1} = P_{p1} = P_1$. Referring to (1.4), the density difference is then

$$\begin{aligned} d\rho &= \frac{P_1}{R_d}\left(\frac{1}{T_{p1}} - \frac{1}{T_{e1}}\right) \\ &= \frac{P_1}{R_d}\left((T_0 + \Gamma_d dz)^{-1} - (T_0 + \Gamma dz)^{-1}\right) \\ &= \frac{P_1}{R_d T_0}\left(\left(1 + \frac{\Gamma_d}{T_0}dz\right)^{-1} - \left(1 + \frac{\Gamma}{T_0}dz\right)^{-1}\right). \end{aligned} \tag{1.48}$$

As $\Gamma_d dz$ and Γdz are small, the first order Binomial expansion of (1.48) is

$$\begin{aligned} d\rho &\approx \frac{P_1}{R_d T_0}\left(1 - \frac{\Gamma_d}{T_0}dz - 1 + \frac{\Gamma}{T_0}dz\right) \\ &= \frac{P_1}{R_d T_0^2}(\Gamma - \Gamma_d)dz, \end{aligned} \tag{1.49}$$

and substituting into (1.45) gives

$$\omega_0 = \left(\frac{g}{T_0}(\Gamma - \Gamma_d)\right)^{1/2}, \tag{1.50}$$

i.e. the buoyancy frequency is a function of the difference between the environmental and adiabatic lapse rates.

1.2 Mountain lee waves

Mountain lee waves are a type of atmospheric gravity wave (AGW) that are generated by stratified flow over mountains. AGWs are an oscillation arising from buoyancy, as described in Section 1.1.6. In a stable stratified atmosphere the buoyancy is continuously distributed, and if the air is disturbed from equilibrium, the buoyancy force tends to restore any displacement which then causes the oscillation [7]. AGWs can propagate up to altitudes of 100 km and dissipation of wave energy can have a significant impact on the atmospheric circulation and they are of considerable importance in meteorology.

If the disturbance originates from obstacles in the flow, such as mountains and ridges, waves are formed above and downstream of the source. Such terrain generated AGWs are classified into two types: mountain waves and lee waves. Mountain waves are formed over the mountains, propagate vertically, and thus they are found not only at low levels over hills and mountains, but throughout the troposphere and even in the stratosphere. The highest amplitudes of these waves are well above the mountains. Lee waves are trapped or resonant waves that form in the lee of the barrier under particular conditions of the vertical structure of stability and wind speed, as illustrated in Fig. 1.4. Trapped lee waves reach their highest amplitude in the confined layer on the lee side of the mountains. They have shorter wavelengths than mountain waves (typically 2-20 km) and they can extend far downwind of the mountain and also to large altitudes. Trapping is imperfect however

and there is some propagation upward and the wave loses energy. It is these trapped lee waves that sailplane pilots use to gain altitude and they are the subject of this thesis. The two types of waves are collectively called orographic waves or simply mountain waves. Classification of waves on a particular day can be difficult because the two types can be present simultaneously and because there is a continuum between the two. In general, mountain waves are found higher in the atmosphere and tend to have longer wavelengths and smaller amplitudes than lee waves [8].

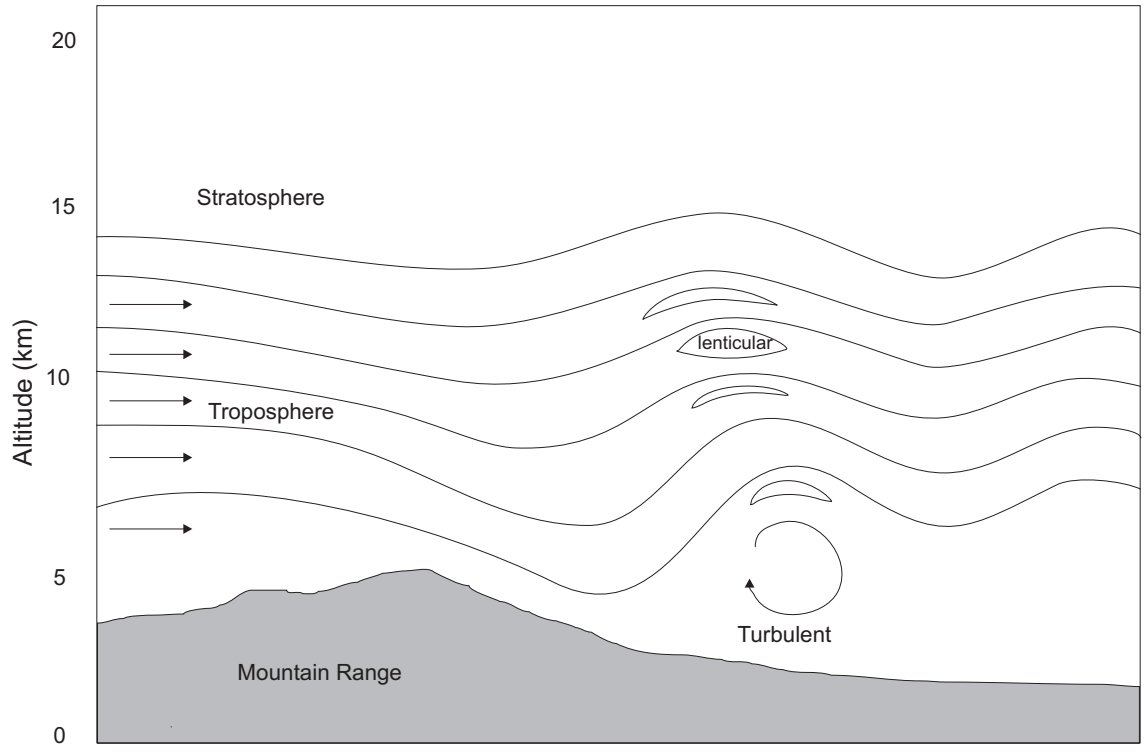

Figure 1.4 Lee wave structure [6]

Lee waves are of significant importance in meteorology. They can influence the vertical structure of wind speed and temperature fields, cause fluctuations in wind speeds in the lower atmosphere, and can affect ozone concentration [9, 10, 11]. Wave momentum dissipation with height results in drag that affects the general circulation of the atmosphere [6, 12, 13]. Turbulence associated with lee waves can produce strong vertical velocities, particularly down drafts, that can be an aviation hazard [14, 15]. Strong waves can generate thin layers of turbulence due to wave breaking [6, 16]. Lee waves also play a role in the vertical transport of aerosols and trace gasses.

Lee waves may be indicated by specific wave cloud formations if there is sufficient moisture in the atmosphere, and sufficient vertical displacement to cool the air below the dew point. These wave clouds, often called lenticulars, do not move downwind with the flow as convective clouds do, but remain fixed in position relative to the obstruction that forms

them. Lee wave clouds are characterised by narrow middle level cloud bands parallel to the mountain chain, as shown in Fig. 1.5. The distance between the cloud bands gives the wavelength of the lee waves. The clouds show as white in visible satellite images, and in

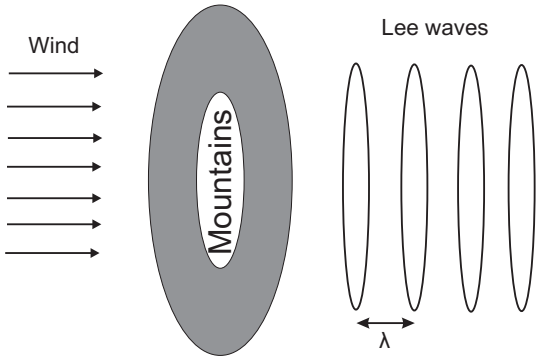

Figure 1.5 Lee wave clouds.

infrared satellite images they can vary from white to dark grey depending on their temperature. Examples of lee wave patterns in visible and infrared satellite images are shown in Fig. 1.6(a) and (b), in which the parallel cloud bands correspond to the crests of waves.

Atmospheric parameters, particularly the spatial distribution of 3D wind velocities, of mountain lee waves can be measured with a variety of observational techniques. Radiosonde soundings have been used to study mountain waves [19]. Radiosondes give a trace of the horizontal wind speed and direction over the ascent path which is determined by the wind profile with altitude. Vertical speeds and vertical wavelengths can be estimated from radiosonde data, however this method is error sensitive and limited to space-time paths of the radiosonde. VHF Doppler radar uses processing of backscattered signals from inhomogeneities in radio refractive index to estimate three-dimensional wind speeds [10, 20, 21]. This technique has good spatial and temporal resolution and a range of up to 100 km. The equipment used, however, is large and expensive. Satellite scatterometer synthetic aperture radar (SAR) measurements of wind speeds are based on measurements of the ocean surface roughness and appropriate processing to derive surface wind speeds. SAR images have been used successfully to study gravity waves by their effect on near surface wind field variations [22, 23, 24]. However, this technique is suitable only over the ocean and for low level phenomena.

Instrumented aircraft have also been used to study mountain lee waves. One of the first such studies was by Lilly and Kennedy [25] and Lilly and Lester [26] in 1970, in waves in the lee of the Colorado Rockies. They used four or five instrumented aircraft that flew horizontal upwind/downwind legs at various altitudes. Temperature, pressure and navigational data were recorded from which horizontal and vertical wind velocities were derived. Mountain waves have also been studied using instrumented aircraft as part of the Mesoscale Alpine Program (MAP) [27] in the European Alps [28], the Pyrenees Experiment

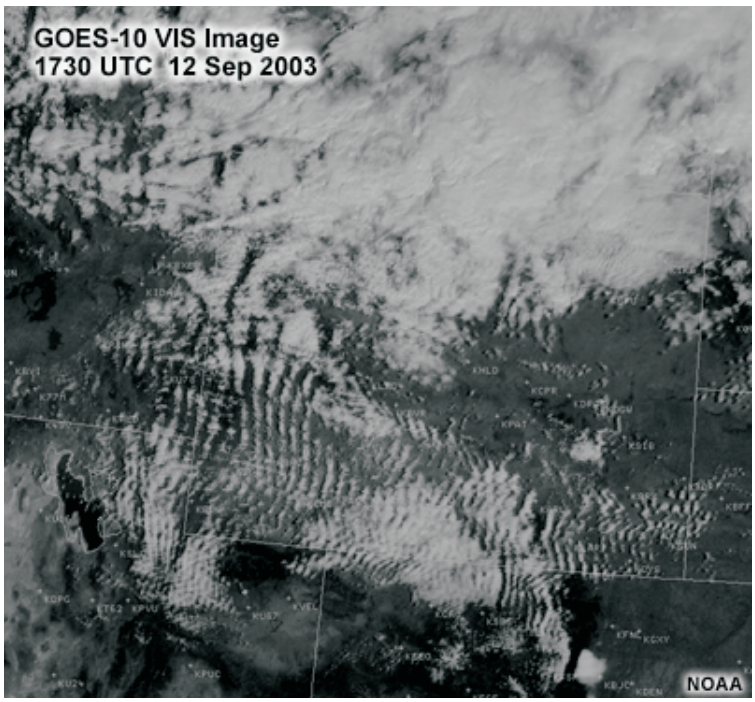

(a)

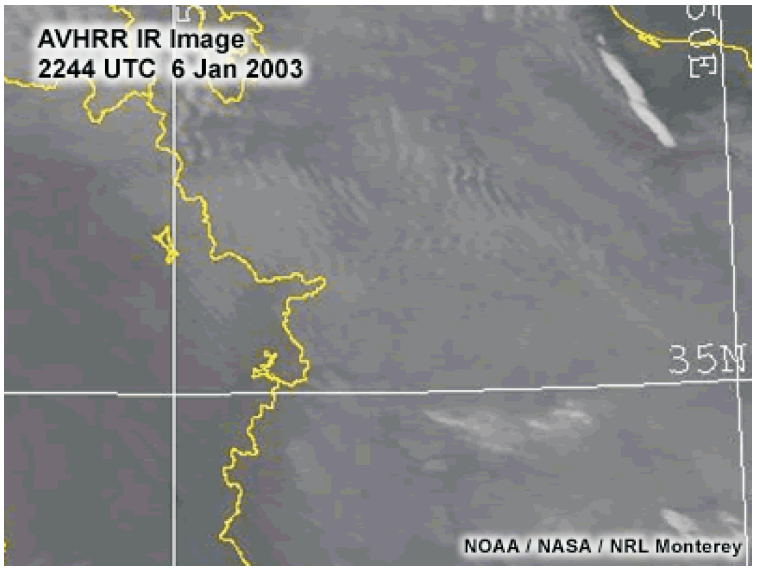

(b)

Figure 1.6 Lee wave cloud patterns shown by (a) GOES-10 visible image of Wyoming on 12 September 2003 [17] and (b) AVHRR infrared image of western Iran on 6 January 2003 [18].

(PYREX) [29], and the Terrain-Induced Rotor Experiment (T-REX) in the Sierra-Nevada wave [30]. All of these programs used multiple, highly instrumented aircraft with multiple sensors, and represent, of course, substantial and expensive experimental campaigns.

Sailplanes are often flown in mountain wave systems and there is potential to use recorded flight data to derive the wind velocities along the flight path. In fact, some of the earliest information on mountain waves was obtained from sailplane flights [31]. One approach is to install in a sailplane a sophisticated flight measurement system that records sufficient data to make a direct measurement of the wind speed and direction. Such a system has been described for a sailplane that uses airspeed, acceleration, altitude, heading, position, and control surface deflection data to derive wind speed and direction [32]. This is an expensive approach, however, and is limited to only a few sailplanes. A second option is to use the limited data recorded from conventional sailplane flight recorders that are often installed in sailplanes. Such an approach offers the possibility of analysing data from many sailplane flights, and methods for implementing this are the topic of this thesis.

Modern sailplane flight computers generally calculate estimates of the wind speed and direction, and the vertical wind speed (lift). There are, however, a number of limitations with using these instruments for accurate data collection for postflight analysis. The wind speed and direction estimates are generally based on circling flight but the precision when the pilot is not executing a constant rate turn is unclear. Estimates also may be made for a dogleg in the flight path but the precision of the estimates obtained in this case is not clear. Estimates of lift (vertical wind speed) are generally based on data from a total energy or Netto variometer. The precision obtained is dependent on the kind of the total energy correction used and the time constants of the instrument. Furthermore, estimates of wind speed and direction and lift are made in real time and displayed to the pilot, but are usually not logged in the instrument and so are not available for later analysis. Any data (aside from position) that is recorded, is usually stored only in summary (statistical) form.

There has been limited use of sailplane data for studying mountain waves. A number of early studies were qualitative in nature [31]. More recently, the OSTIV Mountain Wave Project [33] has collected data from a well-instrumented sailplane and results have been presented for lee waves in the Andes [34]. Methods have been developed to extract wave climbs from databases of sailplane flight logs [35]. Flight data from multiple flights also have been analysed to derive statistical characteristics of lee waves in northern Germany [36]. Flights in a sailplane fitted with a digital variometer and a gyroscope/ accelerometer also have been used to study internal rotor structures [37].

1.2.1 Linear mountain wave theory

General theory for waves in the atmosphere is very complicated. A full analysis needs to consider the fluid dynamics, gravity, thermodynamics and rotation of the Earth. However, various approximations can be made and if the height of the mountain is small compared to the vertical wavelength then the main characteristics of mountain waves are captured by

the linear theory. This is sufficient for the purpose of understanding the basics of lee waves for this thesis. For horizontal ranges less than 100 km the effect of rotation of the Earth can be neglected. Compressibility of the atmosphere can also be neglected. The density and pressure can be separated into background parts and a deviation that depends only on altitude. Consider the two-dimensional problem, i.e. the effect of a long mountain or ridge, in two variables x and z representing horizontal distance and height. Under these conditions the atmosphere can be described by the two-dimensional Boussinesq model which is represented by the following equations [38]

$$\frac{\partial u}{\partial t} + u\frac{\partial u}{\partial x} + w\frac{\partial u}{\partial z} = -\frac{1}{\rho}\frac{\partial P}{\partial x} \tag{1.51}$$

$$\frac{\partial w}{\partial t} + u\frac{\partial w}{\partial x} + w\frac{\partial w}{\partial z} = -\frac{1}{\rho}\frac{\partial P}{\partial z} - g \tag{1.52}$$

$$\frac{\partial u}{\partial x} + \frac{\partial w}{\partial z} = 0 \tag{1.53}$$

$$\frac{\partial \rho}{\partial t} + u\frac{\partial \rho}{\partial x} + w\frac{\partial \rho}{\partial z} = 0, \tag{1.54}$$

where $u = u(x, z, t)$ and $w = w(x, z, t)$ are the horizontal and vertical velocity, respectively. Equation (1.51) describes momentum in the x-direction, (1.52) describes momentum in the z-direction, (1.53) is the mass continuity equation, and (1.54) represents the conservation of thermal energy.

Assuming that the velocities u and w can be separated into steady, horizontally uniform background values and small perturbations, i.e. $u(x, z, t) = u_0(z) + u_1(x, z, t)$ and the background value $w_0(z) = 0$, the Boussinesq equations (1.51)-(1.54) can be linearised, and integrating twice with respect to x gives

$$\frac{\partial^2 w}{\partial x^2} + \frac{\partial^2 w}{\partial z^2} + l^2 w = 0, \tag{1.55}$$

where l is the Scorer parameter defined as [39, 40]

$$l^2(z) = \frac{\omega_0^2}{u_0^2} - \frac{1}{u_0}\frac{d^2 u_0}{dz^2}. \tag{1.56}$$

The second term in (1.56) is usually small and can be neglected.

Equation (1.55) is a wave equation, and assuming a time-harmonic solution of the form

$$w(x, z, t) = \tilde{w}(z)\exp(i(kx - \omega t)), \tag{1.57}$$

where k is the horizontal wavenumber and ω is the angular frequency, (1.55) becomes

$$\frac{d^2\tilde{w}}{dz^2} + (l^2 - k^2)\tilde{w} = 0. \tag{1.58}$$

Such a solution would occur with a sinusoidal boundary condition at the surface of the

form $z = h(x) = \sin(kx)$ since $dw(x, z)/dz$ must vanish on the surface.

1.2.2 Homogeneous atmosphere

If l is constant with altitude, then solutions to (1.58) take the form

$$\tilde{w}(z) = A \exp(imz) + B \exp(-imz), \tag{1.59}$$

where $m = (l^2 - k^2)^{1/2}$, which leads to a disturbance that decays with height if $l < k$, but which is sinusoidal with height if $l > k$. In the latter case, the solution takes the form

$$w(x, z, t) = \cos(kx + mz) \exp(-\omega t), \tag{1.60}$$

where m is the vertical wavenumber, and the wave propagates upwards. The lines of constant phase tilt off the vertical at an angle β where

$$\cos \beta = \frac{k}{\sqrt{k^2 + m^2}}. \tag{1.61}$$

The wave propagates at an angle β to the horizontal and the frequency is $\omega_0 \cos \beta$, as shown in Fig. 1.7.

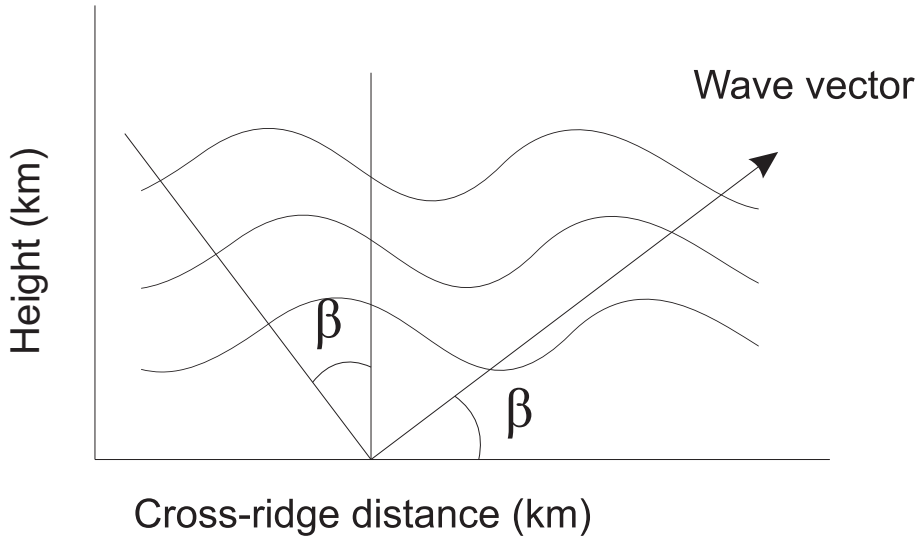

Figure 1.7 Illustration of streamlines of the waves with a phase tilt of β.

Consider now an isolated feature (hill or mountain) in the topography. The topography $z = h(x)$ can be represented by its Fourier components through a Fourier integral. Since (1.58) is linear, the solution is then the sum of the responses (1.59) for each Fourier component, with each weighted by the Fourier transform of the topography. Queney [41] conducted this calculation for profile $h(x) = 1/(a^2 + x^2)$ which has a simple Fourier transform. In this

case there is no trapping mechanism and the wave propagates upwards and lee waves are not generated (Fig. 1.8(a)).

1.2.3 Trapped lee waves

Trapped lee waves can be generated only if there is a variation of the stability or wind speed with altitude. Scorer [39] considered the simple case where the atmosphere consists of two layers with Scorer parameters l_1 and l_2 for the lower and upper layers, respectively. For convenience, the interface is taken at $z = 0$ and the ground at $z = -h$. Requiring that the disturbance in the upper layer decays with height gives

$$\tilde{w}(z) = A \exp(-\mu_2 z), \tag{1.62}$$

where

$$\mu_2 = \sqrt{k^2 - l_2^2}, \tag{1.63}$$

and in the lower layer for a sinusoidal topography the solution has the form

$$\tilde{w}(z) = B \exp(i\mu_1 z) + C \exp(-i\mu_1 z), \tag{1.64}$$

where

$$\mu_1 = \sqrt{l_1^2 - k^2}. \tag{1.65}$$

Enforcing the boundary conditions at the interface, i.e. continuity of $\tilde{w}$ and $d\tilde{w}/dz$ at $z = 0$, and seeking a resonance solution, Scorer showed that the condition

$$\cot(\mu_1 h) = -\frac{\mu_2}{\mu_1} \tag{1.66}$$

must be satisfied. He then showed that (1.66) has a solution only if

$$l_1^2 - l_2^2 > \frac{\pi^2}{4h^2}. \tag{1.67}$$

Hence the Scorer parameter in the lower layer must be larger (more stable or lower wind speed) than in the upper layer (less stable or larger wind speed). The solution for the case of an isolated topography can be obtained as in the previous section by summing over the wavenumbers each with relative weight determined by Fourier Transform of the topography. The dominant horizontal wavenumbers are those whose corresponding wavelength matches the width of the topography. An example is shown in Fig. 1.8(b). Trapped lee waves have no phase tilt although in practice the trapping is not perfect and there is some phase tilt and some loss of energy upwards. In general, the Scorer parameter must decrease significantly over some altitude range in order to support resonant lee waves. From (1.65), in the lower layer $l_1 > k$ so that the wave in the lower layer propagates vertically. However, the wave is repeatedly reflected from the upper layer and the flat ground downwind from the mountain and the superposition of upward and downward propagating waves

gives the standing wave.

Referring to (1.63) and (1.65) shows that the horizontal wavenumber in the two-layer system satisfies

$$l_2 < k < l_1. \tag{1.68}$$

The horizontal wavelength is given by $\lambda = 2\pi/k$ so that the lee wave wavelength satisfies

$$\frac{2\pi}{l_1} < \lambda < \frac{2\pi}{l_2}. \tag{1.69}$$

Using (1.50) shows that the wavelength is restricted to the interval

$$2\pi u_0 \left(\frac{g}{T_1}(\Gamma_1 - \Gamma_d)\right)^{-1/2} < \lambda < 2\pi u_0 \left(\frac{g}{T_2}(\Gamma_2 - \Gamma_d)\right)^{-1/2}, \tag{1.70}$$

where the subscripts 1 and 2 refer to values in the lower and upper layers, respectively. Equation (1.70) can be used to estimate bounds on the wavelength if approximate layers can be identified in a particular case.

The above analysis provided basic information on trapped lee waves, but in practice of course the situation is very complex. The effect of complex terrain, variable distributions of stability and wind speed with altitude, and nonlinearities require numerical solution of the general equations of fluid dynamics for a full solution ([43][44][45]). Nonlinearities become significant when the Froude number F, where

$$F = \frac{v_a}{\omega_0 h}, \tag{1.71}$$

is less than about unity, i.e. for a tall obstacle, slow flow or the stratification becomes very strong [46].

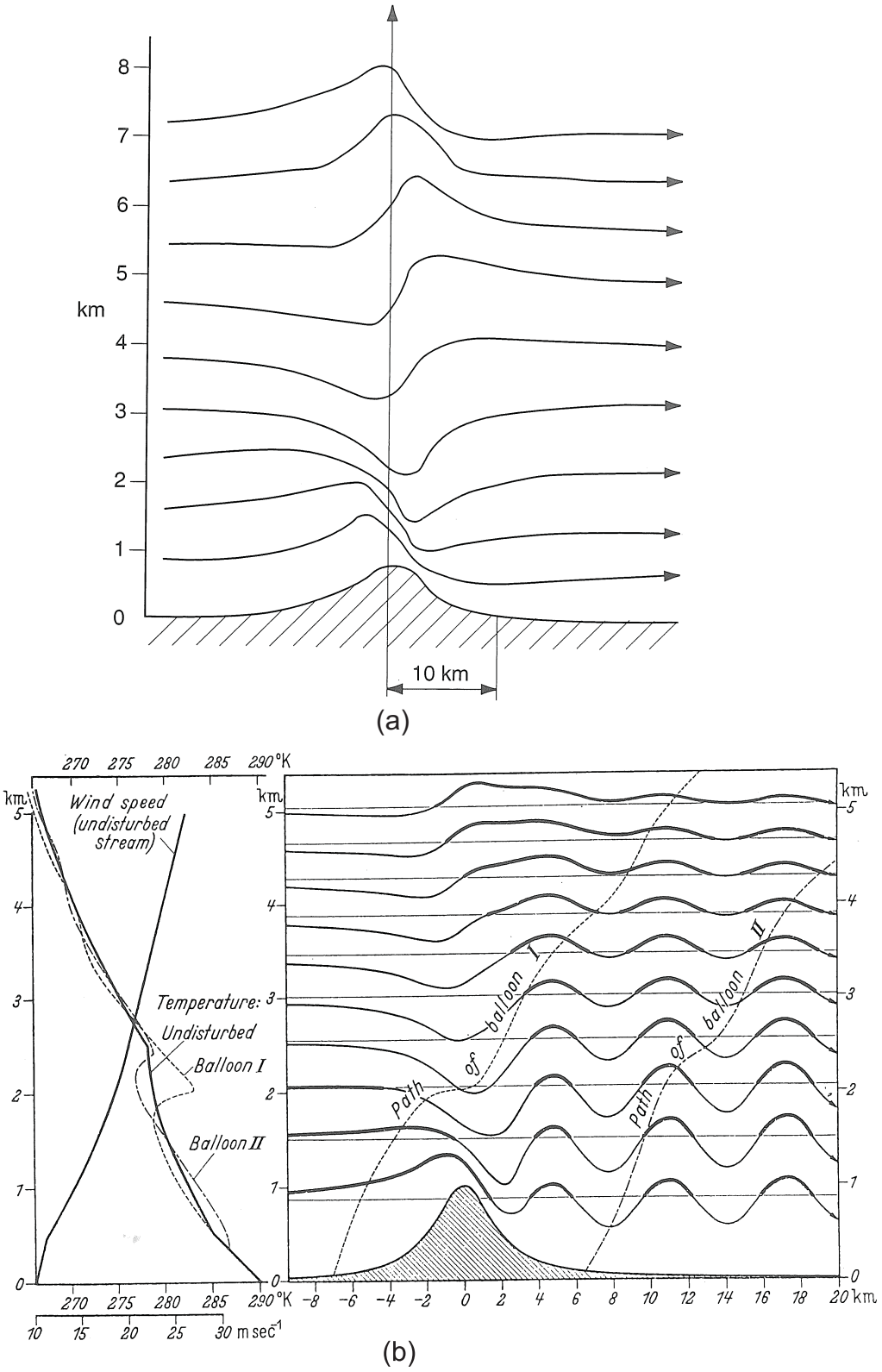

Figure 1.8 Illustrations of streamlines of (a) a vertical propagating wave and (b) a trapped lee wave [42].

1.3 Sailplanes

Sailplanes, or gliders, are heavier-than-air aircraft whose free flight does not use the power of an engine. Sailplanes usually do not carry an engine, and therefore need to be launched to a suitable altitude before free flight begins. Launch methods include towing by a powered aircraft, or using a ground-based winch or vehicle tow. Some sailplanes are equipped with an engine, allowing them to be launched under their own power. With the engine shut down, they display the same flight characteristics as non-engine-powered sailplanes.

Sailplanes are generally flown for recreation, in which the objective is to gain altitude and remain aloft by flying in regions of rising air (referred to by sailplane pilots as "lift"). Since the sailplane is unpowered, it is always sinking through the air, but altitude can be gained if the airmass in which it is flying is rising faster than the glider sink rate. Long distance flights of hundreds of kilometers are possible by using multiple lift sources along the track to regain the height lost between lift sources. "Cross-country soaring" is one of the objectives of many recreational glider flights in which the pilot attempts to fly a maximum distance or over a prescribed course. Another goal may be to attain the highest altitude possible. In gliding competitions, the objective is to fly around a course in the shortest time, and strategic and efficient use of lift sources is necessary.

Although sailplanes are generally flown for recreation, they have also been used for atmospheric research [31, 32], but this has been limited and there is further potential for this application. One advantage of the use of sailplanes is their relatively simple and well-documented aerodynamics. This thesis is concerned with the use of sailplane flights for studying atmospheric mountain waves.

There are three main sources of lift utilised by sailplane pilots: thermal lift, ridge lift and wave lift. The most common form of lift is created by thermals, which are warm columns of air, often created by uneven heating on the ground, that ascend due to lower density than the surroundings. Thermals may be marked by cumulus clouds that form when the moist air rises above the LCL. The sailplane pilot gains altitude by turning in tight circles within the rising air column [47, 48]. Ridge lift occurs when the wind blows over an obstacle (hill or slope) and the air is deflected upward along the face of the windward slope. Wave lift occurs when stable air flows over a hill or mountain and oscillates on the lee side of the mountain forming a wave that extends downwind, as described in Section 1.2. Sailplanes are flown in the regions of ascending air in the wave, gaining altitude. Such waves can extend many times higher than the mountain range to altitudes of over 40,000 feet and extend up to one hundred kilometers downwind of the mountain [47, 48]. The only lift source considered in this thesis is wave lift.

1.3.1 Sailplane maneuvers and controls

A sailplane is maneuvered around three axes of rotation by moving pilot controls that move control surfaces, as shown in Fig. 1.9. These axes of rotation are the vertical axis, the

lateral axis, and the longitudinal axis relative to the sailplane, with origin at the center of gravity of the sailplane. The sailplane rotation around these axes are yawing, pitching, and rolling, respectively. These rotations are controlled using a control stick and two rudder pedals. The rudder pedals control yawing of the sailplane about the vertical axis. The pilot presses on the left pedal to yaw the nose to the left, and right pedal to yaw the nose to the right. Pushing forward or pulling back the control stick operates the elevator, a horizontal control surface on the tail, and results in nose-down and nose-up pitching rotations of the sailplane about the lateral axis. Left or right movement of the control stick operates the ailerons, horizontal control surfaces on the wingtips. The ailerons move in opposite directions which results in the left or right banking (rolling) of the sailplane about the longitudinal axis. When the controls are "centered", the attitude of the sailplane remains

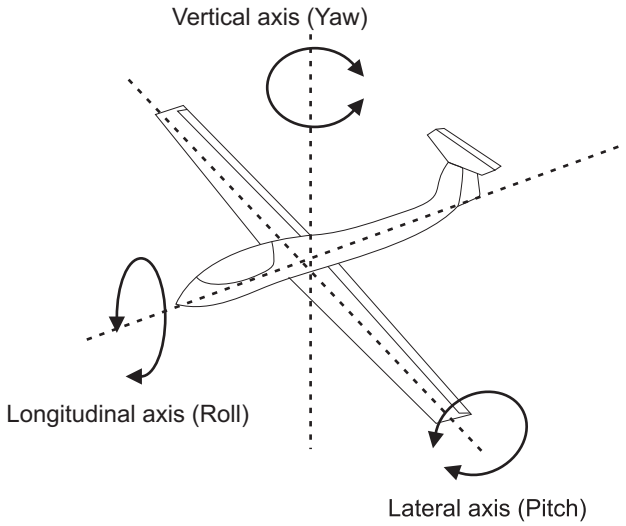

Figure 1.9 The axes of rotation of the sailplanes.

constant. Deflection of the ailerons rolls the aircraft and the amount of deflection determining the roll rate. Once the desired roll has been obtained, the control is centered to sustain that value. To "un-roll" the aircraft, opposite control deflection is required. Deflection of the rudder produces a yaw acceleration until the yawing moment produced by the rudder is balanced by yaw moments induced by the resulting sideslip. Control of pitch works in a similar fashion to yaw. The elevator produces a pitch acceleration until the pitching moment induced by the elevator is balanced by the pitching moment of the aircraft at its new angle of attack. For the sailplane to turn, it must be held in a banked rotation. The horizontal component of the lift of the banked wing provides the centripetal force for the turn as described in Section 1.3.3.

1.3.2 Sailplane aerodynamics - steady flight

A rigorous description of the production of lift by an airfoil is complicated in general and involves solving the Navier-Stokes equations for fluid flow. For the purpose of this thesis

however, it is sufficient to note that the shape of a lifting airfoil has the overall effect of deflecting the air downwards as shown in Fig. 1.10. The air therefore exerts an upwards force on the airfoil which is the lift. The shape of the airfoil is such that the average static pressure on the upper surface is lower than on the lower surface, the pressure difference producing the lifting force.

A more optimal explanation is that the airfoil at an angle of attack forces the flowing air to follow a locally downward turning path, as shown in Fig. 1.10. The flow experiences a downward force from the wing, and by Newton's third law (for each force there must be an equal force in the opposite direction) the flow applies an equal force upwards to the wing, which is the lift [49].

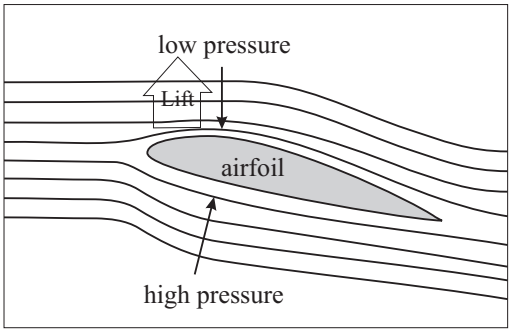

Figure 1.10 A flow field around an airfoil.

In steady flight there are three forces acting on a sailplane, namely lift (L), drag (D) and weight (W), as shown in Fig. 1.11. In a steady straight glide, the three forces are balanced and the vector sum of the lift and drag (the total aerodynamic force) is the negative of the weight and so is directed vertically upwards. A straight line drawn between the leading edge and the trailing edge of an airfoil is called the chord line. The angle between the chord line and the relative wind direction (the direction of air flow experienced by the airfoil) is called the angle of attack, α (Fig. 1.11). The magnitude of the relative wind is the speed of the glider through the air, or its airspeed.

The lift L is defined as the component of the aerodynamic force on the airfoil that is perpendicular to the relative wind (Fig. 1.11) and is given by [50, 51]

$$L = \frac{1}{2}\rho v_a^2 A C_L, \tag{1.72}$$

where C_L is the coefficient of lift, v_a is the airspeed, ρ is the air density, and A is the wing (airfoil) surface area. C_L depends on α (and the shape of the airfoil). As α increases, C_L increases until a critical angle of attack α_c is reached, which gives the maximum lift (Fig. 1.12). Thereafter, the lift reduces as the angle of attack further increases.

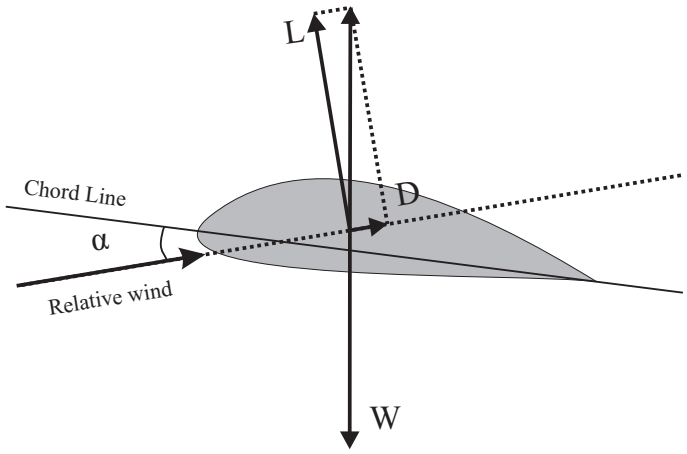

Figure 1.11 Forces on an airfoil and the angle of attack

Drag is the component of the aerodynamic force on the airfoil that is parallel to the relative wind (Fig. 1.11). The drag is given by [50, 51]

$$D = \frac{1}{2}\rho v_a^2 A C_D, \tag{1.73}$$

where C_D is the drag coefficient. C_D increase with angle of attack (Fig. 1.12). The drag consists of two components called induced drag and parasitic drag. Induced drag is associated with the generation of lift (i.e. it is "induced" by the lift) and parasitic drag is due to other interference of the airflow by the sailplane [50, 51]. The drag coefficient C_D is therefore divided into two components,

$$C_D = C_{Di} + C_{D0}, \tag{1.74}$$

where C_{D0} is the parasitic (zero-lift) drag coefficient and C_{Di} is the lift-induced drag coefficient. The coefficient of induced drag depends on C_L by [50, 51]

$$C_{Di} = \frac{C_L^2}{\pi e AR}, \tag{1.75}$$

where e is the Oswald's efficiency factor (typically $e < 0.85$), and $AR = b^2/S$ is the aspect ratio of the wing with wingspan (length) b and area S (the aspect ratio is approximately the span of the wing divided by its width or chord). The coefficient of parasitic drag C_{D0} is independent of C_L.

The configuration of a sailplane airfoil for low and high airspeeds is shown in Fig. 1.13. At low airspeeds, the angle of attack is large, the relative wind is close to horizontal, and the L/D is large. Since α is large, C_L is large, and so C_{Di} is large and the induced drag dominates. As the airspeed increases, the angle of attack decreases, C_L decreases and the

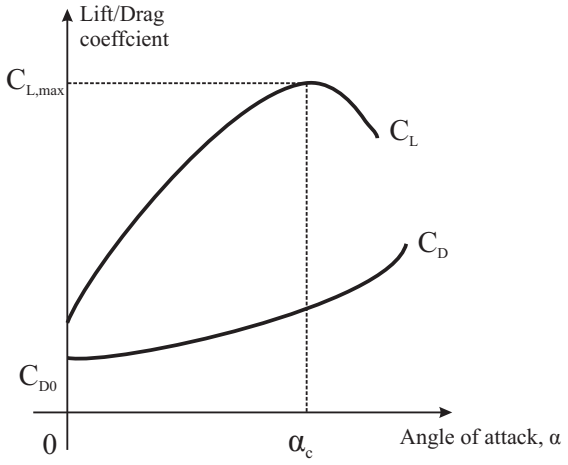

Figure 1.12 Lift and Drag coefficients versus angle of attack [52].

induced drag reduces rapidly, and as a result of the increased airspeed the parasitic drag increases and eventually dominates over the induced drag. The total drag is therefore as shown in Fig. 1.14 and is minimised at a particular airspeed.

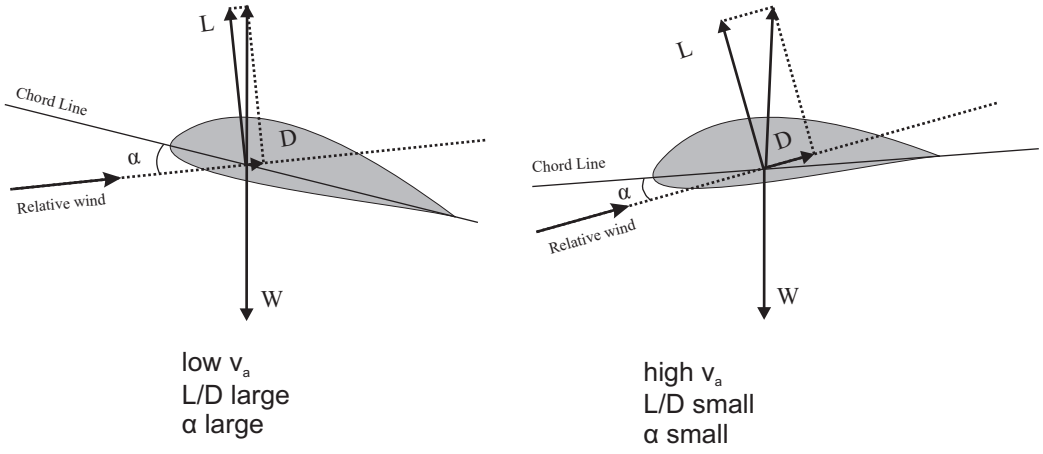

Figure 1.13 Sailplane airfoil configurations at low and high airspeeds.

1.3.3 Sailplane aerodynamics - turning flight

Turning maneuvers cannot be performed with yawing only, instead they are achieved by applying bank with the control stick. Sailplanes turn in downward spiral due to drag. Consider now a sailplane in a constant rate turn at constant airspeed. The sailplane is then

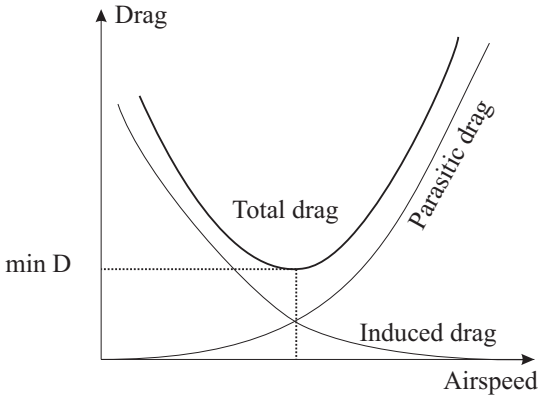

Figure 1.14 Drag versus airspeed (parasitic, induced, and total drag), minimum total drag as shown [52].

flown at a constant bank angle ϕ (the angle between the longitudinal axis of the wing and the horizontal) (Fig. 1.15). Now the vertical component of the lift $L_v = L\cos\phi$ supports the sailplane's weight and the horizontal component $L_h = L\sin\phi$ provides the centripetal force for the turn (Fig. 1.15). Here, for simplicity, we ignore the drag component. If L_v is less than the weight in a turn, the weight will pull the sailplane downward, causing it to descend. The pilot can maintain the altitude by increasing the airspeed or pulling the control stick slightly back to increase the angle of attack. For a constant rate turn the vertical forces are balanced, i.e. $L_v = W$. The centripetal force is equal to the horizontal

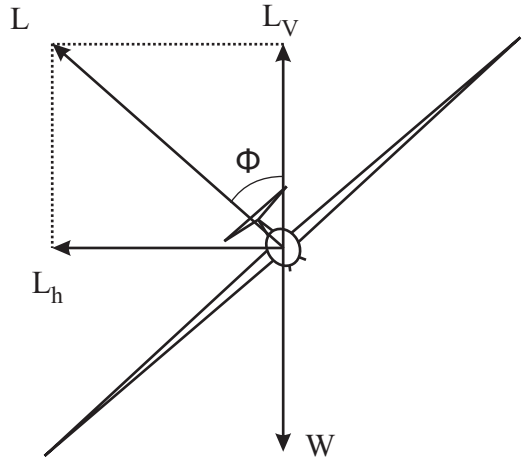

Figure 1.15 The forces acting on a sailplane in a turn with bank angle ϕ.

component of the lift L_h, so that

$$L_h = L\sin\phi = \frac{mv_a^2}{r}, \tag{1.76}$$

where r is the turn radius and m is the mass of the sailplane (Fig. 1.15). Using the above relationships, the bank angle can be expressed in terms of the airspeed and turn radius as

$$\tan\phi = \frac{L_h}{L_v} = \frac{mv_a^2}{r}\frac{1}{mg} = \frac{v_a^2}{gr}. \tag{1.77}$$

The rate of turn ω is given by

$$\omega = \frac{v_a}{r} = \frac{g\tan\phi}{v_a}. \tag{1.78}$$

An important parameter is the load factor n, the ratio of the load supported by the wing to the weight of the sailplane, i.e.

$$n = \frac{L}{W} = \frac{1}{\cos\phi}. \tag{1.79}$$

The load factor is usually expressed in g's and it indicates the acceleration experienced by the pilot and the aircraft. As the bank angle is increased, a larger angle of attack is required to provide the increased lift and the airspeed is generally larger as well. Since an increased load factor increases the stress on the airframe, there is limitation on the maximum load factor of a particular sailplane.

1.3.4 Sailplane performance

Sailplane performance refers to the effect of drag which dissipates energy which results in a loss of potential energy or sinking of the sailplane. Sailplane performance is therefore determined primarily by its sink rate. The sink rate depends mainly on the airspeed but also depends on the air density (altitude) and the sailplane weight.

1.3.4.1 Steady flight

The most important information quantitating a sailplane's performance is the "flight polar" which is provided in the manufacturers flight manual. The flight polar is a plot of the sailplane sink rate versus airspeed in straight flight at sea-level, for a number of different sailplane weights. Figure 1.16(a) shows an example of a polar curve. The stall speed (point A) is the left-hand end point of the polar curve and is the airspeed at which the wing no longer generates lift. The minimum sink rate is the peak point of the curve which occurs at the "minimum sink airspeed" (point B). Flying at the minimum sink airspeed gives the smallest loss of altitude for a fixed time.

There is an important relationship between the lift and drag of the wing and the glide slope of the sailplane, which can be seen by referring to Fig. 1.17. At a particular airspeed v_a with corresponding sink rate s in level flight, in still air, the sailplane follows the direction of the relative wind with glide slope (angle to the horizontal) denoted γ. Referring to Fig. 1.17, the two triangles are similar so that there is a relationship between the glide slope and the lift and drag, which is

$$\cot\gamma = \frac{L}{D}. \tag{1.80}$$

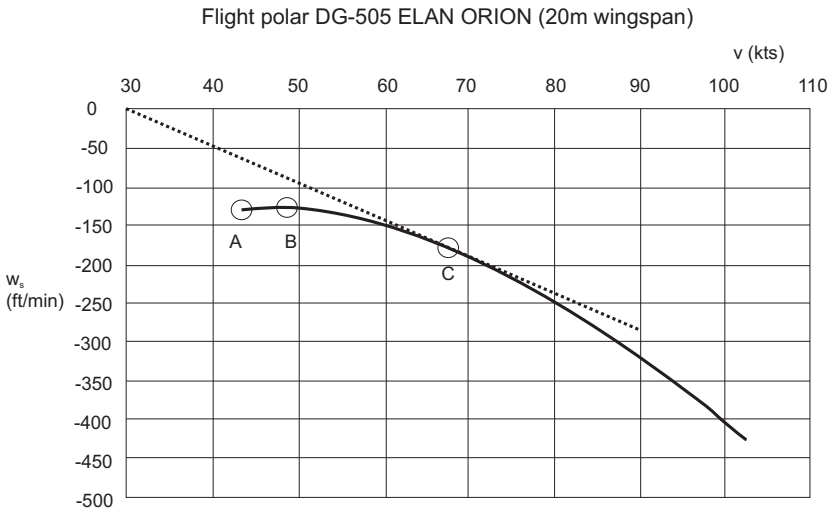

(a)

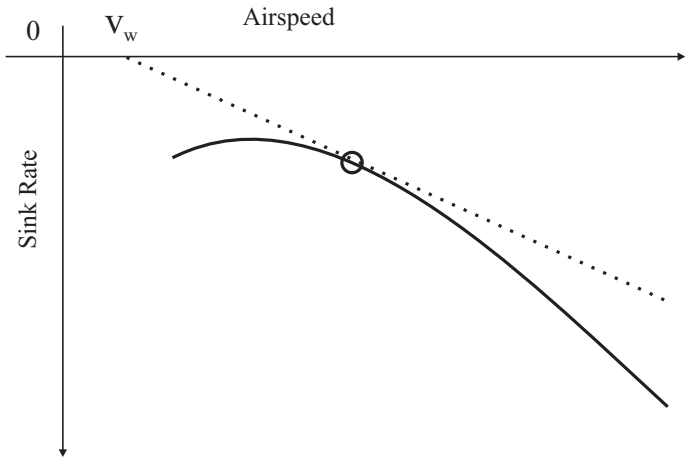

(b)

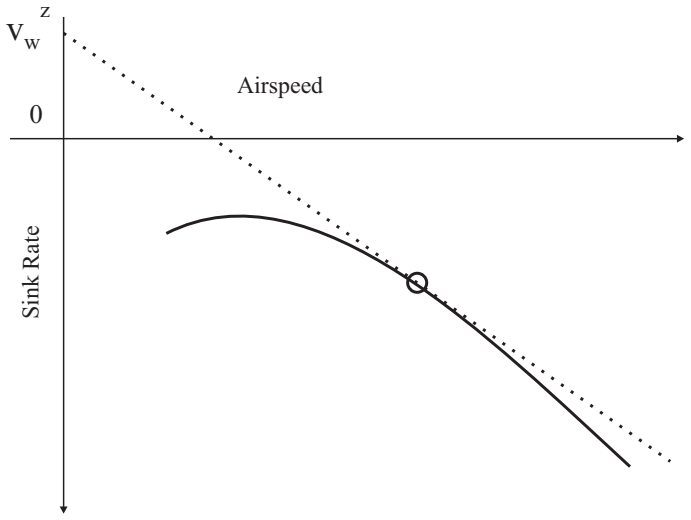

(c)

Figure 1.16 (a) Example of a glider polar curve [53], the dashed line indicates a tangent line of the curve from the origin, point A: stall speed, point B: minimum sink airspeed, point C: best L/D airspeed. Best speed-to-fly (denoted by the circle) in (b) a headwind with speed v_w and (c) sinking air with speed v_w^z.

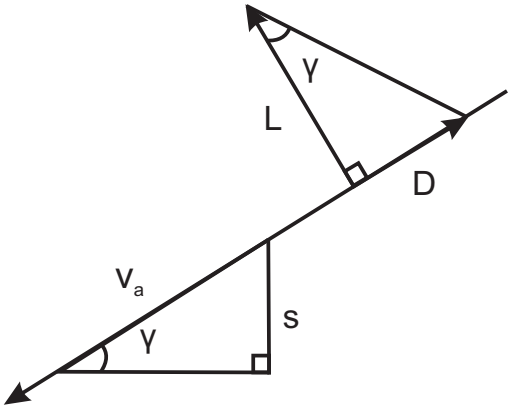

Figure 1.17 L/D Triangle and the glide slope triangle.

An important performance parameter is how far the sailplane travels horizontally for unit loss of altitude, which is equal to $\cot\gamma$, and from (1.80) is also equal to L/D. This performance parameter is often referred to as the "L/D" of the sailplane. Note also that considering the distance traveled in unit time, we also have

$$\operatorname{cosec}\gamma = \frac{v_a}{s}, \tag{1.81}$$

where s is the sink rate of the sailplane. Referring to Fig. 1.16(a) and (1.81), $\operatorname{cosec}\gamma$ is maximised at the point C where a line from the origin is tangent to the polar curve. Since $\cot\gamma$ and $\operatorname{cosec}\gamma$ are both monotonically decreasing functions of γ for γ in the relevant interval, the airspeed at C is also that which gives the maximum L/D, or the shallowest glide slope. This airspeed is often called the "best L/D airspeed," or the "best speed to fly." Flying at the best L/D airspeed allows the pilot to cover the maximum distance for a given loss of altitude in still air. Note that for small glide slopes $\tan\gamma \approx \sin\gamma$, so that

$$\frac{L}{D} \approx \frac{v_a}{s}, \tag{1.82}$$

but not for larger glide slopes.

Since the polar curve is for still air, it is easy to show that the best speed to fly in a moving airmass is determined by shifting the origin of the tangent line accordingly. In a horizontal headwind, the best speed-to-fly is found by shifting the origin of the tangent line to the right along the horizontal axis by the speed of headwind as shown in Fig. 1.16(b). For a tail-wind it is shifted to the left. In sinking air, the origin of the tangent line is shifted upward by the vertical speed of the sinking air, as shown in Fig. 1.16(c), and in rising air it is shifted down. For a head/tail wind and rising/sinking air, both shifts are made.

The performance or sink rate characteristics of a sailplane also depends on the air density, or altitude. This is a result of the lift and drag of an airfoil being proportional to the density

in (1.72) and (1.73). Letting ρ_0 be a reference air density (at sea-level, say), reference to (1.72) and (1.73) shows that the lift and drag at density ρ is the same as at density ρ_0 with an airspeed of $v_a(\rho/\rho_0)^{1/2}$. This quantity is called the "indicated airspeed" IAS, denoted v_a^{ind}, (for reasons described in Section 1.3.5), i.e.

$$v_a^{ind} = \left(\frac{\rho}{\rho_0}\right)^{1/2} v_a. \tag{1.83}$$

The airfoil therefore behaves at density ρ with airspeed v_a, as it would at density ρ_0 with airspeed v_a^{ind}. Therefore at altitude, the airfoil behaves as if it were flying slower. Furthermore, refering to (1.72) and (1.73) shows that

$$\frac{L}{D} = \frac{C_L}{C_D}, \tag{1.84}$$

i.e. the L/D is independent of air density for a fixed angle of attack. If we let the flight polar at sea-level be represented by the function $s_0(v_a)$, then the sink rate at density ρ is given by

$$s = \left(\frac{P_0}{P}\right)^{1/2} s_0\left(v_a^{ind}\right) = \frac{v_a}{v_a^{ind}} s_0\left(v_a^{ind}\right). \tag{1.85}$$

Referring to (1.4) shows that the IAS is given by

$$v_a^{ind} = \left(\frac{P}{P_0}\frac{T_0}{T}\right)^{1/2} v_a, \tag{1.86}$$

so that (1.85) can be used to calculate the sink rate at altitude.

1.3.4.2 Turning flight

Consider now the effect of the sailplane turning on its performance. The flight polar is measured in level flight. The performance cannot be predicted exactly without measurements in turning flight because the effect of, for example, different control surface settings cannot be predicted. However, the performance can be estimated approximately as follows [54]. Consider the sailplane in a turn at IAS v_a^{ind} and bank angle ϕ. Referring to (1.72) and (1.79), the wing is operating at the same lift coefficient in level flight as if the speed were $v_a^{ind}\cos^{1/2}\phi$. The equivalent sink rate can then be obtained from the level-flight polar and the lift-to-drag ratio calculated. The sink rate can then be calculated, noting the vertical component of the lift is $L\cos\phi$. Putting all this together, and using (1.85) shows that the sink rate $s(\phi)$ at bank angle ϕ and IAS v_a^{ind} is

$$s(\phi) = \left(\frac{v_a}{v_a^{ind}}\right) s_0(v_a^{ind}\cos^{1/2}\phi)\cos^{-3/2}\phi. \tag{1.87}$$

This effect is shown in Fig. 1.18 by plotting the difference in sink rate due to bank, $\Delta s(\phi) = -(s(\phi) - s(0))$, as a function of bank angle for two typical sailplane airspeeds at sea level

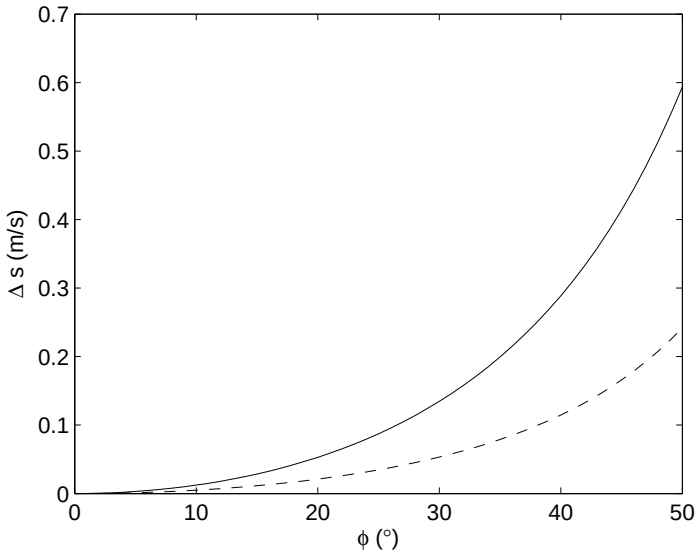

Figure 1.18 Error in sink rate due to banked flight at sailplane IAS of 30 m/s (solid line) and 50 m/s (dashed line) at sea-level for the DG-505M.

using the DG-500M polar. It is seen that the effect is small for bank angles less than $30°$. The effect will also be small at altitude.

1.3.5 Sailplane instruments

Sailplanes have a number of instruments to assist the pilot. The primary instruments are an airspeed indicator (ASI), altimeter, variometer, and compass. Ancillary instrument include radio, flight computer, data logger, transponder, and collision avoidance. The altimeter, ASI and variometer are based on pneumatic measurements although they may be relayed to electrical signals for display. Sailplanes usually collect the pneumatic data.

Typical sailplanes use a pitot-static system which consists of two parts: (1) pitot pressure lines and (2) static pressure lines. The pitot pressure is measured from an open-end tube directly pointed to the relative wind flowing around the sailplane. The pressure of the still air, or static pressure is taken from the static line, which is attached to a vent or vents mounted flush with the side of the fuselage or tube mounted on the vertical stabilizer. The static ports are in locations where the air is not disturbed, and they are normally in pairs, one on either side of the sailplane. The pitot-static system provides sources for the airspeed indicator (ASI), altimeter, and variometer.

The ASI calculates the airspeed from the difference between the pitot and static pressures. For the typical airspeeds and altitudes of sailplanes we can use an incompressible flow approximation and application of Bernoulli's equation [55] shows that the measured airspeed

is given by

$$\left(\frac{2\Delta P}{\rho_0}\right)^{1/2}, \tag{1.88}$$

where $\Delta P = P_{pitot} - P_{static}$ and is often called the impact (or dynamic) pressure, and the air density used is ρ_0, since the ASI is calibrated at sea level where $\rho = \rho_0$. Therefore, the instrument measures the airspeed

$$\left(\frac{2\Delta P}{\rho_0}\right)^{1/2} = \left(\frac{2\Delta P}{\rho}\right)^{1/2}\left(\frac{\rho}{\rho_0}\right)^{1/2} = \left(\frac{\rho}{\rho_0}\right)^{1/2} v_a = v_a^{ind}, \tag{1.89}$$

from (1.83), i.e. the ASI measures the indicated airspeed (hence the word "indicated"), defined by (1.83), rather than the true airspeed. Referring to (1.86), the "true airspeed" (TAS) can be calculated from the IAS by

$$v_a = \left(\frac{T}{T_0}\frac{P_0}{P}\right)^{1/2} v_a^{ind}. \tag{1.90}$$

In practice, the IAS measured by the ASI needs to be corrected for installation errors. The resulting airspeed is called the calibrated airspeed (CAS). For simplicity, we refer to the CAS simply as the IAS in the rest of the thesis.

Since wave flights can reach quite high altitudes, it is advisable to consider the effects of compressibility. It can be shown that for a low Mach number M (the ratio of the TAS to the speed of sound), the airspeed corrected only for density must be multiplied by the additional factor [56]

$$x = \left(1 + \frac{1}{8}(1 - \frac{P}{P_0})M^2\right)^{-1} \tag{1.91}$$

to obtain the TAS. The relative error due to ignoring compressibility, is $\delta = (1 - x)$. This is calculated versus altitude, assuming a standard atmosphere, for two typical sailplane IAS of 30 and 50 m/s, and shown in Fig. 1.19. The error due to ignoring compressibility is therefore less than about 1%.

An altimeter is an aneroid barometer that measures the absolute ambient air pressure at the level where the altimeter is located, and presents altitude indication based on a standard sea-level pressure. For nonstandard conditions a barometric scale is adjusted to calibrate the altimeter. Sailplanes also have magnetic compass which indicates and records the heading of the sailplane.

A variometer provides almost real-time information on performance of the sailplane, which enables the pilot to manoeuver the sailplane to remain in rising air. The variometer uses the rate of change of static pressure to determine rate of climb or descent. The variometer provides means for the pilot to detect rising air and find the location of the strongest lift. Basic variometers are sensitive to changes in pressure altitude caused by changes in airspeed. They therefore measure ascent/descent rate of the sailplane, rather than of the surrounding air. A manual change of airspeed (pull-up or dive manoeuver) can cause

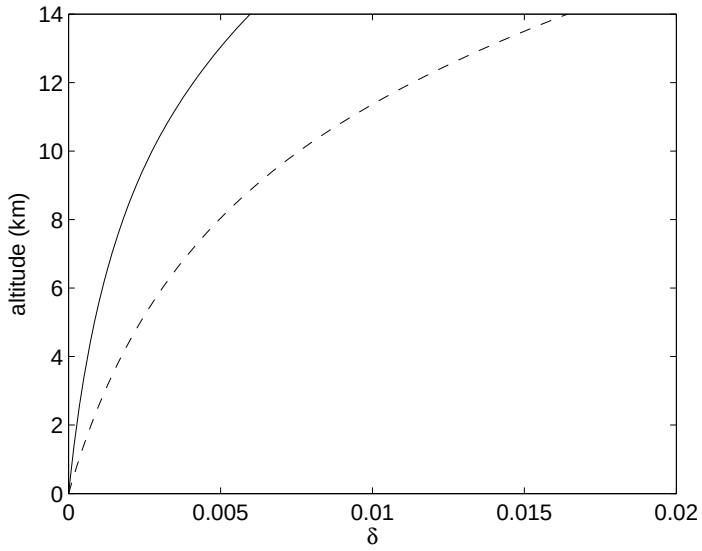

Figure 1.19 The relative error in the TAS due to ignoring compressibility versus altitude for two sailplane IAS of 30 m/s (solid line) and 50 m/s (dashed line).

large transient readings of the variometer. This is due to potential-kinetic energy exchange which is described in more detail in Section 2.3. A variometer with a total energy system compensates for the pressure changes due to changes of airspeed, and hence gives more accurate reading of the vertical air motion (which is what the pilot is interested in). A Netto variometer also compensates for the intrinsic sink rate characteristics of the sailplane based on the polar curve, the airspeed and the sailplane weight.

Modern sailplanes have electronic flight computers on board, which primarily include an electric variometer, a Global Positioning Satellite (GPS) receiver, and a microprocessor. Although a flight computer may measure various quantities, usually only position and time are recorded.

Sailplane flight data are often recorded and archived for evidence of a flight. The International Gliding Commission (IGC) has specified standards for position-recording of the gliding sport. Typical IGC-approved flight recorders consist of a pressure altitude sensor and a Global Navigation Satellite System (GNSS) receiver. The flight position data is recorded and formatted according to the IGC standard. The data can be viewed and analysed using programs such as SeeYou [57]. The IGC format is described in Appendix A.

1.4 Inverse problems and Bayesian inference

In many fields of applied physics, it is often desired to reconstruct the spatial (or other) distribution of a quantity of interest, sometimes referred to as the "object," from measurements of a set of data that are in some way related to the object. If the object is known and an accurate mathematical-physical model is available that allows the data to be calculated from the object (the forward model), then calculation of the data is referred to as a "direct" or "forward" problem. It is common however to have measured the data, and to have knowledge of the forward model, and the need to calculate the object. This is referred to as an "inverse problem." When dealing with inverse problems one usually faces some difficulties, primarily due to a mathematical-physical "inverse" model for explicit calculation of the object from the data not generally being available. Furthermore, the measured data are often incomplete in the sense that there are not enough data to uniquely define the object. Moreover, the problem may be ill-posed, in which case small errors in the data (which are inevitable) can lead to large errors in the solution.

Consider an inverse problem where the object, is characterised by a set of N parameters x_j for $j = 1, ...N$, which are collected together in a vector $\mathbf{x}$, i.e. $\mathbf{x} = (x_1, ..., x_N)$. A finite number M of data are measured which are denoted $\tilde{y}_j$ for $j = 1, ..., M$, and are collected together in the vector $\tilde{\mathbf{y}} = (\tilde{y}_1, ..., \tilde{y}_M)$. The vector $\mathbf{y} = (y_1, ..., y_M)$ is used to denote the results of evaluating $f(\mathbf{x})$, where $f(\mathbf{x})$ represents the forward model. The data $\tilde{\mathbf{y}}$ are different to $\mathbf{y}$ because of measurement noise. The data are then related to the object by

$$\tilde{\mathbf{y}} = f(\mathbf{x}) + \mathbf{n} = \mathbf{y} + \mathbf{n}, \tag{1.92}$$

where $\mathbf{n}$ is a noise vector. Additive noise is assumed but the noise may take any form, depending on the problem at hand.

If a unique solution $\mathbf{x}\{f, \tilde{\mathbf{y}}\}$ exists and varies continuously on the data, the inverse problem is said to be well-posed. Otherwise, the inverse problem is said to be ill-posed. A well-posed problem allows for robust (algorithm convergence, noise tolerance) estimation of the object. However, for an ill-posed problem, the solution may not be unique and may be exquisitely sensitive to the errors (noise) in the data. Obtaining a robust solution for an ill-posed problem requires the incorporation of additional information to stabilise the problem. The additional information can be incorporated by using either deterministic or statistical approaches [58].

Deterministic approaches to solving inverse problems involve the use of deterministic models of the forward problem, and any random components (such as measurement noise) are usually included in the form of weights on the data terms. Two such methods, data matching and regularization, are described in the next two sections. Probabilistic methods on the other hand, model the object, observations and noise as random variables. They make use of probability density functions for estimating object parameters. Two such methods, maximum likelihood and Bayesian are described in the following two sections.

1.4.1 Data matching

In data matching, a solution $\hat{\mathbf{x}}$, where the hat indicates "estimated value," is selected and the corresponding computed "data" $\hat{\mathbf{y}} = f(\hat{\mathbf{x}})$ is calculated and matched against $\tilde{\mathbf{y}}$. The mismatch, measured using some function $\Delta(\tilde{\mathbf{y}}, \hat{\mathbf{y}})$, is minimised by varying $\hat{\mathbf{x}}$, to give the solution

$$\hat{\mathbf{x}}_{DM} = \underset{\hat{\mathbf{x}}}{\operatorname{argmin}} \left\{ \Delta(\tilde{\mathbf{y}}, f(\hat{\mathbf{x}})) \right\}, \tag{1.93}$$

where $\underset{\mathbf{x}}{\operatorname{argmin}} \{f(\mathbf{x})\}$ means the value of $\mathbf{x}$ that minimises $f(\mathbf{x})$. Note that (1.93) can generally be solved only if the problem is over-determined (more data than object parameters) unless regularization (described below) is used. For ill-posed problems however, errors in the data can lead to large errors in $\hat{\mathbf{x}}_{DM}$. The classical least-squares estimate is obtained when the mismatch is measured by the squared difference between $\mathbf{y}$ and $\hat{\mathbf{y}}$, i.e.

$$\Delta_{LS}(\tilde{\mathbf{y}}, \hat{\mathbf{y}}) = ||\tilde{\mathbf{y}} - \hat{\mathbf{y}}||^2, \tag{1.94}$$

where $|| \cdot ||$ denotes the L_2-norm.

1.4.2 Regularization

Regularization is a deterministic scheme used to reduce the effects of noise and allow solution of under-determined problems. Let $\mathbf{x}_0$ be a default (preferred) solution in the absence of data. The idea is that $\mathbf{x}_0$ is a simple solution that incorporates physical constraints on the solution, say for example that it has finite energy. A regularized solution minimises a weighted sum of the mismatch between the observed and computed data, and the mismatch between the preferred and computed solutions, i.e.

$$\hat{\mathbf{x}}_R = \underset{\hat{\mathbf{x}}}{\operatorname{argmin}} \left\{ \Delta_y(\tilde{\mathbf{y}}, f(\hat{\mathbf{x}})) + \lambda \Delta_x(\mathbf{x}_0, \hat{\mathbf{x}}) \right\}, \tag{1.95}$$

and the relative emphasis λ is called the regularization parameter. The regularization term $\Delta_x(\mathbf{x}_0, \hat{\mathbf{x}})$ can be used to reduce non-physical behavior of the solution due to the ill-posed nature of the problem, and to obtain solutions for under-determined problems. Regularization provides better estimation than data matching, but it often does not provide a good model of noise in the data and information on the preferred solution.

1.4.3 Likelihood methods

Likelihood methods are a probabilistic approach that explicitly incorporate information on the statistics of errors in the data and the forward model. Equation (1.92) relates the observed data to the object and the noise and is known as the observation model. The statistics of the noise samples are represented by the probability density $p_n(n)$. The likelihood function $l(\mathbf{x})$ represents the physics of the forward problem as the conditional density

$p(\tilde{\mathbf{y}}|\mathbf{x})$ of the data given the object, i.e.

$$l(\mathbf{x}) = p(\tilde{\mathbf{y}}|\mathbf{x}), \tag{1.96}$$

where $\tilde{\mathbf{y}}$ is the experimentally observed data. The maximum likelihood solution for the model is then obtained as

$$\hat{\mathbf{x}}_{ML} = \underset{\mathbf{x}}{\operatorname{argmax}} \{l(\mathbf{x})\} = \underset{\mathbf{x}}{\operatorname{argmin}} \{-\ln l(\mathbf{x})\}, \tag{1.97}$$

where $-\ln l(\mathbf{x})$ is often called the "negative log-likelihood." When $f(\mathbf{x})$ is deterministic (i.e. the model is assumed to be known exactly), referring to (1.92), (1.97) can be replaced by

$$\hat{\mathbf{x}}_{ML} = \underset{\mathbf{x}}{\operatorname{argmin}} \{-\ln(p_n(\tilde{\mathbf{y}} - f(\mathbf{x}))\}. \tag{1.98}$$

If the noise n_i are mutually independent, zero-mean Gaussian with variances σ_i^2, the probability density is

$$p_n(\mathbf{n}) = \prod_{i=1}^{M} (2\pi\sigma_i^2)^{-1/2} \exp\left(-n_i^2/2\sigma_i^2\right), \tag{1.99}$$

so that

$$p_n(\tilde{\mathbf{y}} - f(\mathbf{x})) = \prod_{i=1}^{M} (2\pi\sigma_i^2)^{-1/2} \exp\left(-(\tilde{y}_i - y_i(\mathbf{x}))^2/2\sigma_i^2\right). \tag{1.100}$$

The maximum likelihood estimate is then

$$\hat{\mathbf{x}}_{ML} = \underset{\mathbf{x}}{\operatorname{argmin}} \left\{ \sum_{i=1}^{M} (\tilde{y}_i - y_i(\mathbf{x}))^2/2\sigma_i^2 \right\}, \tag{1.101}$$

which is equivalent to the weighted least square solution.

Likelihood methods are effective if the problem is over-determined and good noise models are available, but they are not effective if the problem is underdetermined.

1.4.4 Bayesian methods

A Bayesian approach is based on a scheme where models of the physical process, and the nature of the observations and solutions, are used to obtain probability density functions for the solution. Probability based methods for solving inverse problems are more powerful since they explicitly deal with uncertainties in the data, models and the solutions obtained.

The Bayesian approach to obtaining the probability density makes use of additional information about the object, which is expressed in the form of the prior probability density. An analytical framework is used to obtain the conditional probability of the object given the observed data, called the posterior density. Bayesian estimation involves choosing an

appropriate prior distribution and evaluating the posterior distribution. An inference or estimation rule is then used to obtain an estimate of the image from the posterior density. Bayesian methods provide a route to solving underdetermined inverse problems since the incomplete data are supplemented by information from the prior density for the object.

1.4.4.1 Conditional probability and Bayes' theorem

The conditional probability of the occurrence of event A given that the event B has already occurred, $p(A|B)$, can be calculated using

$$p(A|B) = \frac{p(A,B)}{p(B)}. \tag{1.102}$$

where $p(A,B)$ is the joint probability of events A and B. Rearranging the terms, and noting that the events of A and B are arbitrary, gives

$$p(A,B) = p(A|B)p(B) = p(B|A)p(A), \tag{1.103}$$

from which it follows that

$$p(A|B) = \frac{p(B|A)p(A)}{p(B)}. \tag{1.104}$$

For a set of mutually independent events A_i, which span the set of possible outcomes, the total probability theorem states that

$$p(B) = \sum_i p(A_i,B) = \sum_i p(B|A_i)p(A_i). \tag{1.105}$$

Combining (1.104) and (1.105) gives Bayes' theorem

$$p(A_i|B) = \frac{p(B|A_i)p(A_i)}{p(B)} = \frac{p(B|A_i)p(A_i)}{\sum_j p(B|A_j)p(A_j)}. \tag{1.106}$$

1.4.4.2 Application to inverse problems

Bayes' theorem provides an analytical method for obtaining $p(A|B)$ from $p(B|A)$ and $p(A)$. If A and B correspond to the object and observed data respectively, then $p(A)$ corresponds to a prior model for the object, and $p(B|A)$ is a probabilistic representation of the forward, or observation, model (1.92). Bayes' theorem provides the conditional probability of the object given the observed data, the so-called posterior density, from the prior and the observation models.

For the inverse problem (1.92), our knowledge about the object is cast in the form of the prior distribution $p(\mathbf{x})$, where $\mathbf{x}$ is an instance of the object. Combining the statistics of the noise $p_n(\mathbf{n})$, assuming a deterministic operator $f(\cdot)$, the forward model is represented by the likelihood function $p(\tilde{\mathbf{y}}|\mathbf{x})$. A Bayesian inversion provides the posterior density $p(\mathbf{x}|\tilde{\mathbf{y}})$. Inference rules can then be applied to obtain estimates of the object from the posterior

density. A common inference rule, and the only one considered in the thesis, is to select the solution that maximises of the posterior density. The resulting estimate is referred to as the maximum *a posteriori* (MAP) estimate and is given by

$$\hat{x}_{MAP} = \underset{\mathbf{x}}{\operatorname{argmax}} \{p(\mathbf{x}|\tilde{\mathbf{y}})\} = \underset{\mathbf{x}}{\operatorname{argmax}} \{p(\tilde{\mathbf{y}}|\mathbf{x})p(\mathbf{x})\}, \tag{1.107}$$

since $p(\tilde{\mathbf{y}})$ is independent of $\mathbf{x}$. The MAP estimate can therefore be calculated from the forward model, the data and the prior model.

The noise and prior densities usually have parameters associated with them (such as variances), often called hyperparameters, and hence the quality of the solution depends on their accuracy. If the values of the hyperparameters cannot be directly obtained from the data, they must be estimated along with the estimate of the object to obtain the best solution. Typical methods involve iterations of alternate cycles of estimating the hyperparameters and the solution.

The MAP (or other Bayesian) estimate provides a reconstruction of the object that incorporates the data and prior information on the object in an optimum way. It is a particularly powerful approach for solving inverse problems with incomplete data if reasonably good prior information is available.

1.5 Previous work on wind velocity estimation from aircraft flight data

Aircraft flight data have been used to measure wind velocities in a number of applications. The most comprehensive, and expensive, options are highly instrumented, specialized research aircraft that generally use GPS, inertial navigation (INS) and multi-hole pressure probes to derive ground velocities, platform attitude and vector airflow, from which the 3D wind vector can be relatively easily calculated. Such systems have been used to measure mean and turbulent wind vectors [59, 60], and to measure winds in mountain waves [61, 62]. However, they provide a limited facility due to their expense in terms of capital outlay, maintenance, deployment and operation.

A number of less expensive options are available based on light aircraft [63] or unmanned aerial vehicles (UAVs) [64, 65]. These usually incorporate similar instrumentation to research aircraft but in some cases use less expensive equipment such as an inertial measurement unit (IMU) or a scalar airflow probe. However, they are still relatively expensive, require considerable calibration, and the lower-instrumented units require special flight maneuvers such as helical or circular flight patterns to derive the vector wind speed. Some of the wind field estimation techniques using UAVs are described here.

Mayer *et al.* [66] have developed a 'no-flow-sensor' wind velocity estimation algorithm that uses only onboard GPS information (time, altitude, flight path azimuth and ground

speed) from a small UAV. The algorithm relies on the aircraft performing a helical or circular flight pattern to determine the vertical and horizontal wind velocity, respectively. The aircraft is flown at a constant true airspeed, and the wind velocity is found by effectively fitting the flight path relative to the air to a circle or spiral. The algorithm was applied to the Small Unmanned Meteorological Observer (SUMO) and the results showed good agreement with the measurements of conventional atmospheric profiling systems [66].

A method for estimating a spatially and temporally varying vector wind field using small and mini UAVs is described by Langelaan *et al.* [67]. This approach uses sensors from a standard autopilot sensor suite including GPS, IMU, airspeed indicator and magnetometer. The wind field is calculated using two approaches: one using measurements of aircraft motion with respect to the earth and predictions of aircraft motion obtained from the dynamic model, and the other using GPS velocity and measurements of vehicle acceleration. Results of Monte Carlo simulations for gusty wind fields give good agreement with uncertainties of approximately 0.5 m/s.

Lawrance and Sukkarieh [68] describe an interesting method for both mapping a spatially and temporally varying wind field as well as using the estimated wind field for optimal flight planning of an unmanned soaring aircraft. They assume that measurements of the air-relative velocity (airspeed, angle of attack and sideslip) and ground-relative position and velocity (from GPS) are available. They use a dynamic model of the glider and Gaussian process regression (a machine learning algorithm to characterise an underlying function from a finite set of observations) to estimate the wind field. The result is a Gaussian distribution of functions from which estimates of the wind values can be drawn at any selected test point. The method was tested with simulated flights and the results showed robust mapping of the wind field. In reality the method may be limited by the computational capability of the flight computer and the relatively small number of previous observations used for the wind velocity estimation.

Instrumented UAVs have also been used to make measurements of the wake of wind turbines [69]. The wind velocity measurements are given by the vector sum of the UAV's velocity with respect to the Earth (measured with an auto-pilot system) and the wind velocity with respect to the UAV (measured with a seven-sensor fast response aerodynamic probe). The method was tested on a 2MW wind turbine in complex terrain. The wind velocity estimates were assessed in wind tunnel experiments and in circle-flight mode in the atmosphere. The wind velocity estimates in the atmosphere were verified using LIDAR measurements. The measurements yielded an uncertainty of 0.7 m/s.

A method for estimating airspeed, angle of attack and sideslip without conventional air-data sensors (pitot static system and angle of attack vanes) is described in [70]. Although estimation of the wind velocity field is not an objective of this work, it is a byproduct of it. The method consists of two Kalman filters: the first one uses data from GPS, IMU to estimate the aircraft's ground velocity and altitude. The second filter uses the aircraft dynamic model for its time update equations and the estimates from the first filter as its

measurement update to estimate airspeed, angle of attack and sideslip. The method assumes uncorrelated white Gaussian noise in the measurements. Simulation and flight test results of the method are presented. Rms errors from the simulations gave less than 1 m/s for the airspeed estimate, and the errors from the experimental flight test are less than 2.5 m/s, 2° and 1° for the airspeed, angle of attack and sideslip, respectively.

Chapter 2

Problem Characteristics

In this chapter some basic characteristics of the problem of determining wind velocities from flight data are investigated. The focus is on what data are sufficient to determine the wind velocity and the sensitivity of the solution to errors in the data. The general 3D problem is described first, however it turns out to be convenient to resolve the problem into the horizontal (2D) and vertical (1D) components. The 2D problem is the most difficult and most of the chapter addresses this. The vertical problem is relatively straightforward.

2.1 The 3D problem

The problem considered is that of estimating the 3-dimensional (3D) wind velocity along the flight path (i.e. as a function of space and time as defined by the flight path) from a record of on-board measurements of simple flight data. The data considered are samples of the aircraft position at specified times (derived from a GPS recorder) and samples of the aircraft airspeed and/or heading. The GPS position data are subject to PRN code noise (~ 1 m) and receiver noise (~ 1 m). Moreover, bias errors may be present resulting from selective availability and other sources such as clock and multi-path error [71]. Therefore, care must be taken when deriving the ground velocity from the position data. Instead of differentiating the position data directly, the velocity is calculated by first low-pass filtering the position data and then differentiating over a time window using central differences, thus reducing the effects of GPS noise and bias. It is assumed in the following that the position data has been immediately processed to obtain the ground velocity. It is assumed here that logged flight data are post-processed. The fundamental relationship used is that the ground (inertial) velocity of an aircraft is the sum of the 3D air velocity (velocity of the aircraft relative to the airmass) and the 3D wind velocity, i.e.

$$\mathbf{v}_g^{(3)} = \mathbf{v}_a^{(3)} + \mathbf{v}_w^{(3)}, \tag{2.1}$$

where the subscripts g, a, and w denote "ground", "air", and "wind", respectively and the superscript (3) indicates the 3D velocity.

The relationship (2.1) applies at any time instant during the flight. The velocities are resolved into 3 Cartesian components, i.e. $\mathbf{v}_g^{(3)} = (v_g^x, v_g^y, v_g^z)$, $\mathbf{v}_a^{(3)} = (v_a^x, v_a^y, v_a^z)$, and $\mathbf{v}_w^{(3)} = (v_w^x, v_w^y, v_w^z)$, where x denotes East, y denotes North, and z denotes vertical. The ground velocity is obtained from differentiation of the 3D GPS coordinates and altitude data with respect to time. Clearly, if two of the vectors in (2.1) are known, the third can be determined. In the case at hand, if the 3D ground velocity and 3D air velocity are measured then the 3D wind velocity can be calculated.

The ground, air and wind velocities can also be resolved into a magnitude (speed) and two angles (equivalent to a spherical polar coordinate system) as shown in Fig. 2.1. This is particularly relevant for the air velocity, which gives the airspeed v_a, the heading θ_a, and θ_a^z is equal to the glide slope in still air γ as described in Section 1.3.4 (Fig. 2.1(b)). The sailplane heading may be measured with a compass, but the glide slope is generally not measured.

Consider first the case where the ground velocity and the airspeed are measured, but the two angles θ_a and θ_a^z are not measured. Drawing the relationship (2.1) as a vector triangle (Fig. 2.2(a)) shows that there is a two-parameter ambiguity in the wind velocity that corresponds to the tail of the wind velocity vector lying on the surface of a sphere. If the airspeed and heading θ_a are measured, then there is a one-parameter ambiguity and the wind velocity vector lies on a semicircle (Fig. 2.2(b)).

For a sailplane, the glide slope is small, and to a good approximation the airspeed and its horizontal component can be taken as equal. It is then convenient to resolve the 3D problem into its horizontal and vertical components and treat them separately. The horizontal components of the ground, air and wind velocities are denoted $\mathbf{v}_g$, $\mathbf{v}_a$ and $\mathbf{v}_w$, respectively, and the (scalar) vertical components as v_g^z, v_a^z, v_w^z (Fig. 2.1). The angles of the horizontal components are denoted θ_g, θ_a, and θ_w, and the inclinations to the horizontal are denoted θ_g^z, θ_a^z, and θ_w^z (Fig. 2.1). The resulting horizontal and vertical problems are described in the next two sections.

2.2 The horizontal (2D) problem

The same relationship (2.1) applies to the horizontal components, i.e.

$$\mathbf{v}_g = \mathbf{v}_a + \mathbf{v}_w. \tag{2.2}$$

Note that θ_g is the direction of travel over the ground, θ_a is the aircraft heading, and θ_w is what is normally referred to as the wind direction.

Consider an aircraft flying through a region of the atmosphere where the horizontal component of the wind velocity is constant, and the data are not corrupted by noise. Since airspeed or heading data may not be available, four different cases are considered corre-

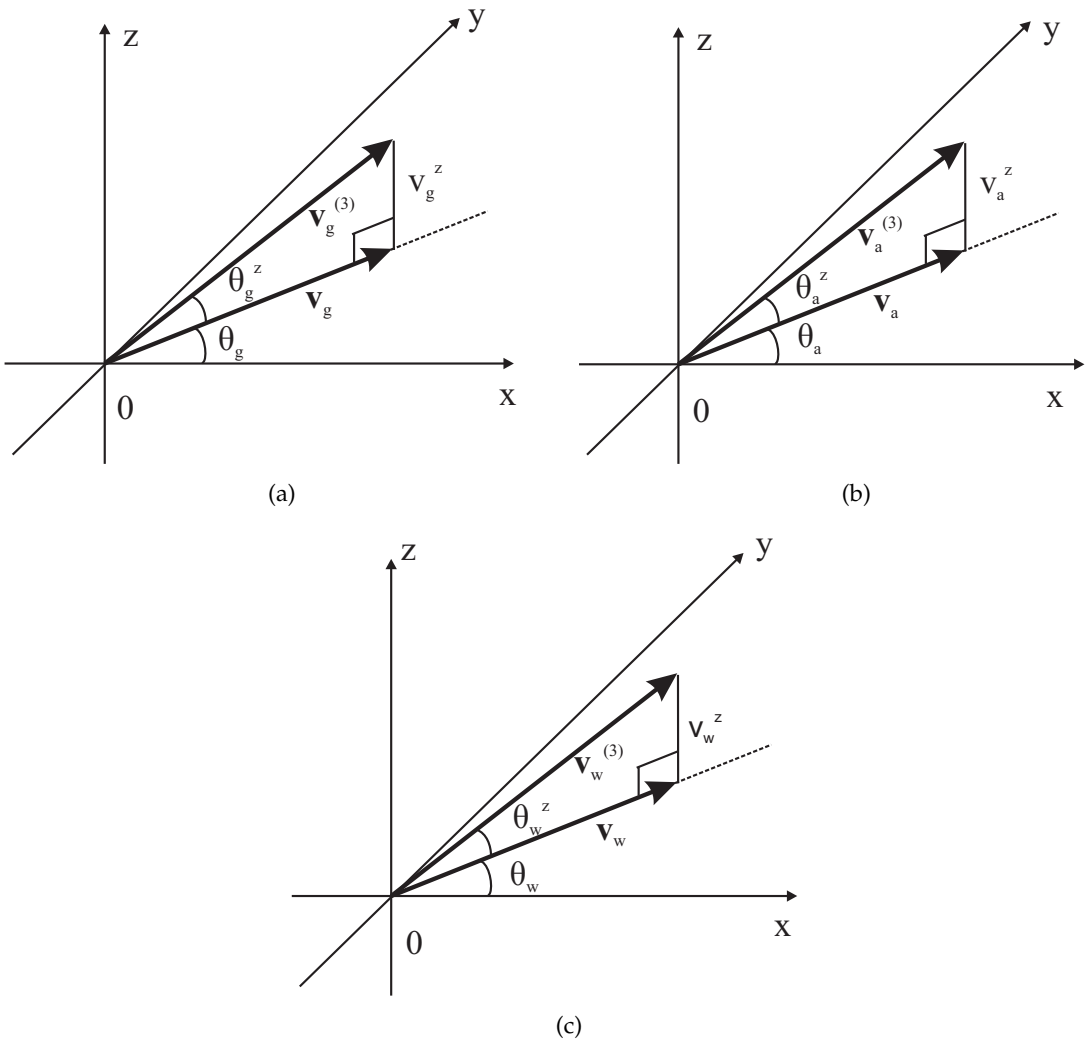

Figure 2.1 The components of the 3D ground, air and wind velocities.

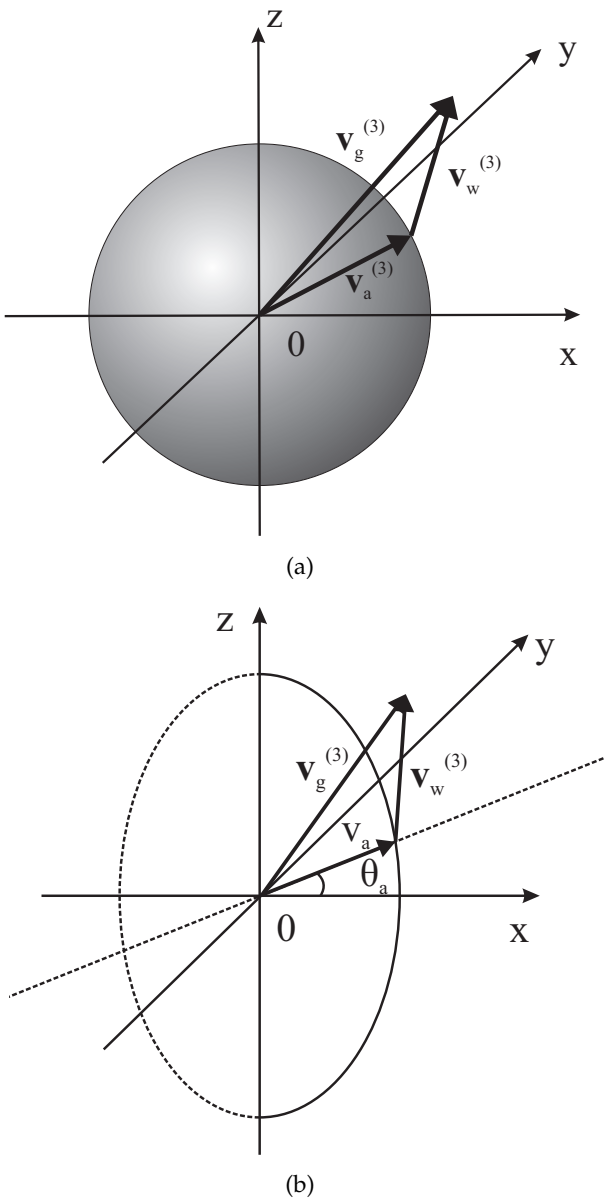

Figure 2.2 The 3D cases for (a) given ground velocity and airspeed and (b) given ground velocity, airspeed and heading.

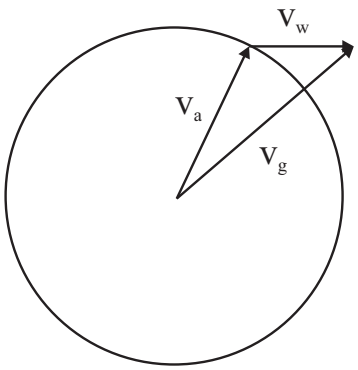

Figure 2.3 Relationship between the horizontal components of the air velocity and the ground velocity for a fixed airspeed.

sponding to ground velocity data but with or without airspeed and/or heading data.

2.2.1 Case 1: Ground velocity, airspeed and heading

If the ground velocity (derived from the GPS coordinates) and the air velocity (i.e. the airspeed and heading) are measured, then the wind velocity can be calculated directly from (2.2) as

$$\mathbf{v}_w = \mathbf{v}_g - \mathbf{v}_a. \tag{2.3}$$

2.2.2 Case 2: Ground velocity and airspeed

Consider now the case where the heading is not measured, i.e. the only data are the ground velocity and the airspeed. Since only the magnitude of $\mathbf{v}_a$ is known, $\mathbf{v}_a$ is restricted to lie on a circle and there is therefore a one-parameter family of solutions for $\mathbf{v}_w$ as shown in Fig. 2.3. There is therefore insufficient information, at a single time-point, to uniquely determine the wind velocity.

Consider now the case where data are measured at two different times, giving two ground velocities, $\mathbf{v}_{g1}$ and $\mathbf{v}_{g2}$, and the two corresponding airspeeds, v_{a1} and v_{a2}, in a region of constant wind velocity. The two corresponding vector diagrams as in Fig. 2.3 are translated such that the origins of the vectors $\mathbf{v}_{g1}$ and $\mathbf{v}_{g2}$ coincide as shown in Fig. 2.4. With this construction, the solution for the wind velocity must lie on the two circles, and the one-parameter family of solutions reduces to two possible solutions, one at each of the two intersections of the circles. Referring to Fig. 2.4, the angle θ is given by

$$\cos\theta = \frac{v_{a1}^2 + c^2 - v_{a2}^2}{2v_{a1}c}, \tag{2.4}$$

where $\mathbf{c} = \mathbf{v}_{g1} - \mathbf{v}_{g2}$ and $c = \|\mathbf{c}\|$, and the two solutions for the wind velocity are given by

$$\mathbf{v}_w = \mathbf{v}_{g1} - v_{a1} R_{\pm\theta}\, \hat{\mathbf{c}}, \tag{2.5}$$

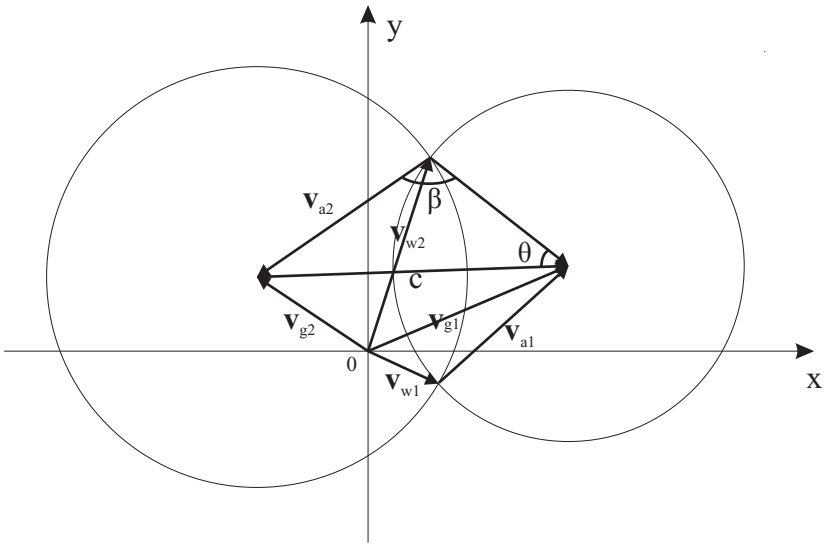

Figure 2.4 Relationships between two ground velocities and two airspeeds in a region of constant wind velocity.

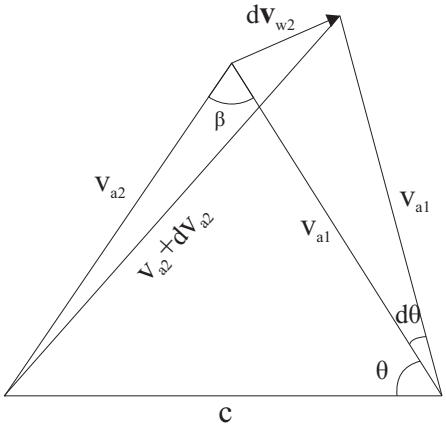

Figure 2.5 Vector relationships for a small change in estimated wind velocity $d\mathbf{v}_{w2}$ due to a small change in airspeed dv_{a2}.

where R_θ denotes rotation by θ, and $\hat{}$ denotes a unit vector. Alternatively, (2.5) can be written as

$$\begin{aligned} v_{w1}^x &= v_{g1}^x - v_{a1}\cos(\theta_c + \theta), \\ v_{w1}^y &= v_{g1}^y - v_{a1}\sin(\theta_c + \theta), \\ v_{w2}^x &= v_{g2}^x - v_{a1}\cos(\theta_c - \theta), \\ v_{w2}^y &= v_{g2}^y - v_{a1}\sin(\theta_c - \theta), \end{aligned} \tag{2.6}$$

where θ_c is the angle between $\mathbf{c}$ and the x-axis, i.e.

$$\theta_c = \tan^{-1}\left(v_{g1}^y - v_{g2}^y, v_{g1}^x - v_{g2}^x\right). \tag{2.7}$$

The two circles coincide if and only if $||\mathbf{v}_{g1} - \mathbf{v}_{g2}|| \leq v_{a1} + v_{a2}$. The circles will always intersect for exact data, but errors in the data may cause them not to intersect in which case no solution is obtained. In summary, given two ground velocities and the corresponding airspeeds in a region of constant wind velocity, the wind velocity can be determined up to a two-fold ambiguity. If measurements are made at multiple pairs of time-points, it is clear that the requirement for consistency between the multiple two-fold ambiguous solutions may lead to a unique solution. Methods for doing this in practice are a major part of this thesis and are discussed in the later chapters.

If the data are exact, exact solutions will be obtained, but success in practice depends critically on the sensitivity of the solution to errors in the data. This sensitivity is examined here in detail by considering the case for a pair of ground velocity and airspeed data. Referring to Fig. 2.4, the one-parameter family of solutions is reduced to two solutions (i.e. there are two intersections) only if the two circles have different centres, i.e. the two ground velocities are different. The sensitivity of the wind speed estimate to errors in the airspeed measurements is derived as follows. Consider the change $|d\mathbf{v}_{w2}|$ in the magnitude of wind velocity estimate $\mathbf{v}_{w2}$ due to a small change dv_{a2} in the airspeed v_{a2}, for fixed v_{a1} and ground velocities, as shown in Fig. 2.5. The sensitivity, denoted $s(dv_{a2})$, of $\mathbf{v}_{w2}$ to errors in v_{a2} is defined by

$$s(dv_{a2}) = \frac{|d\mathbf{v}_{w2}|}{dv_{a2}}. \tag{2.8}$$

Referring to Fig. 2.4 shows that

$$v_{a2}^2 = v_{a1}^2 + c^2 - 2v_{a1}c\cos\theta, \tag{2.9}$$

and differentiating (2.9) with respect to θ gives

$$\frac{dv_{a2}}{d\theta} = \frac{v_{a1}c\sin\theta}{v_{a2}}. \tag{2.10}$$

Using (2.10) and the relationships

$$\frac{|d\mathbf{v}_{w2}|}{d\theta} = v_{a1}, \tag{2.11}$$

and

$$\frac{v_{a2}}{\sin\theta} = \frac{c}{\sin\beta}, \tag{2.12}$$

where the angle β is shown in Figs. 2.4 and 2.5, and substituting into (2.8) gives

$$s(dv_{a2}) = \operatorname{cosec}\beta. \tag{2.13}$$

Referring to Fig. 2.4, the angle β is the difference in heading at the two time-points, i.e.

$$\beta = \theta_{a2} - \theta_{a1} = \Delta\theta_a. \tag{2.14}$$

The sensitivity therefore depends only on the heading difference for the two measurements, and is low if the two headings differ by 90° but is high if they differ by close to 0° or 180° (Fig. 2.6(a)), the latter being unlikely. Low sensitivity is required for a good solution and a large sensitivity will render the wind velocity solutions unusable due to excessive amplification of the noise. Figure 2.6(a) shows that measurements during straight flight do not provide wind velocity estimates and that a heading difference greater than about 20° is needed to obtain reliable estimates. This analysis therefore highlights a fundamental property of the problem at hand. This sensitivity is used explicitly in Chapter 4 to select which data to use for wind velocity estimation. The headings are not known but β is easily calculated as

$$\cos\beta = \frac{v_{a1}^2 + v_{a2}^2 - c^2}{2v_{a1}v_{a2}}. \tag{2.15}$$

Since the heading is not measured in this case, it is useful to derive an expression for the sensitivity as a function of the ground velocities. For simplicity, consider the case $v_{a1} = v_{a2} = v_a$, then $\sin(\beta/2) = c/2v_a$, so that

$$\begin{aligned} \sin\beta &= 2\sin(\beta/2)\cos(\beta/2) \\ &= \frac{c}{v_a}\left(1 - \frac{c^2}{4v_a^2}\right)^{1/2}. \end{aligned} \tag{2.16}$$

Defining the difference in ground velocities relative to the airspeed by

$$r = \frac{c}{v_a}, \tag{2.17}$$

and substituting (2.16) into (2.8) gives the sensitivity as

$$s(dv_{a2}) = r^{-1}\left(1 - \frac{r^2}{4}\right)^{-1/2}. \tag{2.18}$$

The sensitivity is therefore a function of the difference in the two ground velocities relative to the airspeed. The sensitivity is plotted versus r in Fig. 2.6(b), and is seen to be small when $c \approx v_a$ ($r \approx 1$) and to diverge at $c = 0$ and $c = 2v_a$ where two circles are tangent to

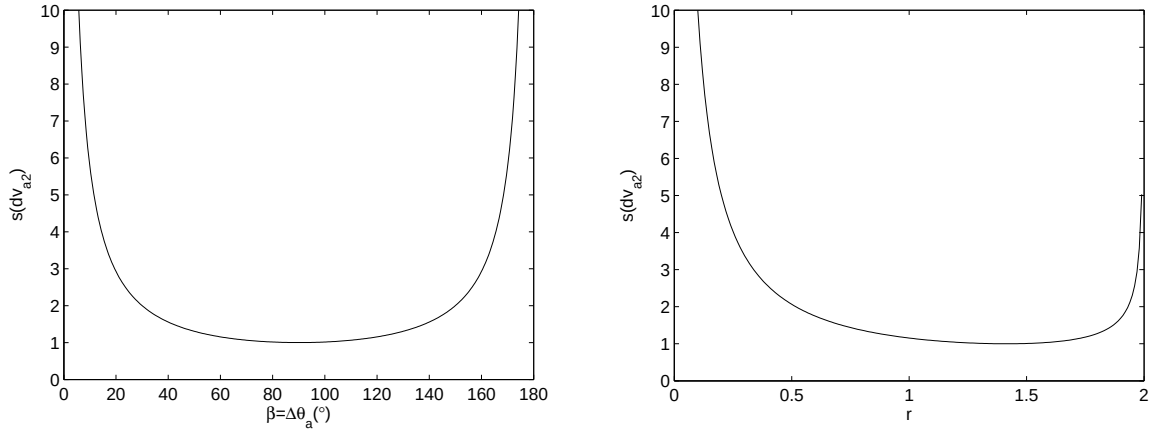

(a) (b)

Figure 2.6 Sensitivity to errors in the airspeed versus (a) the heading difference and (b) the ratio $r = c/v_a$.

each other. Differentiating (2.18) with respect to r gives

$$\frac{ds(dv_{a2})}{dr} = \frac{1}{4}\left(1 - \frac{r^2}{4}\right)^{-\frac{3}{2}} - r^{-2}\left(1 - \frac{r^2}{4}\right)^{-\frac{1}{2}}, \tag{2.19}$$

and setting $ds/dr = 0$ shows that the minimum sensitivity occurs at $r = \sqrt{2}$ where $s = 1$.

Consider now the sensitivity to errors in the ground velocities, i.e. the change in $\mathbf{v}_{w2}$ due to a small change $d\mathbf{v}_{g1}$ in the ground velocity $\mathbf{v}_{g1}$, with $\mathbf{v}_{g2}$, v_{a1} and v_{a2} fixed, as shown in Fig. 2.7. Denote the new ground velocity by $\mathbf{v}'_{g1} = \mathbf{v}_{g1} + d\mathbf{v}_{g1}$. An error in the ground velocity will generally be in magnitude and direction as shown in Fig. 2.7(a). In order to simplify the analysis two cases are considered.

First consider a change in the ground velocity $d\mathbf{v}_{g1}$ that is parallel to the vector $\mathbf{c}$ as shown in Fig. 2.7(b). The sensitivity, denoted $s'(dv_{g1})$, is defined by

$$s'(dv_{g1}) = \frac{|d\mathbf{v}_{w2}|}{|d\mathbf{v}_{g1}|}, \tag{2.20}$$

and referring to Fig. 2.7(b) gives the following relationships:

$$\frac{d\mathbf{v}_{w2}}{d\gamma} = v_{a2}, \tag{2.21}$$

$$\frac{v_{a1}}{\sin\gamma} = \frac{c}{\sin\beta}, \tag{2.22}$$

$$d\mathbf{v}_{g1} = dc, \tag{2.23}$$

$$v_{a1}^2 = v_{a2}^2 + c^2 - 2v_{a2}\,c\cos\gamma, \tag{2.24}$$

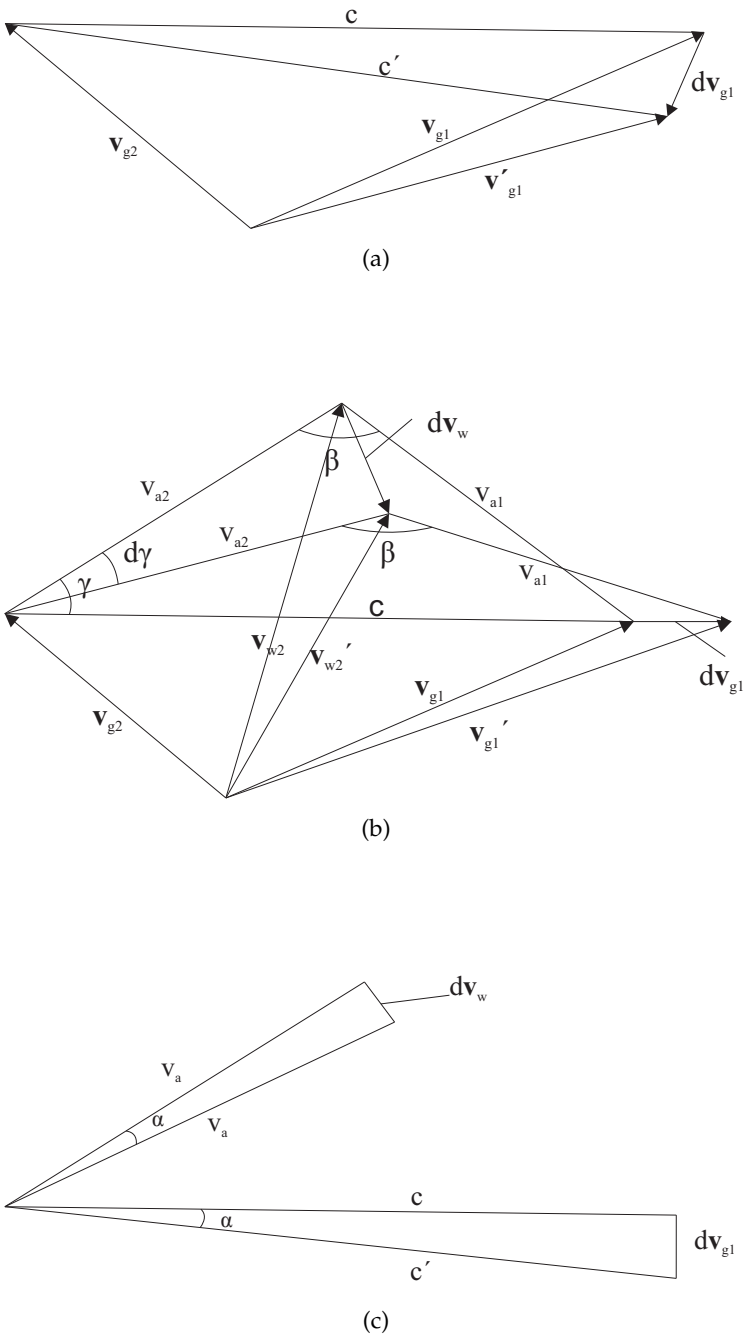

Figure 2.7 (a) Vector relationships for a small change in wind speed $d\mathbf{v}_{w2}$ due to a small change in ground speed $d\mathbf{v}_{g1}$. The cases where (b) $d\mathbf{v}_{g1}$ is parallel to **c**, and (c) $d\mathbf{v}_{g1}$ is perpendicular to **c**.

where γ is the angle shown in Fig. 2.7(b). Differentiating (2.24) with respect to γ and rearranging gives

$$\frac{dc}{d\gamma} = \frac{c\, v_{a2} \sin\gamma}{v_{a2}\cos\gamma - c}. \tag{2.25}$$

Using (2.20), (2.21), (2.23), (2.25) and simplifying then gives the sensitivity as

$$s'(dv_{g1}) = \frac{c - v_{a2}\cos\gamma}{c\sin\gamma}. \tag{2.26}$$

Using (2.22) allows this to be written in terms of the heading difference β as

$$s'(dv_{g1}) = \frac{v_{a2}}{v_{a1}}\left[\frac{c}{v_{a2} - \left(1 - (v_{a1}/c)^2 \sin^2\beta\right)^{1/2}}\right] \operatorname{cosec}\beta, \tag{2.27}$$

which is the same as (2.13) with an additional factor. To simplify this expression, assume that the two airspeeds are the same, i.e. $v_{a1} = v_{a2} = v_a$, and (2.27) reduces to

$$s(dv_{g1}) = [r - (1 - r^{-2}\sin^2\beta)^{1/2}] \operatorname{cosec}\beta, \tag{2.28}$$

and using (2.16) and (2.17) allows this to be written in terms of r as

$$s'(dv_{g1}) = \frac{1}{2}\left(1 - \frac{r^2}{4}\right)^{-1/2}. \tag{2.29}$$

This is seen to be the same as (2.18) except that the factor $1/r$ is not present. The result is that (2.29) shows the same behaviour as (2.18) near $r = 2$, but it is finite at $r = 0$. This is because moving the two circles apart on the line joining their centres when their centres are close does not lead to an instability as is the case if the radius of one of the circles is increased (i.e. when the airspeed changes).

Consider now the second case where the small change in ground velocity $d\mathbf{v}_g$ is perpendicular to the vector $\mathbf{c}$. Referring to the construction in Fig. 2.7(c), it is clear that the change in wind velocity $|d\mathbf{v}_{w2}|$ is the same as $|d\mathbf{v}_{g1}|$ but is amplified by the factor v_{a2}/c. Assuming the two airspeeds are equal, the sensitivity to this change in ground speed, denoted $s''(dv_{g1})$, is given by

$$s''(dv_{g1}) = \frac{1}{r}. \tag{2.30}$$

Hence, this sensitivity shows the singularity at $r = 0$ as in (2.18) and reduces to $1/2$ at $r = 2$. This reflects the sensitivity at the intersection of the two circles whose centers are close and are moved perpendicular to the line joining their centres.

In general, a variety of ground speed errors are to be expected, equally distributed between the above two extremes. For a particular error, let the angle between $d\mathbf{v}_{g1}$ and $\mathbf{c}$ be θ. The

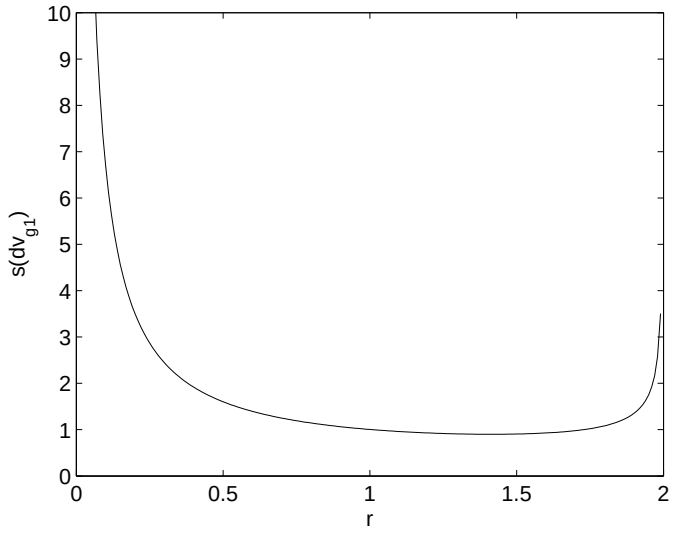

Figure 2.8 Sensitivity to errors in the ground velocity versus the ratio $r = c/v_a$.

sensitivity can then be written as

$$s(dv_{g1}) = s'(dv_{g1})\cos\theta + s''(dv_{g1})\sin\theta. \tag{2.31}$$

Averaging over θ uniformly distributed on (0,$\pi/2$) gives the expected value of the sensitivity as

$$\begin{aligned} s(dv_{g1}) &= \frac{2}{\pi}\left[s'(dv_{g1}) + s''(dv_{g1}))\right] \\ &= \frac{2}{\pi}\left[\frac{1}{r} + \frac{1}{2}\left(1 - \frac{r^2}{4}\right)^{-1/2}\right], \end{aligned} \tag{2.32}$$

which is plotted in Fig. 2.8. Comparison with Fig. 2.6(b) shows quite similar behaviour. For simplicity, (2.18) is used as the measure of the intrinsic sensitivity of the wind velocity estimates.

2.2.3 Case 3: Ground velocity and heading

If the airspeed is not measured, then the available data are the ground velocity and the heading. Since the angle of $\mathbf{v}_a$ is known but not the magnitude, there is a one-parameter family of solutions for $\mathbf{v}_w$ that lies on a line (Fig. 2.9(a)). The wind velocity therefore cannot be uniquely determined from data at a single time-point.

Consider again the case of two sets of such data measured at different time-points in a region of constant wind velocity. The data include two ground velocities $\mathbf{v}_{g1}$ and $\mathbf{v}_{g2}$, and two headings θ_{a1} and θ_{a2}. The vector diagram (Fig. 2.9(b)) shows that the solution for the

wind velocity is reduced to a unique solution, which lies on the intersection at the two lines at the given headings. Inspection of Fig. 2.9(b) shows that

$$\begin{aligned} v_{g1}^x - v_{a1}\cos\theta_{a1} &= v_{g2}^x - v_{a2}\cos\theta_{a2}, \\ v_{g1}^y - v_{a1}\sin\theta_{a1} &= v_{g2}^y - v_{a2}\sin\theta_{a2}, \end{aligned} \tag{2.33}$$

and solving this system of equations for v_{a1} and v_{a2} gives

$$\begin{aligned} v_{a1} &= \frac{(v_{g1}^x - v_{g2}^x)\sin\theta_{a2} - (v_{g1}^y - v_{g2}^y)\cos\theta_{a2}}{\sin(\theta_{a2} - \theta_{a1})} \\ v_{a2} &= \frac{(v_{g1}^x - v_{g2}^x)\sin\theta_{a1} - (v_{g1}^y - v_{g2}^y)\cos\theta_{a1}}{\sin(\theta_{a2} - \theta_{a1})}. \end{aligned} \tag{2.34}$$

The derived airspeeds coupled with the headings allows the air velocities $\mathbf{v}_{a1}$ and $\mathbf{v}_{a2}$ to be determined and the wind velocity is then given by $\mathbf{v}_w = \mathbf{v}_{g1} - \mathbf{v}_{a1} = \mathbf{v}_{g2} - \mathbf{v}_{a2}$. A solution exists only if the two headings are different, i.e. $\theta_{a1} \neq \theta_{a2}$ and $\theta_{a1} \neq \pi + \theta_{a2}$. Note that if the headings are different then the ground velocities must be different for a non-zero airspeed.

Referring to Fig. 2.9(b), it can be seen that the sensitivity of the solution to errors increases as θ_{a1} and θ_{a2} become more similar and is minimised when they differ by $90°$. This is therefore analogous to the case for ground velocity and airspeed data. The sensitivity of the wind velocity estimate to errors in the heading is defined as

$$s(d\theta_{a1}) = \frac{|d\mathbf{v}_w|}{d\theta_{a1}}, \tag{2.35}$$

assuming that θ_{a2}, $\mathbf{v}_{g1}$, and $\mathbf{v}_{g2}$ are fixed. Referring to Fig. 2.9(c), it is easily seen that $|d\mathbf{v}_w| = dv_{a2}$. Differentiating (2.34) with respect to θ_{a1} gives the sensitivity as

$$\begin{aligned} s(d\theta_{a1}) &= \frac{|d\mathbf{v}_w|}{d\theta_{a1}} = \frac{dv_{a2}}{d\theta_{a1}} = \frac{(v_{g1}^x - v_{g2}^x)\sin\theta_{a2} - (v_{g1}^y - v_{g2}^y)\cos\theta_{a2}}{\sin^2(\theta_{a2} - \theta_{a1})} \\ &= v_{a1}\,\mathrm{cosec}(\theta_{a2} - \theta_{a1}) = v_{a1}\,\mathrm{cosec}(\Delta\theta_a). \end{aligned} \tag{2.36}$$

The sensitivity is therefore a function of the difference in the two headings as anticipated, and is a minimum when this difference is $90°$. The sensitivity diverges as the heading difference approaches $0°$ or $180°$, when there is no solution for the wind velocity. The sensitivity is proportional to the airspeed and it is convenient to consider the sensitivity normalised by the airspeed, which is plotted in Fig. 2.10.

Consider now the sensitivity to errors in the ground velocity. Two cases are considered, one denoted $s'(v_{g1})$, for which the small change in $\mathbf{v}_{g1}$ is parallel to $\mathbf{v}_{a1}$ and the other for which it is perpendicular to $\mathbf{v}_{a1}$, denoted $s''(v_{g2})$. The two cases are shown in Figs. 2.11(a) and (b), respectively. For the former case the resulting wind velocity remains unchanged

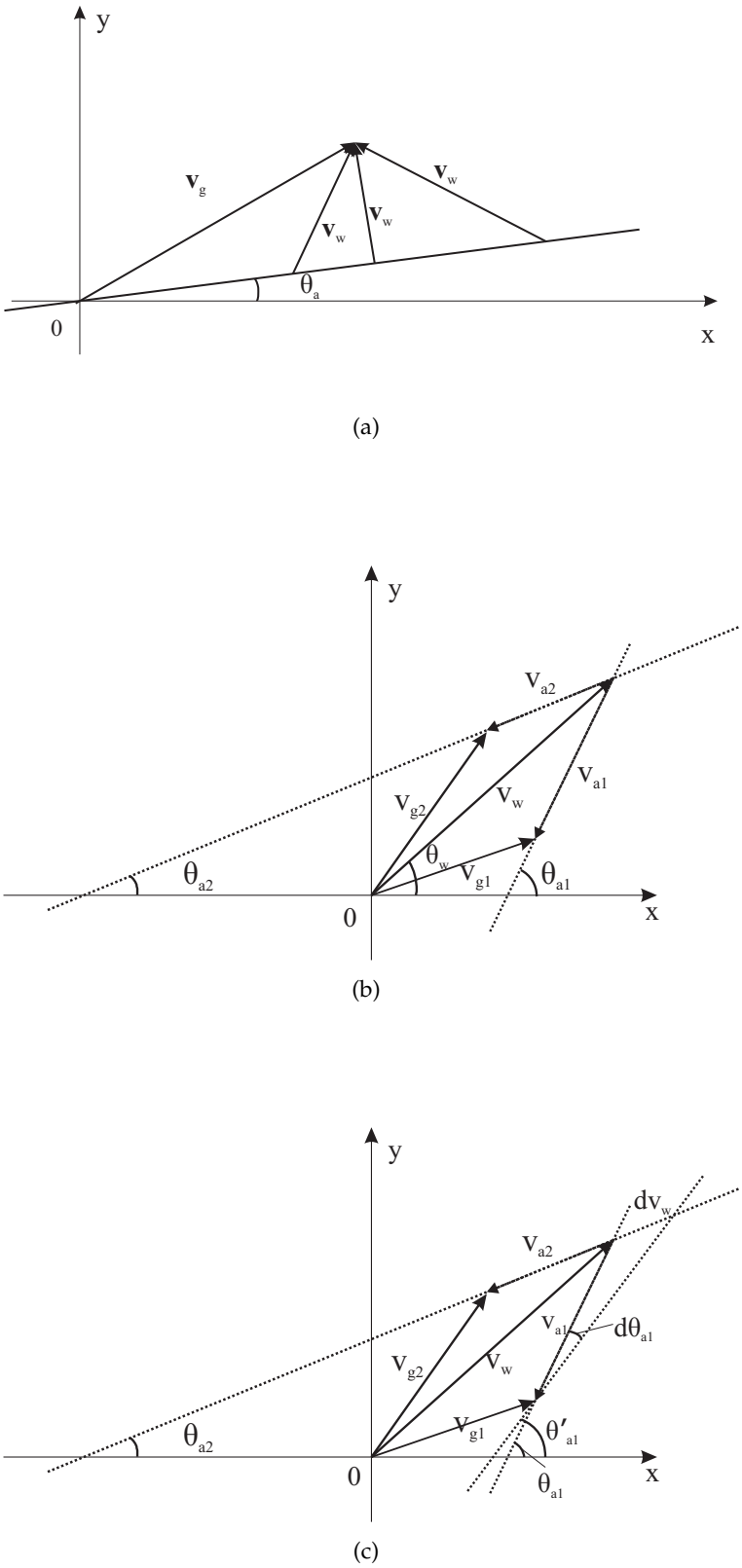

Figure 2.9 (a) Relationship between the air velocity and ground velocity for a fixed heading. (b) Two sets of ground velocity and heading data giving a unique wind velocity solution. (c) The change in $\mathbf{v}_w$ due to a change in θ_{a1}.

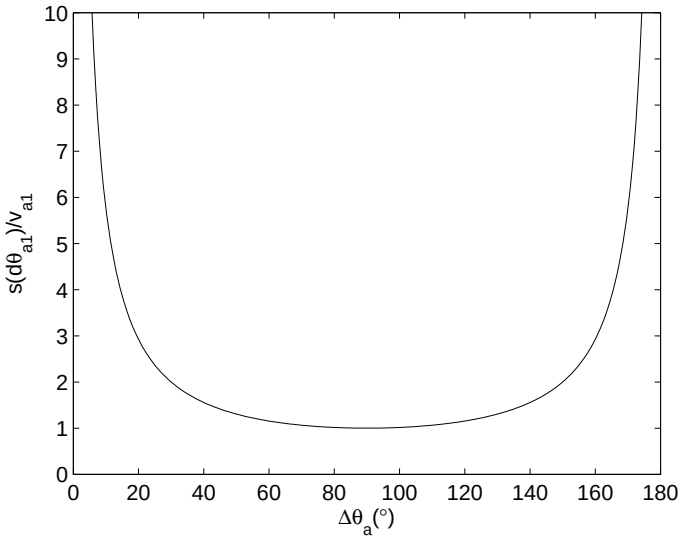

Figure 2.10 Sensitivity to heading errors scaled by $1/v_{a1}$ versus the heading difference ($\Delta\theta_a$). The sensitivity to ground velocity errors has the same form.

so that $s'(dv_{g1}) = 0$. For the second case it is easily seen from Fig. 2.11(b) that

$$s''(dv_{g1}) = \frac{|d\mathbf{v}_w|}{|d\mathbf{v}_{g1}|} = \operatorname{cosec}(\theta_{a1} - \theta_{a2}) = \operatorname{cosec}(\Delta\theta_a). \tag{2.37}$$

Averaging over all orientations of $d\mathbf{v}_{g1}$ therefore gives the expected sensitivity as

$$s(dv_{g1}) = (2/\pi)\operatorname{cosec}(\Delta\theta_a). \tag{2.38}$$

The sensitivity of the wind velocity to errors in the ground velocity is therefore a function of the heading difference also and has the same form as the sensitivity to errors in the heading, Eq. (2.36) and Fig. 2.10.

2.2.4 Case 4: Ground velocity data only

Although sailplanes are always equipped with an ASI and a compass, they are usually not equipped with equipment to log data from these instruments. In this case, the only logged data available are the ground velocities. At a single time-point there are 2 data and 4 unknowns to be determined in (2.2). The problem is therefore in general highly underdetermined. Even with a pair of different ground velocities measured at two time-points in a region of constant wind velocity, there is a two-parameter family of solutions. However, other *a priori* information is available in general that helps constrain the problem. For example, there are minimum and maximum airspeeds for the sailplane which we denote $v_{a,min}$ and $v_{a,max}$, respectively. At one time-point, the wind velocity is then restricted to an annulus of inner and outer radii $v_{a,min}$ and $v_{a,max}$, respectively, centered at $\mathbf{v}_g$ as shown in Fig. 2.12(a).

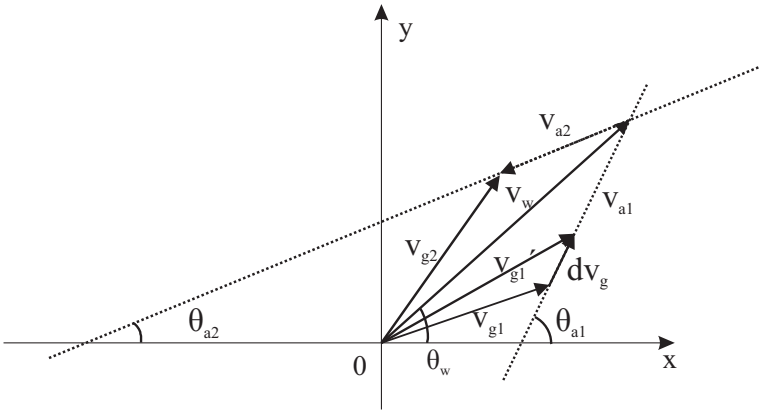

(a)

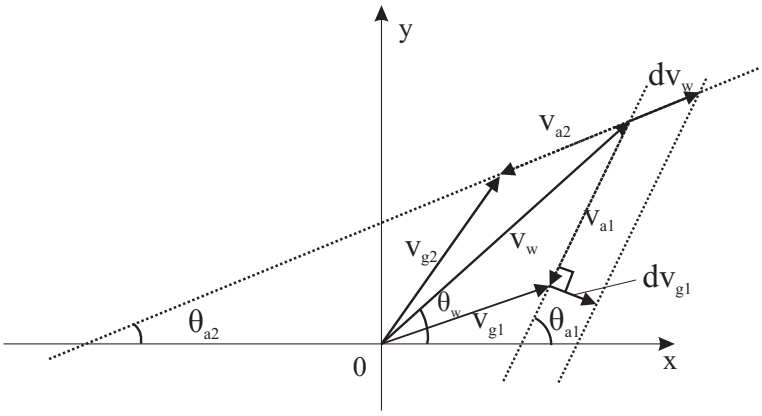

(b)

Figure 2.11 The change in wind velocity, $d\mathbf{v}_w$ due to a change in the ground velocity $\mathbf{v}_{g1}$ for the cases (a) $d\mathbf{v}_{g1}$ parallel to $\mathbf{v}_{a1}$, and (b) $d\mathbf{v}'_{g1}$ perpendicular to $\mathbf{v}_{a1}$.

For two different ground velocities in a constant wind field, the solution for the wind velocity is restricted to the intersection of two annuli, shown as the shaded area in Fig. 2.12(b). The more different the two ground velocities the smaller the overlap region and the more constrained is the solution for the wind velocity (Fig. 2.12(b)). The maximum error in the wind velocity solution is the length of the longest chord in the intersection region which, referring to Fig. 2.12(b), is $d = (v_{a,max}^2 - c^2/4)^{1/2}$. Defining the maximum normalised error in the wind velocity as $e = d/v_{a,max}$ shows that

$$e = 2\left[1 - \frac{1}{4}\left(\frac{|\Delta \mathbf{v}_g|}{v_{a,max}}\right)\right]^{1/2}, \tag{2.39}$$

which is plotted in Fig. 2.13, and illustrates that estimates of the wind velocity require data at different ground velocities.

If multiple ground velocity data are measured in a region of constant wind velocity then the overlap region is reduced and the wind velocity is more constrained (Fig. 2.12(c)). The more different the ground velocities, the smaller the overlap region.

The airspeed of a sailplane is usually slowly varying over short time intervals, so consider the case where the two airspeeds are equal (but unknown) as shown in Fig. 2.14. The solution family then reduces to a line segment as shown in Fig. 2.14. The length of the line segment is the same as above and the maximum error is therefore the same as in Fig. 2.13, although the size of the region, and therefore the expected error, is substantially reduced. Of course the difficulty with that is that if the time interval is short enough that the airspeeds are similar, it is likely that the ground velocities will also be similar, giving a larger error in the wind velocity.

In addition to minimum and maximum airspeeds, additional probabilistic information may also be available to further constrain the solution. This is the topic of Chapter 7.

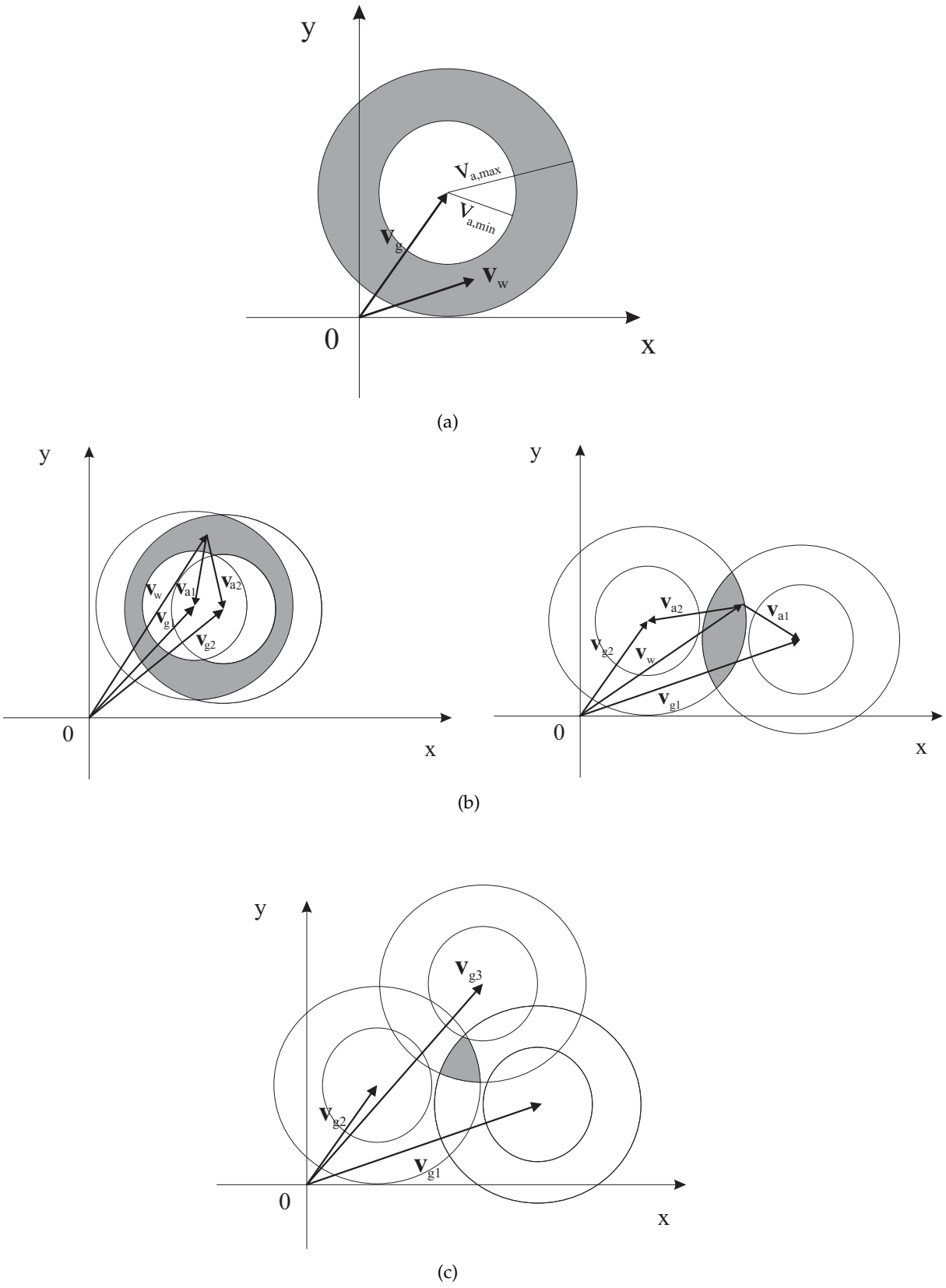

Figure 2.12 Wind velocity solution (shaded area) for ground velocity data only. (a) Data at a single time-point. (b) A pair of ground velocity data in a constant wind field, for small (left) and large (right) differences in the ground velocities, and (c) for 3 ground velocities.

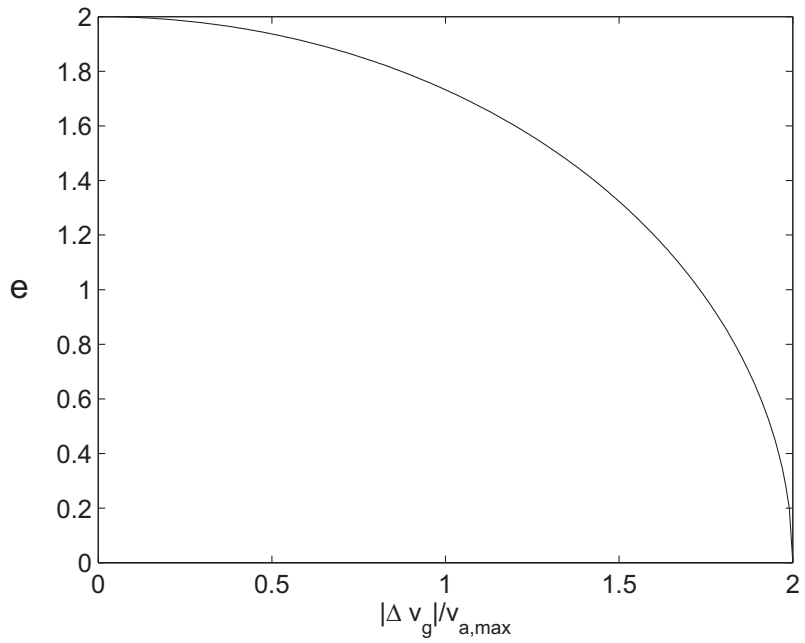

Figure 2.13 Normalised error in estimated wind velocity versus $|\Delta \mathbf{v}_g|/v_{a,max}$.

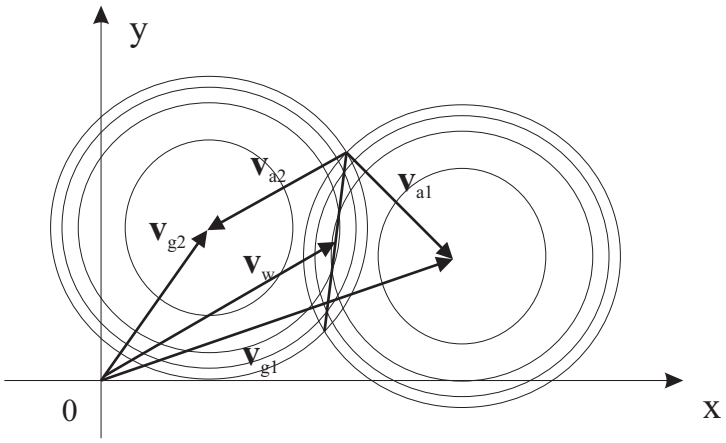

Figure 2.14 Wind velocity solution for 2 ground velocity data and equal airspeeds in a constant wind field.

2.2.5 Effect of wind velocity variation

In the analysis in the previous subsections, solutions for the wind velocity are obtained by assuming that the wind velocities are identical at the time-points when the data are measured. This is a fundamental assumption of the approach that utilizes the slowly varying nature of the wind velocities in mountain waves. However, the wind velocity will not be exactly constant so that this assumption will introduce errors into the estimated wind velocity. The magnitude of this effect is considered here for the case of ground velocity and airspeed data.

Consider a pair of ground velocity and airspeed data associated with two different wind velocities, $\mathbf{v}_{w1}$ and $\mathbf{v}_{w2}$, with a small difference $\Delta\mathbf{v}_w = \mathbf{v}_{w1} - \mathbf{v}_{w2}$ between them. The best wind velocity estimate is the average of $\mathbf{v}_{w1}$ and $\mathbf{v}_{w2}$, denoted $\bar{\mathbf{v}}_w$. The error in the estimated wind velocity $\hat{\mathbf{v}}_w$ is then $\Delta\hat{\mathbf{v}}_w = \hat{\mathbf{v}}_w - \bar{\mathbf{v}}_w$. Two cases are considered, one where $\Delta\mathbf{v}_w$ is parallel to $\mathbf{c}$ and the other where $\Delta\mathbf{v}_w$ is perpendicular to $\mathbf{c}$, as shown in Fig. 2.15. Furthermore, for simplicity, the case where the airspeeds are identical is considered.

Consider first the case where $\Delta\mathbf{v}_w$ is parallel to $\mathbf{c}$ (Fig. 2.15(a)), where $\Delta\mathbf{v}_w$ is denoted B and $\Delta\hat{\mathbf{v}}_w$ is denoted A. The sensitivity of the wind velocity estimate $\hat{\mathbf{v}}_w$ to the difference in the wind velocities for this case is denoted

$$s_{w1} = \frac{|\Delta\hat{\mathbf{v}}_w|}{|\Delta\mathbf{v}_w|} = \frac{A}{B}. \tag{2.40}$$

The key geometry for this case is shown in Fig. 2.15(b). Referring to this figure and considering the difference between $\mathbf{v}_{w1}$ and $\hat{\mathbf{v}}_w$ being due to a small change $\Delta\theta$ in θ, it is seen that

$$A = v_a \Delta\theta \cos\theta \tag{2.41}$$

$$B/2 = v_a \Delta\theta \sin\theta, \tag{2.42}$$

so that

$$s_{w1} = \frac{1}{2}\cot\theta = \frac{1}{2}\tan(\beta/2). \tag{2.43}$$

The sensitivity therefore depends only on the heading difference $\beta = \Delta\theta_a$.

Consider now the case where $\Delta\mathbf{v}_w$ is perpendicular to $\mathbf{c}$ (Fig. 2.15(c)). The sensitivity in this case is denoted $s_{w2} = A/B$. The details are shown in Fig. 2.15(d) and similarly to the first case, it is easily shown that

$$s_{w2} = \frac{1}{2}\cot(\beta/2). \tag{2.44}$$

As previously, considering the average over all possible orientations of $\Delta\mathbf{v}_w$, the mean sensitivity s_w to wind velocity differences is given by

$$s_w = \frac{2}{\pi}(s_{w1} + s_{w2}), \tag{2.45}$$

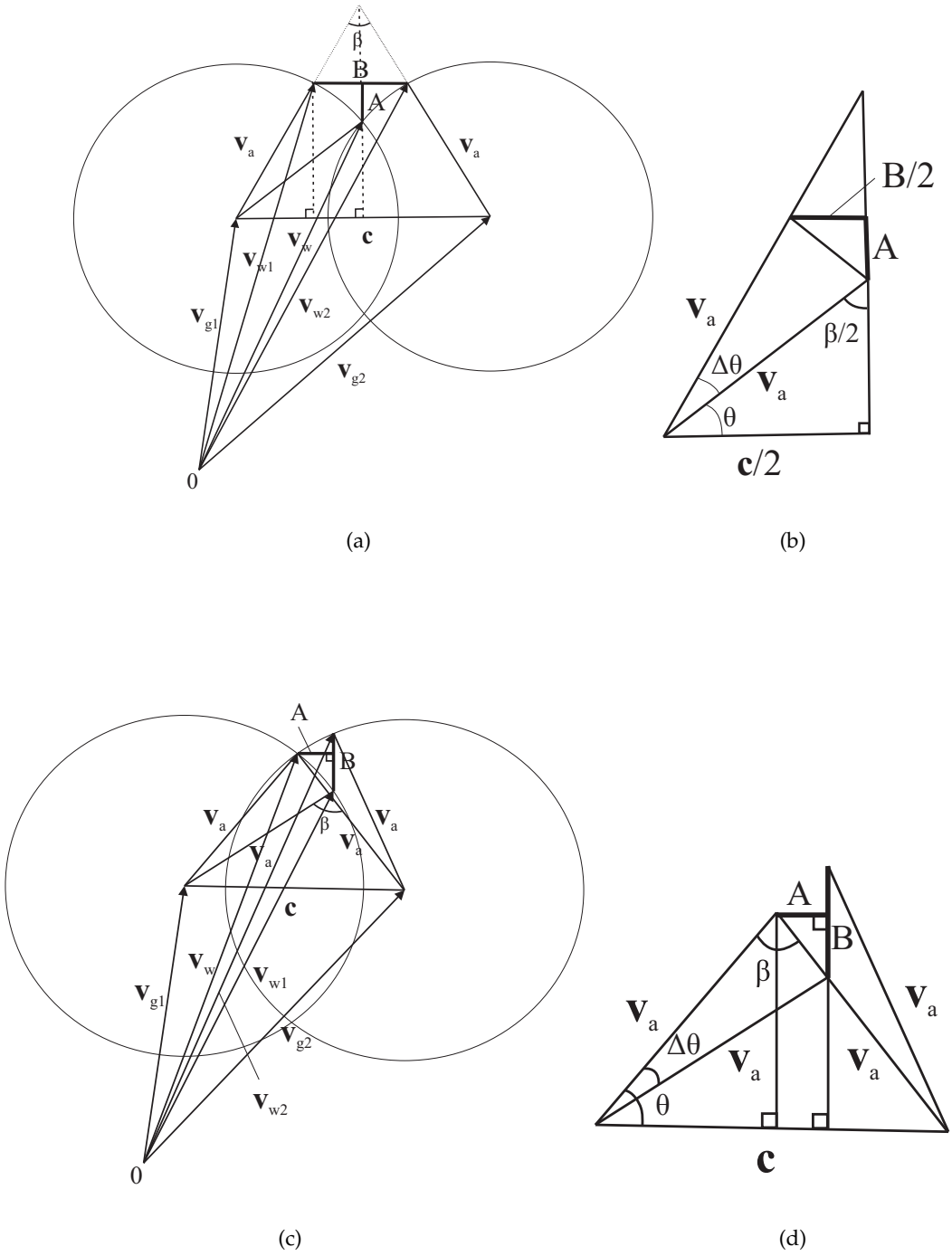

Figure 2.15 Error in the wind velocity estimate determined from a pair of airspeed and ground velocity data when the true wind velocities $\mathbf{v}_{w1}$ and $\mathbf{v}_{w2}$ are different. (a)(b)$\Delta\mathbf{v}_w$ parallel to $\mathbf{c}$, (c)(d) $\Delta\mathbf{v}_w$ perpendicular to $\mathbf{c}$.

and using (2.43) and (2.44) shows that this reduces to

$$s_w = \frac{2}{\pi}\operatorname{cosec}\beta = \frac{2}{\pi}\operatorname{cosec}(\Delta\theta_a). \tag{2.46}$$

Hence, as with the other sensitivities, the sensitivity to small differences in the wind velocities is a function of the heading difference, with a minimum sensitivity at $\Delta\theta_a = 90^\circ$ and maximum sensitivity at $\Delta\theta_a = 0^\circ$ or 180°, as shown in Fig. 2.16. This emphasises, again, that solutions for the wind velocity are most insensitive to errors when there is a large heading difference.

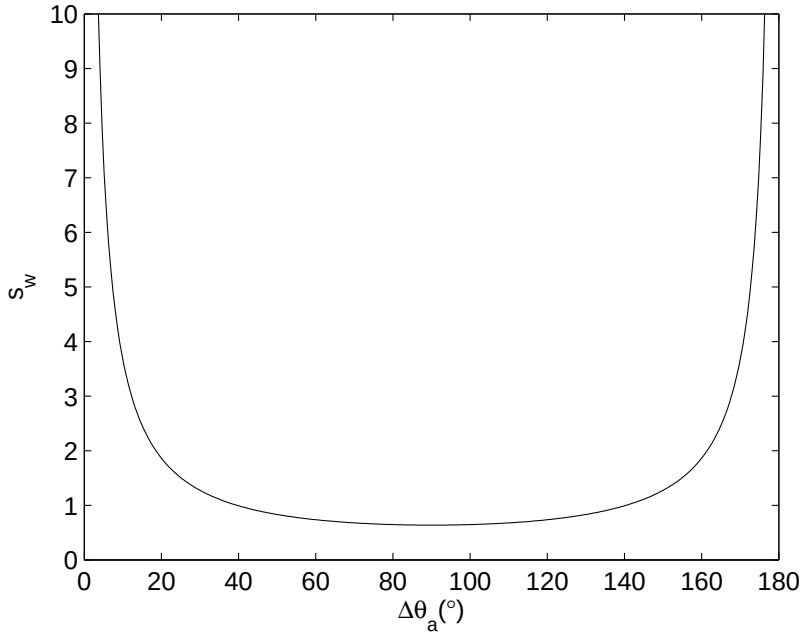

Figure 2.16 Sensitivity to the difference in the wind velocities, s_w versus $\Delta\theta_a$.

2.3 The vertical problem

Referring to (2.1), the vertical component of the wind velocity is given by

$$v_w^z = v_g^z - v_a^z. \tag{2.47}$$

The vertical velocity (relative to the ground) v_g^z is obtained by differentiating the GPS altitude. Since the GPS altitude measurements are noisy, this needs to be done with care and is described in Section 4.2. The vertical speed of the sailplane relative to the air corresponds to the sailplane sink rate as described in Section 1.3.4, i.e. $v_a^z = s$, noting that s is negative. As described in Section 1.3.4, the sink rate can be calculated from the sailplane IAS using the sailplane flight polar and correcting for the effect of altitude. Note that calculation of the sink rate requires that either the airspeed is measured or that the horizontal wind ve-

locity has been determined so that it can be used in conjunction with the ground velocity to calculate the airspeed.

Equation (2.47) applies in steady state, but an addtional effect needs to be included if the airspeed of the sailplane is changing. For example, if the pilot increases the up elevator the sailplane airspeed decreases. While the airspeed is decreasing the sailplane sinks less slowly. This can be seen by considering the resulting energy exchange. While the sailplane is decelerating, its kinetic energy decreases, and since energy is considered, the potential energy increases and there is an additional climbing component. The opposite occurs if the sailplane airspeed increases. The additional vertical speed component can be calculated be equating the rates of change of kinetic and potential energy. Consider a constant wind velocity and the pilot making a change to the elevator setting that changes the airspeed by dv_a. The kinetic energy of the sailplane $(1/2)mv_a^2$ changes by $mv_a dv_a$. In the absence of losses, energy is conserved and there is a corresponding change in potential energy $mgdz$ such that

$$mv_a dv_a + mgdz = 0. \tag{2.48}$$

In time interval dt therefore,

$$v_a \frac{dv_a}{dt} + g\frac{dz}{dt} = 0. \tag{2.49}$$

There is therefore an additional vertical speed component dz/dt, denoted v_e, given by

$$v_e = -\frac{v_a}{g}\frac{dv_a}{dt}, \tag{2.50}$$

where dv_a/dt is the rate of change of airspeed. This additional vertical speed adds to the vertical speed relative to the air, i.e. $v_a^z = s + v_e$. This effect can be significant, even for modest rates of change of airspeed. Substituting into (2.47), the vertical wind speed is then given by

$$v_w^z = v_g^z - s - v_e. \tag{2.51}$$

Calculation of the vertical wind speed in practice is described in detail in Chapter 4.

2.4 Summary

A number of fundamental characteristics of the problem of determining the wind velocity from limited sailplane flight data have been derived in this chapter. These are summarised as follows.

It is convenient to resolve the problem into the horizontal and vertical components. The vertical component of the wind velocity is relatively straightforwardly obtained from the measured sailplane vertical velocity relative to the ground and correcting for the effects of sailplane sink rate and acceleration. The corrections require the airspeed, which if not measured must be calculated using a prior calculation of the horizontal component of the wind velocity.

The horizontal wind velocity can be calculated directly if the sailplane ground velocity, airspeed and heading are measured. However, the problem is underdetermined if any of these data are not available. If the ground velocity and airspeed, or ground velocity and heading, are measured, then there is a one-parameter family of solutions for the wind velocity. However, if multiple sets of measurements are made in a region where the wind velocity is constant (as is likely in the case of mountain wave) then the family of solutions may be reduced to a single solution. A key result is that this reduction depends on the differences in the sailplane heading where the multiple data are collected. This is shown by calculating the sensitivity of the solution to errors (in the airspeed, ground velocity, or heading, or in the assumption of a constant wind velocity) for the case of two sets of measurements. The sensitivity is a function of the heading difference and is a minimum near 90° and diverges at 0° and 180°. The sensitivity can also be written in terms of the difference in ground velocities relative to the airspeed. The significant outcome is that turning flight is required for wind velocity estimation from these data, and that estimates cannot be obtained for straight flight.

If ground velocity data only are measured then there is a two-parameter family of solutions for the wind velocity, even for multiple data in a constant wind field. The space of solutions can be reduced if *a priori* constraints on the airspeed (or heading) are available. The precision of solutions obtained will depend on the strength of these constraints and on the differences in ground velocities at the times at which multiple data are measured.

Chapter 3

Flight Data

Data collected during four sailplane flights were used as data for the algorithms described in this thesis. These flights, the data collected, and some ancillary information are outlined in this chapter. These flights are part of the Perlan Project (described below). One flights was flown in California, two in Argentina, and one in New Zealand, in 2003, 2005, 2006, and 2002, respectively. These flights were used because they were well-documented, used the same sailplane which was more highly instrumented than in usual sailplane flights and therefore provided more data, and flight objectives were to explore the wave system and reach a high altitude. The flights, data, and other information are summarised in Table 3.1. Each of the flights are described in the following sections.

3.1 The Perlan project

The Perlan Project [72] is a current research project with an objective of flying a sailplane to an altitude of 100,000 ft using stratospheric mountain waves and the Polar Vortex [73]. The project is to be carried out in 3 phases. Phase 1 involves climbing well past the tropopause into an increasingly strong wave in the stratosphere, not to exceed 62,000 ft (18,900 m). Flight data used for this thesis is from Phase 1. A modified Glaser-Dirks Flugzeugbau GmbH DG505M sailplane with an unpressurised cabin was used for Phase 1. A few attempts were made in the Southern California and Omarama, New Zealand, but the stratosphere was not reached. The goal was accomplished by E. Enevoldson and S. Fossett on 29 August 2006, who achieved an altitude of 50,671 ft (15,447 m) which was well into the stratosphere, and set a new world record altitude for gliders [72]. Phase 2 is underway, which involves redesign of a high performance sailplane with a pressurised cabin to fly up to 90,000 ft [72]. Flight testing is scheduled to begin in California City, California, in spring 2013, while the first attempts to reach 90,000 ft will be launched from El Calafate, Argentina, deep in the south of Patagonia, in the Southern Hemispheric late winter and spring later that year. Phase 3 will be determined depending on the progress of Phase 2.

Table 3.1 Summary of the flights, data, and other information.

Flight No.	1	2	3	4
Perlan Flight No.	39	63	66	24
Pilots	Steve Fossett and Einar Enevoldson			
Aircraft	DG505M			
Location	Southern California	Argentina	Argentina	New Zealand
Launch place	California City	El Calafate	El Calafate	Omarama
Launch place Lat/Log	35.2N 118.0E	50.3S 72.1W	50.3S 72.1W	44.5S 170.0E
Launch place altitude (m)	750	207	207	420
Launch time (UTC)	2140 24/4/2003	1113 25/9/2005	1410 29/8/2006	2101 10/8/2002
Launch time (Local time)	1340 24/4/2003	0813 25/9/2005	1110 29/8/2006	0901 11/8/2002
Wave system	Sierra Nevada	Southern Andes	Southern Andes	Southern Alps
Flight duration (h)	4.8	4	4.8	4.6
Release time after launch (min)	30	30	25	20
Release altitude (km)	3.2	1.9	2	1.4
Max. altitude (km)	13.0	10.0	15.4	9.2
GPS data	Y	Y	Y	Y
Airspeed data	Y	Y	Y	Y
Heading data	N	N	Y	N
Pressure data	Y	Y	Y	Y
Temp. data	Y	Y	Y	Y
Variometer data	Y	N	Y	Y
Nearby Radiosonde data	Y	N	N	Y
Satellite pictures	Y	Y	Y	Y
Reanalysis - wind	Y	Y	Y	Y
Reanalysis - temp	Y	Y	Y	Y
Reanalysis - analysis	Y	Y	Y	Y

3.2 Flight 1: Perlan Flight 39 Southern California

The first data set is from a Perlan flight in lee waves of the Sierra Nevada Mountains in Southern California. This is flight 39 of the Perlan Project. The flight began at California City (35.2° N, 118.0° E, altitude 750 m) at 2140 Z on 24 April 2003 (1340 local time). The sailplane was launched by towing behind a powered aircraft and released from tow approximately 30 minutes after take-off at an altitude of approximately 3200 m. Pilots were E. Enevoldson and S. Fossett. The flight lasted 4.8 hours and proceeded along the Owens Valley to the east of the Sierra Nevada Mountains to Big Pine and returned to California City. The latitude and longitude coordinates are projected onto an x(East)-y(North) coordinate system in kms in which the take-off point is at the origin. The flight path and the altitude versus time are shown in Fig. 3.1 (a) and (b) respectively. The maximum altitude was 13,044 m. There was extensive middle cloud upwind of the Sierra Nevadas and lenticular clouds were present in layers up to 14,000 m. Large lee rotors were present in the Owens Lake area. For fixed meteorological conditions, the wave structure is, in principle, fixed relative to the topography. A convenient reference point for a hill or ridge is the center of the ridge. For complex terrain the situation is more complicated. However, particularly for the northern part of this flight, the dominant topography is the eastern ridge of the mountain range, running NNW-SSE, to the west of the flight path. Therefore the center line of this ridge is taken as a reference which is referred to as the "ridge line". Points at maximum altitude along this ridge were located manually and the ridge line determined by spline interpolation. The resulting ridge line is shown as the thick black line in Fig. 3.1 (a).

The sailplane was a two-seater production Glaser-Dirks DG-505M (DG Flugzeugbau GmbH, Bruchsal, Germany) specially equipped for high altitude flight and flown at an all up weight of 805 kg (wingspan 20 m and wing loading 45 kg/m^2). The maximum altitude possible with the modified configuration was calculated as 62,000 ft.

In addition to the usual instruments, the sailplane was equipped with a modified Volkslogger GPS positioning system and pressure transducer (Garrecht Avionik GmbH, Bingen, Germany), a Borgelt B-50 airspeed indicator (Borgelt Instruments, Toowoomba, Australia), and a Platinum RTD (resistance temperature detector) outside air temperature probe. GPS fixes were obtained at 1 second intervals from the Volkslogger and pressure recordings made at 8 second intervals. Airspeed and temperature measurements were made at approximately 2.5 second intervals. All data were merged into a serial data stream and recorded on a custom data logger. All data (except GPS fixes) were linearly interpolated onto the one-second GPS time-stamps post flight. Variometer data are also available from the B-50.

The sailplane flight polar was determined using a combination of the 45 kg/m^2 flight polar from the DG-505M flight manual and measurements made by comparison flights with another standard sailplane. The flight polar is shown in Fig. 3.2. The sink rate varies between approximately 0.5 and 1.3 m/s at 25 and 40 m/s IAS, respectively.

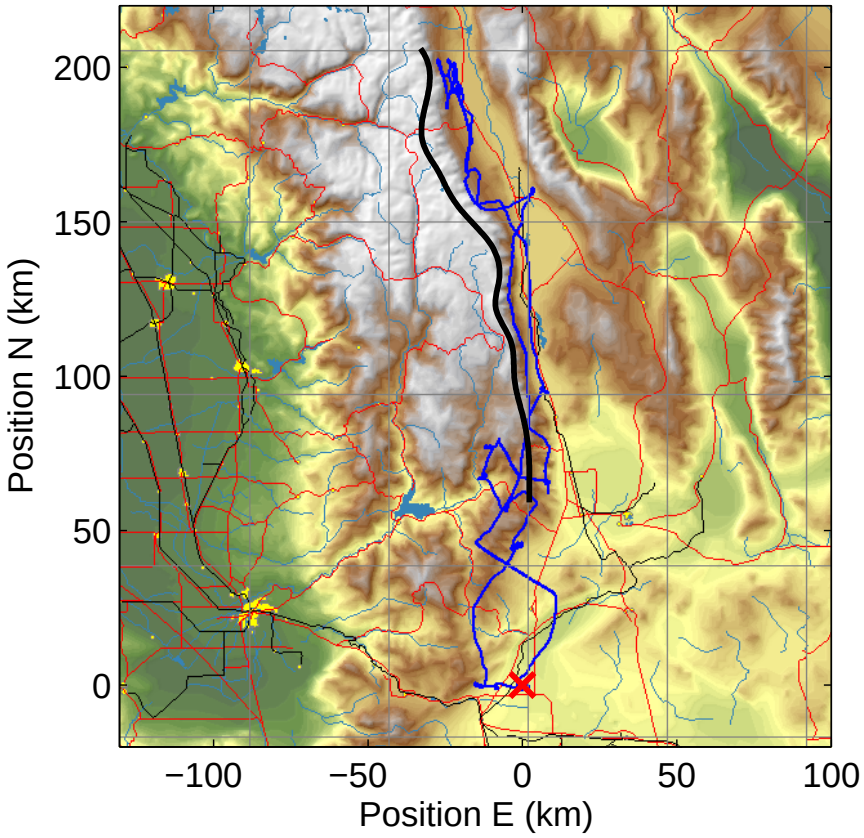

(a)

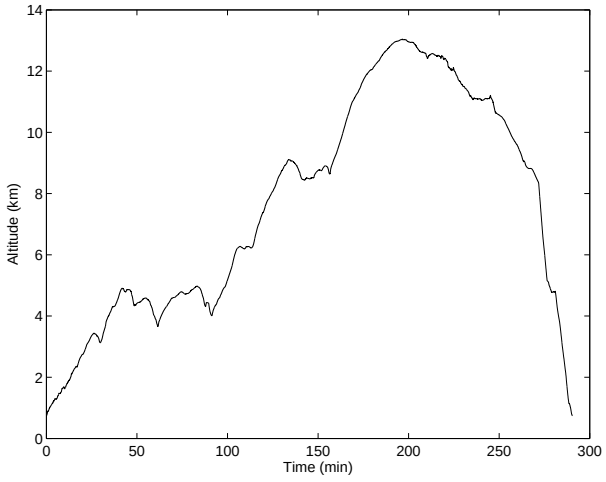

(b)

Figure 3.1 Flight 1: (a) Flight path (blue thin line) on a topography map (displayed with "SeeYou" [57]). The red cross denotes the take-off point at California City. Position as labeled is relative to the take-off point. The thick black line denotes the estimated ridge line as described in the text. (b) flight altitude vs time.

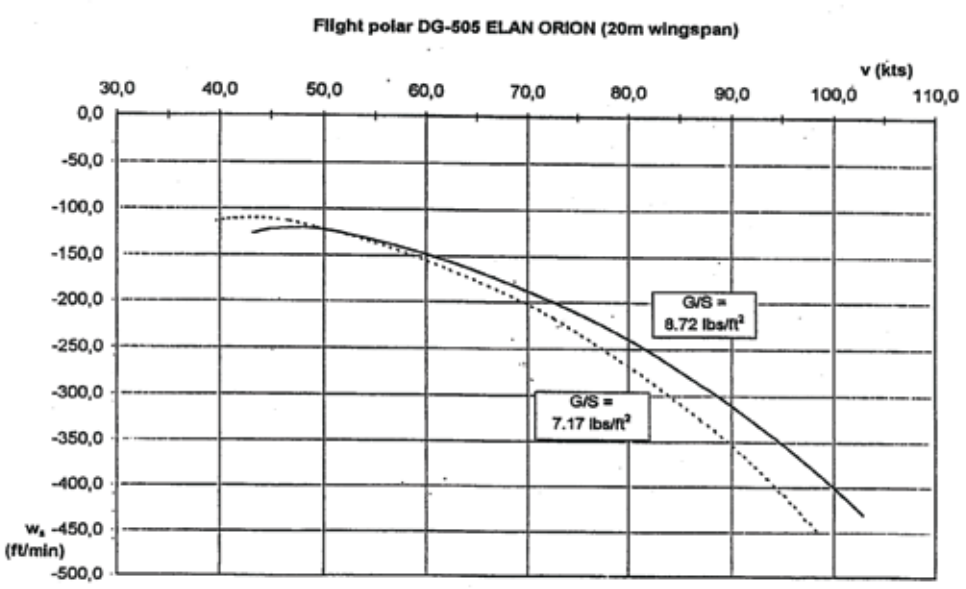

Figure 3.2 The DG505M glider polar from the flight manual for a wing load of 35 kg/m^2 (dashed line) and 42.6 kg/m^2 (solid line) [53].

Various meteorological data are assembled for this flight. Two sets of radiosonde soundings are obtained from University of Wyoming Department of Atmospheric Science weather service website [74]. The radiosondes were released from Edwards Air Force Base, Edwards, California, (approximately 120 km south of the centre of the flight path) at 1500 Z on 24 April 2003, and at Desert Rock, Mercury, Nevada (approximately 180 km east of the centre of the flight path) at 0000 Z on 25 April 2003. The soundings are approximately 9 hours before and at the time at the midpoint of the flight, respectively. The soundings include temperature, pressure, wind speed and direction. The wind speed and direction are shown in Fig. 3.3 (a) and (b). The temperature traces are quite consistent (Fig. 3.3 (c)), and a straight line fitted to the data above 2 km with the equation $T = \Gamma z + T_0$, gives $\Gamma = -6.9$ K/km and $T_0 = 296.5$ K, shown as the dashed line in Fig. 3.3 (c). The sailplane temperature measurements are discussed in Section 4.3.1.

Another useful set of data is from a "Reanalysis." Reanalysis uses a variety of meteorological data [75] which is assimilated in time and space and used as boundary conditions in a numerical model to calculate the state of the atmosphere in a dense grid in time and space. The Reanalysis is calculated after the observation time, so is not used for forecasting, allowing incorporation of data from future time-steps. The Reanalysis data is available for global regions from 1948 to the present, including 4-times daily, daily, and monthly values of the air temperature, geopotential height, humidity, U-wind (zonal wind velocity component), V-wind (meridional wind velocity component). In particular, higher resolution data is available for the North America Region at 3-hourly intervals. The North American Regional Reanalysis model uses the very high resolution NCEP Eta Model together with the Regional Data Assimilation System (RDAS) [76]. The Global Reanalysis data and North American Reanalysis data can be extracted from the NOAA/OAR/ESRL PSD website [77].

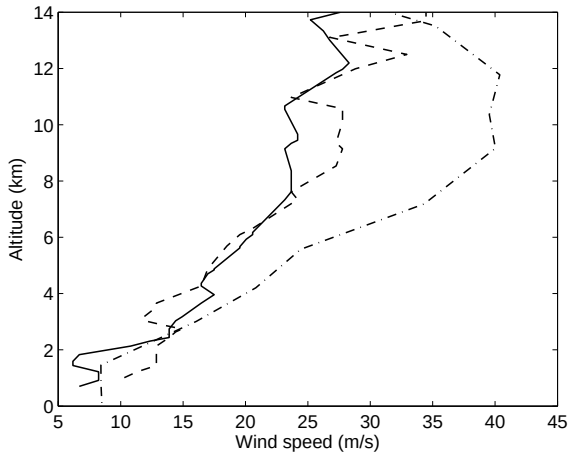

(a)

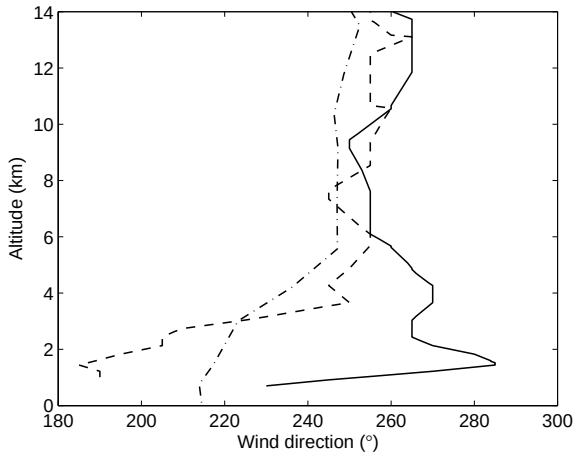

(b)

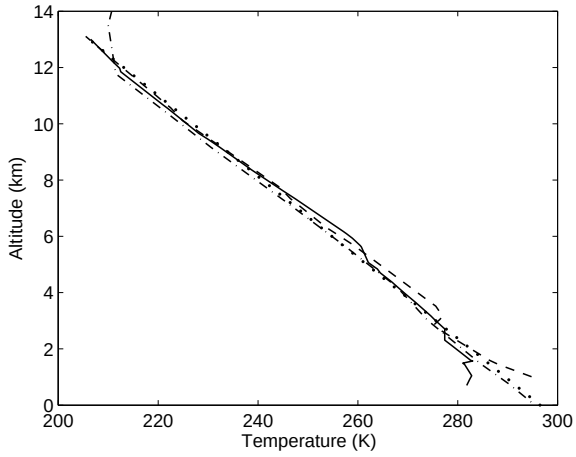

(c)

Figure 3.3 Flight 1: Radiosonde data measured at Desert Rock (solid line) and Edward Air Force Base (dashed line) and reanalysis data (dot-dashed line) versus altitude for (a) wind speed, (b) wind direction, and (c) temperature. A straight (dotted) line is fitted to the temperature traces above 2 km as described in the text.

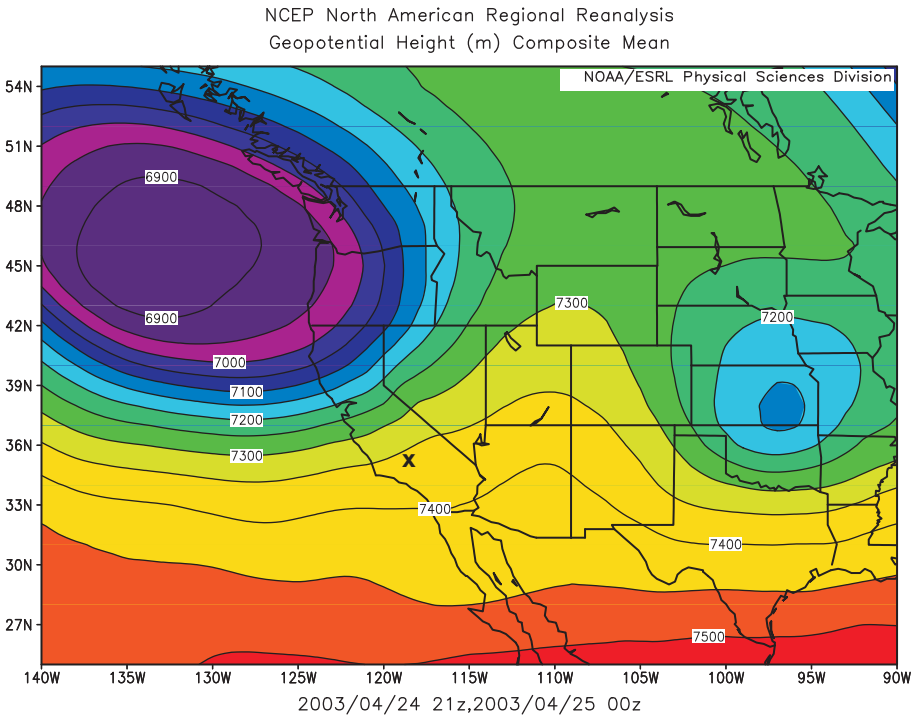

Figure 3.4 Flight 1: Geopotential height of Western U.S.A. at a pressure level of 400 mb [77]. The position of launch of Flight 1 is marked by the cross.

The former is used for comparison with result from this flight, and the latter is used for the three other flights.

A plot of the geopotential height for the Western U.S. at a pressure level of 400 mb (approximately 7200 m), averaged over 3 hours between 2100Z and 0000Z, is extracted from the North American Reanalysis Site [77] and shown in Fig. 3.4. This shows a depression to the North-West of the flight location with an anticlockwise air flow giving a NSW wind over the region of the flight. The wind speed and direction and the temperature versus altitude at the flight launch point extracted from the Reanalysis are also shown in Fig. 3.3. Comparison with the radiosonde data shows that the Reanalysis gives a higher wind speed (about $5\ \mathrm{m/s}$ larger at $4-8\ \mathrm{km}$ and $10\ \mathrm{m/s}$ larger at higher altitudes), and a difference in direction of about $10°$. The temperature data are quite consistent. This gives some idea of the variability in wind speed and direction in time and space to be expected. A satellite picture in the visible band of the flight region is shown in Fig. 3.5. The details of the picture are given in the caption. This shows the upper level cloud formations and this is discussed with respect to results in Section 4.3.1.

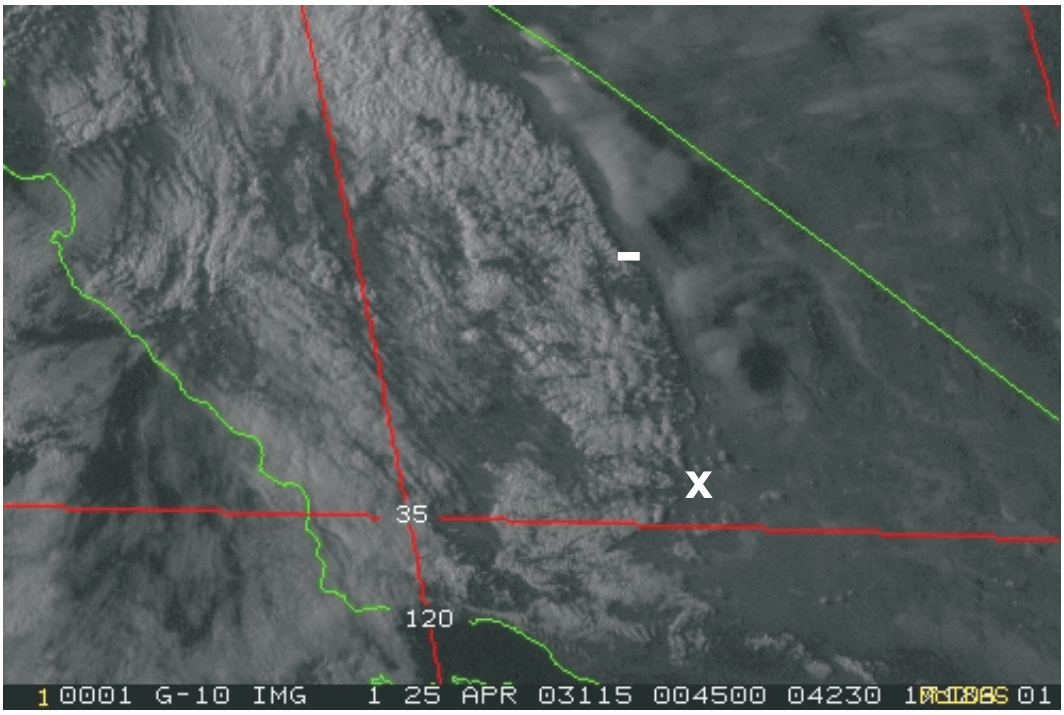

Figure 3.5 Flight 1: Geostationary satellite GOES10 picture, band 1 (visible) on 25/4/2003 at 0045Z for Flight 1 (California) [17]. The take off position is marked by an x. The line segment marks the downwind flight segment described in Section 4.3.1.

3.3 Flight 2: Perlan Flight 63: Argentina

The second set of data is from Perlan Project Flight 63 which took place in Argentina in the lee wave of the Andes. The same sailplane as for Flight 1 was flown with the same instrumentation. The sailplane was launched from the airport Aeropuerto El Calafate in Patagonia, Argentina (50.3S 72.1W altitude 207 m) at 1113 Z on 25 September 2005 (0813 local time), flew along Lake Argentino, south to the Cervo Cervantes mountains and then back to El Calafate. The flight lasted 4 hours. The basic data collected consist of GPS position and indicated airspeed. All data were recorded as for Flight 1. The flight path and topography are shown in Fig. 3.6(a) and the flight altitude versus time is shown in Fig. 3.6(b). The topography is dominated by the eastern ridge of the Southern Andes mountain range, running North-South, to the west of the flight path. The estimated ridge line is shown as the thick black line in Fig. 3.6(a). The maximum altitude reached for this flight was 10 km. The data for the final 30 minutes of the flight were not available.

The geopotential height at 400 mb and averaged over 6 hours between 1200Z and 1800Z in the region the flight was extracted from the Global Reanalysis site [77] and is shown in Fig. 3.7. There is a high pressure region to the North giving WNW winds in the region of the flight path. The wind speed and direction and the temperature versus altitude at the flight location extracted from the Reanalysis are shown in Fig. 3.8. The wind direction is consistent with the geostrophic wind implied by the plot of geopotential height. The lapse rate from the temperature trace above 3 km is approximately -7.2 K/km. A satellite picture in the visible band of the flight region is shown in Fig. 3.9. The details of the picture are given in the caption. This is discussed with respect to the results in Section 4.3.2.

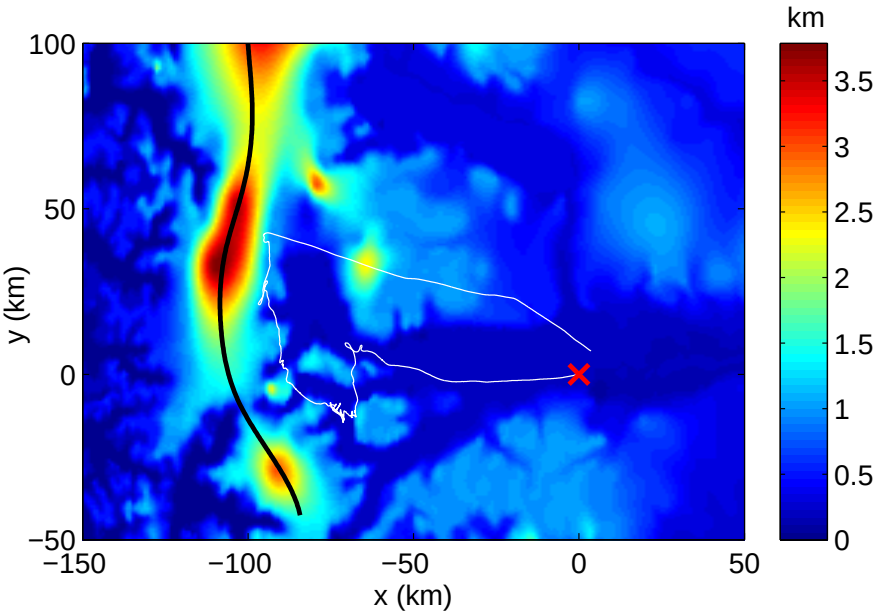

(a)

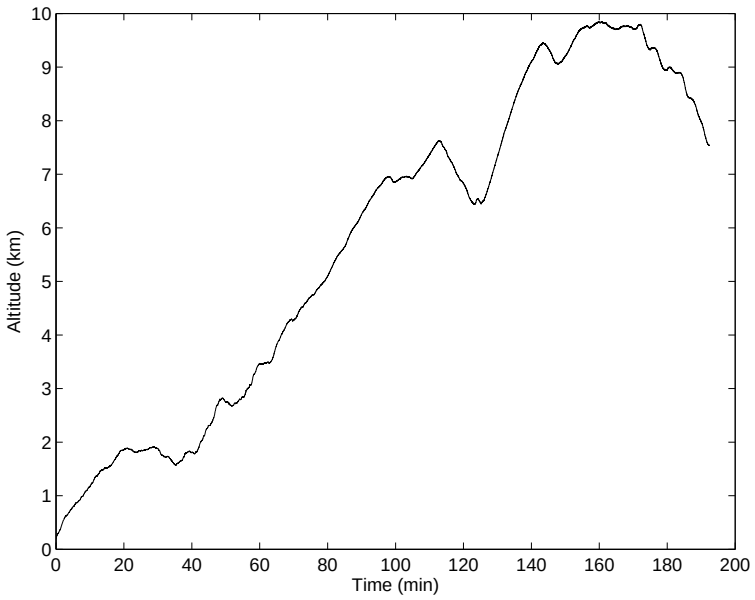

(b)

Figure 3.6 Flight 2: (a) Flight path and topography (altitude scale shown in the colour bar). The red cross denotes the take-off point at EI Calafate, the thick black line denotes the estimated ridge line, and the white line denotes the flight path. (b) Flight altitude versus time.

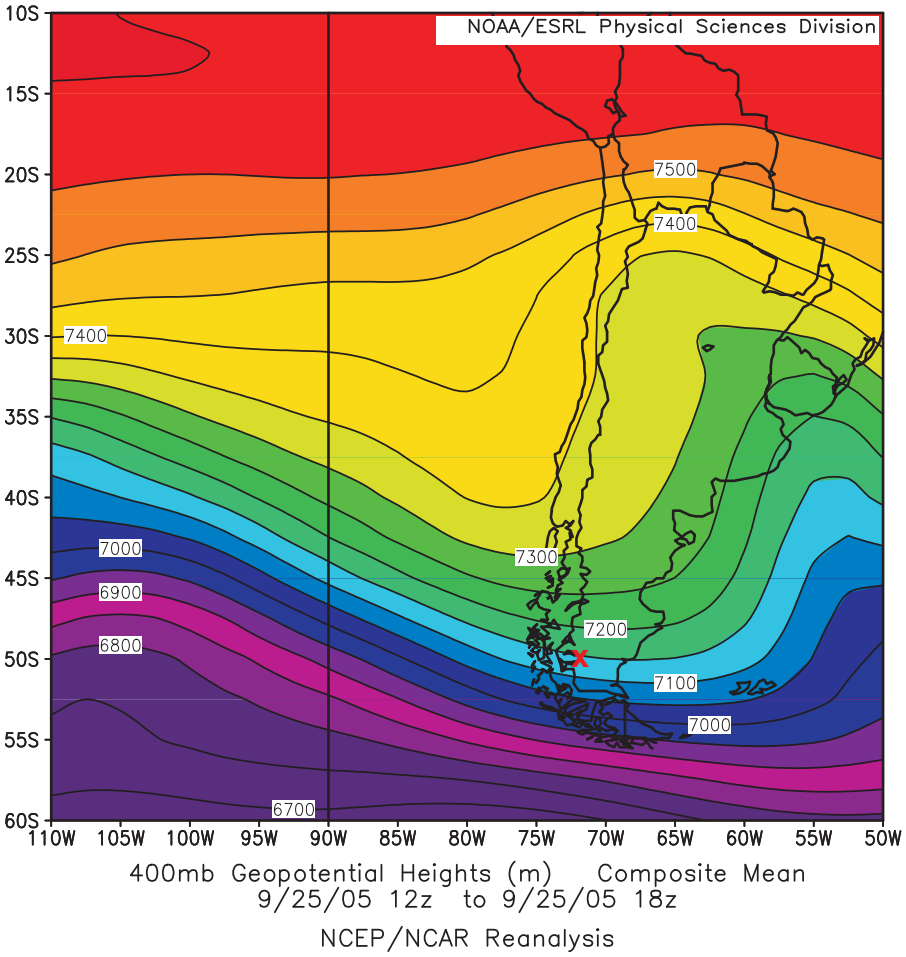

Figure 3.7 Flight 2: Geopotential height plot for the Southern Andes region at a pressure level of 400 mb [77]. The position of the take off of Flight 2 is marked by the cross.

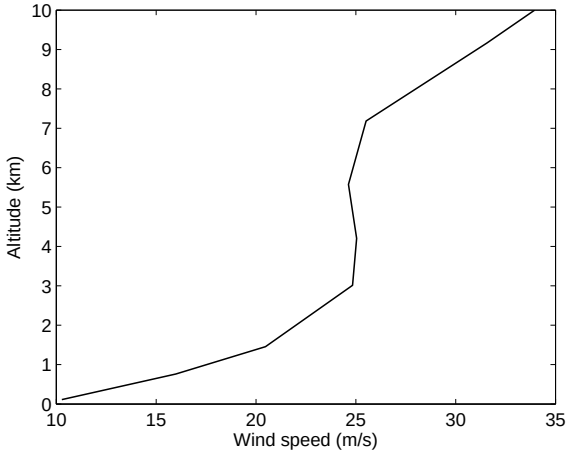

(a)

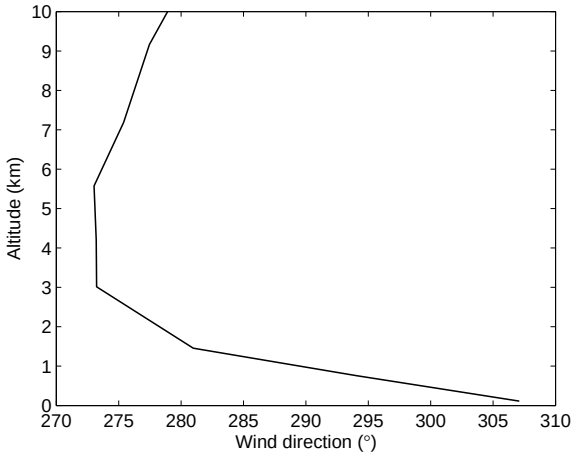

(b)

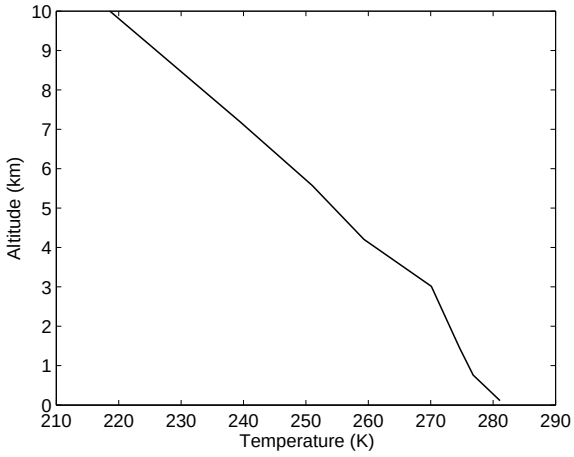

(c)

Figure 3.8 Flight 2: Reanalysis data versus altitude for (a) wind speed, (b) wind direction, and (c) temperature.

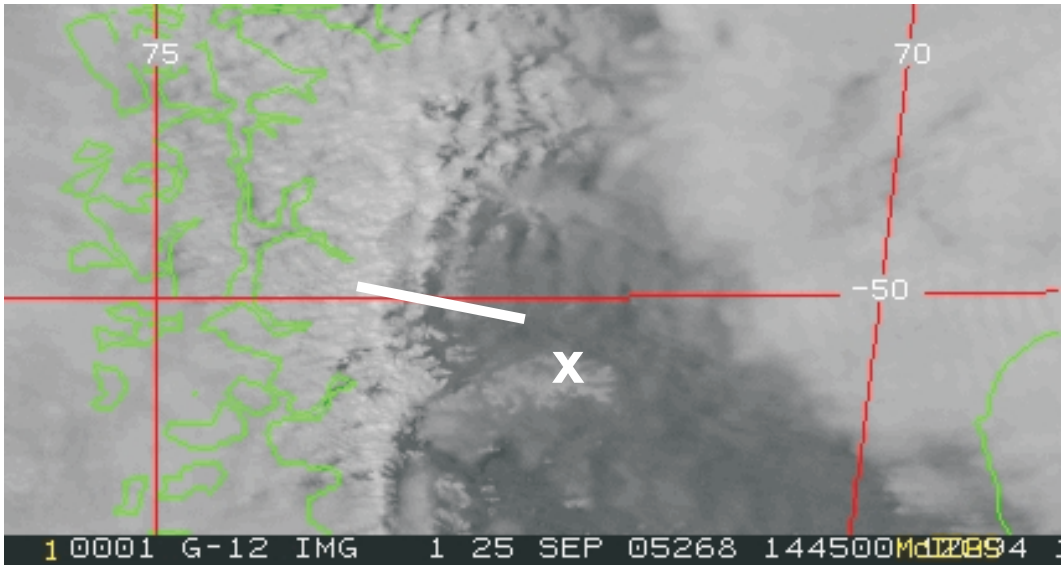

Figure 3.9 Flight 2: Geostationary satellite GOES12 picture, band 1 (visible) on 25/9/2005 at 1445Z in Argentina [17]. The take off position is marked by an x. The line segment marks the downwind flight segment described in Section 4.3.2.

3.4 Flight 3: Perlan Flight 66: Argentina

The third data set is from Perlan Project Flight 66 which took place in Argentina in 2006 at a similar location to Flight 2. The same sailplane as for Flight 39 was flown with the same instrumentation. During this flight, pilots Steve Fossett and Einar Enevoldson set a world-record altitude for gliders of 15,447 m (50,671 ft). The flight entered the stratosphere with the tropopause being at approximately 11 km. The sailplane was launched from the same airport as Flight 2 at 1410Z on 29 August 2006 (1110 local time), flew along Lake Argentino, south to the Cervo Pietronrlli mountain range, then north along the ridges, and finally back to the airport. The duration of the flight was 4.8 hours. Heading data from a electronic compass was also available for this flight. The flight path and topography are shown in Fig. 3.10(a) and the altitude versus time in Fig. 3.10(b). The estimated ridge line is shown as the thick black line in Fig. 3.10(a) and the launch position is marked by the cross. The flight path is further south than Flight 2, and hence the ridge line is extended further south.

The geopotential height plot for the flight region, from the Global Reanalysis [77], is shown in Fig. 3.11 for 400 mb and 100 mb, being in the troposphere and stratosphere, respectively. There is an high pressure region to the North giving a westerly air flow. The wind speed and direction and the temperature versus altitude at the launch location, extracted from the Reanalysis, are shown in Fig. 3.12. The wind direction is consistent with the plot of geopotential height. The lapse rate of the temperature trace is approximately -6.8 K/km below 10 km and zero above 10 km. A satellite picture in the visible band of the flight region is shown in Fig. 3.13. The details of the picture are given in the caption. This is discussed with respect to results from the flight in Section 4.3.3.

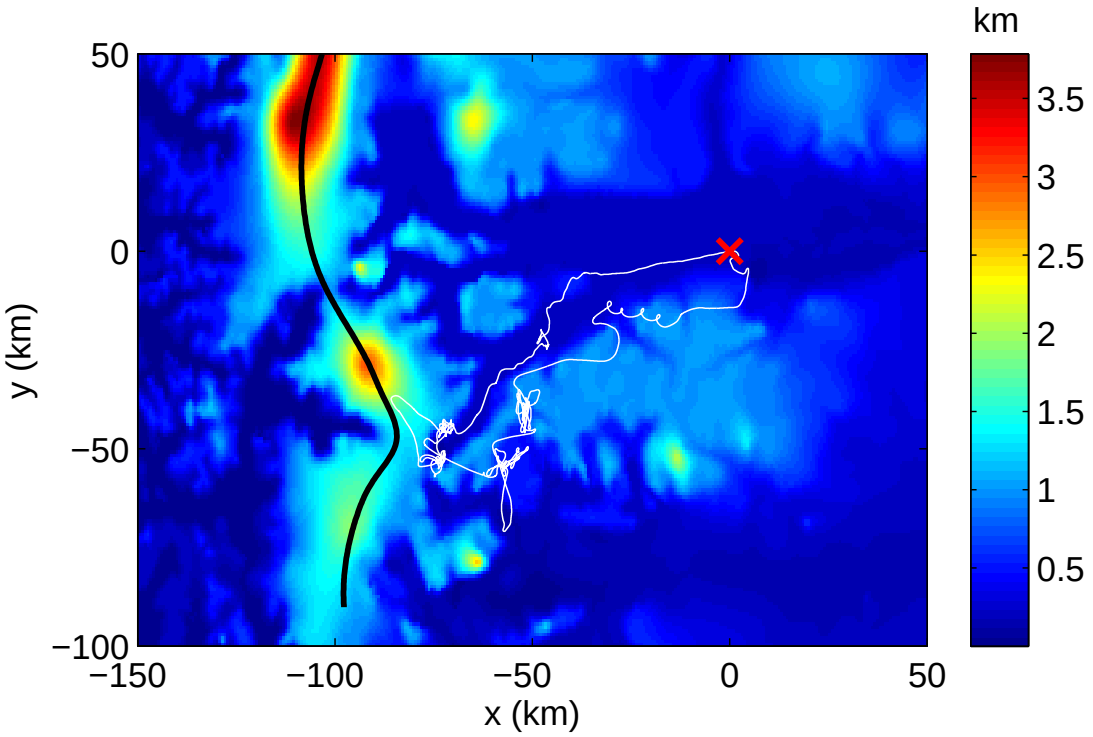

(a)

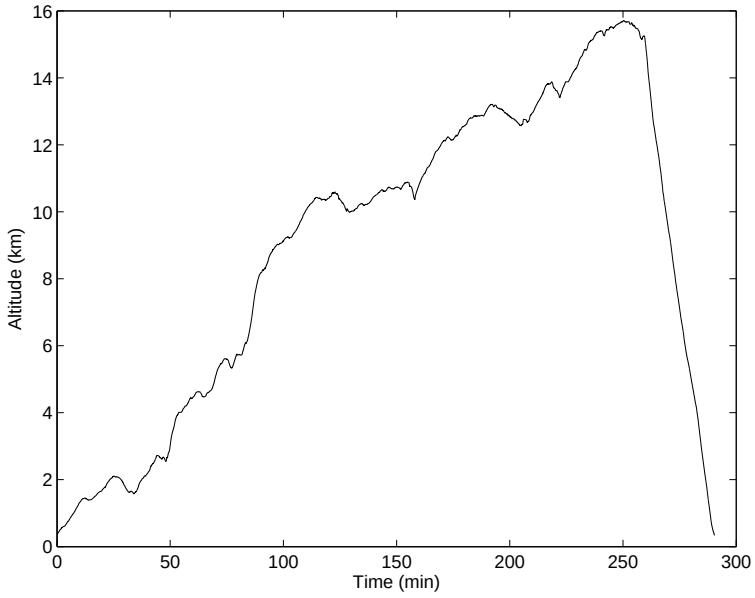

(b)

Figure 3.10 Flight 3: (a) Flight path and topography. The red cross denotes the take-off point at EI Calafate, the thick black line denotes the estimated ridge line, and the white line denotes the flight path. (b) Flight altitude vs time.

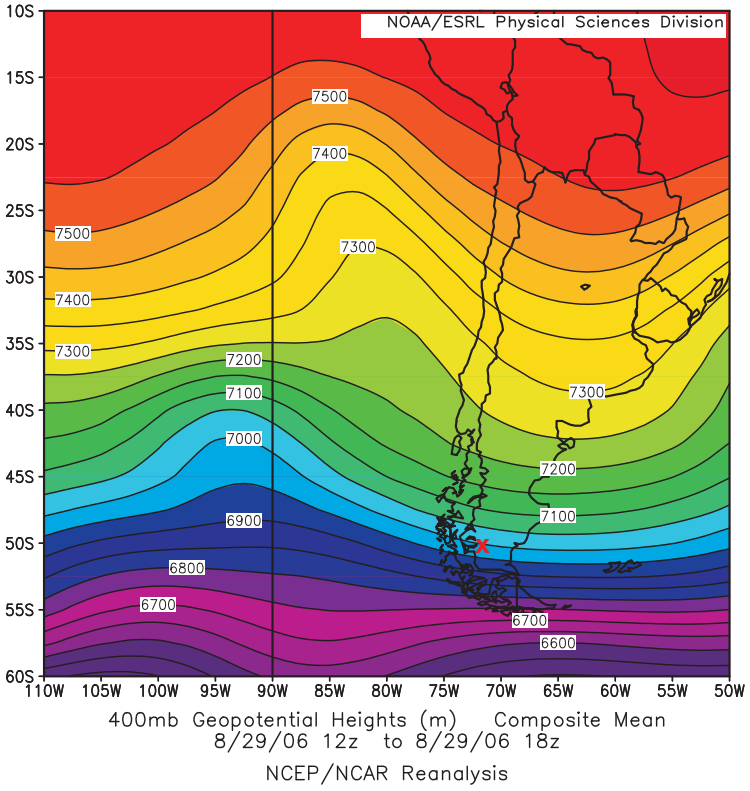

(a)

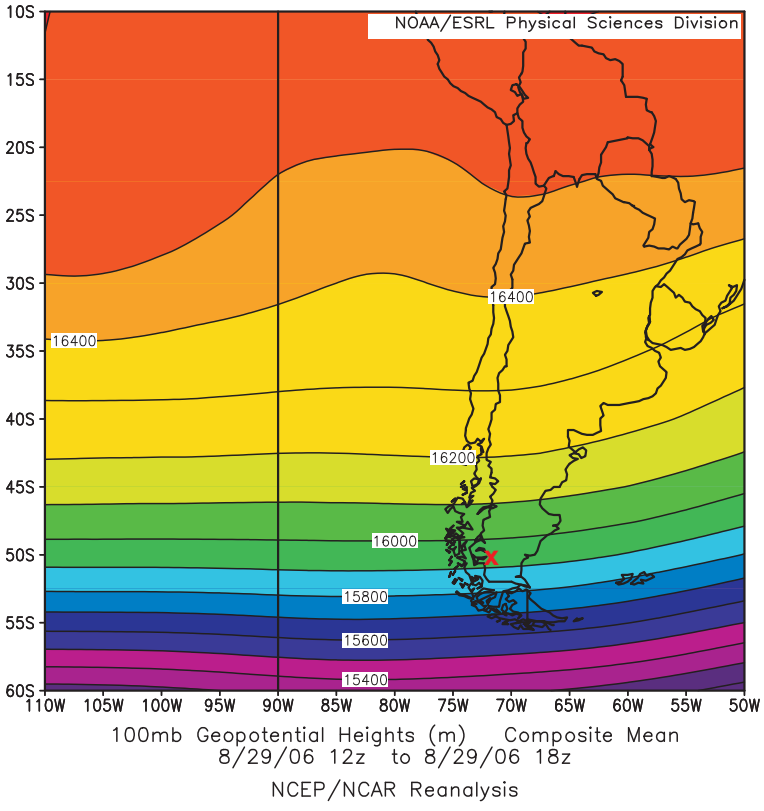

(b)

Figure 3.11 Flight 3: Geopotential height plots for the Southern Andes region at pressure levels of (a) 400 mb (troposphere), and (b) 100 mb (stratosphere) [77]. The position of the take off for Flight 3 is marked by the cross.

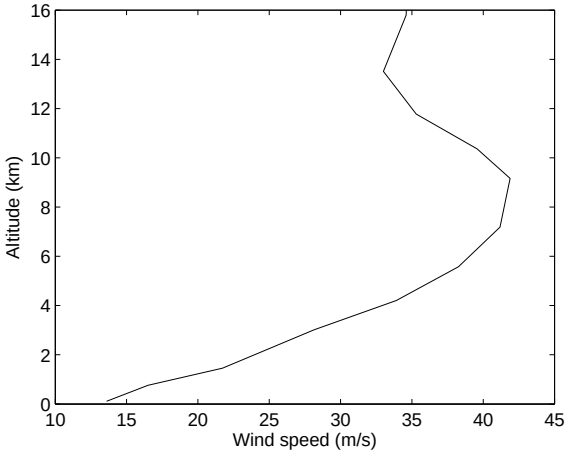

(a)

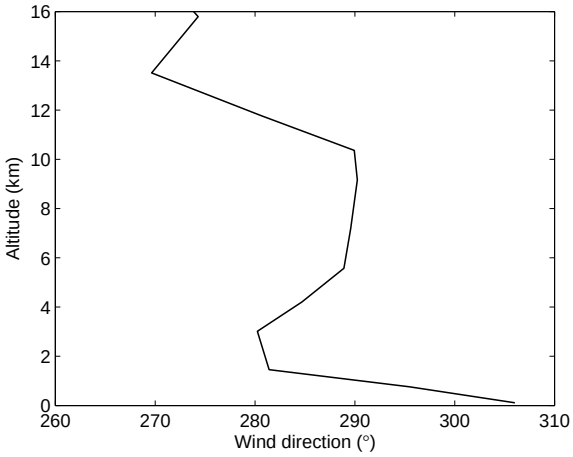

(b)

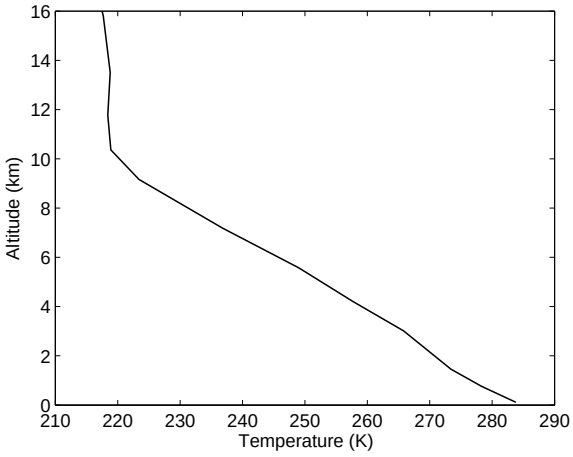

(c)

Figure 3.12 Flight 3: Reanalysis data versus altitude for (a) wind speed, (b) wind direction, and (c) temperature.

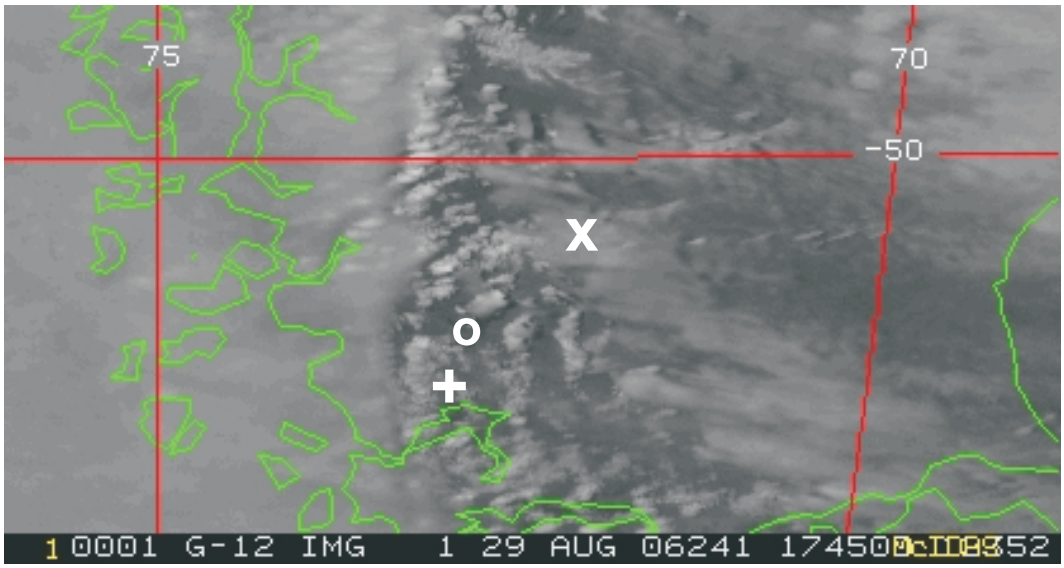

Figure 3.13 Flight 3: Geostationary satellite GOES12 picture, band 1 (visible) on 29/8/2006 at 1745Z in Argentina [17]. The takeoff position is marked by an x. The most Southern point of the flight is marked by a +. The point of highest altitude is marked by a circle.

3.5 Flight 4: Perlan Flight 24: Omarama

The fourth data set is from Perlan Project Flight 24 that took place in Omarama, New Zealand. The Southern Alps of New Zealand form a high barrier which lies across the belt of strong west winds, and when the wind blows extensive lee waves form. Omarama is situated in the lee of the Southern Alps in a hot inter-mountain valley. The same sailplane as described above was flown with the same instrumentation. The sailplane was launched from the Omarama Airfield (44.5S 170.0E, altitude 420 m) at 2101 Z on 10 August 2002 (0901 on 11 August 2002 local time), traveled 100 km along the Southern Alps to Mt. Cook, down South to Cromwell, and then back to Omarama. The flight lasted 4.6 hours. The basic data consisted of GPS position and indicated airspeed. The flight path and topography are shown in Fig. 3.14(a) and the altitude versus time is shown in Fig. 3.14(b). The topography in the vicinity of the flight path is dominated by mountain ranges south of Mt. Cook, running N-S, to the west of the flight path. A long ridge line and two short ridge lines relevant to the flight are shown as the thick black lines in Fig. 3.14(a). The launch position is marked by the cross. The maximum altitude reached during this flight was 9.2 km.

The geopotential height at 400 mb averaged over 6 hours between 1800Z and 0000Z around New Zealand, extracted from the Global Reanalysis, is shown in Fig. 3.15. There is a trough of low pressure to the south and east of the South Island and a high pressure region to the west, creating a SW flow over the South Island. The wind speed and direction and the temperature versus altitude at the launch location, extracted from the Reanalysis, are shown in Fig. 3.16. Radiosonde data measured at 0000Z on 11 Aug 2002 from NZNV Invercargill Aerodrome which is 250 km SW are also shown in Fig. 3.16. For comparison the reanalysis data at the Invercargill Aerodrome at the same time was extracted and also shown in Fig. 3.16. Note that the Reanalysis values are averaged over a 6 hour period prior to the radiosonde measurements. The Reanalysis temperatures are essentially identical at the two locations below 10 km, and they agree well with the radiosonde data. The Reanalysis wind speeds of the two locations are similar below 5 km, and differ by 5-10 m/s above 5 km. The radiosonde wind speed is similar to the Reanalysis at Invercargill below 2 km, but differ by up to 20 m/s above 2 km. The Reanalysis wind directions at the two locations are quite similar above 3 km, and they agree well with the radiosonde sounding. The differences between the radiosonde and Reanalysis wind speeds at Invercargill highlight the difficulty of using the Invercargill radiosonde or Omarama Reanalysis wind speed data for comparison purposes at Omarama. The temperature profile gives a lapse rate of approximately -6.8 K/km above 3 km. A satellite picture in the visible band of the flight region is shown in Fig. 3.17. Unfortunately the GOES10 satellite gives a quite distorted projection in this region. The details of the picture are given in the caption. This picture is discussed with respect to results from the flight in Section 4.3.4.

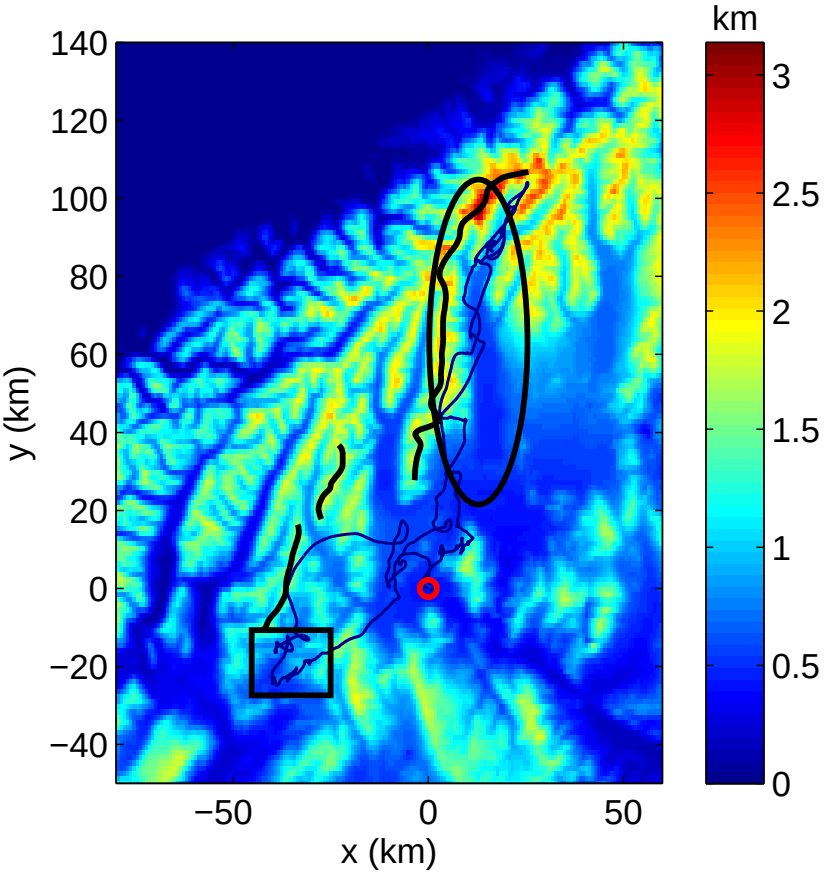

(a)

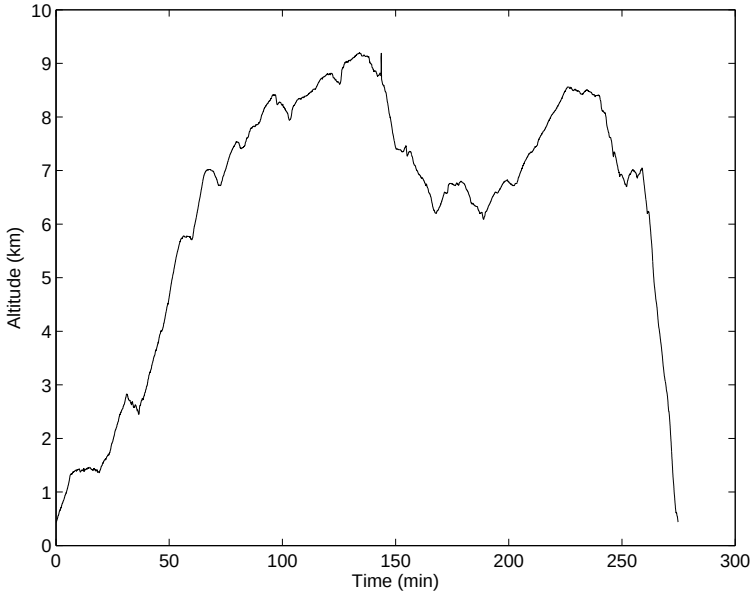

(b)

Figure 3.14 Flight 4: (a) Flight path and topography. The red cross denotes the take-off point at Omarama, the thick black lines denotes some relevant ridge lines, and the thin blue line denotes the flight path. (b) Flight altitude versus time. Two selected flight segments for an altitude range of 3.2-8.1 km and 6.7-8.6 km (as described in Section 3.5) are shown by the ellipse and rectangle, respectively

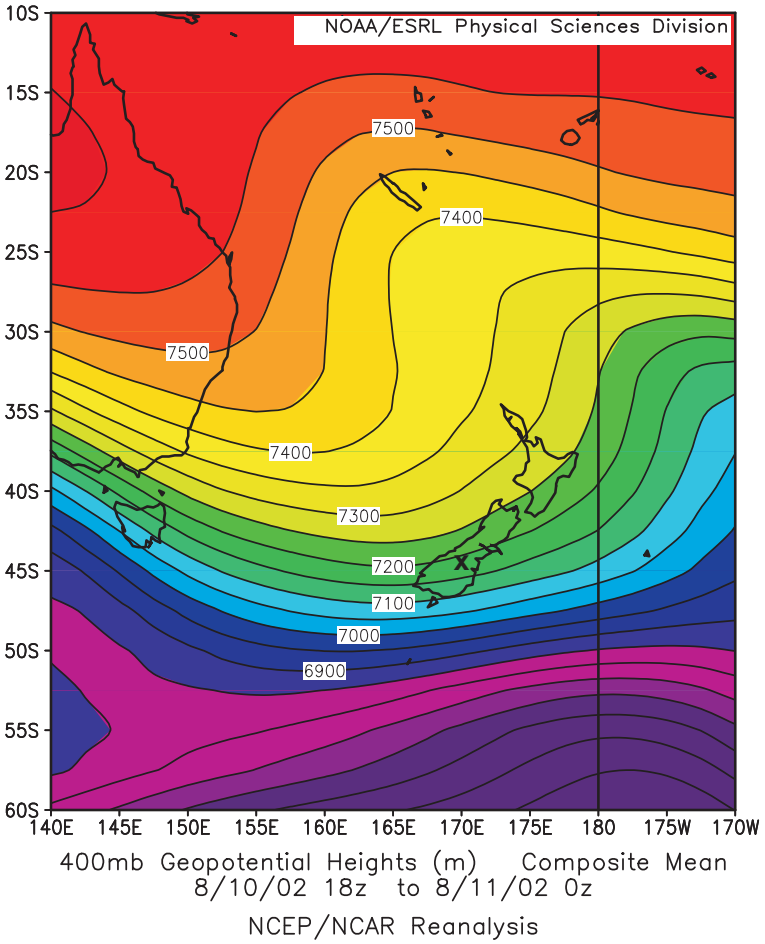

Figure 3.15 Flight 4: Geopotential height plot for the New Zealand region at a pressure level of 400 mb [77]. The position of the launch of Flight 4 is marked by the cross.

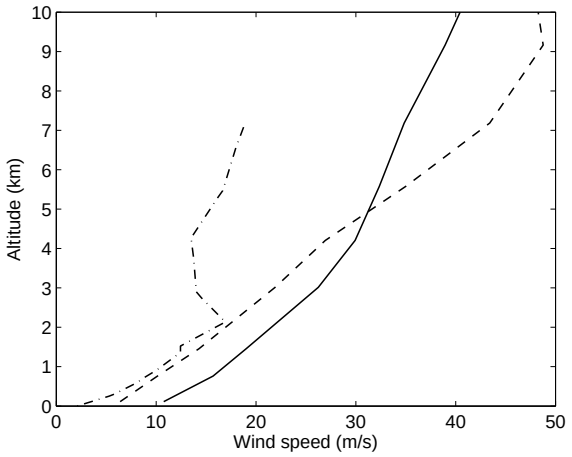

(a)

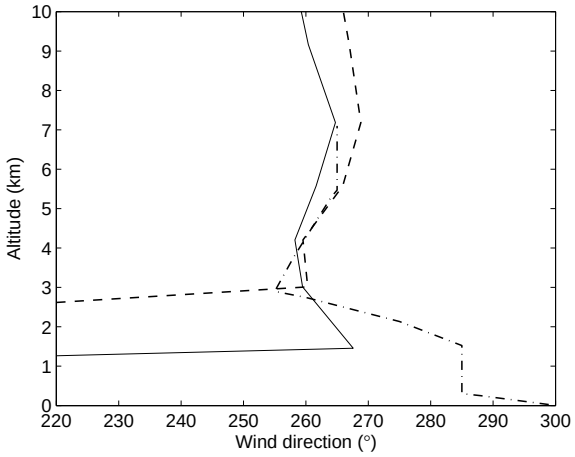

(b)

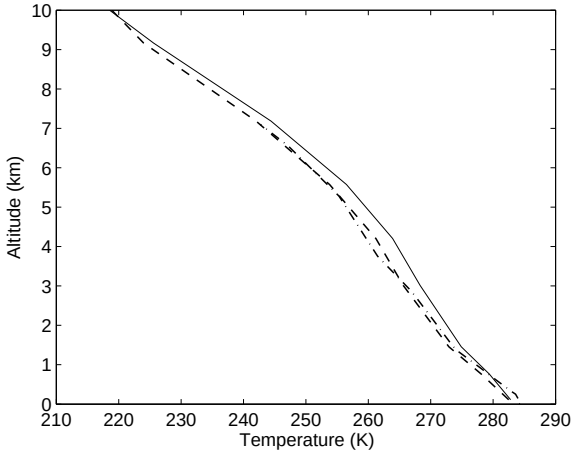

(c)

Figure 3.16 Flight 4: Reanalysis data at the flight launch position (solid line) and at the Invercargill Aerodrome (dashed line) and Radiosonde data at Invercargill (dot-dashed line) versus altitude, for (a) wind speed, (b) wind direction, and (c) temperature.

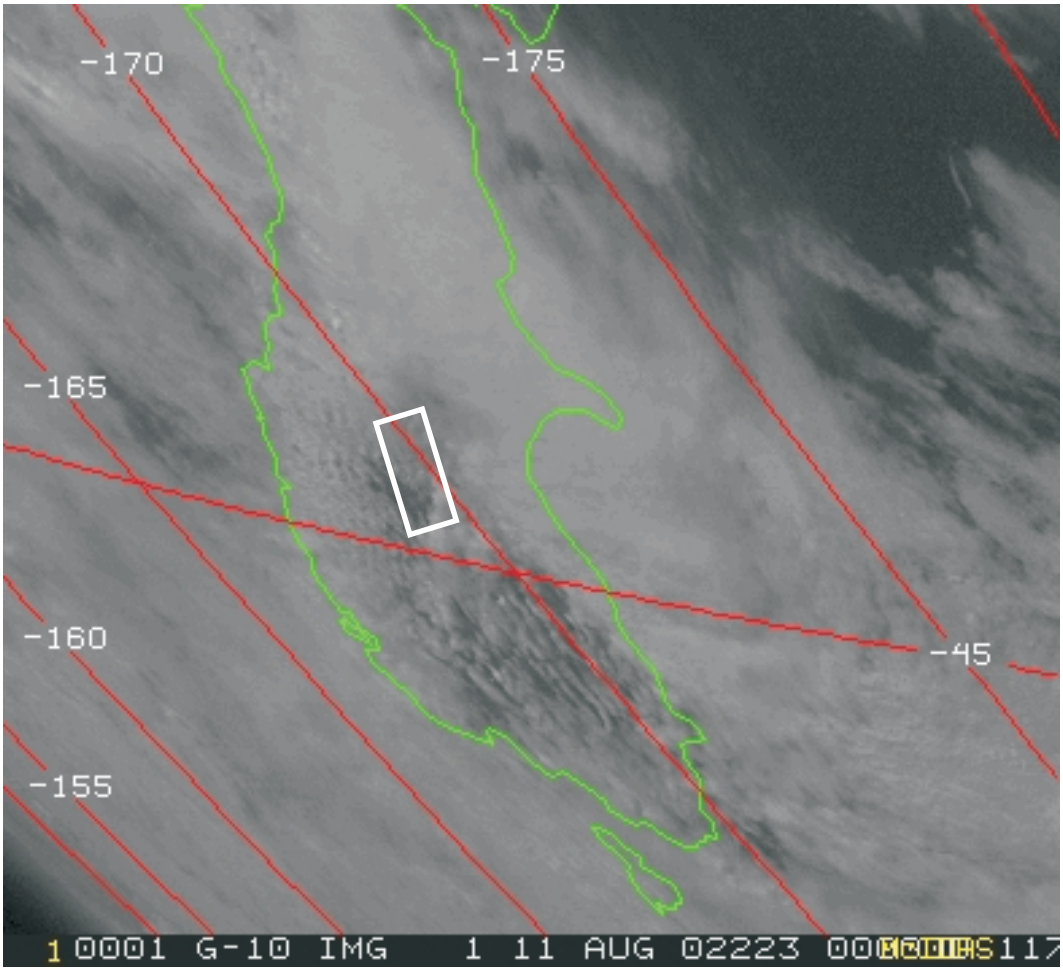

Figure 3.17 Flight4: Geostationary satellite GOES10 picture, on 11/8/2002 at 0000Z in Omarama [17]. The area of the flight path is shown by the rectangle.

3.6 Airspeed correction

As described in Section 1.3.5, the measured (and logged) airspeed is the indicated airspeed that is smaller than the true airspeed due to the effect of the lower air density at altitude. Note that the CAS (Section 1.3.5) is equal to the IAS for IAS < 50 m/s and for larger IAS deviates from the IAS by no more than 3%, based on the DG505 flight manual [53]. For typical airspeeds in the flights considered here these differences are negligible. The relationship between IAS and TAS is given by (1.86) and the effect is significant even at modest altitudes. This is seen from Fig. 3.18 which shows a calculation of the TAS/IAS ratio using the lapse rate of a standard atmosphere ($\Gamma = -6.5$ K/km for $0 < z < 11$ km and $\Gamma = 0$ K/km for $z > 11$ km) and a surface temperature of 288 K. Wind velocity estimation that utilises the sailplane ground velocity data requires the TAS, so that correction of IAS data to obtain the TAS is common throughout the remainder of the thesis. This correction is described here.

As described in Chapter 1, if the altitude is not too high, the incompressible approximation applies and the IAS need be corrected only for air density as ((1.83) and (1.86)), i.e.

$$v_a = v_a^{ind}\left(\frac{\rho_0}{\rho}\right)^{1/2} = v_a^{ind}\left(\frac{T}{T_0}\cdot\frac{P_0}{P}\right)^{1/2}, \tag{3.1}$$

where ρ_0, P_0 and T_0 are the standard sea level values (1.22 kgm^{-3}, 101325 Pa and 288 K, respectively). If the pressure and temperature are logged then this correction is made straightforwardly. If however, temperature and/or pressure are not measured, then estimates of these must be made based on standard atmosphere values. This is generally sufficiently accurate in practice. Sometimes the pressure data may be recorded indirectly as "pressure altitude", which can be converted to pressure using standard equations [78].

For a constant lapse rate, (1.12) and (1.14) show that the pressure varies with altitude as

$$\frac{P}{P_0} = \left(\frac{T}{T_0}\right)^{\alpha} = \left(\frac{T_0+\Gamma z}{T_0}\right)^{\alpha}. \tag{3.2}$$

Therefore, if pressure but not temperature is recorded, then v_a can be calculated as

$$v_a = v_a^{ind}\left(\frac{P}{P_0}\right)^{(1-\alpha)/2\alpha}, \tag{3.3}$$

using the surface pressure P_0 (known or estimated). If temperature but not pressure is recorded, then v_a can be calculated as

$$v_a = v_a^{ind}\left(\frac{T}{T_0}\right)^{(1-\alpha)/2}. \tag{3.4}$$

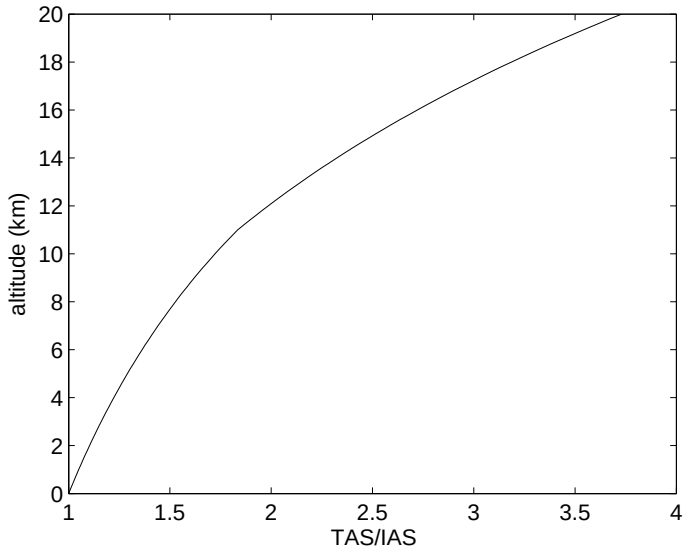

Figure 3.18 TAS/IAS ratio versus altitude calculated based on a standard atmosphere.

If neither temperature nor pressure are recorded, then v_a must be calculated using

$$v_a = v_a^{ind} \left(\frac{T_0 + \Gamma z}{T_0} \right)^{(1-\alpha)/2} \tag{3.5}$$

using a standard lapse rate Γ and the surface temperature T_0 (known or estimated).

Chapter 4

A Heuristic Method for Estimating 3D Wind Velocities

In this chapter methods are described for estimating the 3D wind velocities from logged data consisting of GPS position and airspeed. The methods and some results have been published in [79] and an earlier version in [1]. This data is available relatively accurately for the Perlan Project flights described in the previous chapter. Since these methods do not use a statistical estimation approach as in Chapters 6 and 7, it is referred to here as an "heuristic" method. As described in Chapter 2, the horizontal and vertical components of the wind velocity are determined separately. In the following sections, an algorithm for determining the horizontal wind velocity, calculation of the vertical wind velocity, data preprocessing, and results are described.

4.1 Horizontal wind velocity estimate

In this section an algorithm to estimate the horizontal wind velocity from ground velocity and airspeed data is described. The method is based on the relationships between ground and wind velocities and the airspeed described in Chapter 2. As noted in Chapter 2, since the glide angle of a sailplane is small, the difference between the airspeed and its horizontal component is small. For convenience therefore, no distinction is made between the airspeed and its horizontal component, and v_a is used to denote both. Note also that because the airspeed is the sailplane speed relative to the air, the relationship between the airspeed and its horizontal component is unaffected by flying in moving air.

The data are first preprocessed to reduce the effects of errors. The GPS coordinates and airspeed are low-pass filtered with a cut-off frequency of 1 Hz. The ground velocity is calculated, separately for the longitude and latitude components, by differentiating the filtered position data using central differences over a window of length 3. Note that correlations between horizontal GPS fixes less than one minute apart reduce the effects of GPS

errors when calculating the velocity (see Section 6.2). The TAS is calculated as described in Section 3.6.

Referring to Section 2.2.2, there is a one-parameter family of solutions for $\mathbf{v}_w$ and there is insufficient information at a particular time point to uniquely determine the wind velocity. However, if two ground velocities, $\mathbf{v}_{g1}$ and $\mathbf{v}_{g2}$, and the two corresponding airspeeds, v_{a1}

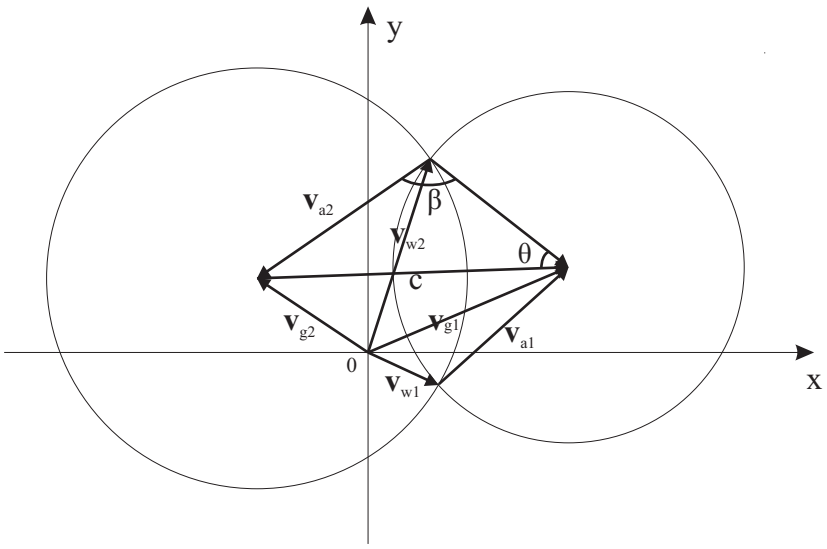

Figure 4.1 Relationships between two ground velocities and two airspeeds in a region of constant wind velocity.

and v_{a2}, are measured in a region of constant wind velocity, then solutions are obtained for the wind velocity. This is described by the vector diagram in Fig. 2.4 which is repeated here as Fig. 4.1. Since a pair of data give a pair of wind velocity estimates, the approach taken is to consider a number of pairs of data on the flight path in a small region of space for which the wind velocity can be considered (approximately) constant. The resulting set of multiple two-fold ambiguous solutions is then analysed to find the most consistent solution. To do this in a near optimum way requires consideration of the likely accuracy of each pair of solutions. The likely precision of a pair of estimates is directly related to the sensitivities of the solutions to errors in the data as detailed in Chapter 2. In fact, for fixed Gaussian errors in the data, s is proportional to the standard deviation of the wind speed estimate. This assumption is made and s is treated as a relative standard deviation. Referring to Chapter 2, the sensitivity is a function of the heading difference $\Delta\theta_a$ at the two time-points. The sensitivity is a minimum when $\Delta\theta_a = 90^\circ$ and maximum when $\Delta\theta_a = 0^\circ$. The sensitivity can be calculated from the ground velocities and airspeed using (2.13) and (2.15) for any pair of data. This is then used as a measure of the suitability of the data pair for wind velocity estimation. Consideration of these relationships shows that the region referred to above must be large enough to include pairs of data with significantly different headings, i.e. some turning flight. If a region contains only a relatively straight flight segment then it will not be possible to obtain accurate wind velocity estimates.

In summary then, in a region of constant wind velocity, multiple pairs of data at multiple

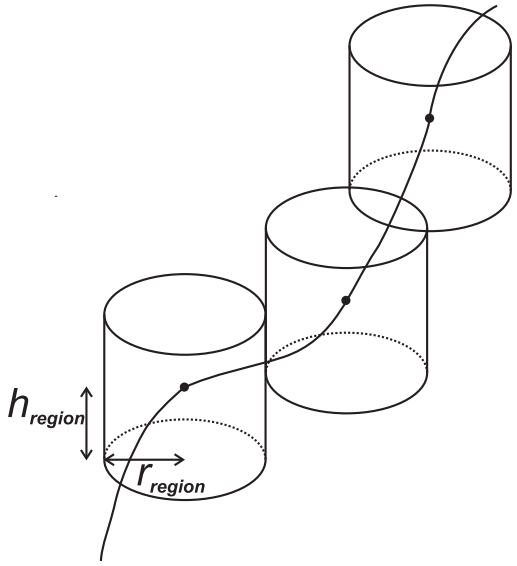

Figure 4.2 Partitioning of the flight path into cylindrical regions.

time points can be used to find multiple sets of two-fold-ambiguous wind velocity estimates. The ambiguities can then be resolved by choosing one of the two estimates from each pair of data such that the set of resulting estimates are most similar (or most consistent) amongst all choices. The measure of consistency is made more quantitative below. A final unique wind velocity estimate is then obtained by averaging these consistent estimates. Since data at adjacent sample points (times) may be highly correlated, every n^{th} datum is used for the analysis. The value of n used depends on the sampling period.

As noted previously, the horizontal wind velocity in high altitude mountain waves will generally be a slowly varying function of position and time, the flight path is partitioned into a sequence of regions and it is assumed that the horizontal wind velocity is constant in each region. The wind velocity for each region is then estimated using the data within the region. Cylindrical regions are used as shown in Fig. 4.2, with the radius and half-height of the cylinder denoted r_{region} and h_{region}, respectively. The parameters chosen will also depend on the spatial resolution desired and the number of data points needed within a region in order to obtain good estimates. The entire flight path is partitioned into such regions using a simple algorithm. Note that the cylinders abut each other either at their sides or on their ends, depending on the shape of the flight path.

The wind velocity estimate in each region is found by selecting pairs of data, using each pair to generate a pair of solutions and then selecting the members of each solution pair that are most consistent. The concept is illustrated in Fig. 4.3. A full solution to this problem would involve finding the solution from each pair that is the most consistent over all possible combinations of the pairs. For d data within a region there are $m = d(d-1)/2$ pairs of data that give m pairs of wind velocity estimates. An exhaustive search to find the

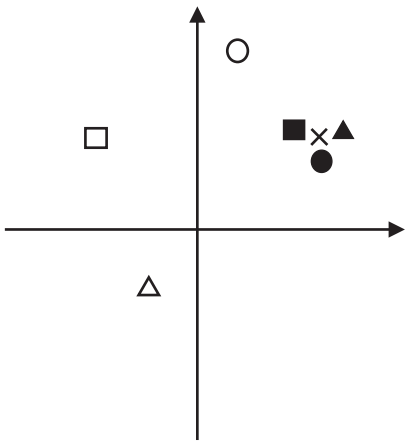

Figure 4.3 Illustration of the clustering analysis used to resolve the two-fold ambiguity from 3 pairs of data for the horizontal wind velocity estimate. The three kinds of symbol show the 2 solutions from each pair of data. The clustering analysis determines that the 3 filled symbols are the most consistent amongst the set of 6 estimates. The final wind velocity estimate is the centroid of those three and is denoted by the x.

most consistent set of solutions would require considering $2^m = 2^{d(d-1)/2}$ partitions of the estimates into two sets. Such a computation is not feasible. The search is therefore limited by using only pairs of data with a sensitivity less than a threshold value, i.e. $s < s_{max}$, and also limiting the number of pairs m used to $m < m_{max}$. It was found that $s_{max} \simeq 1.5$ and $m_{max} \simeq 100$ are generally suitable.

The algorithm proceeds as follows for each region. The sensitivity is first calculated for each pair of data in the region. The m pairs of data with the lowest sensitivity $s < s_{max}$ and such that $m < m_{max}$ are selected and the m wind velocity solution pairs are calculated. For typical values of m used, an exhaustive search of all the 2^m partitions is still not computationally feasible, however. Therefore the $m' < m$ solution pairs with the lowest sensitivity are first selected and all $2^{m'}$ partitions of these pairs are determined. Typically, $m' \simeq 10$ is used, giving about 1000 partitions. The partitions are denoted $\{A_i, B_i\}$, where A_i and B_i are the two sets of a partition and i indexes the $2^{m'}$ partitions. The variance of the wind speed vectors in the set A is denoted σ_A^2, and the labels A_i and B_i for each i are assigned such that $\sigma_{A_i}^2 < \sigma_{B_i}^2$. Hence the set A_i contains the putative correct solutions and B_i the incorrect solutions for partition i. The best (i.e. the most consistent) partition, $\{A_{best}, B_{best}\}$, is that which gives the closest wind velocity estimates in the set A_i, i.e. the best partition $i = best$ is obtained by

$$\{A_{best}, B_{best}\} = \underset{\{A_i, B_i\}}{\operatorname{argmin}}(\sigma_{A_i}^2). \tag{4.1}$$

The weighted (by $1/s^2$) average of the wind velocity estimates in A_{best} gives the best estimate based on the m' pairs of solutions. This estimate is then improved by using the remaining $m - m'$ pairs of solutions by adding one of the solutions from each pair to A_{best}, one at a time in order of increasing sensitivity. The solution of the pair that is added is selected as that which gives the minimum variance when it is added to the current A_{best}.

A new weighted average calculated. This gives the final optimum partition, $\{A_{opt}, B_{opt}\}$, and the final wind velocity estimate.

The wind velocity estimates in A_{opt} will not generally all be independent so the standard deviation of the final estimate, denoted σ_w, will be between $\sigma_{A_{opt}}$ and $\sigma_{A_{opt}}/\sqrt{m}$. Since m is generally large σ_w is estimated as $\sigma_{A_{opt}}/2$. This will generally be a conservative estimate. The quantity $D = \sigma_{B_{opt}}/\sigma_{A_{opt}}$ is also calculated which is a dimensionless measure of the discrimination between the partitions A_{opt} and B_{opt}, with $D = 1$ meaning no discrimination. Wind velocity estimates for which $D < D_{min}$ are discarded, and a value $D_{min} = 3$ was generally used.

The algorithm described above is applied to the data within each cylindrical region to determine the wind velocity estimate at the centre of that region. If the flight path in a particular region is relatively straight, then the ground velocities will be similar and the sensitivities will be large. If the sensitivity is greater than s_{max} for all pairs of data within a region, then no estimate is made for that region.

The GPS and airspeed data contain errors typically of the order of 10 m and 0.5-1 m/s, respectively. The effect of the GPS uncertainty, in particular, is potentially significant. The data are prefiltered before applying the algorithm (see Section 4.3.1), which provides some reduction in these errors. However, the effect of these errors on the wind velocity estimates is ameliorated primarily by the averaging of the estimates in each region. For example, for the value $m = 100$ typically used, a reduction in the rms errors of the wind velocity estimates by a factor of approximately $\sqrt{100} = 10$ is expected.

4.2 Vertical wind speed estimate

The vertical component of the wind velocity is estimated using the vertical speed of the sailplane (relative to the ground), denoted v_g^z, obtained by differentiating the GPS altitude, and correcting for the sailplane sink rate and energy exchange as described in Section 2.3. Referring to Section 2.3, (2.51), the vertical wind speed is given by

$$v_w^z = v_g^z - s - v_e, \tag{4.2}$$

where the sink rate is calculated using the flight polar and altitude by (1.85), and v_e is given by (2.50). The vertical wind velocity estimates are calculated using (4.2) at each point on the flight path and averaged over a suitable time window.

The vertical speed of the sailplane needs to be calculated with care since straight differentiation of the noisy GPS altitude would give erroneous results. The calculation is conducted as follows. The GPS altitude is first low-pass filtered with a cut-off frequency of 1 Hz and the filtered data differentiated using central differences over a window of length 3 (as for the horizontal velocity as as described in Section 4.1). Note that bias in the vertical GPS altitude tends to be canceled out when calculating the vertical speed (see Section 6.2). The

rate of change of airspeed used to calculate v_e needs to be calculated over a time interval longer than the time constant of the low-pass filter applied to the flight data in order to obtain a good estimate. It was found that using finite differences over a time interval of 8 seconds gave good results. The vertical wind speed estimates were then calculated using (4.2). The resulting estimates are then obtained every one second, and since this time resolution is not necessary they were further low-pass filtered with a cut-off frequency of 0.2 Hz.

As described in Section 1.3.4, the flight polar is measured for level (unbanked) flight. A method for estimating the sink rate for banked (turning) flight is described in Section 1.3.4.2 using (1.87). However, this is only an approximation, the precision of which is unknown. Since significant bank is typically present during only a small proportion of a wave flight, and since its effect is not straightforwardly incorporated, the approach taken here is to simply calculate the bank angle ϕ at each position along the flight path, and exclude points where ϕ exceeds some specified maximum value ϕ_{max} for the purpose of calculating the vertical wind velocity. Referring to Fig. 1.18, the change in sink rate is about 0.1 m/s for a bank angle of 30° and so the value $\phi_{max} = 30^\circ$ was generally used. It was found that using $\phi_{max} = 30^\circ$, typically less than 5% of the vertical air velocity estimates are excluded due to excessive bank, so that the above approach is acceptable. This approach requires calculation of the bank angle along the flight path. This is done as follows, assuming that the horizontal wind velocity has already been determined.

1. The flight path relative to the air is determined by subtracting out the integrated horizontal wind velocity from the flight path over the ground. This removes the effect of wind drift.
2. The radius of curvature of the horizontal flight path (relative to the air), r, is calculated at each time-step by fitting a circle to a sliding window of length N samples of the horizontal path relative to the air using non-linear least squares. A value $N = 11$ is generally used for a time-step of 1 s.
3. The bank angle is then calculated using (1.77).

4.3 Results

The methods described above were applied to data from the four Perlan Project flight described in Chapter 3.

4.3.1 Flight 1: Perlan Flight 39: California

The details of this flight are described in Section 3.2. There were some problems with the temperature data measured for this flight and this is described here. The temperature measured during this flight was collected into altitude bins 200 m thick and averaged,

and is shown in Fig. 4.4(a). The deviations of up to 20 K at the same altitude between the ascending and descending flight paths are unlikely to be correct, indicating some kind of instrumentation error. The constant lapse rate temperature fitted to the radiosonde traces (Fig. 3.3(c)) is also shown in Fig. 4.4(a). The measured temperature versus flight time is shown in Fig. 4.4(b). A corresponding plot of the linear radiosonde data versus time was determined by taking the altitude at each time and using the radiosonde temperature. The resulting curve is shown in Fig. 4.4(b). If the radiosonde traces are taken as correct, then Fig. 4.4(b) suggests that the data are suffering from a time-lag. A first-order lag was applied to the fitted radiosonde data versus time as

$$T'(t) = (T(t) + T_0) \otimes \exp(-t/\tau)h(t) \tag{4.3}$$

where $T(t)$ is the radiosonde temperature, T_0 is an offset, τ is a time constant and $h(t)$ is the step function. Adjusting τ and T_0 to obtain a good fit between $T'(t)$ and the flight data gave $\tau = 770$ s and $T_0 = 5$ K. $T'(t)$ is plotted versus altitude and time in Figs. 4.4(a) and (b), respectively. Inspection of these figures shows that the agreement is remarkably good. The results therefore indicate a thermal lag of about 13 minutes, or something else that has a similar effect. The cause of this is unknown but seems to be the only explanation for the data. In view of this, the radiosonde trace was used as the temperature data for this flight. Note that this problem did not occur with the temperature data from the other Perlan flights.

The horizontal wind speeds were estimated as described in Section 4.1 using the parameters given in Table 4.1. The TAS was calculated using (3.1) from the temperature from the average radiosonde lapse rate as described above and the pressure data recorded during the flight. The flight path was partitioned into 217 cylindrical regions, from which 61 estimates were obtained. 11 regions were eliminated due to $D < D_{min}$, and 145 regions were removed for having $m < m'$ pairs of data with $s < s_{max}$. The number of data pairs in the eligible regions was between 14 and 100. Typical values obtained for σ_w were in the range 0.9-3.2 $\mathrm{m/s}$, and typical values for D were in the range 3-51.

An example of the clustering analysis for one horizontal wind speed estimate is shown in Figs. 4.5(a) and (b). In this example there are 100 pairs of data and the partition into the sets A and B are shown by the circles and crosses, respectively. The partition gives a clear solution in this case as shown with $\sigma_w = 0.7$ $\mathrm{m/s}$ and $D = 9$. The overall performance of the clustering analysis was assessed by calculating a histogram of the D values for the final wind velocity estimates which is shown in Fig. 4.5(c). 52% of the values of D are greater than 10, indicating good separation of the two clusters. To assess the errors in the final wind velocity estimates, the distribution of σ_A is shown in Fig. 4.5(d). The values vary between 0.5 and 2.5 m/s, indicating errors in the wind velocity estimates between 0.3 and 1.3 m/s.

The flight path relative the ground is shown in Fig. 4.6(a). The path of the sailplane relative to the air was calculated by integrating the velocities of the sailplane relative to the air

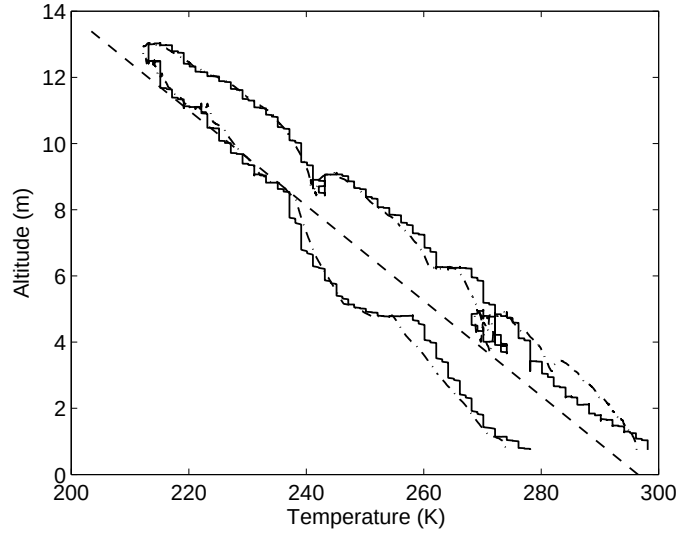

(a)

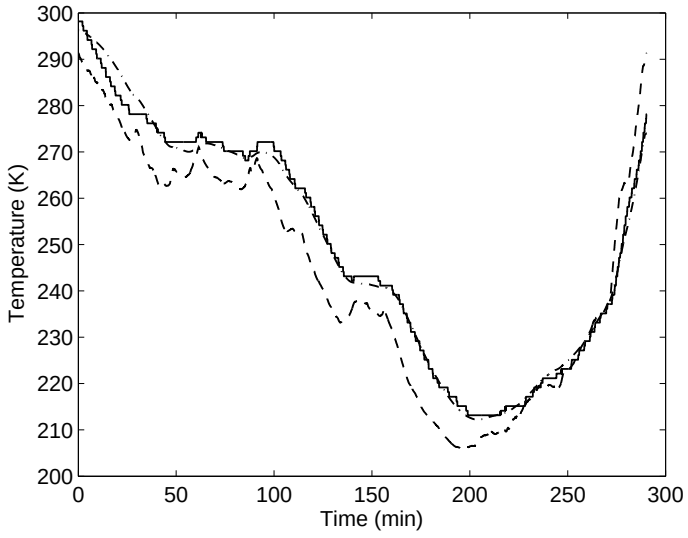

(b)

Figure 4.4 Flight 1: (a) Temperature versus altitude and (b) temperature versus flight time, measured during the flight (solid curve), the constant lapse rate temperature fitted to the radiosonde traces $T(t)$ (dashed line) and the radiosonde data with time lag and offset $T'(t)$ (dot-dashed), as described in the text.

Table 4.1 Parameter values of the heuristic method selected for Flight 1.

r_{region}	2000 m
h_{region}	100 m
s_{max}	2
m_{max}	100
m'	10
D_{min}	3

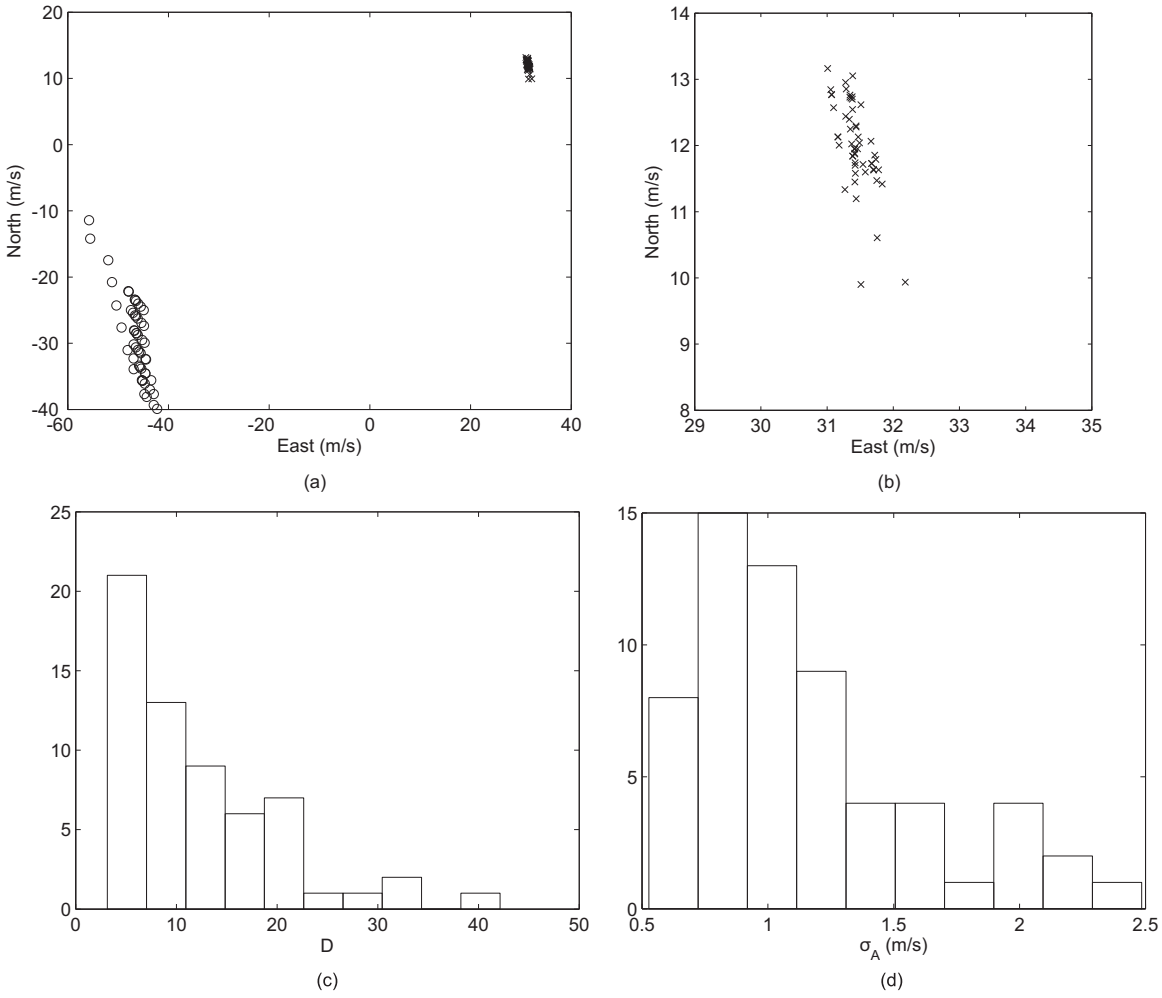

Figure 4.5 Example of partitioning for a horizontal wind velocity estimate. (a) Optimum partition of the pairs of solutions into the sets A_{opt} (x) and B_{opt} (o), (b) a close up of the set A_{opt}. (c) and (d) show histograms of D and σ_A for the whole flight.

derived from the estimated wind velocities (linearly interpolated onto the flight time), and is shown in Fig. 4.6(b).

Close ups of two portions of the flight path and the corresponding horizontal wind velocity estimates are shown in Fig. 4.6(c) and (d). The flight segment in Fig. 4.6(c) is near the centre of Fig. 4.6(a), and that in Fig. 4.6(d) is near the top of Fig. 4.6(a). Note in these figures that estimates of the horizontal wind velocity are obtained where the heading is changing but not where it is relatively constant, as anticipated. Therefore, more estimates are obtained in Fig. 4.6(d) compared to in Fig. 4.6(c) as a result of the more convoluted flight path in the latter, compared to the former. The horizontal wind velocity is expected to be relatively constant in thin altitude layers and over fairly large horizontal areas. This is evident in Fig. 4.6, indicating stability of the method. The estimated wind velocities for the whole flight were collected into altitude bins 200 m thick and averaged, separately for the climbing and descending portions of the flight, and the speed and direction are shown versus altitude in Fig. 4.7. Note the increasing wind speed with altitude and the fairly constant wind direction. The radiosonde traces at Edwards Air Force Base (EAFB) and Desert Rock (DR) are also shown in Fig. 4.7 (refer to Section 3.2). Inspection of the figure shows good consistency between the estimated wind speeds and the soundings, given the different locations and times, and keeping in mind that the radiosondes are drifting east. Note the good agreement between the wind speeds at low levels derived from the ascending flight path data and from the EAFB radiosonde data where the flight path and the radiosonde location are geographically quite close. The rms differences between the sailplane derived estimates of the wind speed and direction and the average of the two soundings are 6 m/s and 8° (above 4 km) respectively. For comparison, the rms differences between the two soundings are 3 $\mathrm{m/s}$ and 9°. Overall then, the precision of the estimates obtained is reasonable, given the variations between the two radiosonde soundings, and their different times and locations relative to the flight.

The turn radius and bank angle were calculated as described in Section 1.3.4.2 using a window length $N = 11$ and are shown in Fig. 4.8(a) and (b), respectively. The flight path relative to the air and the bank angle for a 5-minute flight segment are shown in Fig. 4.8(c) and (d), respectively, which shows the pilot entering and exiting turns. All of the calculated bank angles are below the maximum bank angle of 30°. The bank angle is less than 5° for 99% of the flight, indicating the the bank angle is generally small for this wave flight.

The vertical wind speed along the flight path was estimated as described in Section 4.2. The importance of the total energy correction is illustrated in Fig. 4.9 which shows the airspeed and the corresponding sailplane vertical speed and the derived vertical wind speed versus time for a portion of the flight. The figure shows that large excursions in the measured sailplane vertical speed due to rapid changes in the airspeed are removed when computing the vertical wind speed with the total energy correction as described above.

The vertical speed data taken from the variometer is shown in Fig. 4.9(c) where it is compared with the calculated vertical airspeed as above. There are significant differences (de-

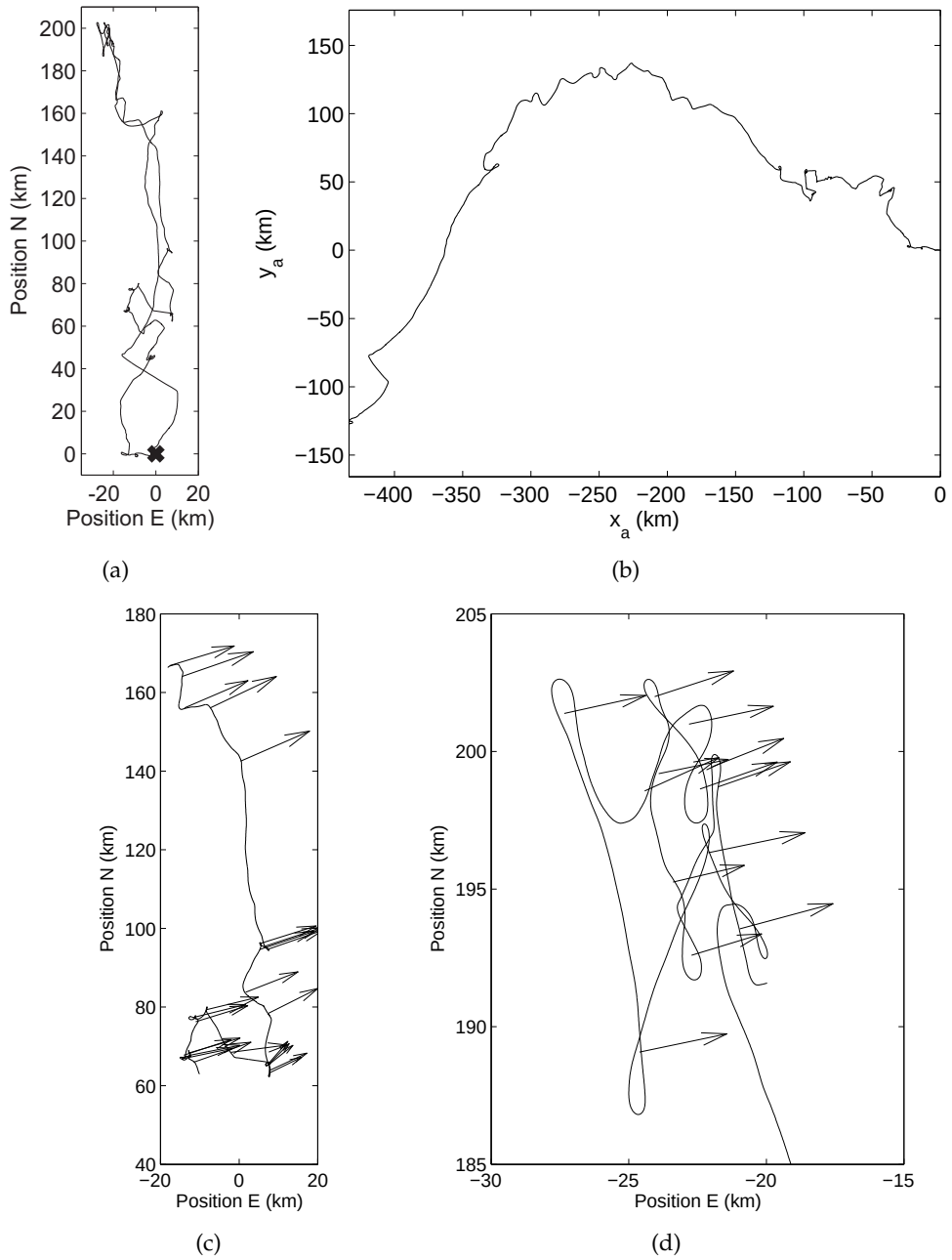

Figure 4.6 Flight 1: Flight path (a) relative to the ground (launch position shown by the x, N for North and E for East) and (b) relative to the air. (c)(d) Wind velocity estimates for two flight segments as described in the text for an altitude range of $3.7-9.0$ km and $9.3-13$ km, respectively. The length and direction of the arrows represent the estimated wind speed and direction, respectively.

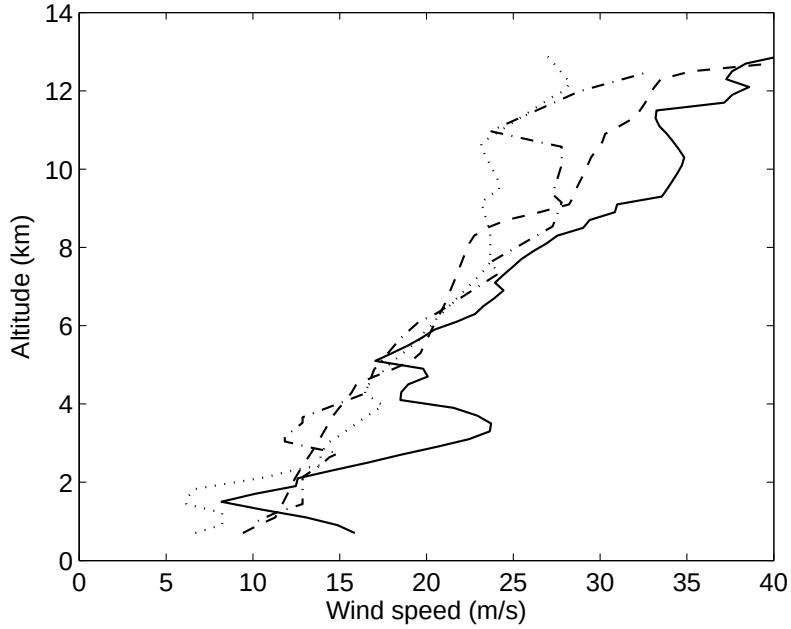

(a)

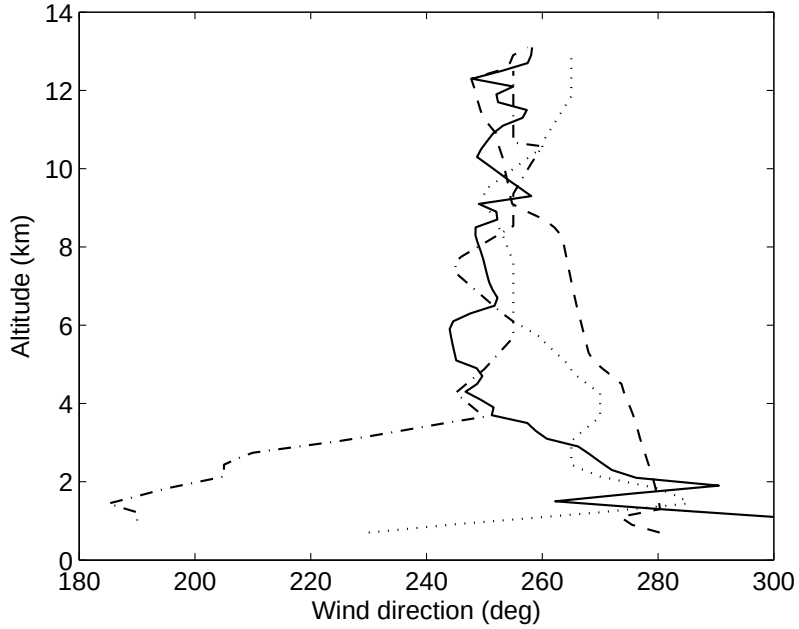

(b)

Figure 4.7 Flight 1: (a) Horizontal wind speed and (b) direction estimates versus altitude. Estimates for the ascending portion of the flight are shown by the solid line, and for the descending portion are shown by the dashed line. The radiosonde sounding taken at EAFB is shown as the dotted line and that at DR by the dot-dashed line.

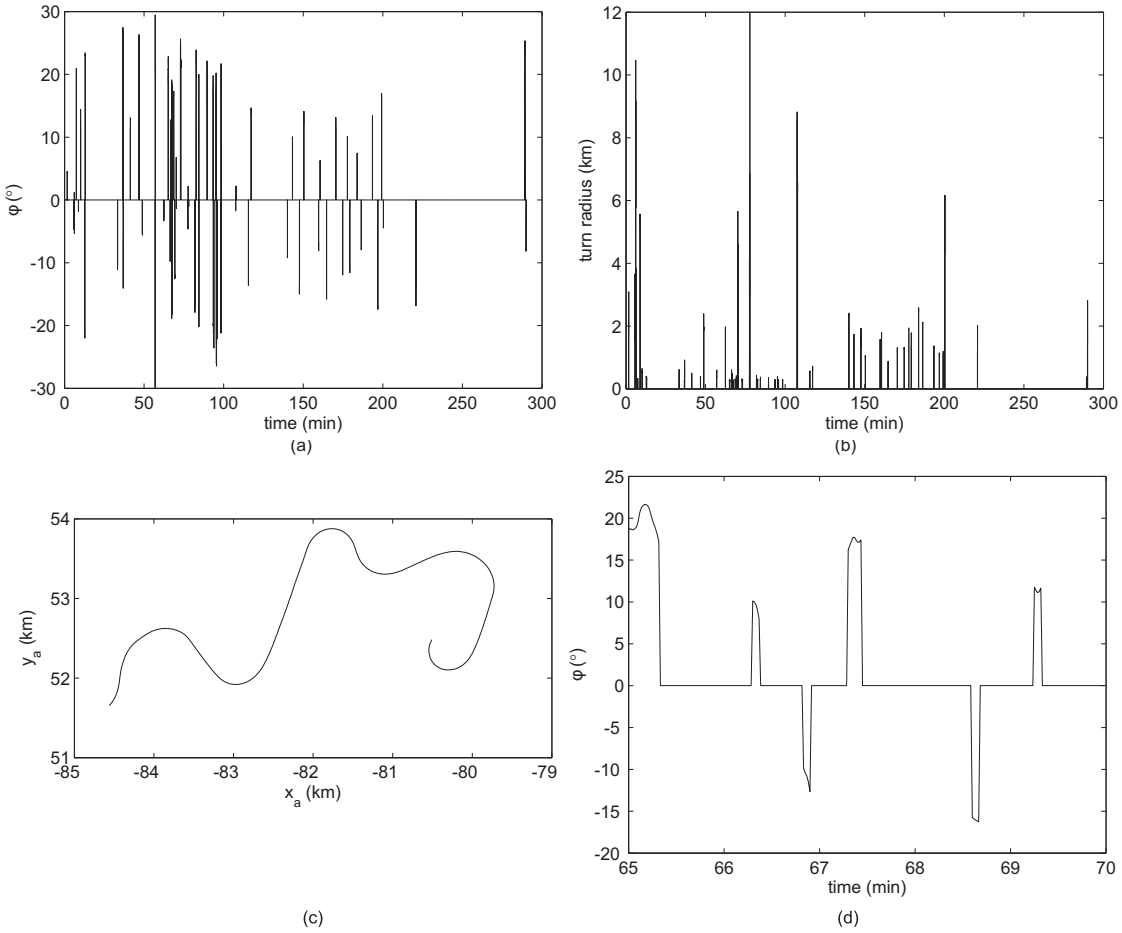

Figure 4.8 Flight 1: (a) Bank angle and (b) turn radius versus time. (c) A close up segment of the flight path relative to the air and (d) the corresponding bank angle.

spite this being a total energy variometer). The measured vertical wind speeds tend to agree when the sailplane airspeed is small, but not when it is large. The measured vertical wind speed is about 3 m/s lower than the calculated value at an airspeed of 66 m/s. The variometer data was not considered further.

Since the flight path traverses a small region of the total volume of airspace in which the wave exists, the estimates obtained are a sparse sampling of the wave structure. An inherent problem then is how to interpret this sparse information. Furthermore, although the wave structure is likely to be stable over periods of the order of 30 minutes, it may vary over hours. The vertical wind speeds in small regions are therefore studied in order to show the local wave structure.

The wave structure is most clearly evident in a plot of the vertical wind speed versus distance downwind from a particular point on the ridge line and at a fixed altitude. The streamlines in such a plot are expected to approximately follow an exponentially damped sinusoid and, for a constant horizontal wind speed, the vertical wind speed is also an exponentially damped sinusoid that is phase-shifted relative to the streamlines. The only

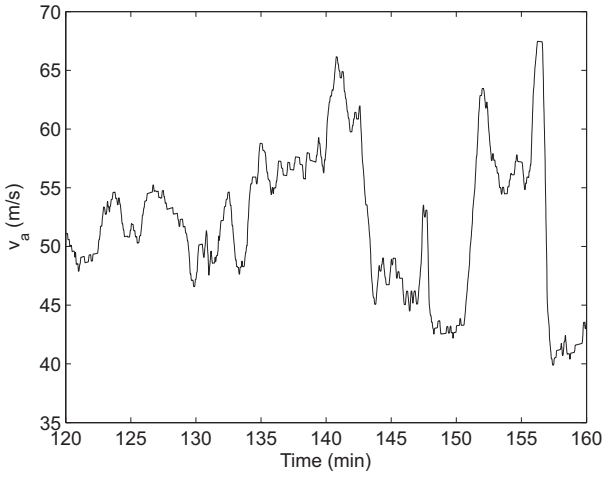

(a)

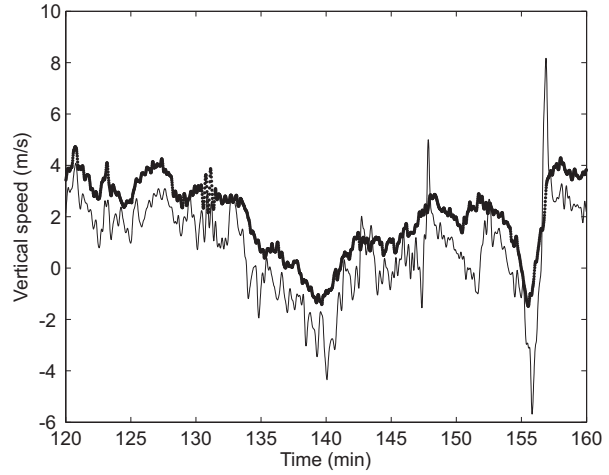

(b)

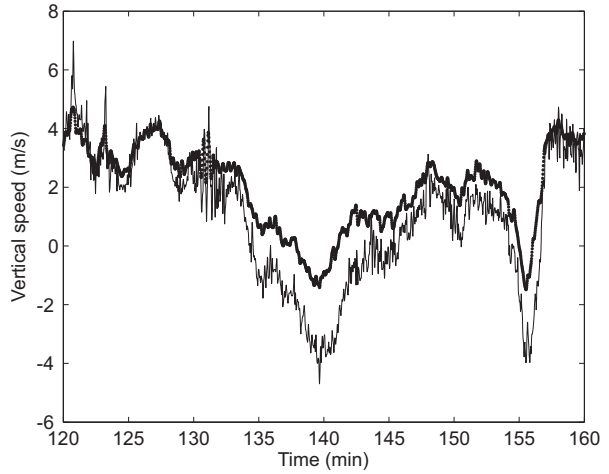

(c)

Figure 4.9 Flight 1: A flight section between 7200 s and 9600 s showing (a) the airspeed and (b) the sailplane vertical ground speed (thin line) and the vertical wind speed (thick line), calculated as described in the text, and (c) vertical wind speed calculated from the GPS data (thick line) and the variometer data (thin line).

primarily downwind segment of significant length in this flight is a 4-minute segment near the maximum altitude of the flight, south of Lone Pine. A close-up of this flight segment is shown in Fig. 4.10(a) and it extends approximately 25.0 km downwind, the altitude varies between 12360 and 12500 m, and it is downwind of a 6 km section of the ridge line. The estimated vertical wind speed versus distance downwind from the ridge-line is shown in Fig. 4.10(b). Inspection of the figure shows a wave structure, and a least squares fit of the exponentially damped sinusoid,

$$v_w^z(x) = a\exp(-bx)\cos(2\pi x/\lambda + c) + d, \tag{4.4}$$

where x is the distance downwind, a, b, λ, c, d are coefficients, to the data is shown in Fig. 4.10(b). The values of the coefficients calculated for the fitted curve in Fig. 4.10(b) are $a = 2.3$ m/s, $b = 0.065$ km^{-1}, $\lambda = 10.0$ km, $c = -1.7$, and $d = 0.7$ m/s. The fit is quite good and gives a wavelength $\lambda = 10.0$ km.

Referring to the satellite picture in Fig. 3.5 which shows this downwind segment as the short line in the upper centre, there is evidence of the leading edge of a cap cloud to the East of this flight segment which could correspond to the second peak in Fig. 4.10(b). The spacing to the next cloud upwind is 11 km. To the West and South of the flight path there are cloud streets with spacings between 9 and 13 km, that might correspond to other wave activity in the area.

Using the fitted temperature profile and the calculated horizontal wind speed, the Scorer parameter was calculated and collected into 200 m altitude bins and averaged, and are shown in Fig. 4.11. The decreasing Scorer parameter with altitude is indicative of conditions conducive for lee wave development as described in Section 1.2.3. There is no particularly obvious layering of the atmosphere with different Scorer parameters. At an altitude of 12 km where the wave is evident, the Scorer parameter varies between 0.3 and 0.4 km^{-1}, with corresponding minimum lee wave wavelength between 16 and 21 km. The observed wavelength of 10 km is somewhat smaller than these values although prediction of the wavelength is difficult with this complex vertical structure. Note that the average vertical wind speed is expected to be zero, but that Fig. 4.10(b) indicates an offset of 0.7 m/s. The single sine wave is a simple approximation and it is possible that the vertical velocity averages to zero only over distances greater than the 1.5 wavelengths shown here. For example, measurements of sailplane vertical velocity in lee waves of the Andes that cover 4-8 wavelengths [34] show that although it averages to close to zero over many wavelengths, it can average to non-zero values over distances of 2-3 wavelengths.

Another informative flight segment is shown in Fig. 4.12(a) which shows a close-up of a 30-minute flight segment that is approximately parallel to the ridge line. The flight path is replotted in Fig. 4.12(b) as a function of distance downwind from the ridge line and colour-coded by the derived vertical wind speed. The fight altitude versus position North is shown in Fig. 4.12(c). The results in Fig. 4.12(b) show a strong vertical wind speed for positions between 6 and 12 km downwind from the ridge line, corresponding to the leading

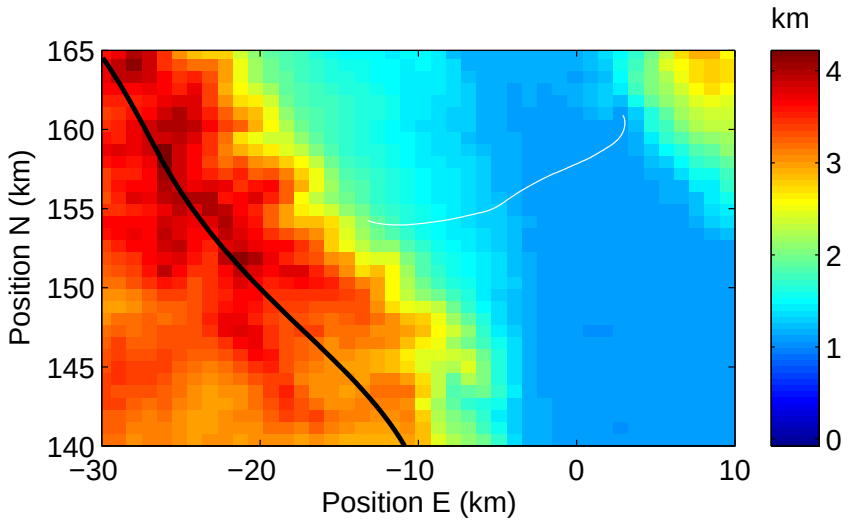

(a)

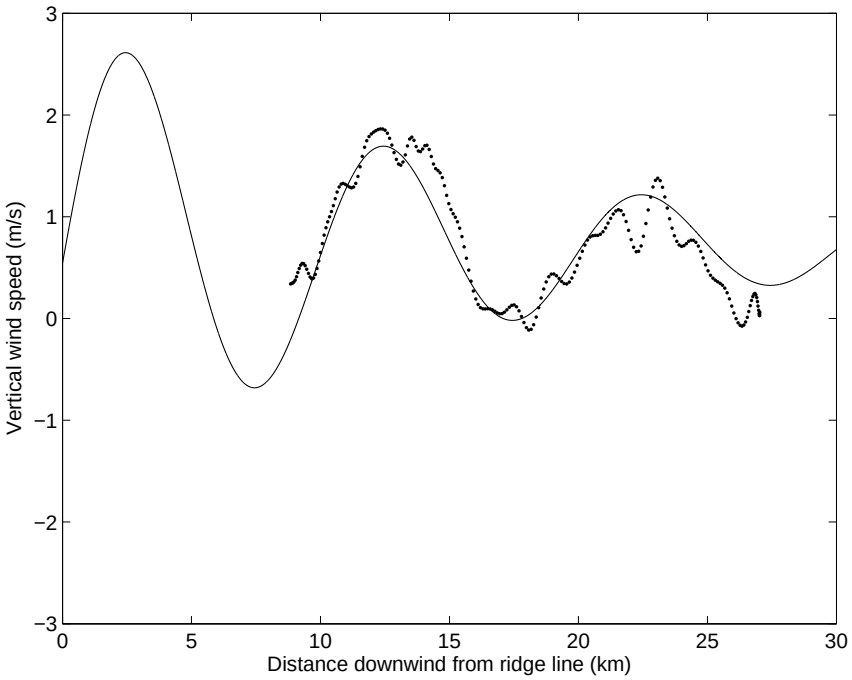

(b)

Figure 4.10 Flight 1: A flight segment near the maximum altitude of the flight showing (a) the flight path relative to ground (altitude colour coded as shown), and (b) the vertical wind speed estimates versus distance downwind from the ridge line and the fitted damped sinusoid described in the text.

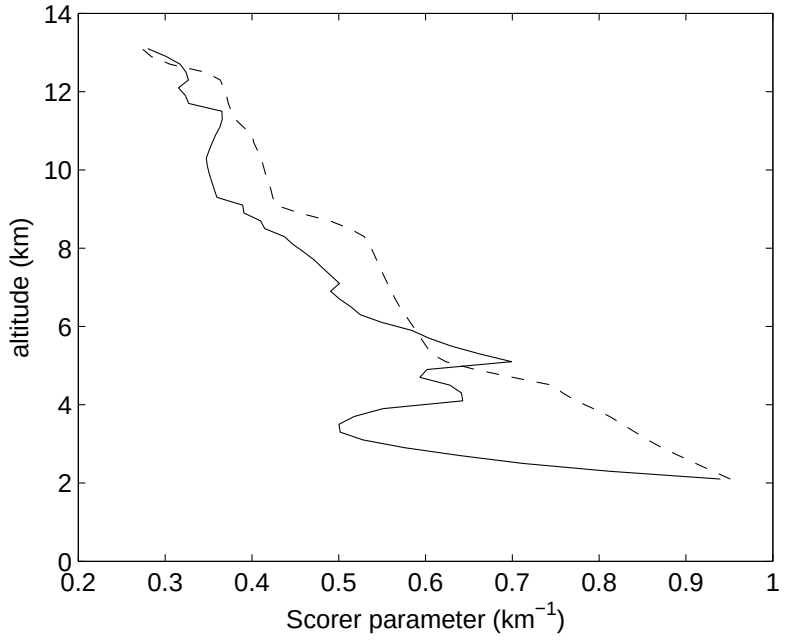

Figure 4.11 Flight 1: The Scorer parameter versus altitude for the ascending (solid line) and descending path (dashed line) portions of the flight.

edge of the wave. The short excursion of the flight path upwind to between 1 and 5 km downwind from the ridge line takes it out of the leading edge and weaker vertical speeds are evident. This is consistent with expected behaviour.

Derived vertical wind speeds for longer flight segments are more difficult to interpret because of the complicated effects of complex terrain upwind of the flight path. However, if the ridge cross section was uniform and conditions time-invariant then the vertical speed would depend, approximately, only on the altitude and the distance downwind from the ridge. A one-hour flight segment that is around the maximum altitude of the flight and is downwind of a 50 km length of the ridge line is considered. The derived vertical wind speed in this flight segment, as a function of distance down wind from the ridge line and altitude is shown in Fig. 4.13, with the vertical wind speed coded by colour. Inspection of the figure shows the sailplane tracking the leading edge of the wave with large vertical wind speeds, the leading edge tilted upwind with increasing altitude, indicating some leakage of the trapped wave as described in Section 1.2.3, and the expected decrease of wave strength with increasing altitude. A secondary weaker wave crest located approximately 10 km downwind is evident and is the same as that shown in Fig. 4.10.

In summary, application of the algorithm to data from this flight gives horizontal wind velocities consistent with radiosonde data, and vertical wind speeds that show expected characteristics of the wave structure relative to the topography.

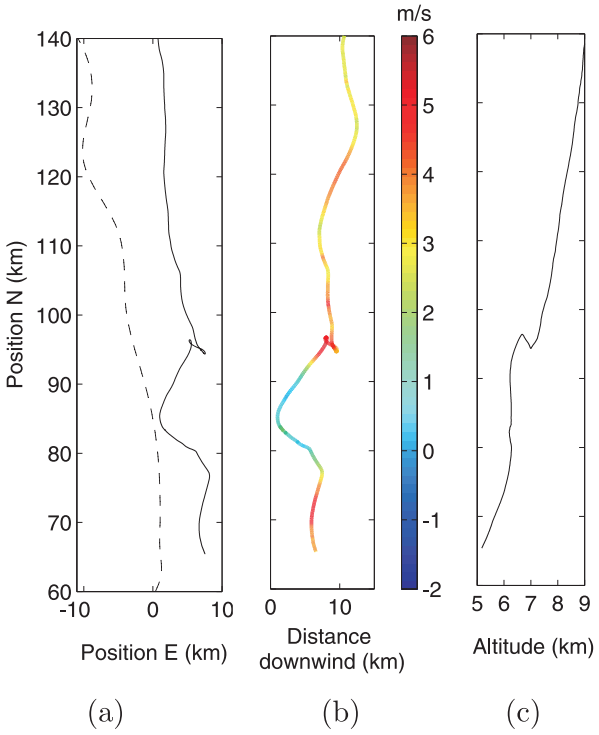

Figure 4.12 Flight 1: A flight section parallel to the ridge line as described in the text. (a) Flight path (solid line) and ridge line (dashed line). (b) Estimated vertical wind speed (colour coded as indicated) versus distance downwind from the ridge line. (c) Flight altitude versus position North.

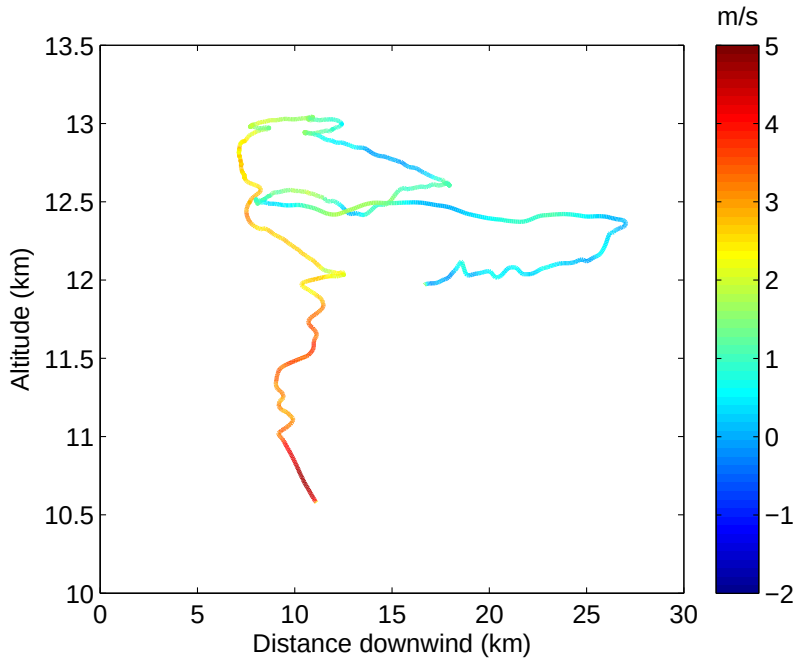

Figure 4.13 Flight 1: Vertical wind velocity (colour coded as indicated) versus distance downwind from the ridge-line and altitude as described in the text.

4.3.2 Flight 2: Perlan Flight 63: Argentina

The algorithm was applied to Flight 2 as described in Section 3.3 using the parameters specified in Table 4.1. The temperature data measured during the flight were collected into 200 m thick altitude bins and averaged, and are shown in Fig. 4.14. The Reanalysis temperature is shown on the same graph. The two data agree quite well and the lapse rate from the measured data is -7 K/km above 3 km. The measured temperature and pressure were used for calculation of the TAS. There is no radiosonde data near this flight.

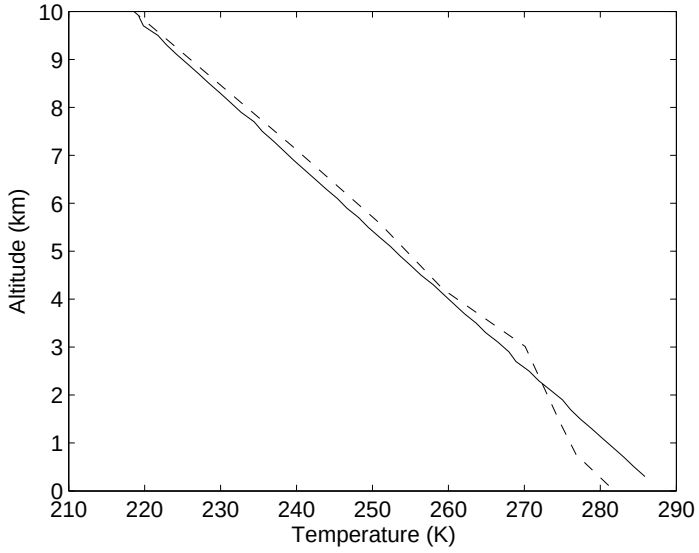

Figure 4.14 Flight 2: Temperature vs altitude measured from the flight (solid line) and the Reanalysis temperature (dashed line).

Using the algorithm described above, the flight was partitioned into 106 regions, 18 of which were suitable for wind velocity estimation. Referring to Fig. 3.6(a), this flight has many straight segments which is the reason only about 20% of the regions are suitable for wind velocity estimation. The result is that a fairly sparse sampling of the wind velocity is obtained. Values obtained for σ_w were in the range 0.9-9.0 m/s and values for D were in the range 3-11. Only two estimates had $\sigma_w > 4$, occurring near the end of the flight record where the path is fairly straight and the sailplane is descending rapidly, and so these two estimates were removed. The estimated wind velocity along the flight path is shown in Fig. 4.15. The figure illustrates, again, that wind velocity estimates can be obtained only where the heading is changing. The straight flight segments therefore do not give wind velocity estimates as shown.

The estimated wind speed and direction were collected into 200m thick altitude bins and averaged, and are shown in Fig. 4.16 above 2 km altitude. For comparison, the Reanalysis wind speed and direction are also shown in Fig. 4.16. The wind direction estimates agree quite well with the Reanalysis, variations up to 10° being considered quite small. However,

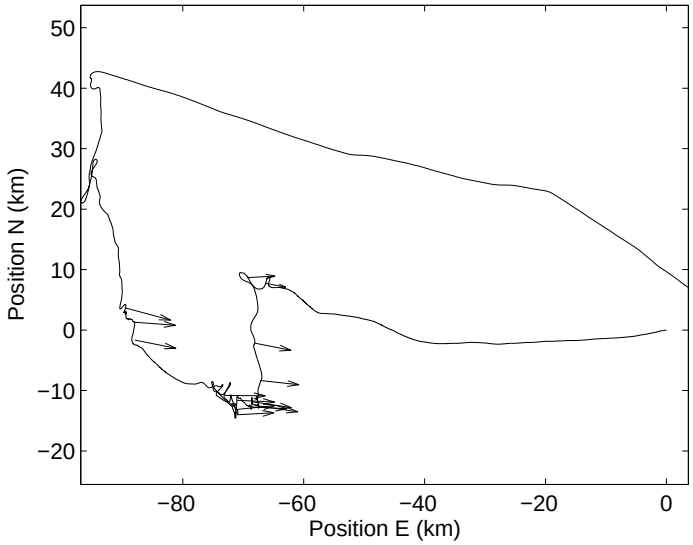

Figure 4.15 Flight 2: Estimated wind velocity vectors along the flight path. The launch position is shown by the x.

the estimated wind speeds are approximately 10 m/s larger than the Reanalysis values above 3 km. The estimated wind speeds are quite consistent and so are taken as being reliable.

The vertical wind speed was calculated as described in Section 4.2. The colour-coded vertical speed is shown as a function of altitude above 2 km and distance downwind from the ridge line in Fig. 4.17(a). This shows two primary climbs, the first at about 30 km from the ridge line between 3.5 km and 7 km altitude, and the second at about 16 km from the ridge line between 6.5 km and 9.5 km altitude. This is followed by gradual descending flight downwind through a clear pattern of a number of wavelengths until the data record ends. The sailplane climbs mark the leading edges of the wave, and the estimated positions of these rising edges (in a tilted coordinate system defined by the distance downwind and the distance from the takeoff position along the direction perpendicular to the wind) are shown in Fig. 4.17(b). Fairly regular spacings of the leading edges are evident.

The altitude and the vertical wind speed for the long downwind segment at the end of the flight record are shown versus distance downwind from the ridge line in Fig. 4.18(a). This 13-minute flight segment extends approximately 80 km downwind and the altitude varies from 9.8 to 7.6 km, after the maximum altitude of the flight. Wave structure is evident in this flight segment. Inspection shows approximate sinusoidal behaviour up to 60 km downwind. Then there appears to be a phase change with sinusoidal behaviour evident again after 70 km downwind. Damped sinusoids were fitted to each of these segments as shown in Fig. 4.18. This gives coefficients $a = 3.1$ m/s, $b = 0.011$ km^{-1}, $\lambda = 22.0$ km, $c = 1.3$, and $d = -0.06$ m/s for the first flight segment, and $a = 3.0$ m/s, $b = 0.031$ km^{-1}, $\lambda = 17.0$ km, $c = -3.3$, and $d = -1.0$ m/s for the second flight segment. The fitted damped

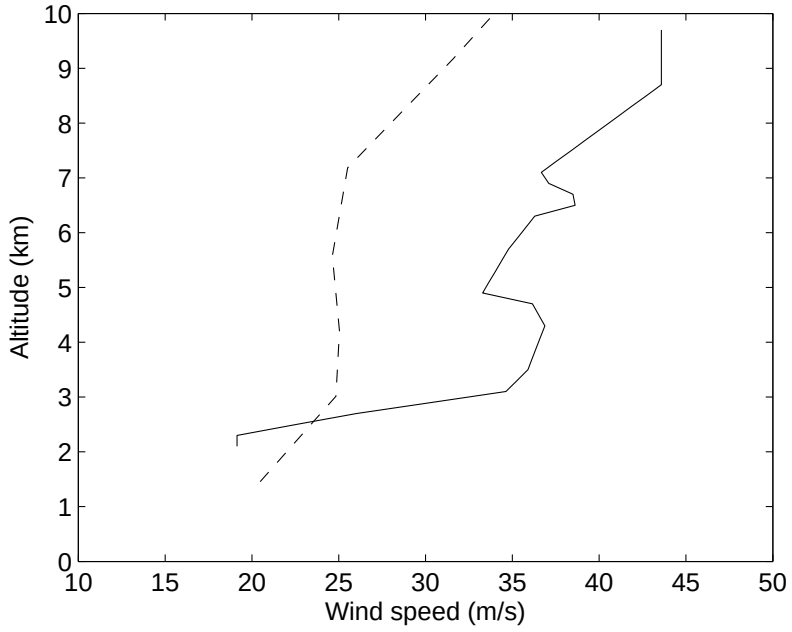

(a)

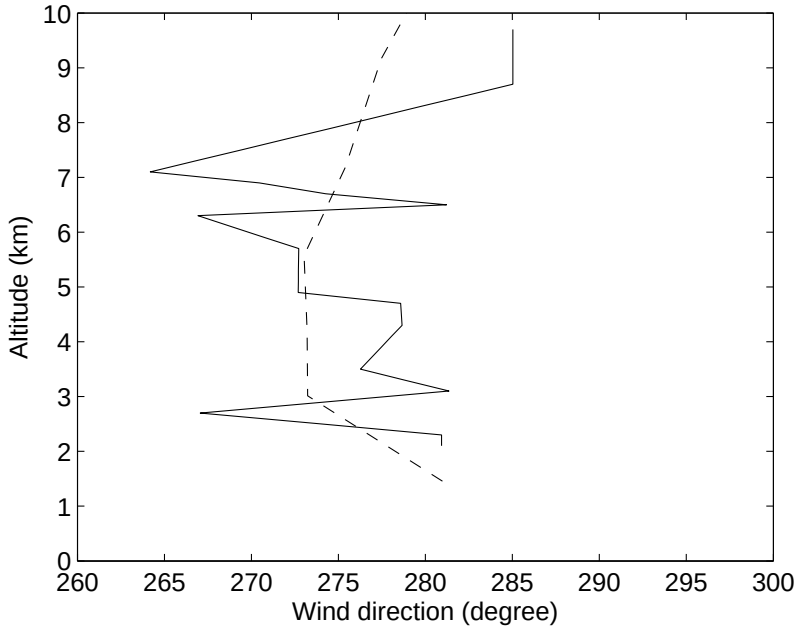

(b)

Figure 4.16 Flight 2: (a) Horizontal wind speed and (b) direction estimates versus altitude. The estimated values are shown by the solid lines and the Reanalysis values by the dashed lines.

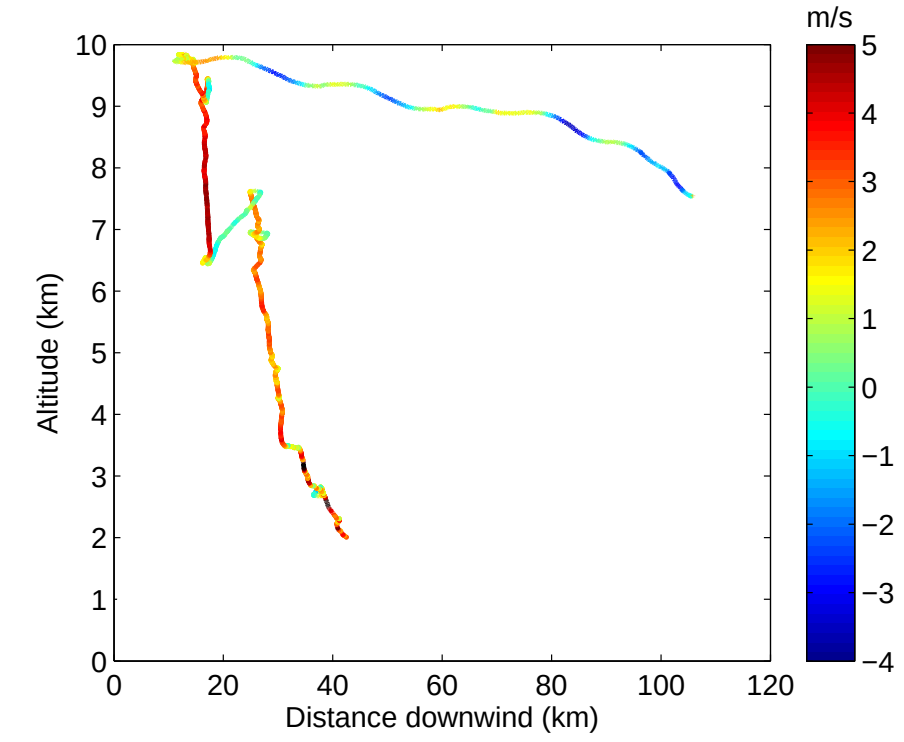

(a)

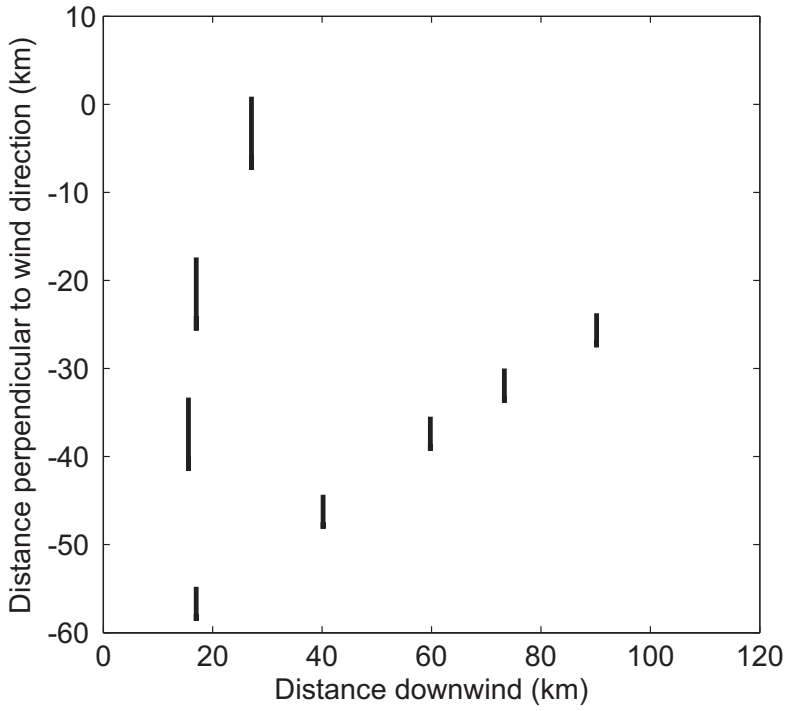

(b)

Figure 4.17 Flight 2: (a) Vertical wind velocity (colour coded as indicated) versus distance downwind from the ridge-line and altitude. (b) The estimated leading edges of thewave bands.

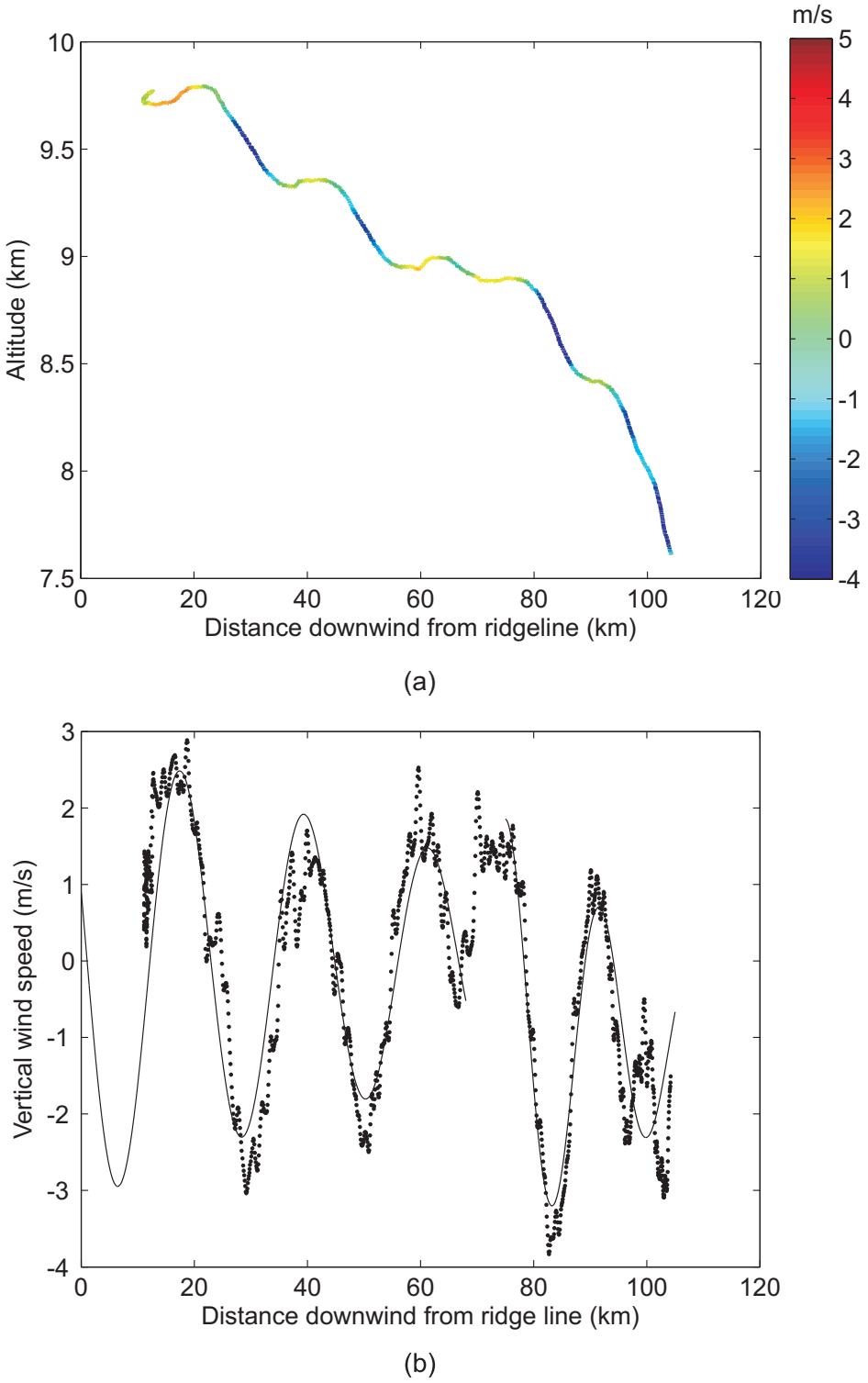

Figure 4.18 Flight 2: (a) Altitude and the derived vertical wind speed (color-coded as shown) and (b) the derived vertical wind speed and the fitted damped sinusoids versus distance downwind for the long downwind flight segment as described in the text.

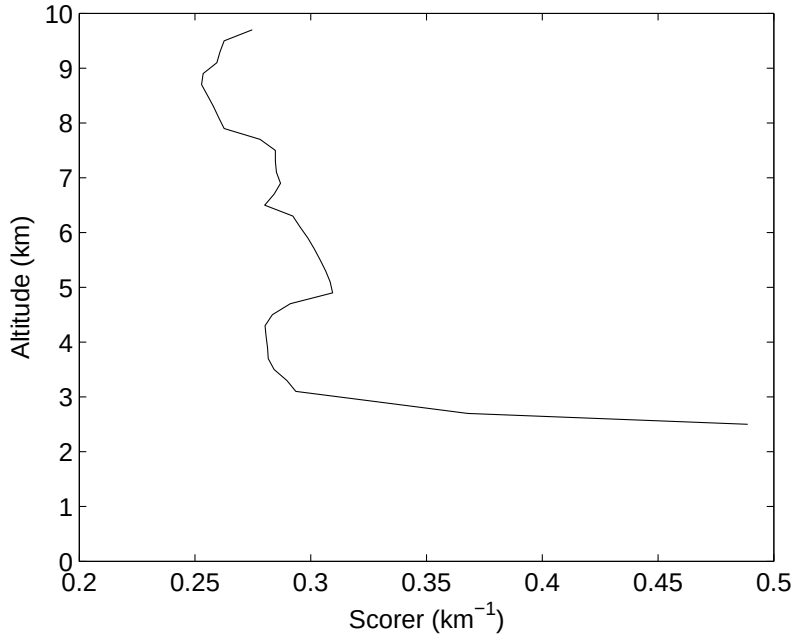

Figure 4.19 Flight 2: The Scorer parameter versus altitude.

sinusoids matches the data quite well for first half of the data, with a wavelength of 22.0 km. For the second flight segment the fit is quite good with a lower wavelength of 17.0 km and a different phase. The average vertical wind speed is close to zero for the first flight segment and -1.0 m/s for the second flight segment.

This downwind flight segment is shown by the line segment on the satellite picture in Fig. 3.9. There is some evidence of cross-wind cloud streets parallel to the topography on this track, and also more clearly to the North, with a spacing of 18 km. This is overall consistent with the above results.

Using the measured temperature profile and the estimated horizontal wind speed, the Scorer parameter was calculated and shown in Fig. 4.19. The Scorer parameter generally decreases gradually with altitude above 5 km. The Scorer parameter is approximately 0.26 km^{-1} at an altitude of 9 km where the wave in Fig. 4.18(b) is located. The minimum lee wave wavelength is therefore 22 km which is consistent with the observed wavelength.

In summary, the horizontal wind velocities estimated for this flight are self consistent. The directions are consistent with Reanalysis values but the wind speeds are significantly larger. There is likely an underestimate in the Reanalysis wind speeds. A long downwind flight segment clearly shows wave structure with derived wavelengths that are consistent with satellite images and the Scorer parameter.

4.3.3 Flight 3: Perlan Flight 66: Argentina

Flight 3 is the altitude record flight described in Section 3.4 that entered the stratosphere. The data from this flight was processed using the parameters in Table 4.1. The temperature data from the flight were collected into altitude bins 200 m thick and averaged, and are shown in Fig. 4.20. There is a clear temperature inversion at approximately 11 km corresponding to the tropopause showing that the flight climbed 4 km into the stratosphere. Fitting two line segments to the temperature data gives lapse rates of -6 K/km in the troposphere, and 2.2 K/km in the stratosphere. The Reanalysis temperature is also shown in Fig. 4.20 and shows quite good agreement with the measured data.

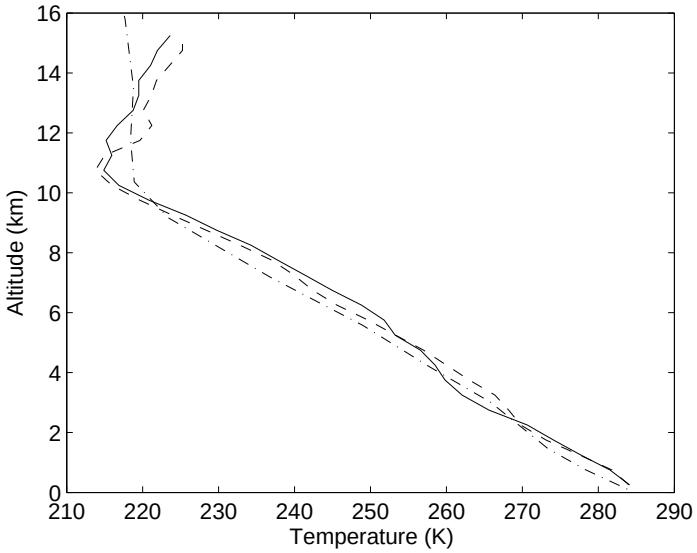

Figure 4.20 Flight 3: Temperature versus altitude measured along the ascending flight path (solid line) and descending flight path (dashed line), and the Reanalysis temperature data (dot-dashed line).

Using the algorithm described above, the flight was partitioned into 211 regions, 84 of which were suitable for obtaining good horizontal wind velocity estimates. Typical values obtained for σ_w were in the range 0.3-3.6 $\mathrm{m/s}$, and typical values for D were in the range 3-52. Hence the expected errors are within an acceptable range. The estimated wind velocity along the flight path is shown in Fig. 4.21. Circling flight is evident near the North-East region of the flight path and the derived wind direction is consistent with the drift seen during the circling flight. Clusters of a large number of wind velocity estimates are evident in the circling and curved segments of the flight path. The wind speed and direction estimates were more variable for this flight and were collected into altitude bins 500 m thick and averaged for the whole flight, and are shown in Fig. 4.22. The greater variability in the wind speed and direction are evident in this figure. The Reanalysis wind speed and direction are also shown Fig. 4.22. As with the previous flight, the estimated wind directions are consistent with the Reanalysis but there are differences between the wind speeds up to

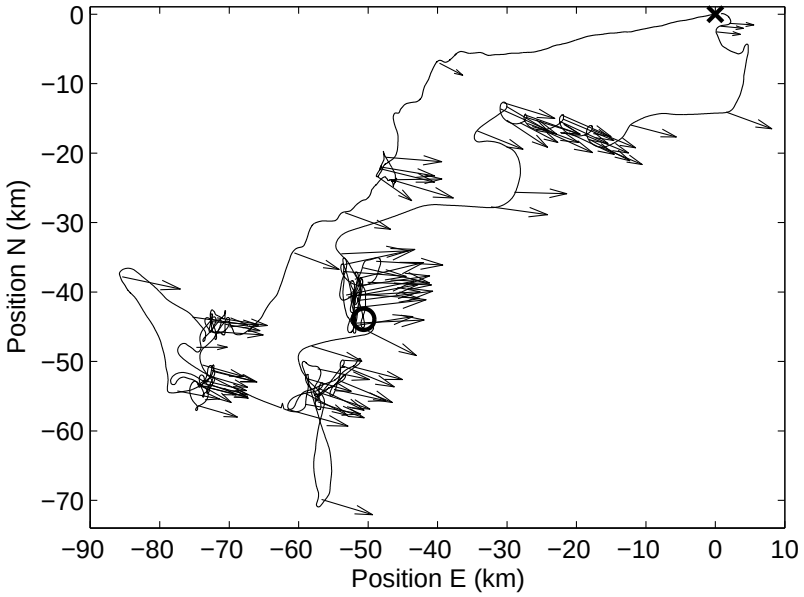

Figure 4.21 Flight 3: Estimated wind velocity vectors along the flight path. The launch position is shown by the x and the flight path is approximately anticlockwise. The position of maximum altitude is marked by a circle.

15 m/s.

The vertical wind speed was calculated as described previously and is shown versus altitude above 2 km and distance downwind from the ridge line in Fig. 4.23(a). From the vertical wind speed, the positions of the leading edges of the waves were estimated and are shown in Fig. 4.23(b). Two downwind segments were selected for mapping the wave, as marked by the ellipses in Fig. 4.23(a). The first segment is in the troposphere at an altitude of about 6 km and the second segment is in the stratosphere at an altitude of about 15 km. The vertical speeds in these two segments are shown in Figs. 4.24(a) and (b) respectively, and sinusoids were fitted to the data. The fitted sinusoid in the troposphere has an amplitude of 4 m/s and a wavelength of 9.0 km, and that in the stratosphere has an amplitude of 4 m/s and a wavelength of 22.0 km.

The satellite picture for this flight (Fig. 3.13) at 1745Z, 3.5 hours into the flight and 40 minutes before the maximum altitude, shows possible evidence of two lenticulars near the climb to maximum altitude. The spacing between these clouds is approximately 25 km. There is a solid cloud sheet further to the west.

The Scorer parameter was calculated and shown in Fig. 4.25. The Scorer parameter does not vary much below 10 km, increases rapidly between 10 and 11 km, then decreases above 12 km. The larger value of the Scorer parameter in the stratosphere is due to the positive lapse rate. The decreasing Scorer parameter in the stratosphere is consistent with the pres-

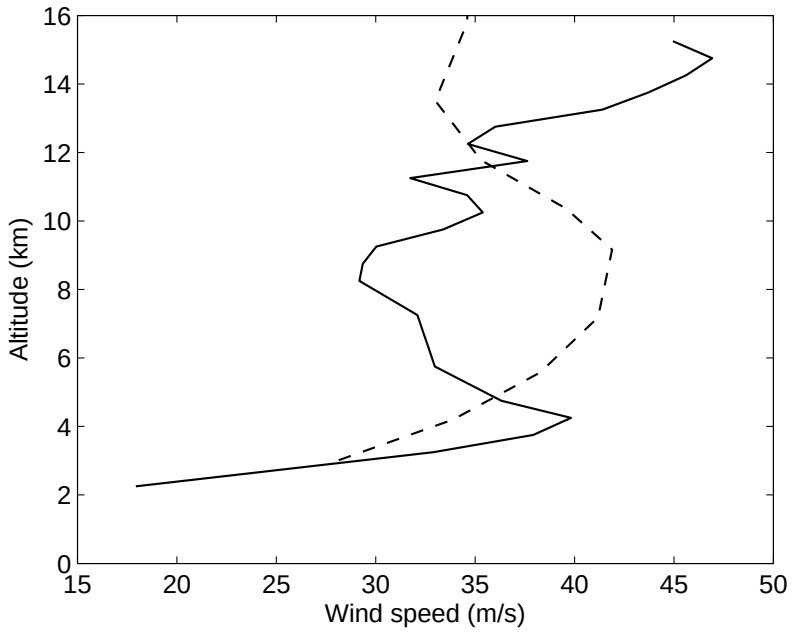

(a)

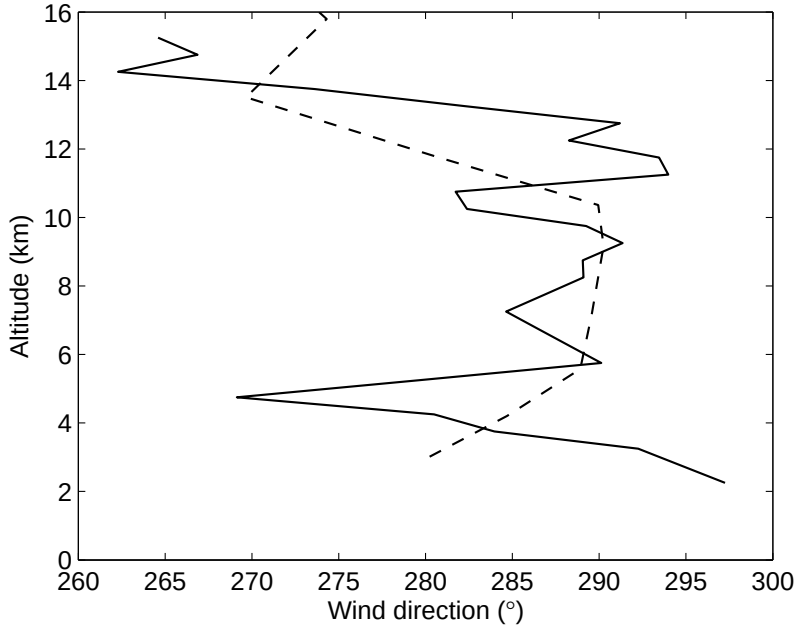

(b)

Figure 4.22 Flight 3: (a) Horizontal wind speed and (b) direction estimates versus altitude shown by the solid line and Reanalysis values shown by the dashed line.

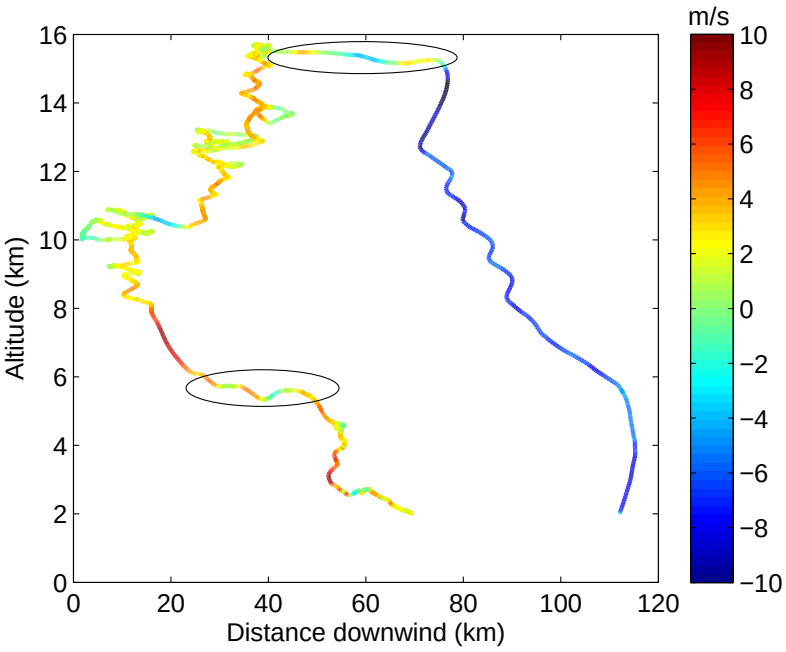

(a)

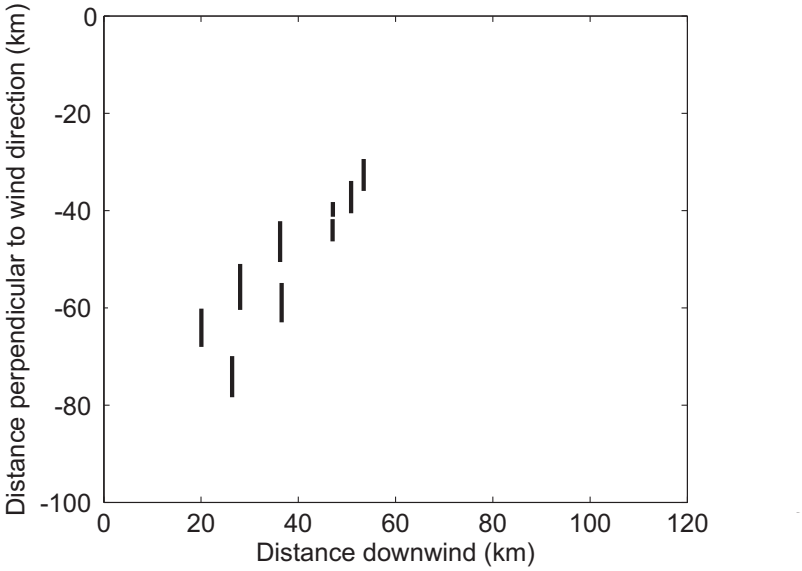

(b)

Figure 4.23 Flight 3: (a) Vertical wind speed (colour coded as indicated) versus distance downwind from the ridge-line and altitude and (b) estimated rising edges of the wave.

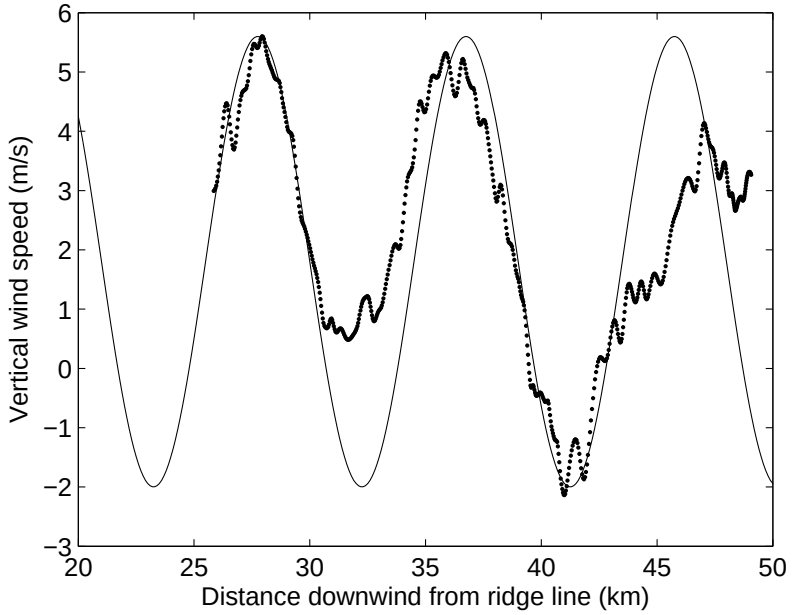

(a)

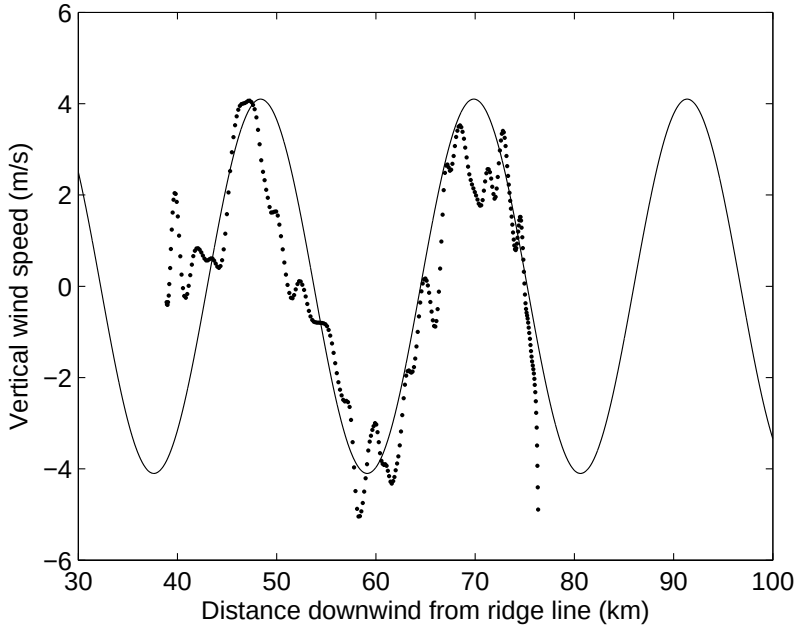

(b)

Figure 4.24 Flight 3: Derived vertical wind speed versus distance downwind from the ridge line and fitted sinusoids for two flight segments as described in the text for an altitude range of (a) 5.3-6.1 km and (b) 15.0-15.6 km.

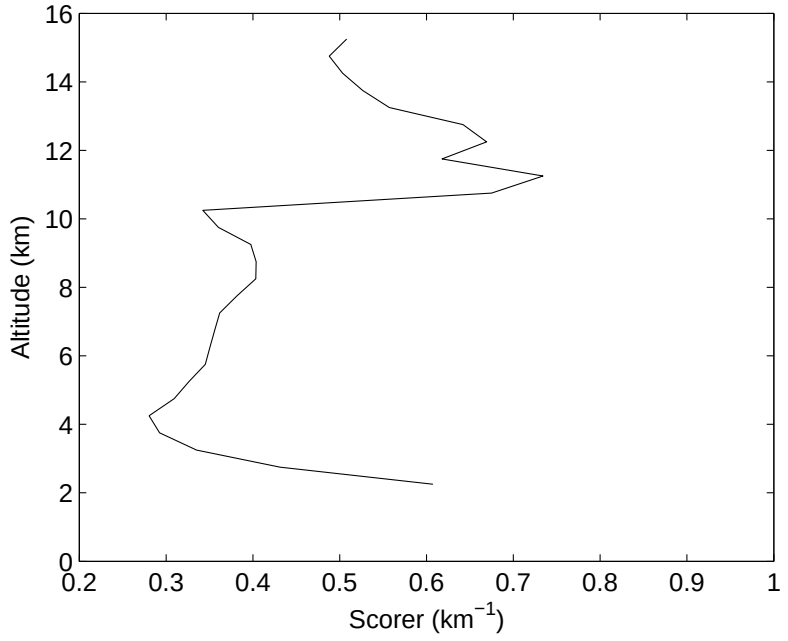

Figure 4.25 Flight 3: The Scorer parameter versus altitude.

ence of trapped stratospheric waves. A calculation of the minimum lee wave wavelength from the Scorer parameter gives approximately 17 km in the troposphere which is significantly larger than that observed as described above; however the Scorer parameter is increasing with altitude at 6 km altitude. The minimum wavelength is calculated as 10 km in the stratosphere. The observed wavelength is larger than this but there is likely to be significant vertical propagation of the stratosphere wave giving a horizontal wavelength larger than the minimum.

The data for this flight also included the heading measured by an electronic compass. Unfortunately, the type of compass used is unknown. Since a compass is subject to various errors, the reliability of the data was considered uncertain enough not to be used for wind velocity estimation. However, once the wind velocity has been determined, the sailplane heading can be calculated and compared with the measured heading. The calculated and measured headings are shown in Fig. 4.26 for two short flight segments. The agreement is quite good. A magnetic compass may be subject to errors when the aircraft is accelerating, particularly when entering and exiting turns, and this is apparent in the figures.

In summary, application of the methods to this flight gave consistent results. The estimated horizontal wind velocities are more variable and the speed is somewhat different from the Reanalysis, although the direction agrees quite well. A wave segment seen in the stratosphere may be informative in terms of stratospheric waves.

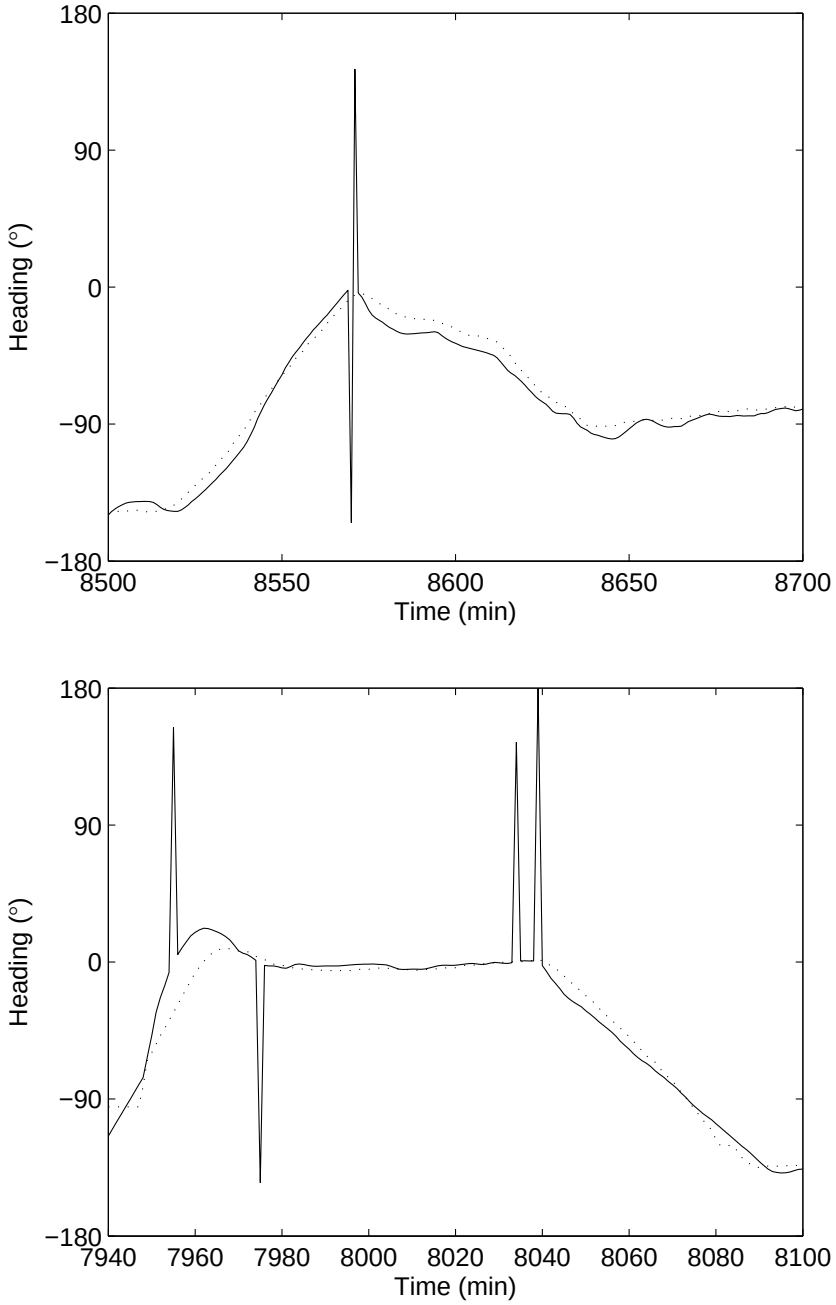

Figure 4.26 Flight 3: Measured heading (solid line) and calculated heading (dashed line) for two flight segments.

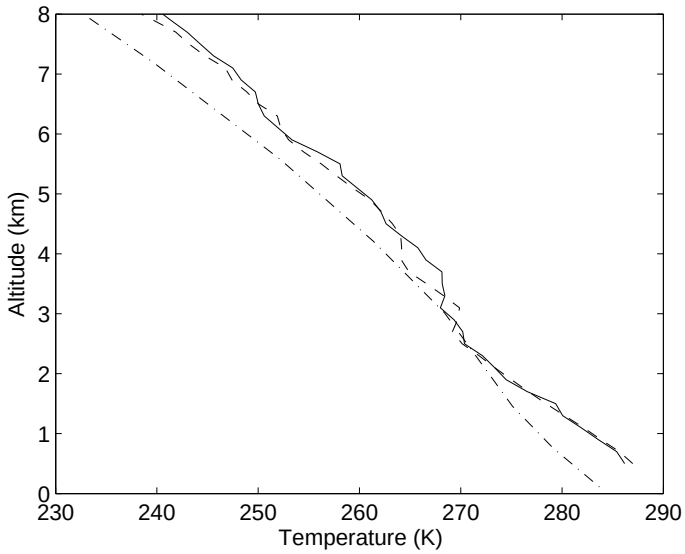

Figure 4.27 Flight 4: Temperature versus altitude measured along the ascending flight path (solid line) and descending flight path (dashed line), and the Reanalysis temperature (dot-dashed line).

4.3.4 Flight 4: Perlan Flight 24: Omarama

Flight 4 was flown from Omarama, New Zealand, in the lee of the Southern Alps as described in Section 3.5. The algorithm was applied to the data using the same parameters as in Table 4.1. The temperature data measured during the flight are collected in 200 m thick altitude bins, averaged and plotted versus altitude for the ascending and descending portions of the flight in Fig. 4.27. The temperature from the Global Reanalysis is shown on the same graph. The two temperatures agree quite well giving a lapse rate of approximately -5.9 K/km, and the measured temperature data are used for calculations below. The flight was partitioned into 171 regions, and 51 wind velocity estimates were obtained. Typical values obtained for σ_w were in the range 0.5-8.9 $\mathrm{m/s}$, and typical values for D were in the range 3-32. Some of the values of σ_w were quite large, indicating that the parameters used may not be suitable. Then r_{region} was reduced to 1000 m and D_{min} was increased to 5, the flight was partitioned into 273 regions, and 45 estimates were obtained. This gave better values of σ_w in the range 0.4-4.8 $\mathrm{m/s}$, and typical values for D were in the range 5.1-30. Some of the σ_w values are still a bit large however, and are shown versus flight time in Fig. 4.28. Most of the large σ_w values were on the tow where large variations in wind velocity can be experienced in the rotor at low levels. The other large values are at a time of approximately 120 mins. The four wind velocities estimates for which $\sigma_w > 4\ \mathrm{m/s}$ were excluded from subsequent analysis. The estimated wind velocity is shown in vector form along the flight path above 3 km in Fig. 4.29(a). The estimated horizontal wind direction is WSW as anticipated from the geopotential plot (Fig. 3.15). Close-ups of two flight segments are shown in Fig. 4.29(b) and (c). The first is near the Northern end of the flight at an altitude of approximately 3.5 km and with flight path parallel to the ridge line. The second is near the Southern end of the flight at an altitude of approximately 7.0 km and shows

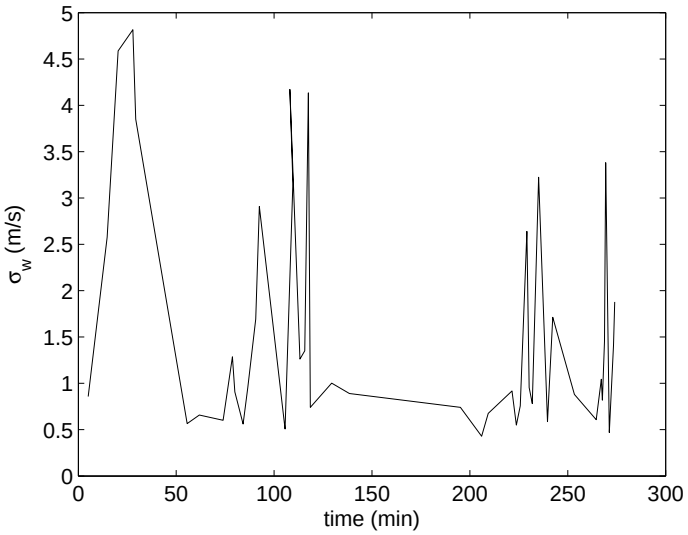

Figure 4.28 Flight 4: Values of σ_w versus time.

some short downwind segments. The two flight segments are in separate wave regions, as shown in the topography plot in Fig. 3.14(a). As seen previously, there are fewer estimates in the first region than the second region, since the first flight path is relatively straight and the heading changes slowly.

The wind speed and direction estimates were collected into altitude bins 200 m thick and averaged, separately for the ascending and descending paths of the flight, and are shown above 2 km in Fig. 4.30. Note that there is a difference in wind direction of up to about 40° at lower altitudes for the ascending and descending portions of the flight. There could be a wind shift between the different locations and times of these flight segments. The Reanalysis wind speed and direction are also shown Fig. 4.30. The estimated wind speed and direction agree quite well with the Reanalysis. The estimated wind speeds are self-consistent so are taken as reliable.

A satellite picture of the southern South Island of New Zealand at 0000Z on 11 August 2002 is shown in Fig. 3.17. Although the projection is distorted, wave clouds are evident in the flight region with a spacing of about 8 km.

Using the fitted temperature profile and the calculated horizontal wind speed, the Scorer parameter is calculated and shown in Fig. 4.31. The Scorer parameter decreases with altitude, supporting the development of trapped lee waves. The Scorer parameter varies between 0.3 and 0.6 km^{-1}, with a corresponding minimum lee wave wavelengths between 10 and 20 km.

There are no long downwind paths during this flight, but long flight segments parallel

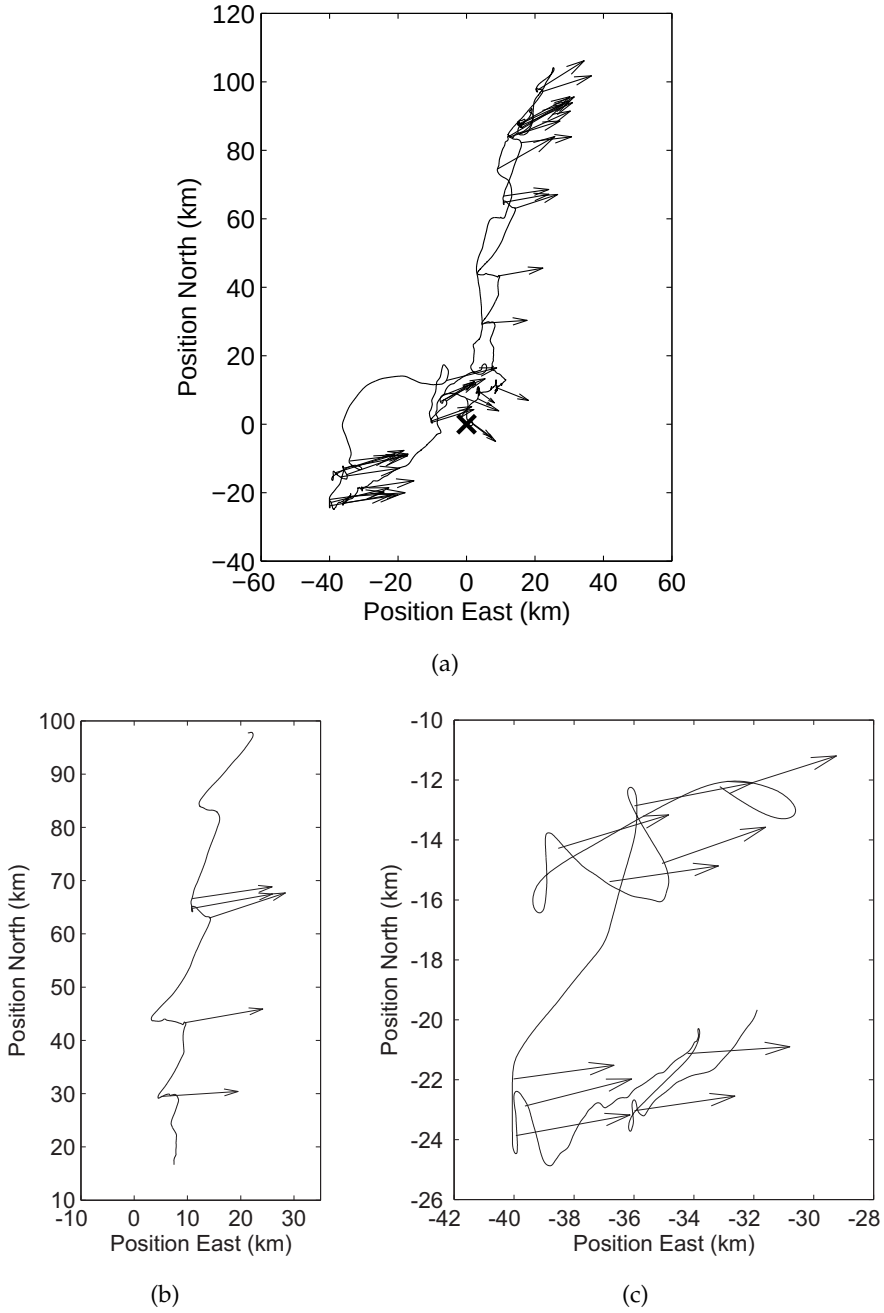

Figure 4.29 Flight 4: (a) Estimated wind velocity vectors along the flight path. The launch position is shown by the x and the flight path is approximately anticlockwise. (b)(c) wind velocity estimates for two flight segments as described in the text for an altitude range of 3.2-8.1 km and 6.7-8.6 km, respectively. The length and direction of the arrows represent the estimated wind speed and direction, respectively.

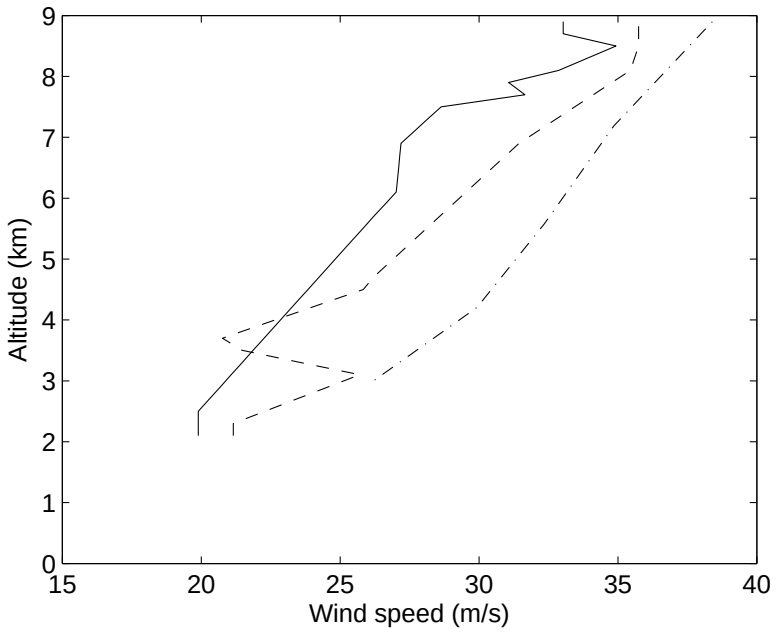

(a)

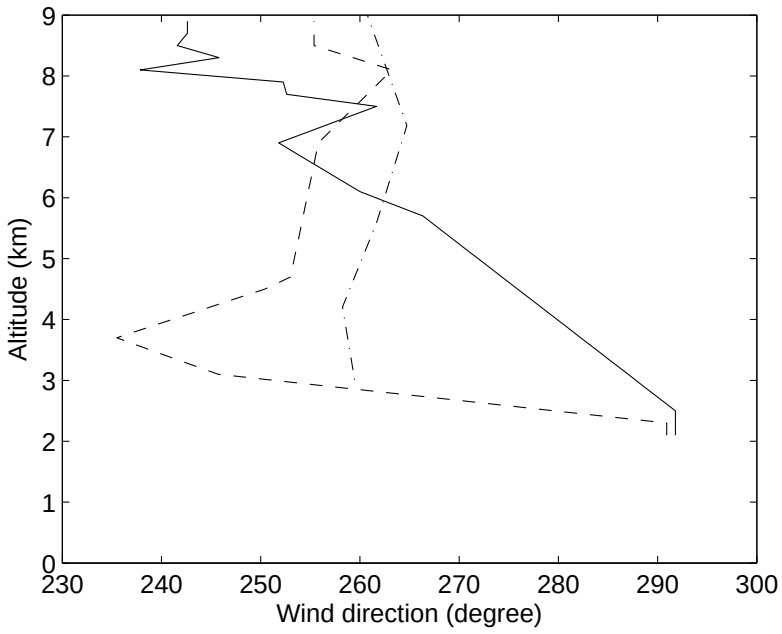

(b)

Figure 4.30 Flight 4: (a) Horizontal wind speed and (b) direction estimates versus altitude. The ascending portion of the flight is shown by the solid line, and descending portion by the dashed line. The Reanalysis values at Omarama are shown by the dot-dashed line.

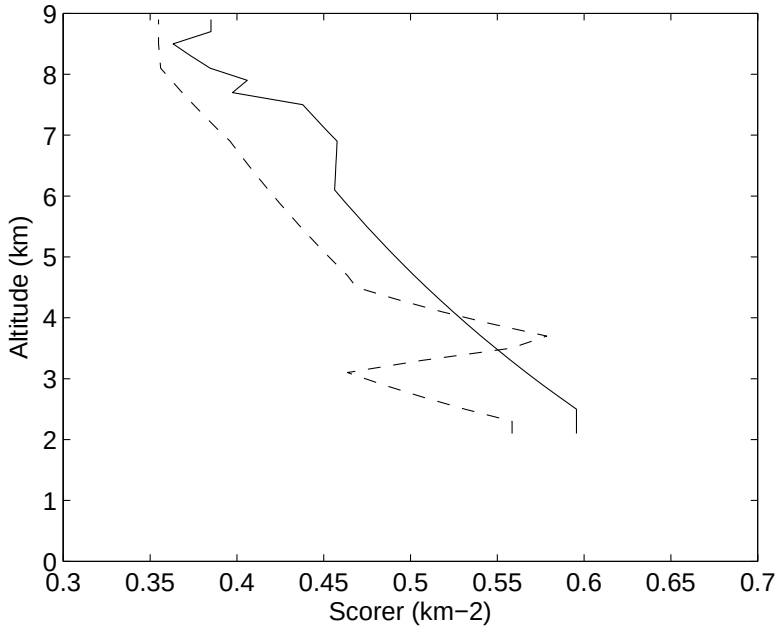

Figure 4.31 Flight 4: The Scorer parameter versus altitude for the ascending (solid line) and descending (dashed line) flight path.

to the ridge line. An 80-minute flight segment approximately parallel to the long ridge line at the Northern end of the flight is shown in Fig. 4.32(a). The sailplane is in the same wave system produced by the long ridge line as shown. The flight altitude versus position North is shown in Fig. 4.32(b). The flight path is replotted in Fig. 4.32(c) as a function of distance downwind from the ridge line, and colour-coded by the derived vertical wind speed. In Fig. 4.32(c) there are four strong vertical wind speed peaks at positions between approximately 8 and 12 km down wind from the ridge line, indicating the leading edges of the wave. The altitude varies between 5 and 8 km. Between the leading edges there are weak vertical wind speeds which indicate wave patterns.

In summary, consistent results were obtained for the horizontal wind velocities which are also consistent with the Reanalysis. The flight consists of long segments parallel to the ridge line. Inspection of the estimated vertical wind speeds showed expected patterns relative to the topography. The decreasing Scorer parameter with altitude indicates suitable conditions for production of trapped lee waves.

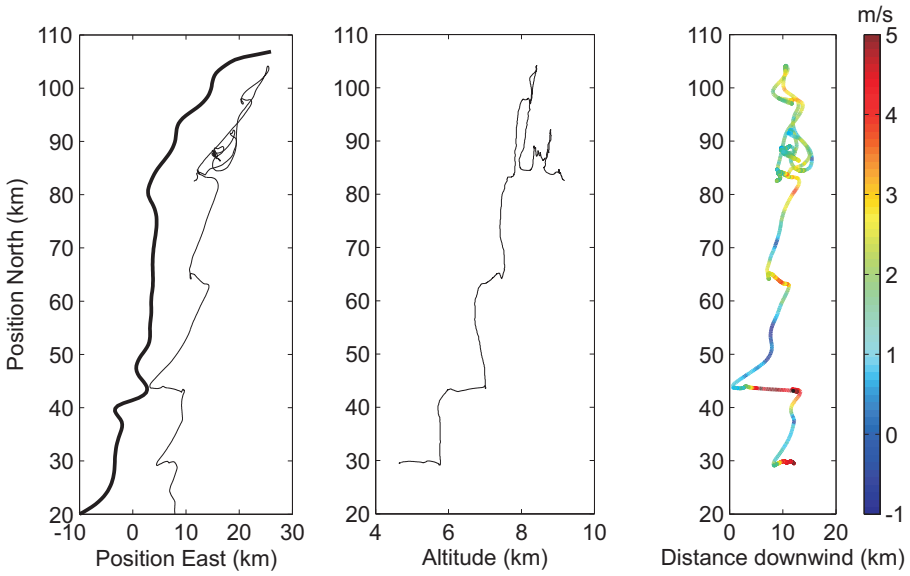

Figure 4.32 Flight 4: A flight section parallel to the ridge line as described in the text. (a) Flight path (thin line) and ridge line (thick line). (b) Flight altitude versus position North. (c) Estimated vertical wind speed (colour coded as indicated) versus distance downwind from the ridge line.

Chapter 5

Flight Simulation

In Chapters 6 and 7, statistical estimation techniques are used to determine wind velocities from flight data. In order to study the performance of these methods they are applied to synthetic data from simulated flights. The nature of these simulations is described in this chapter. It is emphasized that the objective is not a full flight simulation, but a specification of simple flight trajectories in the air in a specified variable wind velocity field of relevance to mountain wave, and calculation of the resulting noisy flight data.

There are three inputs to the simulator, in addition to the time-step δt:

1. The 3D wind field.
2. The indicated airspeed and heading of the sailplane as a function of time.
3. Sink rate characteristics of the sailplane, i.e. the flight polar.

These inputs are described in turn below.

1. Wind field

   The wind field is fixed in time but varies in space. The horizontal component of the wind velocity is defined in terms of its speed and direction, denoted $v_w(x, y, z)$ and $\theta_w(x, y, z)$, respectively. The horizontal wind field is defined by the values $v_{w0} = v_w(0, 0, 0)$ and $\theta_{w0} = \theta_w(0, 0, 0)$ at the origin, by linear rates of change of $v_w(x, y, z)$ and $\theta_w(x, y, z)$ with x with values A and B, respectively, and a linear rate of change C, of $v_w(x, y, z)$ with z. The horizontal wind field is therefore given by

$$v_w(x, y, z) = v_{w0} + Ax + Cz \tag{5.1}$$
$$\theta_w(x, y, z) = \theta_{w0} + Bx \tag{5.2}$$

Note that the horizontal wind speed is independent of y and the horizontal wind direction is independent of y and z. The vertical wind speed is taken to be a sinusoidal wave generated by a source along the y-axis and takes the form

$$v_w^z(x, y, z) = D \sin(2\pi x/\lambda + \phi) \tag{5.3}$$

where D, λ and ϕ are the maximum vertical wind speed, wavelength and phase shift, respectively. Note that the vertical wind speed is independent of y (as expected for a source on the y-axis) and of z. Although the above definition describes a fairly restricted wind field, it is sufficiently general to generate the data required and does not introduce any hidden constrains into the inversion.

2. Sailplane airspeed and heading

   The sailplane trajectory relative to the air is defined by specifying the indicated airspeed (assumed horizontal) and heading as a function of time, $v_a^{ind}(t)$ and $\theta_a(t)$, respectively. The simulation time-step is δt and the airspeed and heading are therefore discretized as $v_{a,i}^{ind} = v_a^{ind}(i\delta t)$ and $\theta_{a,i} = \theta_a(i\delta t)$. The simulation is kinematic except for a component of the sailplane vertical speed due to energy exchange that is calculated from the change in airspeed at each time-step. A standard atmosphere model (Section 1.1.1) is used to transform between IAS and TAS. The initial sailplane position is taken as $(0, 0, z_0)$.

3. Sink rate characteristics

   The sailplane sink rate is specified as a function of IAS using a given flight polar. For the simulations in this thesis the DG505M flight polar at a wing loading of 44 kg/m^2 (see Section 3.2) is used.

The output consists of the following parameters as a function of time-step i. Gaussian noise is added to ground position and airspeed to give data for use in an inversion.

1. Ground position, (x_i, y_i, z_i)
2. Air horizontal position, $(x_{a,i}, y_{a,i})$
3. Horizontal ground velocity, $(v_{g,i}^x, v_{g,i}^y)$
4. 3D wind velocity, $(v_{w,i}^x, v_{w,i}^y, v_{w,i}^z)$
5. TAS, $v_{a,i}$

6. Sink rate, vertical speed component due to energy exchange, and vertical ground speed, (s_i, $v_{e,i}$, $v^z_{g,i}$)
7. Rate of change of heading, $\delta\theta_{a,i}/\delta t$
8. Bank angle, ϕ_i
9. Noisy ground position data, $(\tilde{x}_i, \tilde{y}_i, \tilde{z}_i)$
10. Noisy ground velocity data, $(\tilde{v}^x_{g,i}, \tilde{v}^y_{g,i}, \tilde{v}^z_{g,i})$
11. Noisy IAS and heading data, $(\tilde{v}^{ind}_{a,i}, \tilde{\theta}_{a,i})$

The flight path and related quantities are calculated by linear prediction with a time-step of δt. Since all quantities are slowly varying, this is sufficiently accurate for sufficiently small δt. Given all quantities at time-step i, values at time-step $i+1$ are updated as follows. A flow diagram of the simulator is shown in Fig. 5.1. The new air position is first calculated as

$$\begin{aligned} x_{a,i+1} &= x_{a,i} + v_{a,i}\cos(\theta_{a,i})\delta t, \\ y_{a,i+1} &= y_{a,i} + v_{a,i}\sin(\theta_{a,i})\delta t. \end{aligned} \tag{5.4}$$

The horizontal ground velocity is calculated as

$$\begin{aligned} v^x_{g,i} &= v^x_{w,i} + v^x_{a,i}, \\ v^y_{g,i} &= v^y_{w,i} + v^y_{a,i}, \end{aligned} \tag{5.5}$$

and the ground position is updated as

$$\begin{aligned} x_{i+1} &= x_{g,i} + v^x_{g,i}\delta t, \\ y_{i+1} &= y_{g,i} + v^y_{g,i}\delta t. \end{aligned} \tag{5.6}$$

The TAS $v_{a,i}$ is calculated from $v^{ind}_{a,i}$ and z_i, the vertical ground speed is calculated using

$$\begin{aligned} s_i &= -(v_{a,i}/v^{ind}_{a,i})s_0(v^{ind}_{a,i}) \\ v_{e,i} &= -(v_{a,i}/g)(v_{a,i} - v_{a,i-1})/\delta t \\ v^z_{g,i} &= v^z_{w,i} + s_i + v_{e,i}, \end{aligned} \tag{5.7}$$

and the vertical ground position then updated as

$$z_{i+1} = z_i + v^z_{g,i}\delta t. \tag{5.8}$$

To illustrate use of the simulator, an example of the input and output for a simulation is shown in Figs. 5.2 and 5.3. Parameters used in the simulation are $\delta t = 0.1$ s, $N_t = 1000$ s,

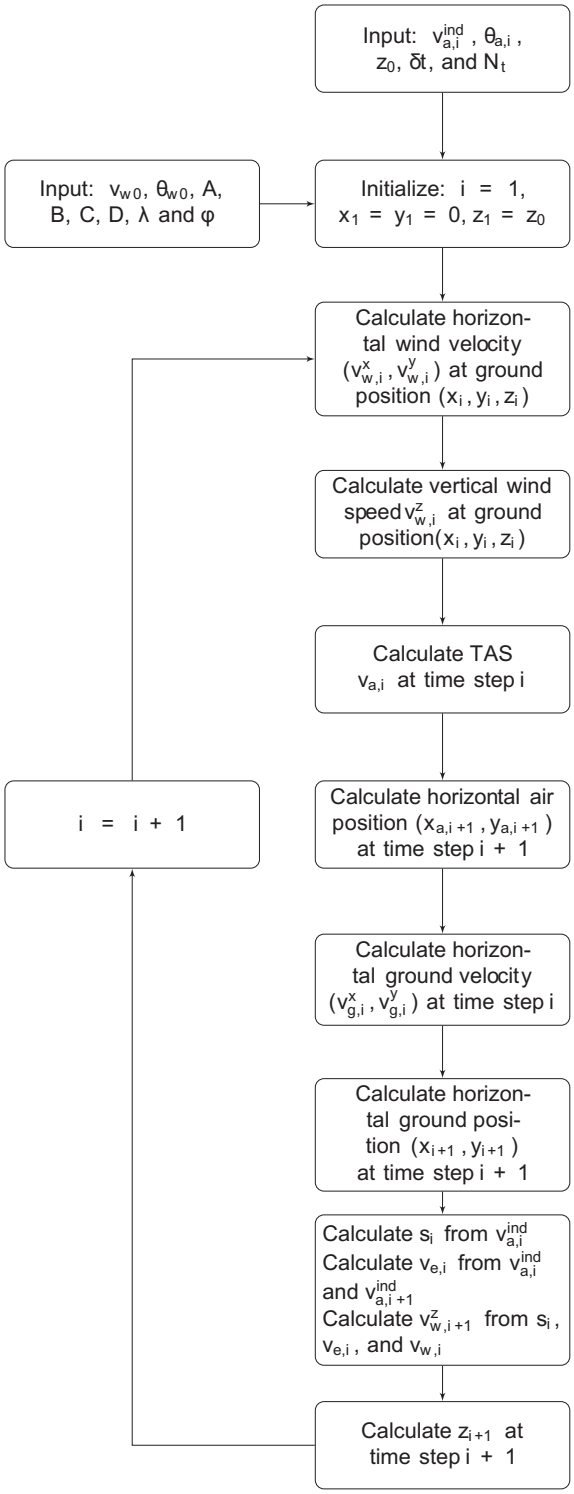

Figure 5.1 Flow diagram of the flight simulator.

$z_0 = 3$ km, $v_{w0} = 35$ m/s, $\theta_{w0} = 305°$, $A = -0.5$ m/s/ km, $B = 1°$/ km, $C = 1$ m/s/ km, $D = 3$ m/s, $\lambda = 10$ km, and $\phi = \pi/6$. Noise was not added to the output data.

The resulting wind field is shown in Fig. 5.3(a) and (b). The airspeed used is a 1000 s segment taken from Flight 1 (Section 3.2), linearly interpolated onto a sampling interval of 1 s, and shown in Fig. 5.2(c). The heading function used is shown in Fig. 5.2(d) and incorporates a number of turns and straight flight segments. The resulting air path and ground path are shown in Fig. 5.3.

To check that $\delta t = 0.1$ s is small enough, the simulation was repeated with $\delta t = 0.02$ s, and the outputs from the two simulations compared. The average differences in position and ground velocity data are 1.3 m and 0.02 m/s respectively. The differences in position and velocity are both very small. This shows that $\delta t = 0.1$ s gives sufficient accuracy for the precision required, i.e. the errors are smaller than typical levels of noise added to the data.

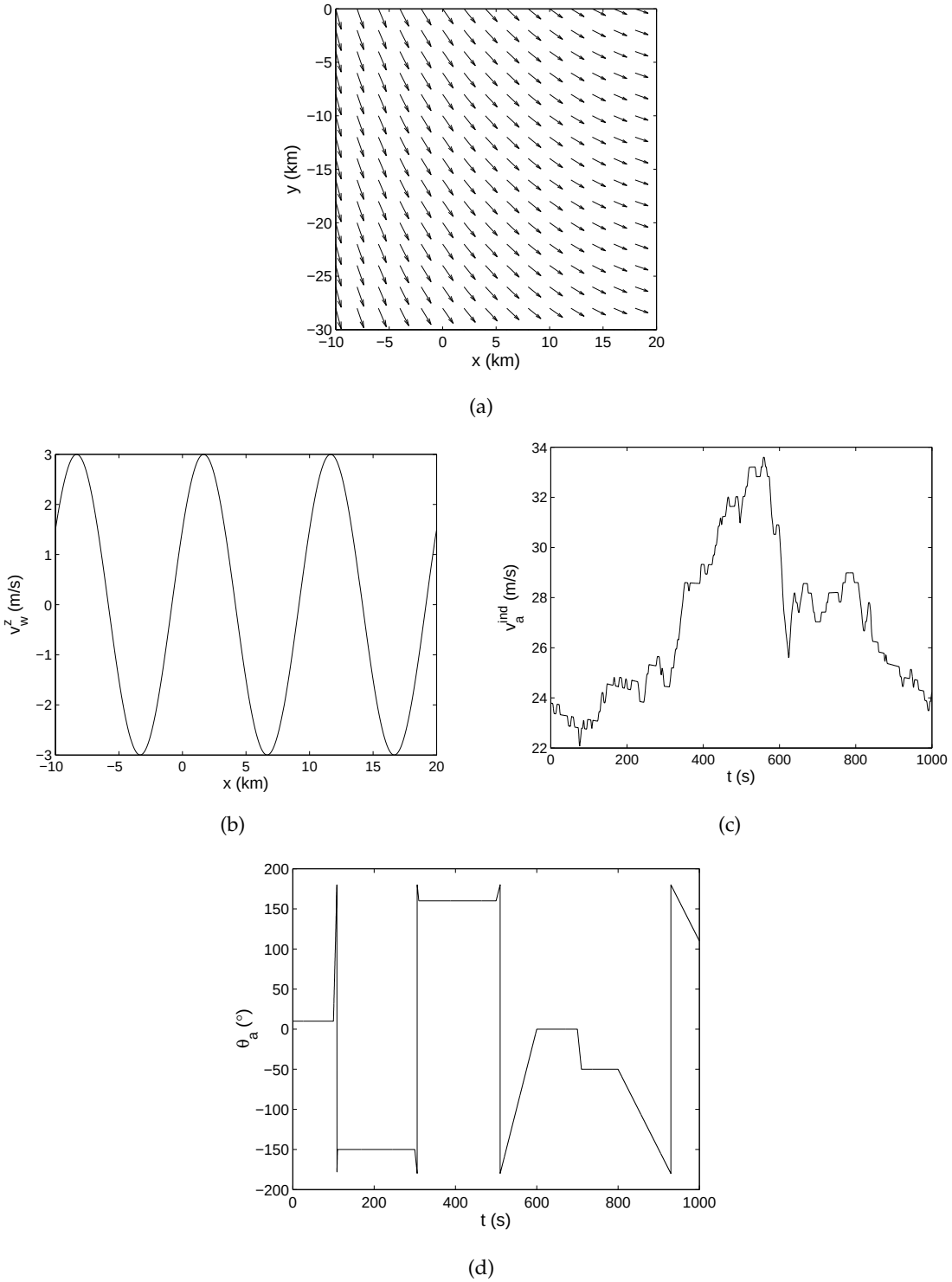

Figure 5.2 Input data for the simulation generated for $\delta t = 0.1$ s showing (a) horizontal wind speed, (b) vertical wind speed, (c) indicated airspeed, and (d) heading.

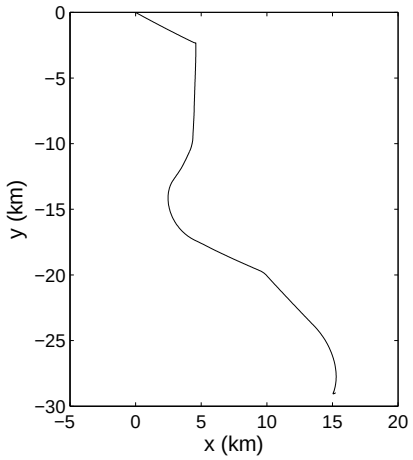

(a)

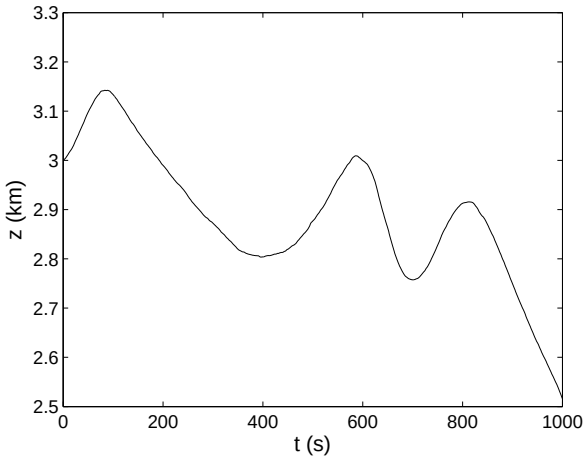

(b)

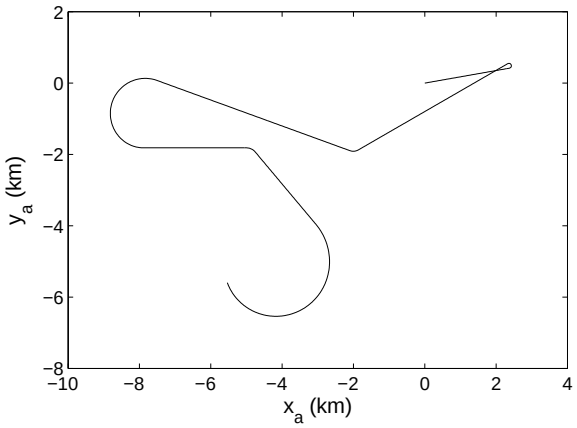

(c)

Figure 5.3 Output data from the simulation generated for $\delta t = 0.1$ s showing (a) ground path, (b) altitude, and (c) air path.

Chapter 6

Maximum Likelihood Estimation

6.1 Introduction

The heuristic method described in Chapter 4 provides good solutions to the problem of wind velocity estimation where GPS and airspeed data are available. The method is specific however to ground velocity and airspeed data. It could be extended to other kinds of data (e.g. heading data) but this would require a reformulation. It is therefore not a particularly general formulation of the problem. Furthermore, the method does not incorporate a rigorous noise model. The cylindrical regions are large and hence the wind velocity estimates obtained are quite sparse. When the noise level increases the reliability of the heuristic method reduces, and better data and noise models are required.

In this chapter and Chapter 7, the problem of wind velocity estimation is formulated as a general statistical estimation problem. This is a standard formulation that allows incorporation of, in principle, any data and any constraints or *a priori* information, and allows incorporation of explicit noise models and the application of standard estimation methods. In this chapter, maximum likelihood (ML) estimators are developed for wind velocity estimation from data consisting of ground velocity and either airspeed or heading data. The methods are illustrated by application to simulated and real flight data. In Chapter 7, the problem of wind velocity estimation from only ground velocity data is addressed, and maximum *a posteriori* (MAP) estimators are developed, and also applied to simulated and experimental data.

As described in Chapter 2, the 3D problem can be decomposed into the horizontal and vertical components. This decomposition is continued here. As seen in Chapters 2 and 4, the 2D problem of determining the horizontal component of the wind velocity is the more difficult problem, the vertical problem being relatively straightforward. Therefore, in this chapter, only the 2D problem is considered, i.e. determination of the horizontal wind velocity from a flight at constant altitude. This is sufficient to illustrate the ML estimator. In Chapter 7, the focus is still on the horizontal component of the wind velocity, but the

3D problem is considered where the horizontal component of the wind velocity varies in three dimensions. Calculation of the vertical wind speed, using the estimated horizontal component, is also considered there.

In the context of statistical estimation it is convenient to make a small change to some of the symbols used in the previous chapters to represent the flight variables. This is because it is conventional in the statistical estimation literature to use a vector to represent a collection of values of a parameter of interest (refer to Section 1.4). For example, the vector $\mathbf{x} = (x_1, x_2, ...x_N)$ may be used to represent an image, where the components x_i represent the values (brightness) of the N pixels of the image. Following this convention, for example, the vector $\mathbf{v}_g$ is used to represent a collection of ground velocities at different time instants, i.e. $\mathbf{v}_g = \{v_{g,i}\}$, where the $v_{g,i}$ are the ground velocities at time-point i. If it is necessary to refer to the components of $v_{g,i}$, then the symbols $v^x_{g,i}$ and $v^y_{g,i}$ are used. Furthermore, the vectors $\mathbf{v}_g$, $\tilde{\mathbf{v}}_g$, and $\hat{\mathbf{v}}_g$ are used to represent the true, measured, and estimated ground velocities, respectively, and the same for other quantities. Similarly, the vectors $\mathbf{v}_w$, $\mathbf{v}_a$, $\boldsymbol{\theta}_a$ are used to represent a collection of of wind velocities, airspeeds and headings, respectively. Note that $\mathbf{v}_a$ does not represent a collection of air velocities, and this particular collection of quantities is not used.

6.2 Measurement model

Referring to Section 1.4, the measurement model describes the measurement (data), including noise, in terms of the object parameters. In the case at hand, the measurement model is quite simple. The data are the ground velocities and airspeed and/or heading. The object parameters are the true ground, wind and air velocities. However, since these are not all independent, the ground and wind velocities are used as the object parameters.

The measured ground velocities are related to the true ground velocity components by

$$\tilde{v}_{g,i} = v_{g,i} + n_{g,i}, \tag{6.1}$$

where $n_{g,i}$ represents the measurement noise. Errors in GPS positioning have been investigated in [80] for consumer-grade GPS receivers with standard positioning service, non-differential GPS. Measurements show that the distribution of horizontal GPS fixes can be approximated by an uncorrelated, bivariate normal distribution, i.e. the (Northerly and Easterly) components are normally distributed. They also show that the position errors are quite strongly correlated (correlation coefficient > 0.6) for fixes less than one minute apart. As a result, calculation of the horizontal velocity from differences in GPS fixes less than one minute apart will cancel out these errors to some degree. They also show that the vertical fixes show approximately Gaussian errors, with a standard deviation of about 5 m, sometimes with a significant bias which may be up to 10 m. The bias is due primarily to variations in ionospheric delay. The effects of the ionosphere generally change slowly in time so that the bias changes slowly with time. Therefore, the bias errors will tend to cancel

out when calculating the vertical velocity. An appropriate model for each component of the error $n_{g,i}$ is therefore zero-mean, white Gaussian noise. The variance, denoted σ_g^2, can then be estimated from known GPS characteristics.

The airspeed data are assumed to have been corrected, if necessary, for air density using standard methods to give the true airspeed. As described in Chapter 2, the airspeed and its horizontal component are assumed to be equal. The measured airspeed at time-step i is then given by

$$\tilde{v}_{a,i} = ||v_{g,i} - v_{w,i}|| + n_{a,i}, \tag{6.2}$$

where $n_{a,i}$ represents the airspeed indicator errors. The primary errors in a pitot-static airspeed indicator are additive pneumatic disturbances [52] and the disturbance in the impact (dynamic) pressure can be approximated as Gaussian. Since the airspeed is proportional to the square-root of the impact pressure, the errors in the derived airspeed will not be strictly Gaussian. However, for convenience we assume that the noise $n_{a,i}$ can be modeled approximately by zero-mean, white Gaussian noise since the errors are small compared to the airspeed. The variance, denoted σ_a^2, can be obtained from the instrument specifications.

The aircraft heading measurements are given by

$$\tilde{\theta}_{a,i} = \tan^{-1}(v_{g,i} - v_{w,i}) + n_{\theta_a,i}, \tag{6.3}$$

where $n_{\theta_a,i}$ are the compass errors, modeled as zero-mean, white Gaussian noise with variance $\sigma_{\theta_a}^2$, and $\tan^{-1}(x)$ is the four-quadrant inverse tangent that gives an angle on $(-\pi, \pi)$ for the vector argument x. The variance $\sigma_{\theta_a}^2$ is considered to be small enough that wrapping of the distribution on $(-\pi, \pi)$ is not a problem. Equations (6.1), (6.2) and (6.3) together form the measurement model.

In the next three sections, three different kinds of data sets are considered, consisting of ground velocity, airspeed and heading; ground velocity and airspeed; and ground velocity and heading, respectively. ML estimators are developed for each case and tested on simulated and experimental data.

6.3 Position, airspeed and heading data

6.3.1 Methods

Consider data consisting of ground velocity, airspeed and heading. The velocity relative to the air is given by the airspeed and heading so that, the wind velocity at each time-step is given simply by

$$v_{w,i} = v_{g,i} - v_{a,i}. \tag{6.4}$$

However, at a single time-step, the number of parameters is equal to the number of data, so that such an estimate would be sensitive to noise. The sensitivity can be reduced by exploiting the assumption of a constant (or slowly varying) wind velocity field, using data from a number of contiguous time-steps, and taking a statistical estimation approach.

Consider a temporal window $(i-N, i+N)$ centered at time-step i and with half width N. If the wind velocity is assumed to be constant within this window then the object parameters are

$$(\mathbf{v}_{g,i}, v_{w,i}) = (v_{g,i-N}, ..., v_{g,i+N}, v_{w,i}), \tag{6.5}$$

and the data are

$$(\tilde{\mathbf{v}}_{g,i}, \tilde{\mathbf{v}}_{a,i}, \tilde{\boldsymbol{\theta}}_{a,i}) = \left(\tilde{v}_{g,i-N}, \tilde{v}_{a,i-N}, \tilde{\theta}_{a,i-N}, ..., \tilde{v}_{g,i+N}, \tilde{v}_{a,i+N}, \tilde{\theta}_{a,i+N}\right). \tag{6.6}$$

The data-to-parameter ratio is now $4(2N+1)/[2(2N+1)+2] \approx 2$, and the problem is over-determined. Using the assumption of Gaussian noise, the likelihood function is

$$\begin{aligned} p\left(\tilde{\mathbf{v}}_{g,i}, \tilde{\mathbf{v}}_{a,i}, \tilde{\boldsymbol{\theta}}_{a,i} | \mathbf{v}_{g,i}, v_{w,i}\right) = K_1 \prod_{j=-N}^{N} \exp\Big(&- ||\tilde{v}_{g,i+j} - v_{g,i+j}||^2 / 2\sigma_g^2 \\ &- \left(\tilde{v}_{a,i+j} - ||v_{g,i+j} - v_{w,i}||\right)^2 / 2\sigma_a^2 - \left(\tilde{\theta}_{a,i+j} - \tan^{-1}(v_{g,i+j} - v_{w,i})\right)^2 / 2\sigma_{\theta_a}^2 \Big), \end{aligned} \tag{6.7}$$

where K_1 is a constant. Care must be taken when calculating the differences in the last term to account for wrapping on $(-\pi, \pi)$. The maximum likelihood estimate of the object parameters is then given by

$$(\hat{\mathbf{v}}_{g,i}, \hat{v}_{w,i})_{ML} = \underset{(\mathbf{v}_{g,i}, v_{w,i})}{\operatorname{argmax}} \left\{ p\left(\tilde{\mathbf{v}}_{g,i}, \tilde{\mathbf{v}}_{a,i}, \tilde{\boldsymbol{\theta}}_{a,i} | \mathbf{v}_{g,i}, v_{w,i}\right) \right\}. \tag{6.8}$$

The minimisation begins with starting values for $(\mathbf{v}_{g,1}, v_{w,1})$, and the estimated values $(\hat{\mathbf{v}}_{g,i}, \hat{v}_{g,i})$ are used as the starting values for solving for $(\mathbf{v}_{g,i+1}, v_{w,i+1})$. The maximisation in (6.8) was performed by minimising $-\ln(p\left(\tilde{\mathbf{v}}_{g,i}, \tilde{\mathbf{v}}_{a,i}, \tilde{\boldsymbol{\theta}}_{a,i} | \mathbf{v}_{g,i}, v_{w,i}\right))$ using the Matlab function `fminunc` [81]. The function `fminunc` employs a local minimiser using the BFGS Quasi-Newton method with a cubic line search procedure [82, 83]. The termination criterion is based on specified values of the maximum number of function evaluations, maximum number of iterations and tolerance of the optimised variable or the cost func-

tion. Suitable termination criteria were selected by experimentation.

6.3.2 Simulation results

The performance of the ML estimator is illustrated using simulated flight data generated as described in Chapter 5. Two flights with different headings were used. The parameters used in the simulation were $\delta t = 0.02$ s, $N_t = 1000$ s, $v_{w0} = 35$ m/s, $\theta_{w0} = 305°$, $A = -1$ m/s/km, $B = 2°$/km, $C = 0$, and $D = 0$. This gives the wind field as shown in Fig. 6.1(a), and the wind direction is approximately northwest. The airspeed data were taken from a segment of Flight 1 (Section 3.2) and linearly interpolated onto a sample spacing of δt as shown in Fig. 6.1(b). The headings for the two flights are shown in Fig. 6.2(a) and (b) respectively, and the paths relative to the air in (c) and (d). During the first flight the sailplane performs a number of circling maneuvers at turn rates of $1 - 3°$/s. The second flight is relatively straight with a few high rate turns at $5°$/s and $20°$/s. The ground paths for the two flights are shown in Fig. 6.2(e) and (f) respectively. Measurements of the ground velocity, airspeed, and heading were taken at 1 s intervals and corrupted by noise with standard deviations of 2 m/s, 2 m/s, and $2°$, respectively.

The ML estimates were calculated as described above using $N = 20$ with known values of σ_g, σ_a, and σ_{θ_a}. A starting value of $(25 \text{ m/s}, 315°)$ was used in the optimisation compared to the true value of $(35 \text{ m/s}, 305°)$. The estimated wind speed and direction from Flight 1 are shown in Fig. 6.3(a) and (b) respectively, and the true values are shown for comparison. Note that the wind speed and direction estimates were not obtained at every single time step, but one in each window. The average rms errors across the whole flight are 0.24 m/s and $0.66°$. The estimates correctly track the true wind velocity. For comparison, the estimates calculated directly from (6.4) are shown in Fig. 6.3 (c) (d), which gives an average rms error of 1.8 m/s and $4.2°$. However, averaging these results over a window of halfwidth 20 s reduces the error to 0.22 m/s and $0.65°$, as shown in Fig. 6.3(e)(f).

For Flight 2, the ML results are shown in Fig. 6.4 (a)(b). The average rms errors in the ML estimates are 0.29 m/s and $0.55°$, those for the direct calculation are 2.0 m/s and $3.9°$ in (c)(d), and averaging gives 0.31 m/s and $0.52°$ as shown in (e)(f). The performance of the ML estimates for the complete data is more-or-less the same as values calculated directly and averaged over the temporal window. A more significant advantage of the statistical estimation accrues when the data are incomplete as described in the following subsections.

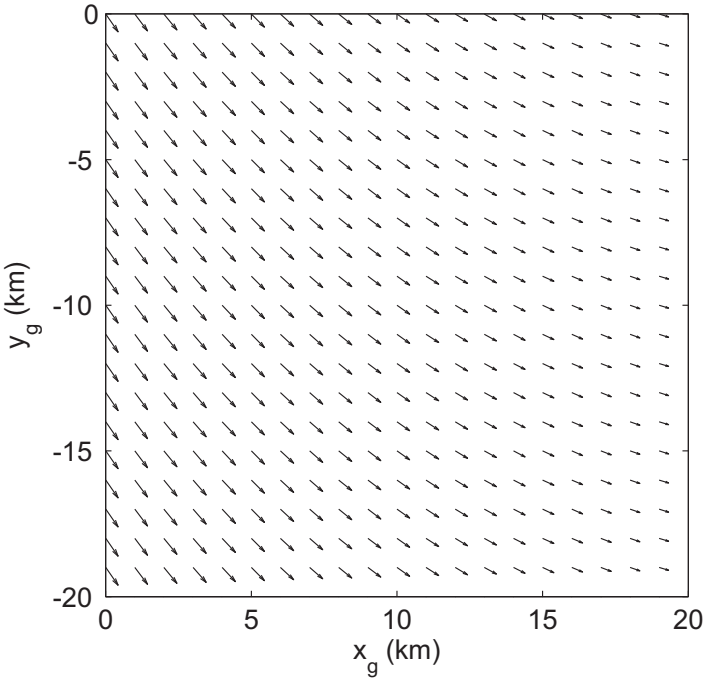

(a)

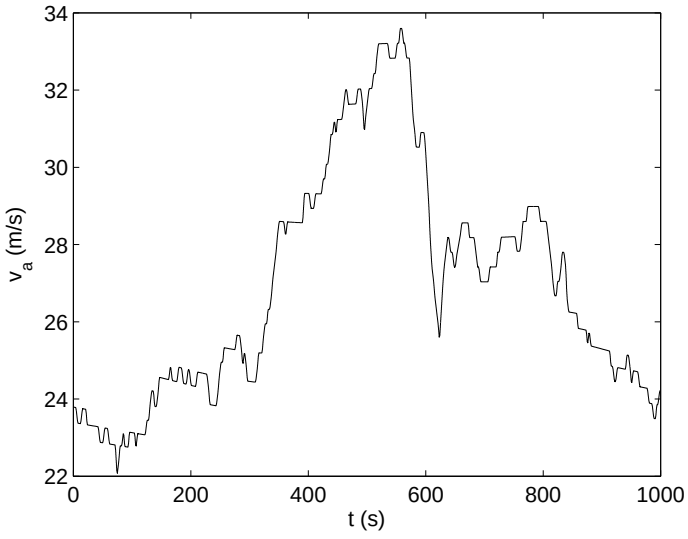

(b)

Figure 6.1 (a) Vector wind field and (b) airspeed for the simulated flights.

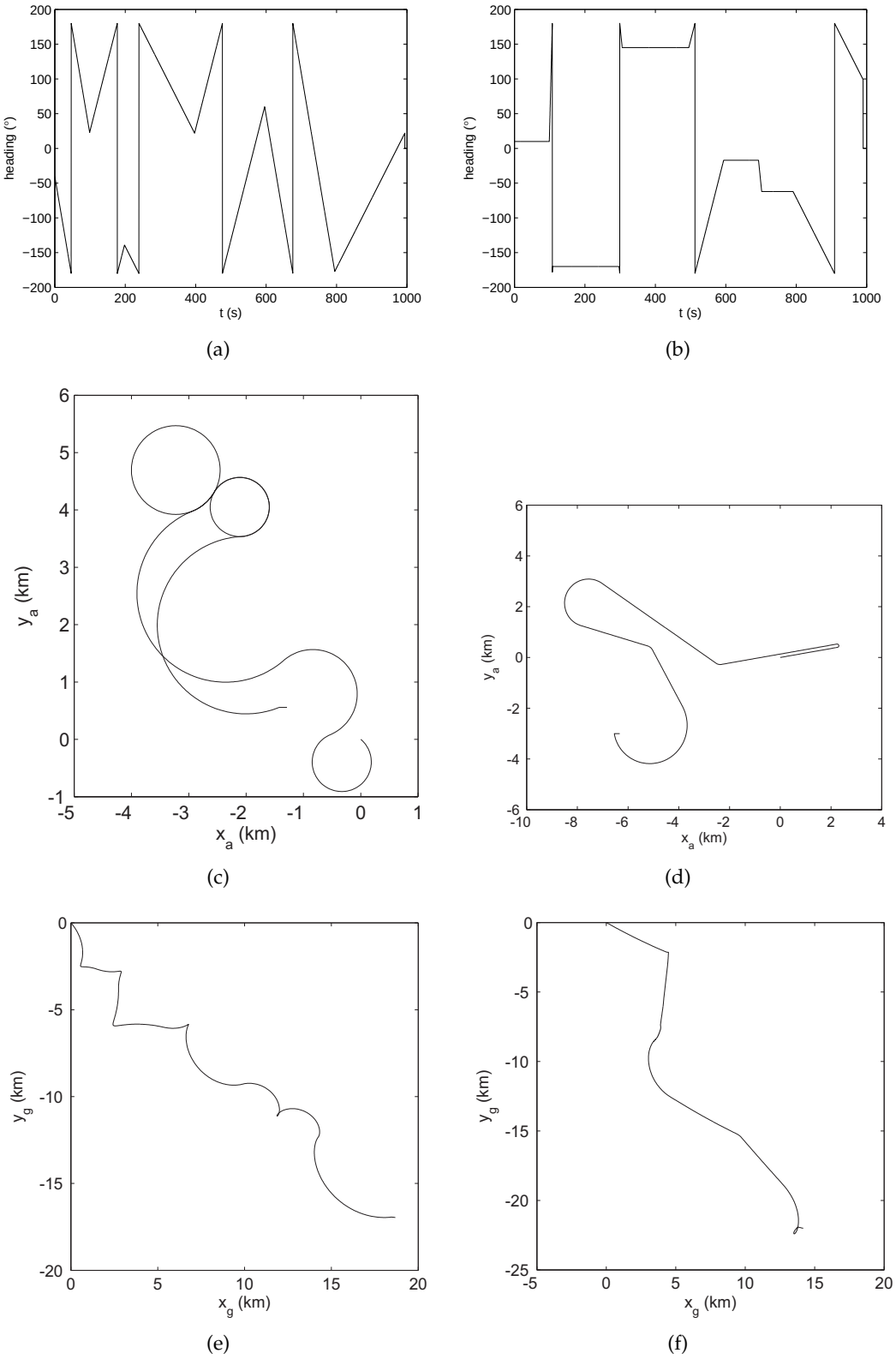

Figure 6.2 Heading versus time of Simulated Flight 1 (a) and 2 (b), flight path relative to the air of flight 1 (c) and 2 (d), and flight path relative to the ground of flight 1 (e) and 2 (f).

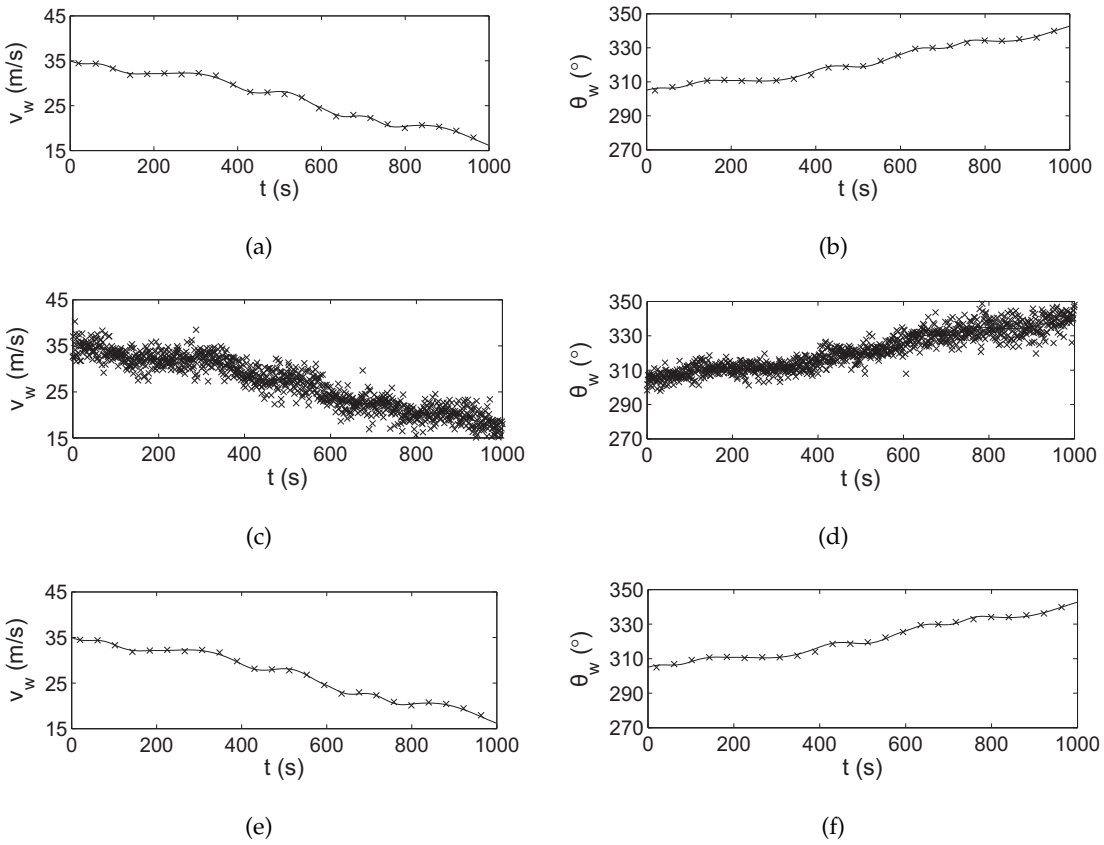

Figure 6.3 Simulated Flight 1: (a) Wind speed and (b) direction estimated from the ground velocity, airspeed and heading data (crosses), and (c) wind speed and (d) direction calculated directly from the data (crosses), and (e) wind speed and (f) wind direction calculated directly from the data and averaged over a time window (crosses). The true values are shown by the solid lines.

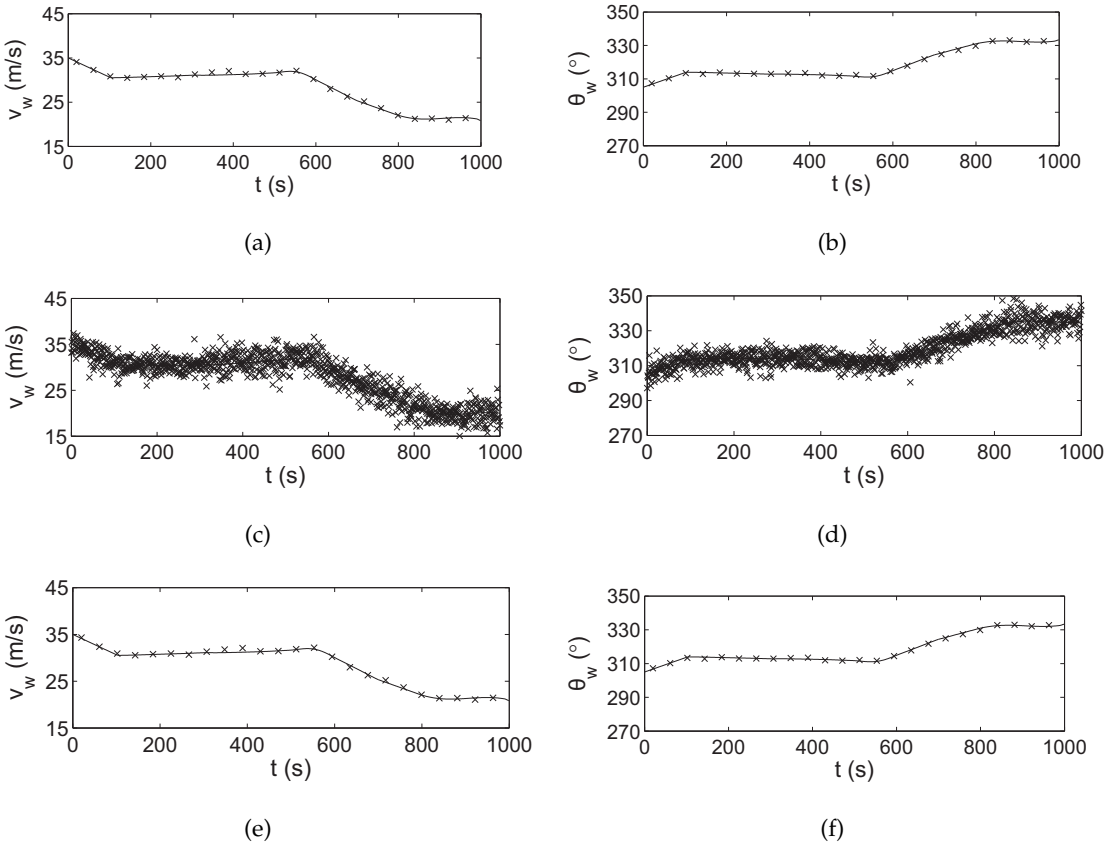

Figure 6.4 Simulated Flight 2: (a) Wind speed and (b) direction estimated from the ground velocity, airspeed and heading data (crosses), and (c) wind speed and (d) direction calculated directly from the data (crosses), and (e) wind speed and (f) wind direction calculated directly from the data and averaged over a time window (crosses). The true values are shown by the solid lines.

6.4 Position and airspeed data

6.4.1 Methods

Although sailplanes always have an airspeed indicator and a compass, data from the latter are usually not logged as described previously. In this section, the case of data consisting of ground velocity and airspeed is considered. As described in Chapters 2 and 4, at a single time step this data provides a one-parameter family of solutions for the wind velocity, although for data at multiple time steps with a constant wind velocity the ambiguity is resolved if the heading of data used for an estimate are sufficiently different. The estimates are more stable for larger heading differences. As shown in Section 2.2.2, the dependence on heading difference translates into differences in ground velocity. The data vector in this case is denoted

$$(\tilde{\mathbf{v}}_{g,i}, \tilde{\mathbf{v}}_{a,i}) = (\tilde{v}_{g,i-N}, \tilde{v}_{a,i-N}, ..., \tilde{v}_{g,i+N}, \tilde{v}_{a,i+N})\,. \tag{6.9}$$

The data-to-parameter ratio is now $3(2N+1)/[2(2N+1)+2] \approx 1.5$ and the problem is over-determined. Using the assumption of Gaussian noise, the likelihood function is

$$\begin{aligned} p\left(\tilde{\mathbf{v}}_{g,i}, \tilde{\mathbf{v}}_{a,i} | \mathbf{v}_{g,i}, v_{w,i}\right) = K_2 \prod_j \exp\Big(&- ||\tilde{v}_{g,i+j} - v_{g,i+j}||^2/2\sigma_g^2 \\ &- (\tilde{v}_{a,i+j} - ||v_{g,i+j} - v_{w,i}||)^2/2\sigma_a^2\Big), \end{aligned} \tag{6.10}$$

where K_2 is a constant. The ML estimate is then

$$(\hat{\mathbf{v}}_{g,i}, \hat{v}_{w,i})_{a,ML} = \underset{(\mathbf{v}_{g,i}, v_{w,i})}{\operatorname{argmax}} \left\{ p\left(\tilde{\mathbf{v}}_{g,i}, \tilde{\mathbf{v}}_{a,i} | \mathbf{v}_{g,i}, v_{w,i}\right) \right\}, \tag{6.11}$$

where the subscript a on the LHS indicates "airspeed data only."

6.4.2 Simulation results

Using the same two simulated flight in Section 6.3.2 with no heading data, and the data were corrupted by noise as described. The ML estimates of the wind velocity were calculated as described above using the known values of the noise variances and $N = 20$ and the same starting values as in Section 6.3.

The estimated wind speed and direction for Flight 1 are shown in Fig. 6.5(a) and (b) respectively. The rms errors in the estimated wind speed and direction are $1.2\ \mathrm{m/s}$ and $2.1°$. The estimated values are quite consistent with the true values, as the heading differences in this flight are sufficiently large for obtaining good estimates.

For Flight 2 the results are shown in Fig. 6.6(a) and (b) respectively. In this case the estimates track the true values some of the time but drift off at other times. The rms errors in the estimated wind speed and direction $6.2\ \mathrm{m/s}$ and $38°$. A plot of the rate of change of heading (Fig. 6.6(c)) shows that the errors occur when the heading is constant or slowly-

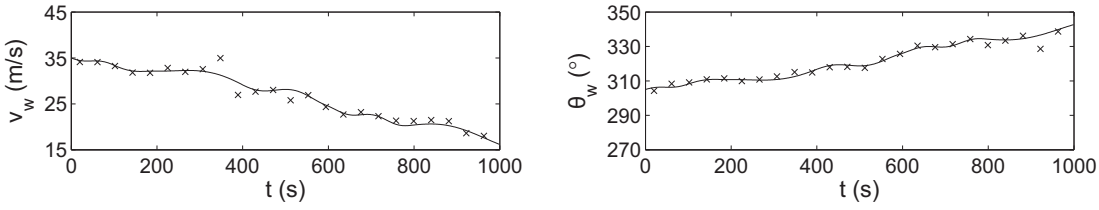

(a) (b)

Figure 6.5 Simulated Flight 1: (a) Wind speed and (b) direction (crosses) estimated from the ground velocity and airspeed data, and the true wind speed and direction (solid lines).

changing as anticipated from Section 2.2.2. Inspection of Fig. 6.6 shows that the estimates drift off the true values when the heading is constant, and converge back to the true values at $t = 100, 300, 500, 700, 800$ s when the sailplane turns.

The instability due to an ambiguity at small heading angle differences is illustrated by plotting the likelihood functions. Two flight segments from the simulated flight were chosen as shown in Fig. 6.7. Flight segment A is almost straight and has small heading differences, and flight segment B is in a turn has large heading differences. 2-D slices of the multi-dimensional log likelihood functions for the x and y components of the wind velocity at the correct values of the other parameters are shown in Fig. 6.8. Fig. 6.8(a) and (b) show a superposition of the individual factors of the likelihood functions for time-steps $i - 10$, i, and $i + 10$, for flight segment A and B, respectively. The corresponding full likelihoods are shown in Fig. 6.8(c) and (d). For large changes in the heading (Fig. 6.8(b) and (d)), the circles corresponding to the individual factors are distinct and the mutual overlap in a single region gives a likelihood function that, although multi-modal, has two well-defined global maxima. Measurement noise can, in some cases, produce a higher value for the secondary maximum causing the estimate to drift to the incorrect maximum. The error corrects once the heading changes. However for small changes in the heading (Fig. 6.8(a) and (c)), the circles are similar, giving a broad maximum in the likelihood function.

To investigate the effect of changing the parameter σ_g, it was increased to 10 m/s with the other parameters values unchanged, the optimisation repeated for Simulated Flight 2, and the results are shown in Fig. 6.9(a) and (b). The estimates are significantly improved and rms errors are 2.3 m/s and $6.7°$. In particular, the large errors at the flight sections with constant heading are improved significantly. Increasing σ_g presumably reduces the dependency of the estimates on the ground velocity data, hence when there is an ambiguity due to a constant heading, the wind velocity estimates are driven more by the starting values at time-step $i + 1$ being the estimated values at time-step i, so the estimates do not tend to drift off as rapidly. Results obtained when increasing σ_a to 10 m/s are shown in (c) and (d). There is no overall improvement in this case with rms errors of 5.4 m/s and $79°$, suggesting that the airspeed data are more important than the ground velocity data in this case. Note that some of the wind direction estimates are so large that they lie outside the range of the figure.

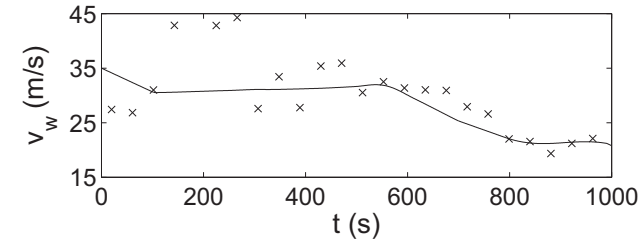

(a)

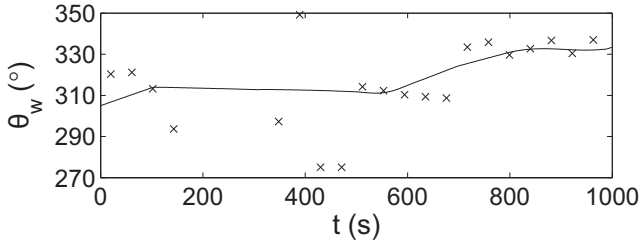

(b)

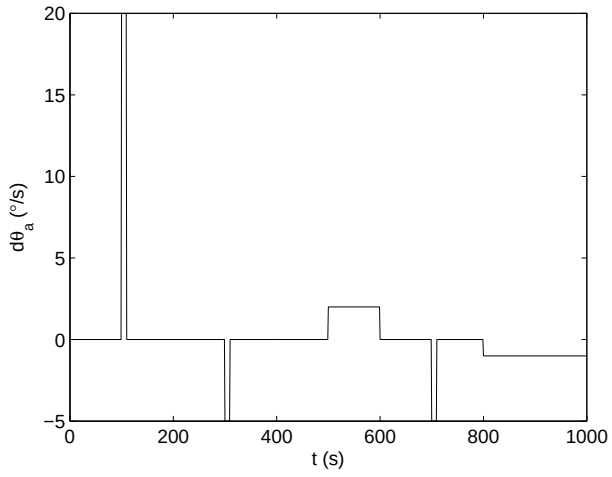

(c)

Figure 6.6 Simulated Flight 2: (a) Wind speed and (b) direction (crosses) estimated from the ground velocity and airspeed data, and the true wind speed and direction (solid lines). (c) Heading differences versus time.

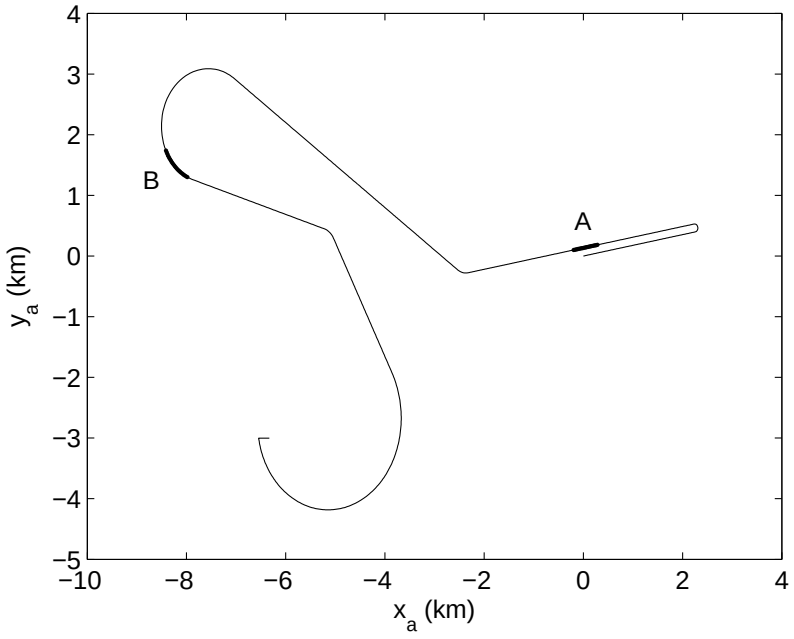

Figure 6.7 Air path showing two flight segments selected with small (A) and large (B) ground curvatures indicated in circles and crosses respectively.

6.4.3 Experimental results

The ML estimator was applied to the data from Flight 1 (Section 3.2), using the position and airspeed data and $N = 40$ s (i.e. time window length 81 s), $\sigma_g = 2$ m/s, $\sigma_a = 2$ m/s, $\sigma_{\theta_a} = 2^\circ$ to estimate the wind velocities. The wind speed and direction estimates are shown in Fig. 6.10, and compared with those obtained using the heuristic method (Chapter 4) as shown in Section 4.3.1. There is good agreement between the two methods with rms differences of 2.2 m/s and 6.2°, showing the utility of the ML approach.

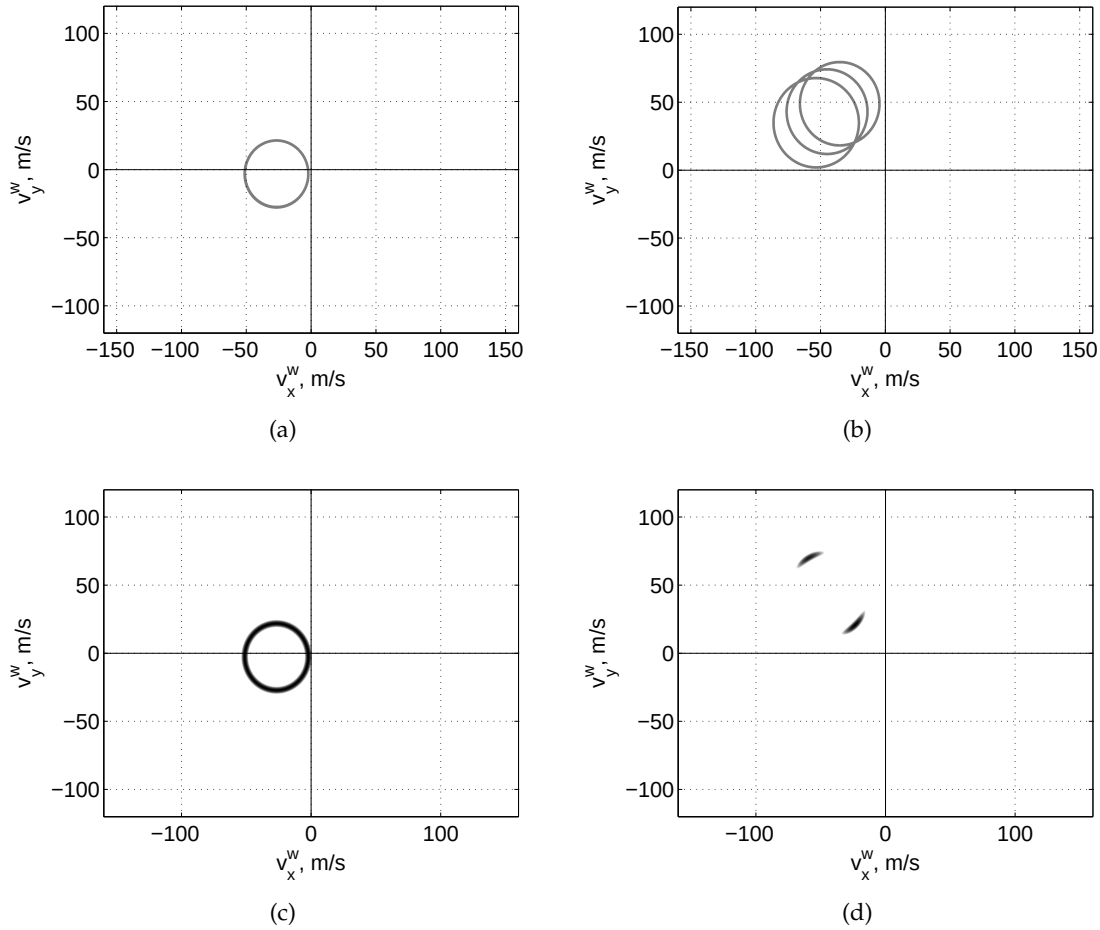

Figure 6.8 Log-likelihood functions using position and airspeed data only for well and ill-determined solutions. Three factors of the likelihood function are shown in (a) and (b), where the gray region represents the mean ± 2 m/s standard deviations. The full likelihood is shown in (c) and (d), where the gray level represents the log likelihood. The regions of the path used for the ill (a,c) and well-determined (b,d) estimates are the segments A and B shown in Fig. 6.7.

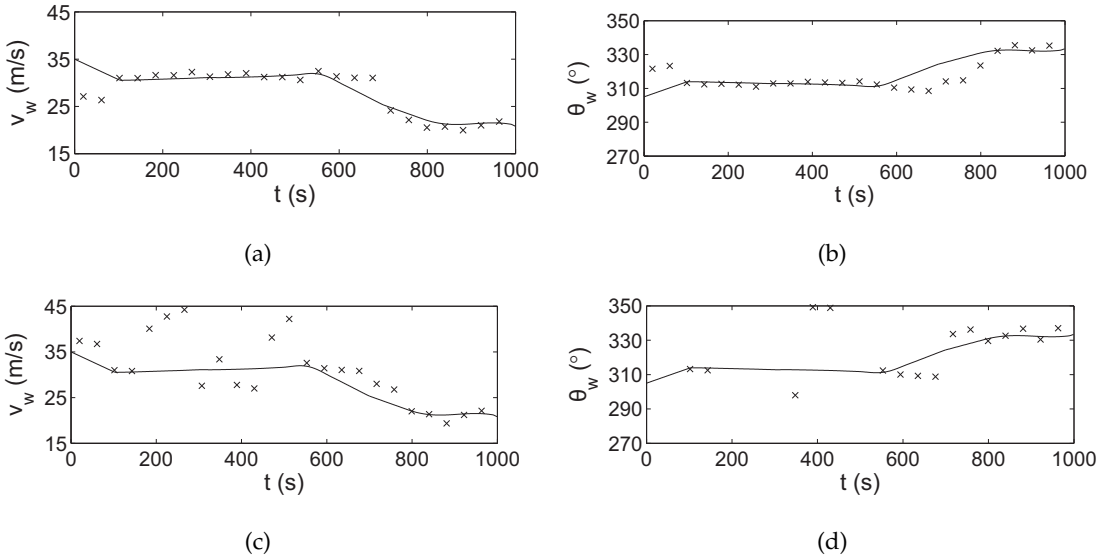

Figure 6.9 Simulated Flight 2: Wind speed and direction estimated from the ground velocity and airspeed data (crosses) and the true wind speed and direction (solid lines), (a)(b) using $\sigma_g = 10\ \mathrm{m/s}$, and (c)(d) using $\sigma_a = 10\ \mathrm{m/s}$.

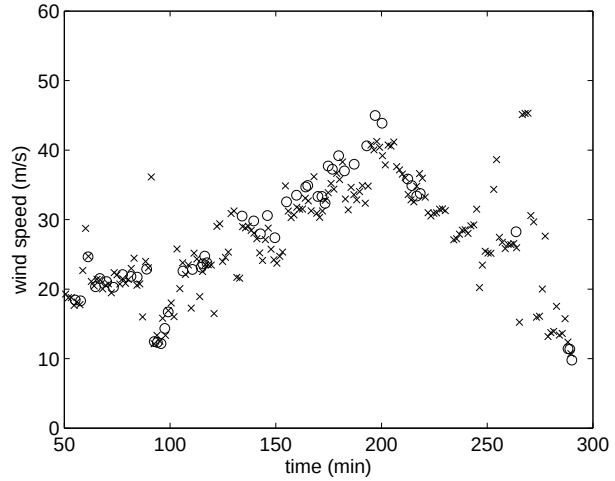

(a)

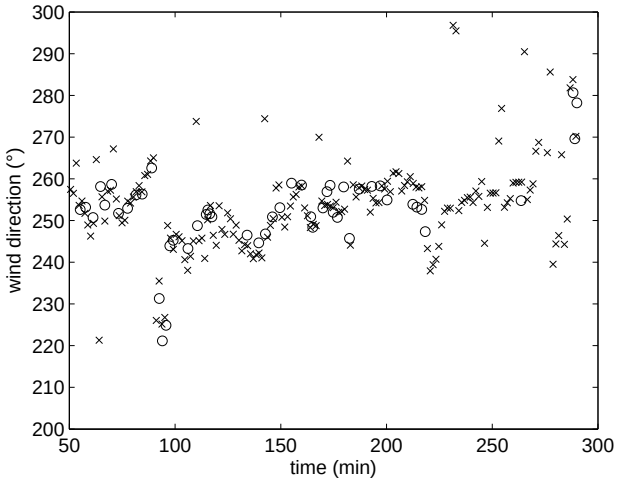

(b)

Figure 6.10 Wind speed and direction estimated from position and airspeed data for Flight 1 using the ML estimator (crosses) and the heuristic method of Chapter 4 (circles).

6.5 Position and heading data

6.5.1 Method

Consider now the case when airspeed data is not available but the heading is measured, in addition to the ground velocity. The data vector is now

$$(\tilde{\mathbf{v}}_{g,i}, \tilde{\boldsymbol{\theta}}_{a,i}) = \left(\tilde{v}_{g,i-N}, \tilde{\theta}_{a,i-N}, ..., \tilde{v}_{g,i+N}, \tilde{\theta}_{a,i+N}\right). \tag{6.12}$$

The data-to-parameter ratio is 1.5 as in the previous case. As described in Chapter 2, for a single time-step the solution is a one parameter family that lies on a line. For multiple data in a constant wind field, the solution lies on the intersection of two lines, giving a unique solution for different headings with no noise. The likelihood function is now

$$\begin{aligned} p\left(\tilde{\mathbf{v}}_{g,i}, \tilde{\boldsymbol{\theta}}_{a,i} | \mathbf{v}_{g,i}, v_{w,i}\right) = & K_3 \prod_j \exp\Big(- ||\tilde{v}_{g,i+j} - v_{g,i+j}||^2 / 2\sigma_g^2 \\ & - [\tilde{\theta}_{a,i+j} - \tan^{-1}(v_{g,i+j} - v_{w,i})]^2 / 2\sigma_{\theta_a}^2 \Big), \end{aligned} \tag{6.13}$$

where K_3 is a constant. The ML estimate is then

$$(\hat{\mathbf{v}}_{g,i}, \hat{v}_{w,i})_{h,ML} = \underset{(\mathbf{v}_{g,i}, v_{w,i})}{\operatorname{argmax}} \left\{ p\left(\tilde{\mathbf{v}}_{g,i}, \tilde{\boldsymbol{\theta}}_{a,i} | \mathbf{v}_{g,i}, v_{w,i}\right) \right\}, \tag{6.14}$$

where the subscript h on the LHS indicates "heading data only."

6.5.2 Simulation results

For the same two simulated flights described in the previous sections with no airspeed data, the ML estimates of the wind velocity were calculated as described above using the known values of the noise variances and $N = 20$. The results for Flight 1 are shown in Fig. 6.11(a) and (b). The estimates closely match the true values and the average rms errors are 0.50 m/s and $1.6°$.

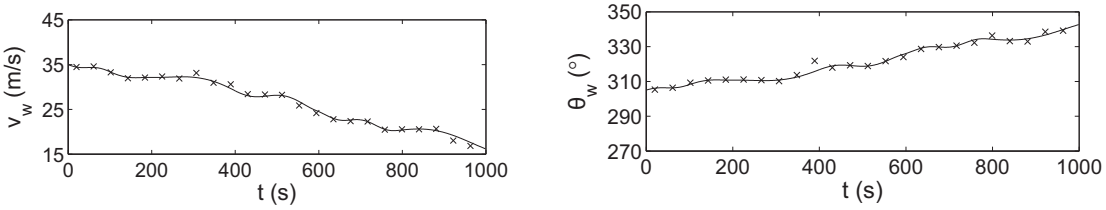

(a) (b)

Figure 6.11 Simulated Flight 1: (a) Wind speed and (b) direction estimated from ground velocity and heading data (crosses), and the true wind speed and direction (solid lines).

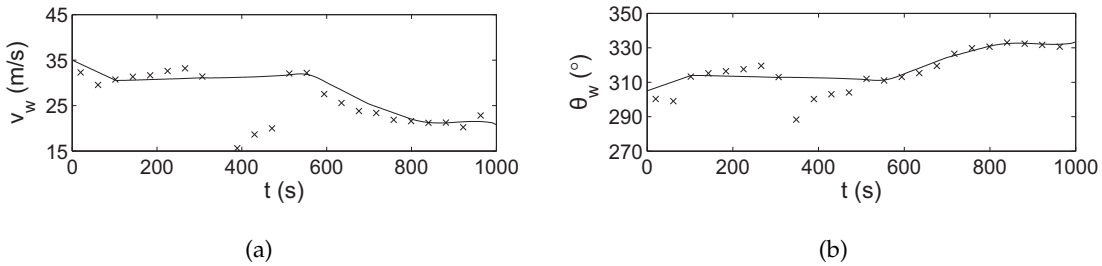

(a) (b)

Figure 6.12 Simulated Flight 2: (a) Wind speed and (b) direction estimated from ground velocity and heading data (crosses), and the true wind speed and direction (solid lines).

For Flight 2 the results are shown in Fig. 6.12(a) and (b). As with the case for position and airspeed data, the results are not as good for this flight as a result of the regions with constant heading. This is evident where the estimates diverge near $i = 400$. The rms errors in the estimated wind speed and direction 6.4 m/s and $7.0°$, respectively, which is particularly large for the airspeed.

Using data from flight segments A and B in Fig. 6.7, the individual likelihood functions for $i - 10$, i, and $i + 10$ are shown in Fig. 6.13(a) and (b), respectively. The full likelihood functions are shown in Fig. 6.13 (c) and (d). Inspection of the figure shows a single well-defined maximum for the case B of large changes in heading, whereas for small changes in heading (case A) the maximum of the likelihood function occurs on a long, narrow ridge. The presence of noise can shift the peak along this ridge, lending to estimates that drift along the ridge.

The effect of increasing σ_g to 10 m/s is shown in Fig. 6.14. The estimates for the flight segments with constant heading are improved significantly (rms errors of 2.4 m/s and $3.8°$), for the same reasons as described in the previous section. The effect of increasing σ_{θ_a} to $5°$ is shown in (c) and (d). The results are quite unstable and most of the wind speed estimates are far off the true values (outside the range shown in the figure), showing the importance of the heading data.

6.5.3 Experimental results

The ML estimator was applied to data from Flight 1 (Section 3.2). The heading data were derived from the wind velocity estimated using the heuristic method, and interpolated onto the flight time. Gaussian noise with a standard deviation of $2°$ was added to the headings. The parameters used were $N = 40$, $\sigma_g = 2$ m/s, and $\sigma_{\theta_a} = 2°$. The results are shown in Fig. 6.15(a) and (b), and compared with those obtained using the heuristic method that uses ground velocities and airspeed data. The results show reasonably good agreement between the two methods, with rms errors of 2.7 m/s and 5.0°, given that the heading data as calculated has limited accuracy.

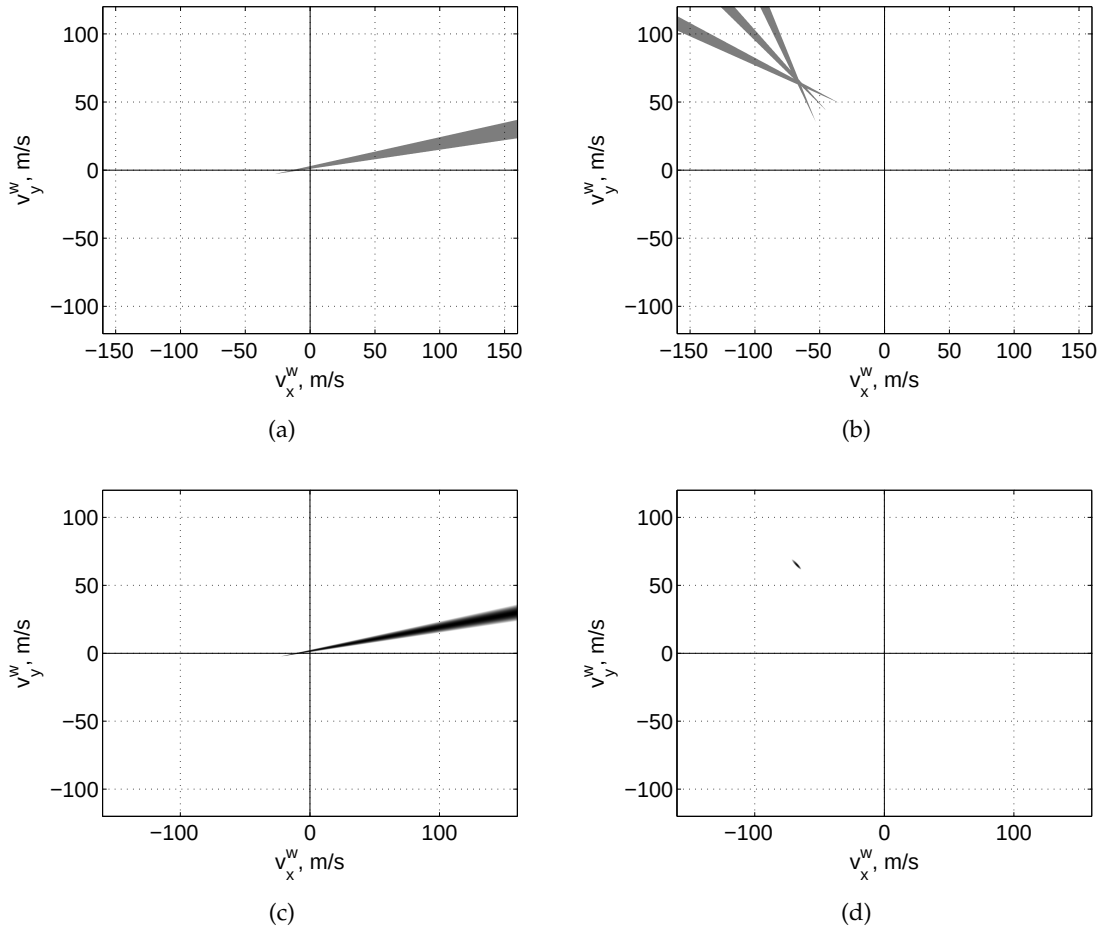

Figure 6.13 Log-likelihood functions using position and heading only for well and ill-determined solutions. Three factors of the likelihood function are shown in (a) and (b), where the gray region represents the mean $\pm 2^\circ$ standard deviations. The full likelihood is shown in (c) and (d), where the gray level represents the log likelihood. The regions of the path used for the well-(a,c) and ill-determined (b,d) estimates are shown in Fig. 6.7.

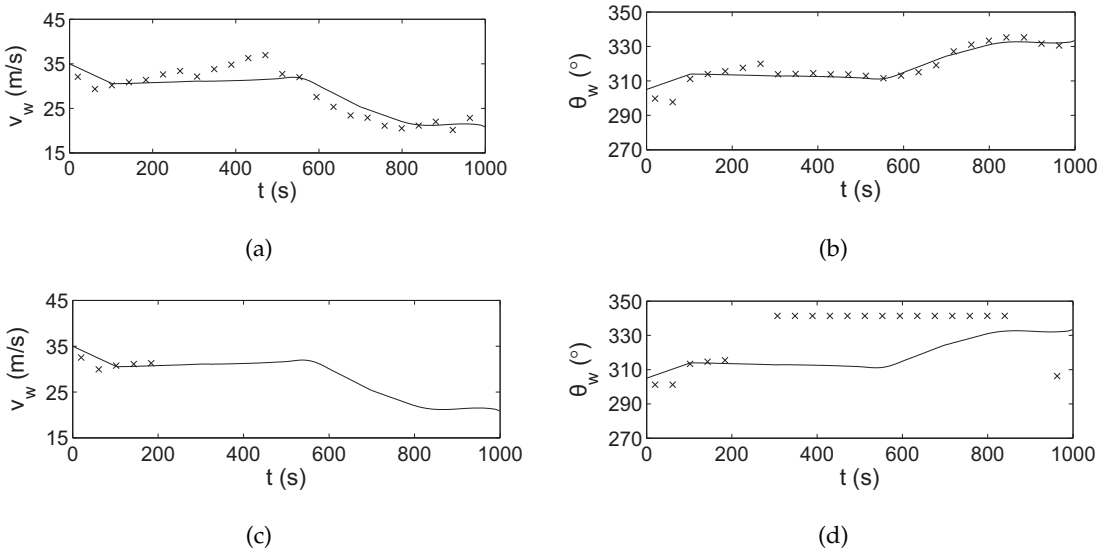

Figure 6.14 Simulated Flight 2: Wind speed and direction estimated from the ground velocity and heading data (crosses) and the true wind speed and direction (solid lines), (a)(b) using $\sigma_g = 10\ \mathrm{m/s}$, and (c)(d) using $\sigma_{\theta_a} = 5°$.

6.6 Discussion

In summary, ML estimation provides a more formally-based method for estimating the wind velocities than that described in Chapter 4. It allows incorporation of different kinds of data as well as noise models. The results show that ML estimation is effective when the problem is overdetermined.

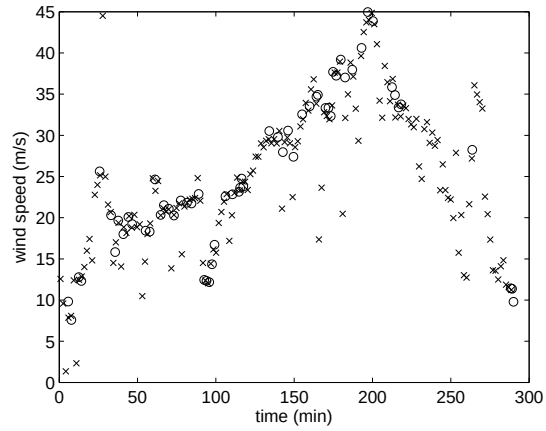

(a)

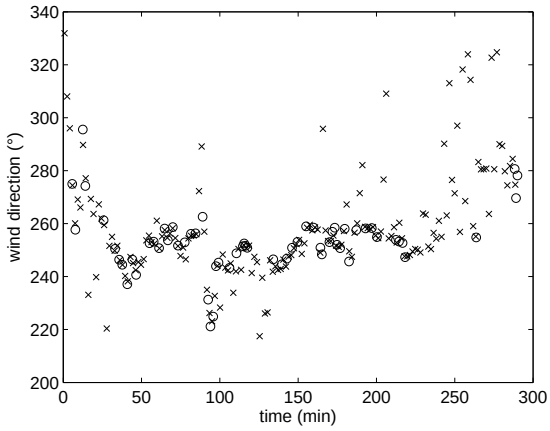

(b)

Figure 6.15 (a) Wind Speed and (b) direction estimates calculated from ground velocity and derived heading data (derived as discussed in the text) for Flight 1 using the ML estimator (crosses), and those obtained using the heuristic method (circles) as described in Chapter 4.

Chapter 7

Maximum a posteriori Estimation

7.1 Introduction

As described previously, the instrumentation installed in most sailplanes records only the GPS position during a flight so that only the ground velocity is measured. Therefore, a method to estimate wind velocities from this data would be applicable to a wider variety of flights than would the methods described previously that use airspeed or heading. This is the problem addressed in this chapter. The problem is highly underdetermined and the approach taken is to solve the problem by using a variety of prior information and Maximum *a posteriori* (MAP) estimation. The methods are applied to simulated and actual flight data.

Determination of the wind velocity in this case is highly underdetermined and, as described in Section 2.2.4 there is a two-parameter family of solutions. However, in the case of a sailplane flying in mountain wave there is considerable *a priori* information that can be used to constrain the solution. As described previously, the wind field in high-altitude mountain wave varies slowly over the flight path. Furthermore, there are also constraints on the sailplane air velocity. The range of possible values of the airspeed is limited and a typical distribution of airspeeds can be estimated. Also the turn rate (the rate of change of heading) of the sailplane has an upper bound and also a typical distribution. MAP estimators for the wind velocity are developed here using ground velocity data and these kinds of prior information.

The sailplane flight logger records GPS position at regular intervals and these are used to calculate the ground velocity at each time-step by central differences as described previously. Two kinds of prior information are considered, one concerning the sailplane flight dynamics and the other concerning the wind field.

The velocity of the sailplane through the air can be parameterised by its airspeed and heading. Neither of these parameters are completely unconstrained. The airspeed must be be-

tween the stall speed and the maximum allowable speed of the aircraft, and these speeds will be known for a particular sailplane. Furthermore, in a wave flight much of the flight will be flown at, or close to, the minimum sink airspeed (while climbing), and much of the remainder of the flight will be flown close to the maximum maneuvering airspeed (between climbs). These speeds will also be known. Therefore, it is possible, at least in principle, to build up a reasonably faithful prior density for the airspeed, based on previous flight behavior. Such prior densities are described in Section 7.2.

There is a maximum rate at which a sailplane turns during normal flight. Typically, a maximum turn rate would be about one turn in 10 seconds so that the maximum rate of change of heading is limited to about 40°/sec. This is an extreme case however, and corresponds to a steep (or high-bank or tight) turn. Although sailplane pilots perform steep turns, and they may be common in thermal flights, they are infrequent once a sailplane is established in a wave system. During a wave flight, the turn rate is very low during much of the flight while the sailplane is climbing, and is larger while the pilot is maneuvering between climbs. Overall, the average rate of change of heading during a wave flight will be very small. Appropriate prior distributions for the rate of change of heading are described in Section 7.3.

The methods described in previous chapters are based on an assumption of a constant wind velocity within an appropriate temporal or spatial region. An important advantage of the Bayesian approach is that more flexible constraints can be applied to the wind velocity. For fixed meteorological conditions, an atmospheric mountain wave structure (the spatial distribution of wind velocities) is fixed relative to the terrain. In high-altitude mountain waves (above the effects of the terrain or about 5000 m altitude), the wind velocity varies slowly with horizontal position (the variation with altitude can be more rapid - see below). For example, we would expect the horizontal component of the wind velocity to vary by no more than about 10% over distances of the order of $10\ \mathrm{km}$. Furthermore, the meteorological conditions tend to vary slowly with time, and the overall wind field structure is often fairly stable over periods of about 30 minutes. Typical wind speeds in mountain waves are 10 - 50 $\mathrm{m/s}$ and typical sailplane airspeeds 25 - 50 $\mathrm{m/s}$, so that ground speeds vary between 0 and 100 $\mathrm{m/s}$. On average then, the sailplane would cover approximately 100 km in 30 minutes. Therefore, temporal changes in the wind velocity experienced by sailplane tend to be dominated by the effect of its changes in position rather than by the temporal change in the wind field itself.

The variation of horizontal wind velocity with altitude is usually more rapid than its variation with horizontal position. In fact, as seen in Section 1.2, the development of lee waves usually requires an increase of wind speed with altitude. Above the terrain height, or above about 5000 m (where the terrain can cause rapid spatial variations in wind velocities), the horizontal wind speed can easily change by $5\ \mathrm{m/s}$ for a 1 km change in altitude. Changes in wind direction with altitude tend to be more modest, typically up to about 5°/km.

In summary then, the wind velocity can be constrained such that it does not vary too

Table 7.1 Flight speeds from the DG505M flight manual [53].

wing loading (kg/m^2)	stall speed (m/s)	minimum sink speed (m/s)	best L/D speed (m/s)	rough air speed (m/s)	never exceed speed (m/s)
35	19	21	35	197	270
40	20	22	38	211	290
45	21	24	36	223	306

rapidly in space. Prior distributions to reflect this constraint are described in Section 7.3.

7.2 Prior models for sailplane air velocity

The MAP estimators described in the next section makes use of prior distributions for the air velocity. The air velocity is resolved into the airspeed and heading for this purpose. As described in Section 7.1, there are constraints on both the airspeed and the rate of change of heading. Prior models for these quantities are developed in this section, based on flight data. Consider first the airspeed. The airspeed must be within the limits of the particular sailplane (stall speed and never-exceed speed), but of more significance is typical speeds flown during a wave flight. This will typically be close to, or slightly above, the minimum sink airspeed (while climbing) for much of the flight, and most of the remainder of the flight will be flown close to the maximum maneuvering airspeed (between climbs). These speeds will be known for a particular sailplane and are listed in Table 7.1 for the DG505M. The idea then is to build up a reasonably faithful prior density for the airspeed, based on previous flight behavior. Since the relevant aerodynamic quantity is the IAS, the prior distribution must be on the IAS and this converted to TAS as needed.

The IAS above the tow release altitude for the four flights described in Chapter 3 was put into airspeed bins of width $2\ \mathrm{m/s}$ and the resulting histograms are shown in Fig. 7.1. Comparison of these histograms show considerable consistency between these different flights. This is good evidence that a reliable prior distribution can be developed. The histograms of the four flights all show positive skewness with a long tail on the right. Various exponential distributions were tried and it was observed that the data is best modeled by the extreme value distribution [84] with a density function given by

$$g_{\mu,\sigma}(x) = \exp\left(\frac{x-\mu}{\sigma}\right)\exp\left(-\exp\left(\frac{x-\mu}{\sigma}\right)\right), \tag{7.1}$$

where μ and σ are the location and scale parameters of the distribution, respectively. This equation models a negative skewed distribution, and for a positive skewed distribution $-x$ and $-\mu$ are used, giving a mirror image of the negative skewed distribution about the x-

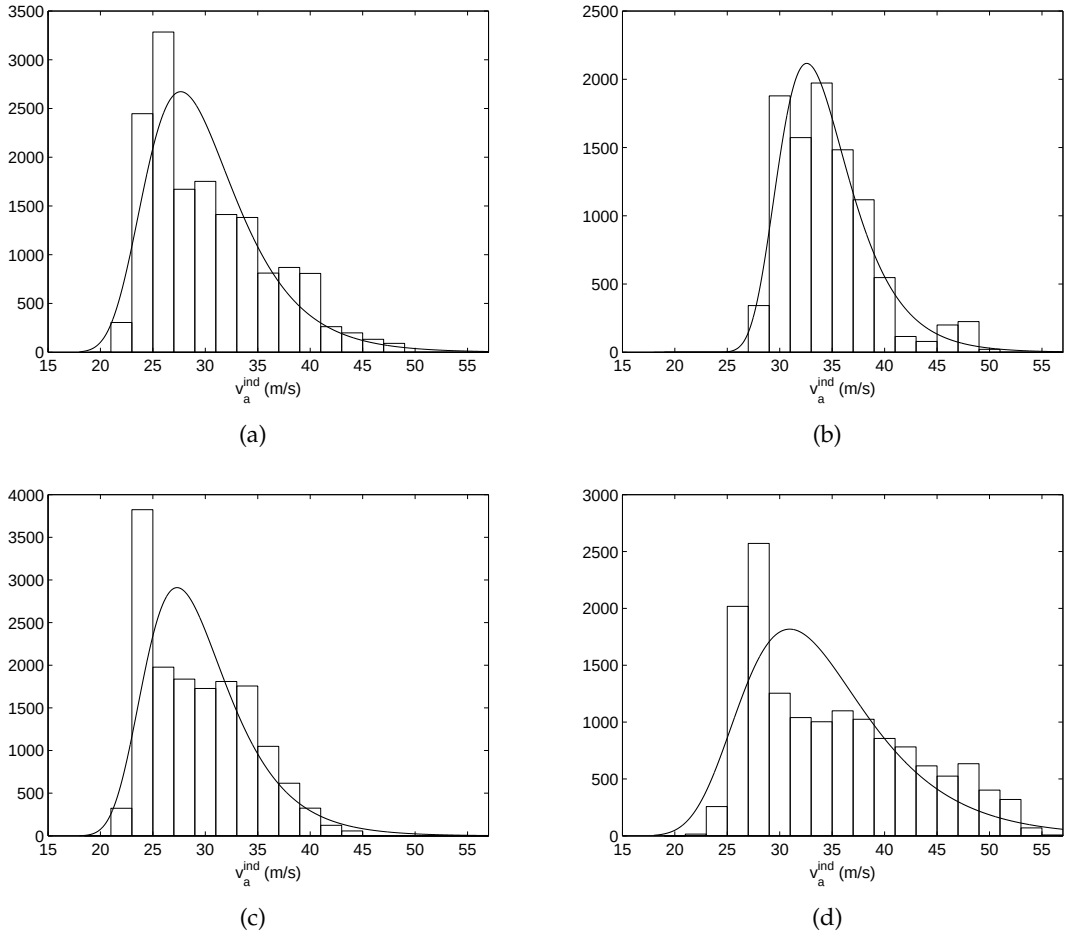

Figure 7.1 Histograms of indicated airspeeds, and the fitted densities as described in the text for (a) Fight 1, (b) Flight 2, (c) Flight 3, and (d) Flight 4.

axis. The extreme value distribution is commonly used for modeling continuous variables with skewness. The model was fitted to the histograms using maximum likelihood as shown in Fig. 7.1 and the resulting parameters μ and σ are listed in Table 7.2. The results show a reasonably consistent distribution for this sailplane and these flights that can be used as an airspeed prior distribution.

The TAS, rather than the IAS, is used at the estimation stage. Therefore, at a particular altitude, the IAS prior must be converted to a TAS prior in order to be applied. This is done as follow. Referring to Section 3.6, TAS is related to the IAS by

$$v_a = v_a^{ind} h(z), \tag{7.2}$$

where $h(z)$ is given in (1.90). Denoting the density of v_a^{ind} by $f^{ind}(v_a^{ind})$ and the density of v_a by $f(v_a)$, the two are related by [85]

$$f(v_a) = \frac{f^{ind}(v_a^{ind})}{h(z)}. \tag{7.3}$$

Table 7.2 Estimated parameters of the extreme value distribution fitted to the Perlan Flight IAS data, and the Gaussian distribution fitted to the heading rate of change data.

Flight	μ_a (m/s)	σ_a (m/s)	$\sigma_h(^\circ/s)$
1	-27.7	4.2	0.83
2	-32.6	3.3	0.44
3	-27.2	3.8	0.75
4	-31.0	5.9	1.1

Substituting from (7.2) into (7.3) gives

$$\begin{aligned} f(v_a) &= \sigma^{-1}h^{-1}(z)\exp\left(\frac{v_a^{ind}/h(z)-\mu}{\sigma}\right)\exp\left(-\exp\left(\frac{v_a^{ind}/h(z)-\mu}{\sigma}\right)\right) \\ &= g_{\mu',\sigma'}(v_a), \end{aligned} \tag{7.4}$$

where $\mu' = \mu h(z)$ and $\sigma' = \sigma h(z)$.

Consider now the sailplane heading. The rate of change of heading was calculated for the four flights by taking the central difference over a time window of 9 s, and put into bins of width 0.5°/s, and the histograms are plotted in Fig. 7.2. The distribution of the rate of change of heading is expected to be, zero-mean, symmetric and narrow. Zero-mean Gaussian distributions of the form

$$f(h) = \frac{1}{\sqrt{2\pi}\sigma_h}\exp\left(-h^2/2\sigma_h^2\right), \tag{7.5}$$

where h denotes the rate of change of heading, were fitted to the histograms and good fits were obtained as shown in Fig. 7.2. The resulting standard deviations σ_h are listed in Table 7.2. The standard deviations are small as expected.

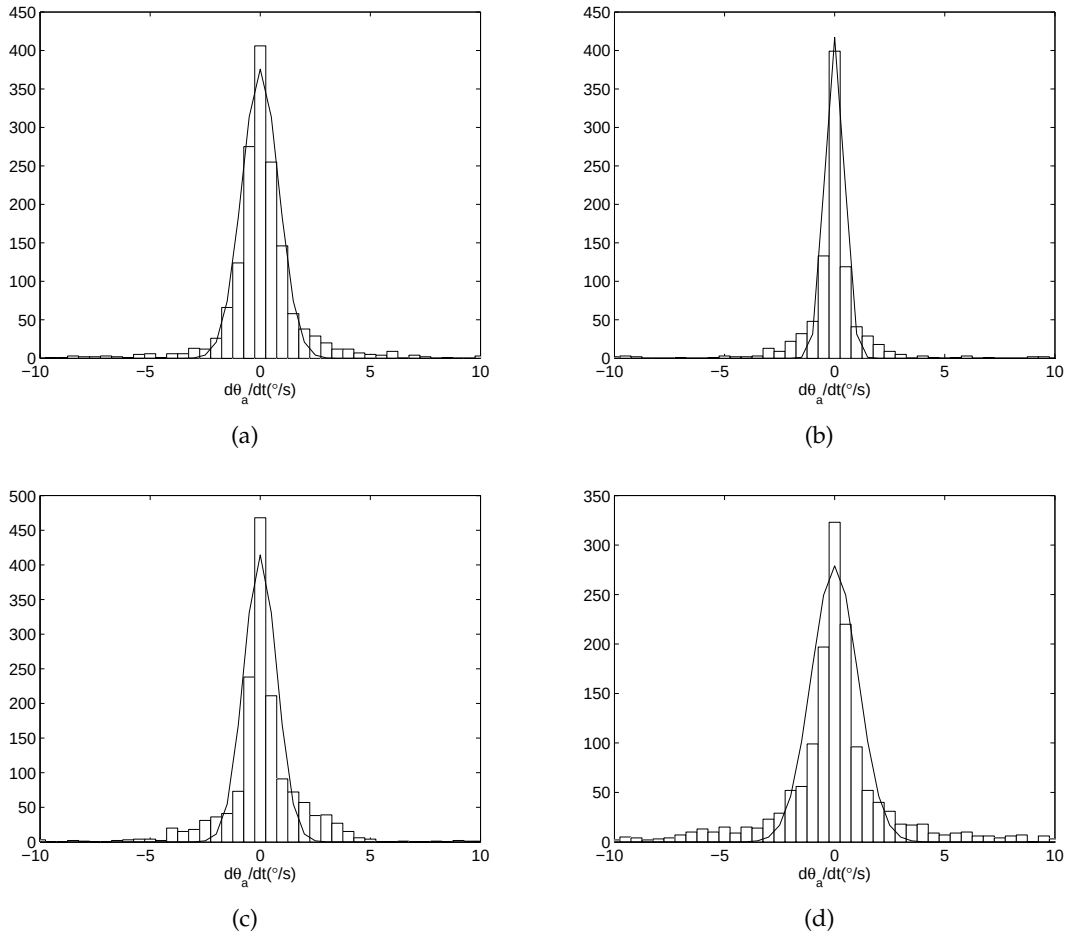

Figure 7.2 Histograms of the rate of change in heading measured for (a) Fight 1, (b) Flight 2, (c) Flight 3, and (d) Flight 4, and the fitted Gaussian densities as described in the text.

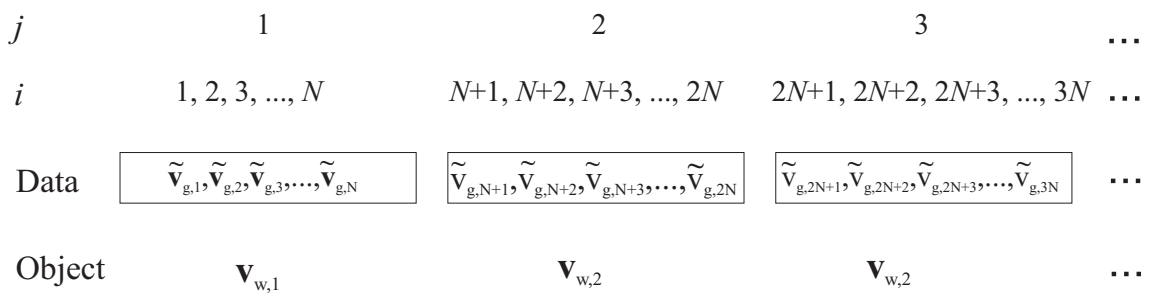

Figure 7.3 Illustration of the temporal region method.

7.3 Maximum a posteriori estimator

MAP estimators for the wind velocity are developed here that use ground velocity data and priors for the air velocity and wind velocity. The wind velocity estimates are made at positions along the flight path. Equation (2.2) applies at each time-step, but at a typical sampling rate of 1 Hz, corresponding on average to a distance of about $0-50$ m, estimation of the wind velocity at each time-step is not appropriate. Therefore, the time-steps are grouped into regions and a single wind velocity estimate is made in each region. Two different methods are used to define the regions. In the first method, each region is defined by a fixed number, N, of consecutive time-steps. Each region then corresponds to a fixed temporal length. This is illustrated in Fig. 7.3, and is referred to as the 'temporal region' method. The second method is based on distance rather than time. One steps along the flight path in steps of distance $2r_0$, where r_0 is a fixed parameter, and draws a cylinder of radius of r_0 and height of h_0, where h_0 is also a fixed parameter, centered at each step. Each cylinder, and the data points within it, then define a region. This is called the 'spatial region' method, as illustrated in Fig. 7.4. For convenience, the partition of the flight is shown in 2D in Fig. 7.4. This is similar to the partitioning of the flight region described in Chapter 4. Since it has been assumed that the important wind velocity constraint is in terms of space rather than time, the second method is expected to be more suitable than the first. However, the first method is computationally more efficient and approximates the second method, since the ground velocity is limited within a finite range of values, so that a temporal window region corresponds, approximately, to an associated spatial region. Obviously, the value of N, r_0 and d_0 must be chosen small enough that the wind velocity does not vary significantly in a region.

Using the same terminology as in Chapter 6, the MAP estimate of the ground and wind velocities $\hat{\mathbf{v}}_g = \{\hat{v}_{g,i}\}$ and $\hat{\mathbf{v}}_w = \{\hat{v}_{w,j}\}$ is denoted $(\hat{\mathbf{v}}_g, \hat{\mathbf{v}}_w)_{MAP}$, where i indexes the ground velocity data that are used (within the regions used) and j indexes the regions where the

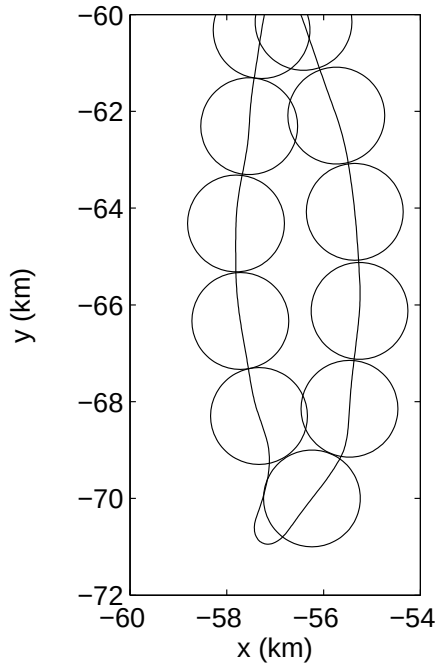

Figure 7.4 Illustration of the spatial region method in 2D where the flight is divided into spatial regions (circles).

wind velocities are estimated. The MAP estimate is then given by

$$\begin{aligned}(\hat{\mathbf{v}}_g, \hat{\mathbf{v}}_w)_{MAP} &= \underset{\mathbf{v}_g, \mathbf{v}_w}{\operatorname{argmax}} \left\{ p(\mathbf{v}_g, \mathbf{v}_w | \tilde{\mathbf{v}}_g) \right\} \\ &= \underset{\mathbf{v}_g, \mathbf{v}_w}{\operatorname{argmax}} \left\{ p(\tilde{\mathbf{v}}_g | \mathbf{v}_g) p_a(\mathbf{v}_g, \mathbf{v}_w) p_h(\mathbf{v}_g, \mathbf{v}_w) p_w(\mathbf{v}_w) \right\}, \end{aligned} \tag{7.6}$$

where $p(\mathbf{v}_g, \mathbf{v}_w | \tilde{\mathbf{v}}_g)$ is the posterior density, $p(\tilde{\mathbf{v}}_g | \mathbf{v}_g)$ is the likelihood, and $p_a(\cdot)$, $p_h(\cdot)$ and $p_w(\cdot)$ are the airspeed, rate of change of heading, and wind velocity prior densities, respectively. The likelihood is given by

$$p(\tilde{\mathbf{v}}_g | \mathbf{v}_g) = \exp(-||\tilde{\mathbf{v}}_g - \mathbf{v}_g||^2 / 2\sigma_g^2). \tag{7.7}$$

The prior density for the airspeed is given by

$$p_a(\mathbf{v}_g, \mathbf{v}_w) = \prod_i f(v_{a,i}) = \prod_i f(||v_{g,i} - v_{w,i}||), \tag{7.8}$$

where $v_{a,i}$ is the true airspeed and $f(\cdot)$ is the true airspeed prior density, as described in Section 7.2. The prior density for the rate of change of heading is

$$p_h(\mathbf{v}_g, \mathbf{v}_w) = \prod_i \exp(-h_i^2 / 2\sigma_h^2) = \exp\left(-\frac{1}{2\sigma_h^2} \sum_i h_i^2 \right), \tag{7.9}$$

where h_i is the rate of change of heading given by

$$h_i = \frac{\tan^{-1}(v_{g,i+1} - v_{w,i+1}) - \tan^{-1}(v_{g,i-1} - v_{w,i-1})}{2\Delta t}. \tag{7.10}$$

As described above, the flight is partitioned into either temporal or spatial regions. For a long flight, it is computationally expensive to obtain estimates for all the regions using a minimisation over the whole flight record. To reduce the computation, the regions are grouped into superregions, each containing J regions, and wind velocity estimates in each superregion are constrained by a wind velocity prior as described below, and the minimisation (7.6) is conducted over each superregion. The wind velocity estimates obtained for one superregion are used as the initial values for the optimisation in the next superregion. The number of superregions for a flight is denoted K, and the set of indices of the centers of the regions $(j_1, ...j_J)$ is denoted S_k for the k^{th} superregion. Note that J must be smaller or equal to the total number of regions. The superregions are defined differently depending on the partition method. For the temporal region method, a superregion is simply a set of J consecutive temporal regions.

For the spatial region method, a superregion is formed by J regions that are adjacent in space. The grouping of spatial regions is performed in the following steps: (1) The distance $d_{i,j}$ between a pair of spatial regions is calculated for all pairs of regions and stored in a matrix (an example of which is shown in Fig. 7.5 for 10 regions). As $d_{i,j} = d_{j,i}$ and $d_{i,i} = 0$, the upper diagonal matrix of size $N(N-1)/2$ is considered. (2) Starting from the first row of the diagonal matrix, where the row index is called the 'pilot', the nearest J regions around the 'pilot' region are selected by searching for J shortest distances in this row, and these regions are grouped into superregion S_1. For any selected region, the column and row associated with that region is then removed from the diagonal matrix. (3) Then step (2) is repeated for the next row of the diagonal matrix (with selected regions removed), until the last row is reached. Unlike the spatial regions , the spatial size of the superregions is variable. Figure 7.6 shows an example of the construction of two spatial superregions for a flight path with $J = 10$. The pilots of the superregion 1 and 2 are marked by A and B, respectively. For superregion 1 the flight path is relatively straight, and hence it spans a large area, and for superregion 2 the flight path curves and crosses often, and hence it is smaller.

A number of different options are considered for wind velocity priors. First note that the wind velocity can generally vary at a faster rate vertically than horizontally, and therefore a larger variance is used for constraining the vertical variation than the horizontal variation. The wind velocity prior is given by either constraining the magnitude of the vector difference between the wind velocity vectors, or by considering differences in wind speed and direction separately. The former approach is expressed as

$$p_w(\mathbf{v}_w) = \prod_{(j_1,j_2)\in S'_k} \exp\left(-||v_{w,j_1} - v_{w,j_2}||^2 \left(\frac{1}{2(d^h_{j_1,j_2})^2\sigma^2_{wh}} + \frac{1}{2(d^v_{j_1,j_2})^2\sigma^2_{wv}}\right)\right), \tag{7.11}$$

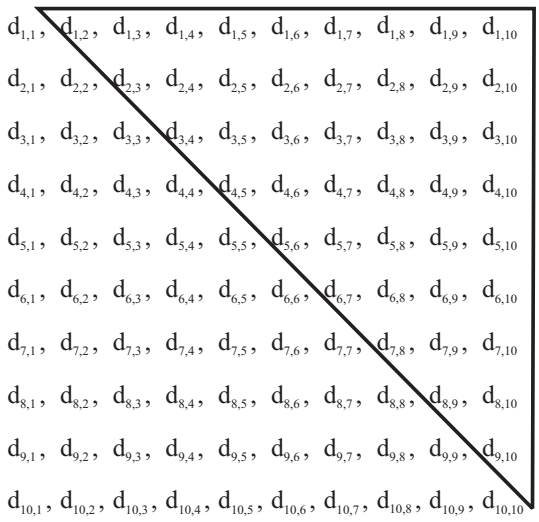

Figure 7.5 A matrix showing all possible pairs of spatial regions of the flight (for 10 regions). The upper diagonal used is marked by the triangle.

for the k^{th} superregion, where (j_1, j_2) denotes a pair of regions (temporal or spatial), the set S'_k denotes the collection of all possible pairs of indices of regions in S_k, $d^h_{j_1,j_2}$ and $d^v_{j_1,j_2}$ are the horizontal and vertical distance between the centers, respectively, of regions j_1 and j_2, and σ^2_{wh} and σ^2_{wv} are the horizontal and vertical variances, respectively.

For the case of separate wind speed and direction there are a number of options. First, the wind speed can be constrained in the same way as the wind velocities as above, i.e.

$$p_{ws}(\mathbf{v}_w) = \prod_{(j_1,j_2)\in S'_k} \exp\left(-(||v_{w,j_1}|| - ||v_{w,j_2}||)^2 \left(\frac{1}{2(d^h_{j_1,j_2})^2\sigma^2_{whs}} + \frac{1}{2(d^v_{j_1,j_2})^2\sigma^2_{wvs}}\right)\right), \tag{7.12}$$

where the subscript "s" denotes wind speed, and $\sigma^2_{wh\theta}$ and $\sigma^2_{wv\theta}$ are the horizontal and vertical variances of the wind direction. Second, the variation in the wind direction can be constrained using the prior density

$$p_{w\theta 1}(\mathbf{v}_w) = \prod_{(j_1,j_2)\in S'_k} \exp\left(-(\theta_{w,j_1} - \theta_{w,j_2})^2 \left(\frac{1}{2(d^h_{j_1,j_2})^2\sigma^2_{wh\theta}} + \frac{1}{2(d^v_{j_1,j_2})^2\sigma^2_{wv\theta}}\right)\right), \tag{7.13}$$

where $\sigma^2_{wh\theta}$ and $\sigma^2_{wv\theta}$ are the horizontal and vertical variances of the wind direction, respectively. Third, often the mean value of the wind direction is known approximately so that a prior of the form

$$p_{w\theta 2}(\mathbf{v}_w) = \prod_{j\in S_k} \exp\left(-(\theta_{w,j} - \theta_0)^2/2\sigma^2_{w\theta}\right), \tag{7.14}$$

could be applied where θ_0 is the approximate wind direction with variance $\sigma^2_{w\theta}$. One or all

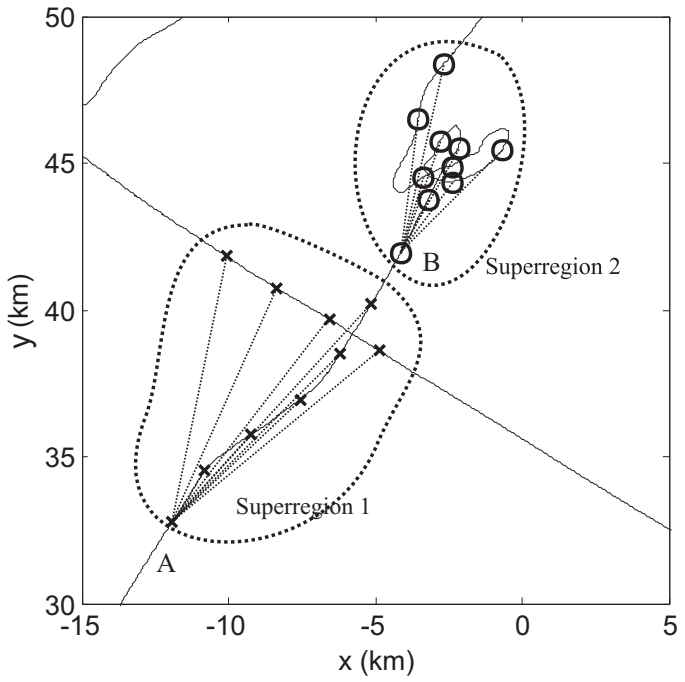

Figure 7.6 An example of the construction of two spatial superregions for a flight segment ($J = 10$). The flight path is shown by the light grey line. The centers of the regions for 2 adjacent superregions are marked by crosses and circles. The centers of the 'pilot' regions for superregions 1 and 2 are marked by A and B, respectively.

of the priors (7.12), (7.13), (7.14) could be used in place of (7.11).

7.4 2D simulation results

In order to study the characteristics of the MAP estimator described in the previous section, simulations are conducted on the somewhat simplified problem in two dimensions. Simple cases are used first to verify the algorithm and then more complicated cases are presented. 3D simulations are presented in the next section. Flights were simulated using the simulator described in Chapter 5 and in a wind field with $v^h_{w0} = 35$ m/s, $\theta^h_{w0} = 305°$, $A = -1$ m/s/km, $B = 2°$/km, $C = 0$ and $D = 0$ as described in Section 6.3 which is shown again in Fig. 7.7. A time-step $\delta t = 0.02$ s was used for generation of the flight data. Details of the simulated flights including the simulation parameters, inversion parameters and estimation errors are summarised in Table 7.3. The simulation results are described below. The prior density for the change of heading was tried and it had little effect on the results, and therefore it is excluded hereafter. The wind velocity prior (7.11) was used instead of the wind speed or direction priors (7.12, 7.13 and 7.14).

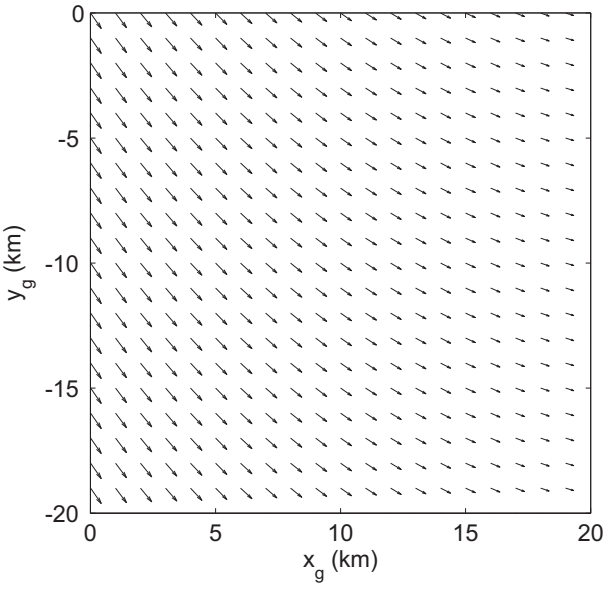

Figure 7.7 The simulated wind field for simulations 1-7 as described in the text.

Table 7.3 Summary of the simulated 2D flights, data, and other information.

No	Simulation Parameters				Method	Inversion Parameters		Estimation errors	
	v_a	θ_a	Noise	$\mathbf{v}_w$		v_a	σ_{wh} (s^{-1})	v_w error (m/s)	θ_w error (°)
1	constant 27 m/s	Fig. 7.8(a)	N	Fig. 7.7	Temporal	Gaussian $\mu = 27$ m/s $\sigma = 1$ m/s	0.005	0.46	2.2
2	constant 27 m/s	Fig. 7.8(a)	N	Fig. 7.7	Temporal	Gaussian $\mu = 27$ m/s $\sigma = 5$ m/s	0.005	0.62	2.7
3	Gaussian $\mu = 27$ m/s $\sigma = 2$ m/s	Fig. 7.8(a)	N	Fig. 7.7	Temporal	Gaussian $\mu = 27$ m/s $\sigma = 2$ m/s	0.005	0.42	2.1
4	Gaussian $\mu = 27$ m/s $\sigma = 2$ m/s	Fig. 7.8(a)	Y	Fig. 7.7	Temporal	Gaussian $\mu = 27$ m/s $\sigma = 2$ m/s	0.005	0.46	2.1
5	flight segment in Fig. 7.11	Fig. 7.8(a)	Y	Fig. 7.7	Temporal	EV $\mu = -27$ m/s $\sigma = 4$ m/s	0.002	1.4	6.1
6	flight segment in Fig. 7.11	Fig. 7.14(a)	Y	Fig. 7.7	Temporal	EV $\mu = -27$ m/s $\sigma = 4$ m/s	0.002	2.5	2.2
7	flight segment in Fig. 7.11	Fig. 7.14(a)	Y	Fig. 7.7	Spatial	EV $\mu = -27$ m/s $\sigma = 4$ m/s	0.002	2.5	2.9

7.4.1 Simulations 1 and 2

For simulations 1 and 2, a simple case is considered with the airspeed constant at $27\ \mathrm{m/s}$, and the sailplane heading varies with time as shown in Fig. 7.8(a). The rates of change of heading are in turn 3, 2, 1, 2, 3, $1\ ^\circ/\ \mathrm{s}$. The wind field, flight path relative to the ground and to the air are shown in Fig. 7.8(b) and (c), respectively. The MAP estimator was applied to the ground velocity data with no noise, using the temporal region method with $N = 21$, which partitions the flight into 47 temporal regions. For simulation 1, a narrow Gaussian distribution with $\mu_a = 27\ \mathrm{m/s}$ and $\sigma_a = 1\ \mathrm{m/s}$ was used for the airspeed prior and $\sigma_g = 2\ \mathrm{m/s}$, $\sigma_{wh} = 0.005\ \mathrm{s}^{-1}$ were used. The rate of change of heading prior was not used. A single optimization was conducted for the whole flight. A starting value of ($25\ \mathrm{m/s}$, 315°) was used for the wind velocity in the optimisation compared to the actual initial value of ($35\ \mathrm{m/s}$, 305°). This initial value was used for all the 2D simulations in this section. The results are shown in Fig. 7.9(a) and (b) and the rms errors in the wind speed and direction estimates are $0.46\ \mathrm{m/s}$ and 2.2° respectively. This is an ideal case with a tight prior on the airspeed and essentially perfect results are obtained, verifying that the algorithm is working correctly. For simulation 2, the airspeed prior standard deviation σ_a was increased to 5 m/s allowing a larger variation of airspeed, and the results are shown in Fig. 7.9(c) and (d) respectively, giving rms errors of $0.62\ \mathrm{m/s}$ and 2.7°. Although σ_a is larger, the prior distribution is centered at the correct value. This shows that an accurate airspeed model leads to good estimates.

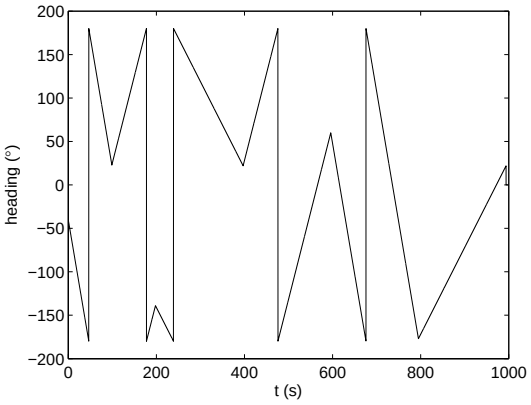

(a)

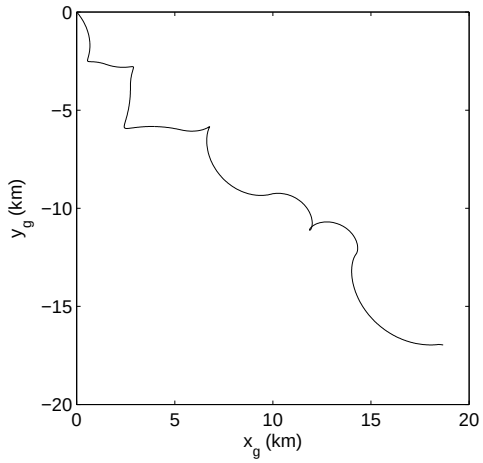

(b)

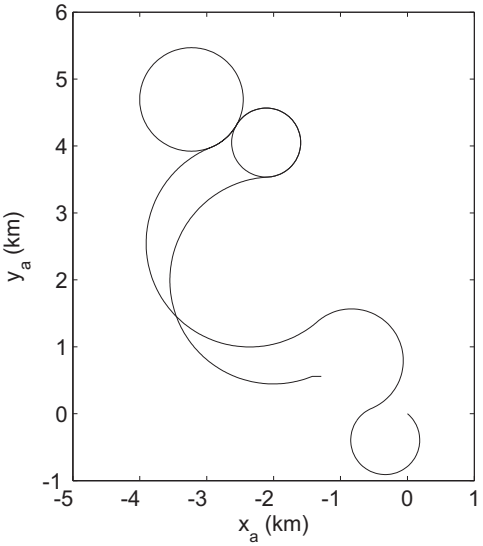

(c)

Figure 7.8 (a) Flight heading and (b) flight path relative to ground and (c) flight path relative to the air for simulations 1-5.

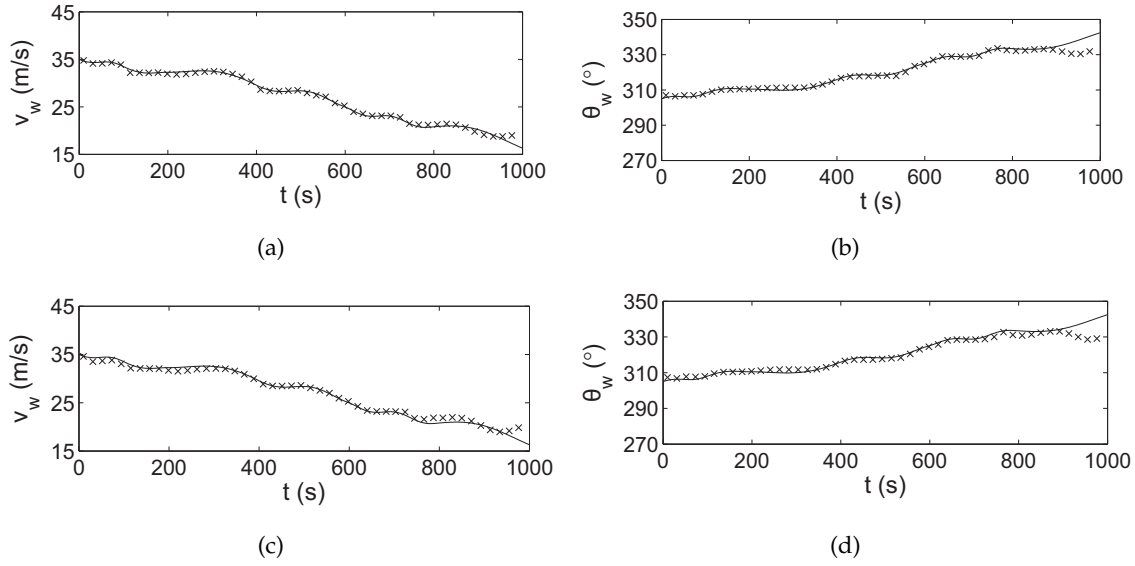

Figure 7.9 True (solid lines) and MAP estimates (crosses) of wind speed and direction from ground velocity data for simulations 1 and 2 (with constant airspeed) estimated using the temporal region method and a Gaussian airspeed prior, with (a),(b) $\sigma_a = 1$ m/s and (c),(d) $\sigma_a = 5$ m/s.

7.4.2 Simulations 3 and 4

In simulations 3 and 4, the same heading data in Fig. 7.8(a) were used, and the constant airspeed was changed to Gaussian distributed airspeeds, with a mean of 27 m/s and standard deviation of 2 m/s. For simulation 3, the MAP estimator was applied to the ground velocity data with no noise, using the temporal region method with $N = 21$ and a Gaussian distribution with the known parameters was used for the airspeed prior density, and $\sigma_g = 2\ \mathrm{m/s}$ and $\sigma_{wh} = 0.005\ \mathrm{s}^{-1}$ were used. The results are shown in Fig. 7.10(a) and (b) and the rms errors in wind speed and direction estimates are $0.42\ \mathrm{m/s}$ and $2.1°$, respectively. For simulation 4, Gaussian noise with a standard deviation of 2 m/s was added to the ground velocity data and using the same estimation parameters as above, and the results are shown in Fig. 7.10(c) and (d), with rms errors of $0.46\ \mathrm{m/s}$ and $2.1°$. This also shows that with a well-characterised airspeed distribution with a variable airspeed, good wind velocity estimates are obtained.

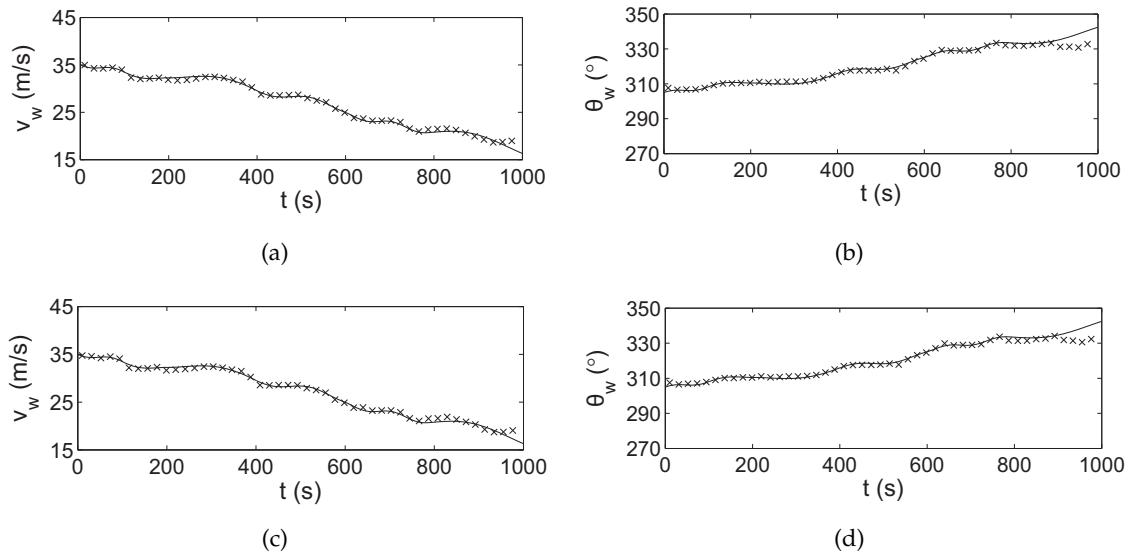

Figure 7.10 True (solid lines) and MAP estimates (crosses) of wind speed and direction from ground velocity data for simulations 3 (a) (b), and 4 (c) (d), using the temporal region method.

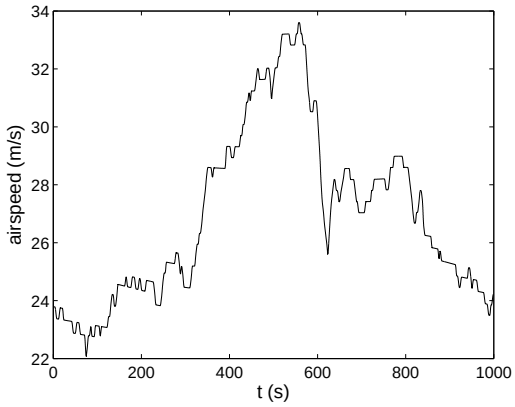

Figure 7.11 Simulation 5: airspeed versus time, taken from a segment of Flight 1.

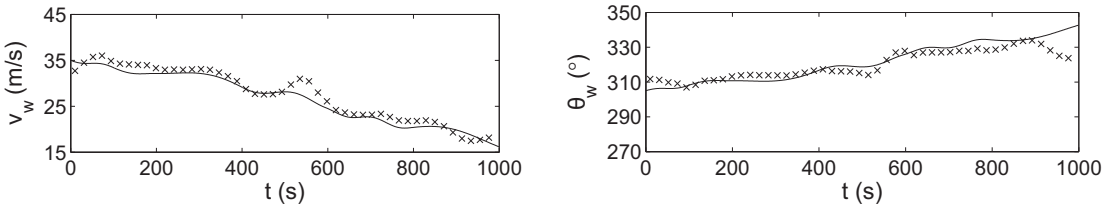

(a) (b)

Figure 7.12 True (solid lines) and MAP estimates (crosses) of (a) wind speed and (b) direction from ground velocity data of simulation 5 using the temporal region method.

7.4.3 Simulation 5

Realistic airspeed data, taken from a 1000 s section of Flight 1 (Section 3.2) as described in Section 6.3, and linearly interpolated onto a sample spacing of 0.02 s, as shown in Fig. 7.11 were used for this simulation. The same heading data were used (Fig. 7.8(a)). Gaussian noise with a standard deviation of 2 m/s was added to the ground velocity data. The MAP estimator with the temporal region method ($N = 21$) was applied to the data. For the inversion, the extreme value airspeed prior fitted to the airspeed data from Flight 1 ($\mu = -27$ m/s and $\sigma = 4$ m/s), and the parameters $\sigma_g = 2$ m/s and $\sigma_{wh} = 0.002$ m/s was used. The results are shown in Fig. 7.12(a), and (b) giving rms errors of 1.4 m/s and $6.1°$. The results are good overall. Errors occur in the estimated wind speed and direction at about 550 s and 1000 s. The wind speed error, $\Delta \mathbf{v}_w$, the heading change, $\Delta\theta_a$, and the airspeed are plotted in Fig. 7.13(a), (b), and (c) respectively. The wind speed errors appear to correlate with either large airspeeds (around 550 s) or with small heading changes (around 1000 s). The former may be because these values fall within the tail of the airspeed distribution.

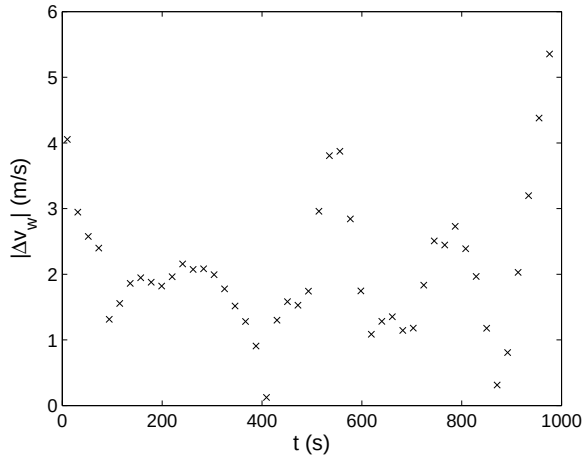

(a)

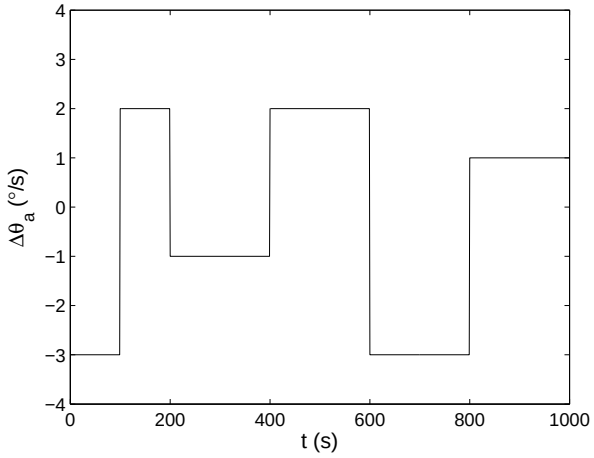

(b)

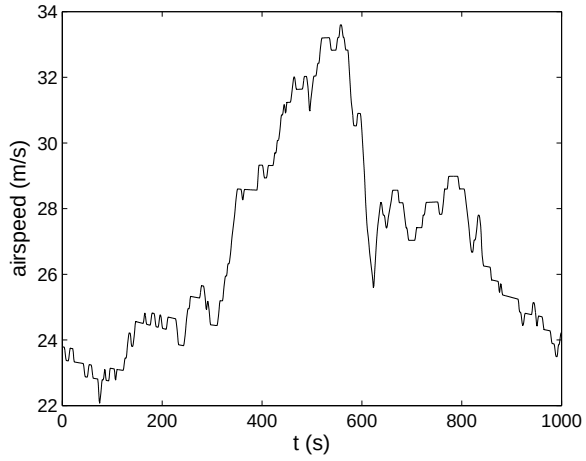

(c)

Figure 7.13 (a) Wind velocity error, (b) heading difference and (c) airspeed versus time for simulation 5.

7.4.4 Simulation 6

For simulation 6, a different set of input heading data was used, as shown in Fig. 7.14(a). The flight has a number of tighter turns (more rapid heading changes) as well as straight segments (constant heading). The rate of change in heading is between 1 and 20 $^\circ$/s, and zero for 67% of the flight. The flight path relative to the ground and to the air are shown in Fig. 7.14(b) and (c), respectively. The other parameters are the same as those used in simulation 5, and the ground velocity data were corrupted by Gaussian noise with a standard deviation of 2 m/s. Using the MAP estimator with the temporal region method with $N = 21$ and the known airspeed prior, $\sigma_g = 2$ m/s, and $\sigma_{wh} = 0.002$ m/s, gives the results shown in Fig. 7.15(a) and (b), with rms errors of 2.5 m/s and 2.2°. The estimates track the true values reasonably well. The errors are larger than those in simulation 5, as the flight heading is constant for much of this flight. The wind velocity error, $|\Delta \mathbf{v}_w|$, and the heading change, $\Delta\theta_a$ are shown in Fig. 7.16(a) and (b), respectively. The larger heading changes at 100, 300, 490, and 690 s correspond to the dips in the wind velocity error as anticipated.

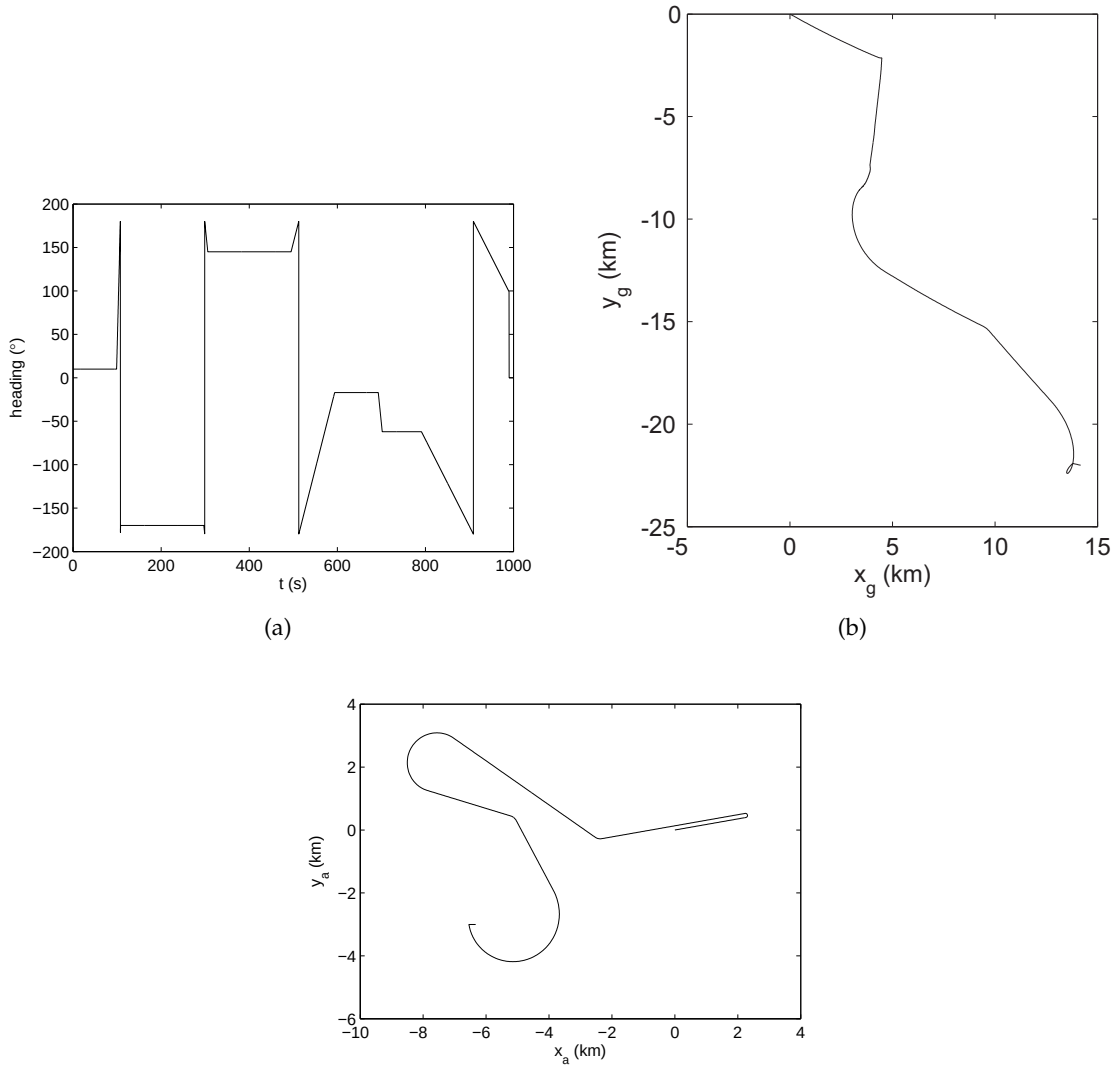

(a) (b)

(c)

Figure 7.14 (a) Heading, (b) flight path relative to the ground and (c) flight path relative to the air, for simulations 6 and 7.

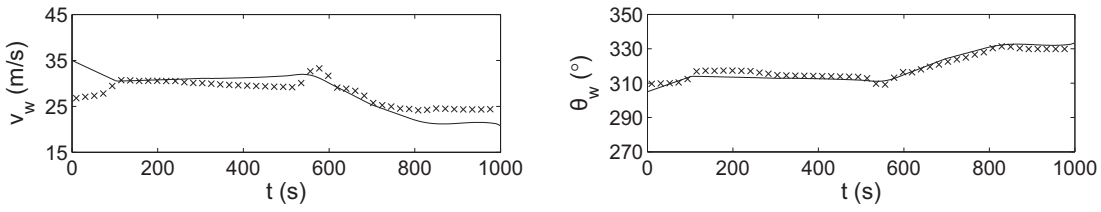

(a) (b)

Figure 7.15 True (solid lines) and MAP estimates (crosses) of (a) wind speed and (b) direction for simulation 6 using the temporal region method.

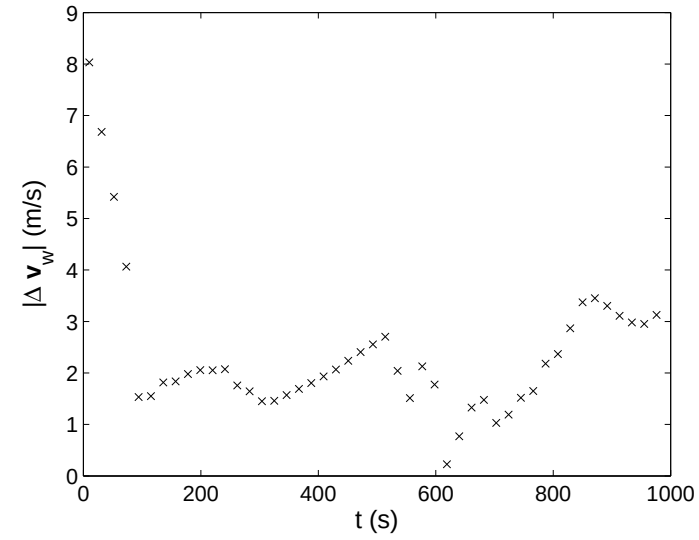

(a)

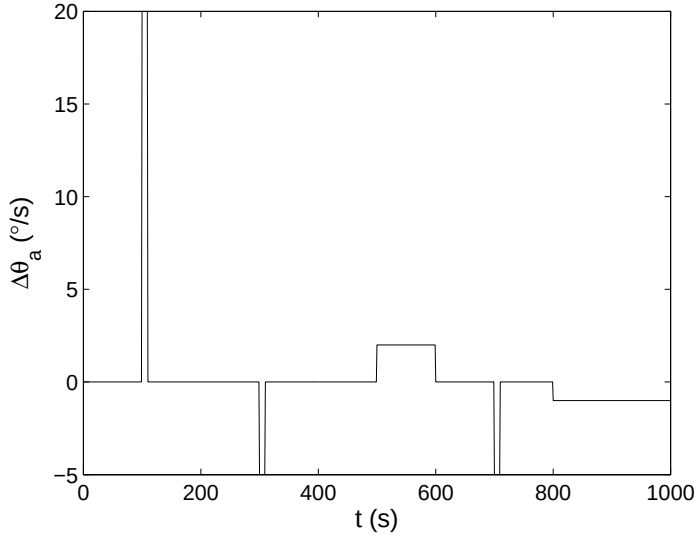

(b)

Figure 7.16 (a) Wind velocity error and (b) heading differences for simulation 6.

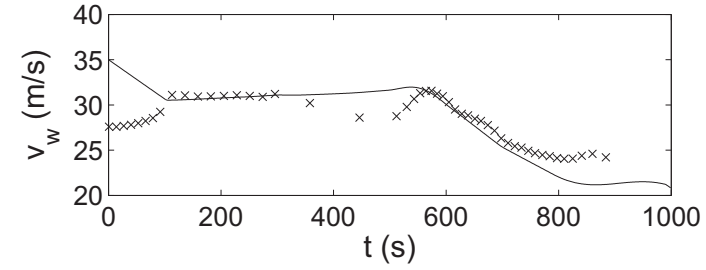

(a)

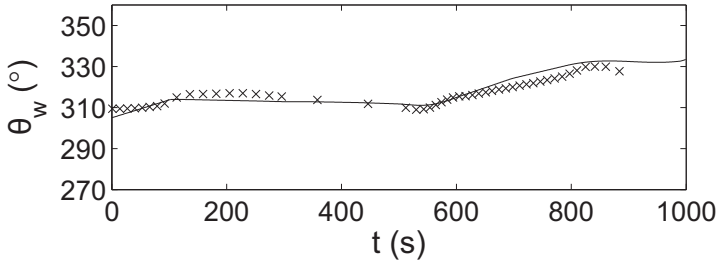

(b)

Figure 7.17 True (solid lines) and MAP estimates (crosses) of (a) wind speed and (b) direction for simulation 7 using the spatial region method..

7.4.5 Simulation 7

For simulation 7, the MAP estimator using the spatial region method was applied to the same flight data as in simulation 6, with $r_0 = 300$ m and the other parameters kept the same, and the results are shown in Fig. 7.17. The rms errors are 2.5 m/s and $2.9°$, and are similar as those shown in Fig. 7.15 using the temporal region method. The wind velocity error, $|\Delta \mathbf{v}_w|$, and the heading change, $\Delta\theta_a$ are shown in Fig. 7.18(a) and (b), respectively. Large error occurs at about the same time as those shown in Fig. 7.16(a), which corresponds to the flight path with constant heading. The spatial region method is expected to give similar results to the temporal region method, and the performance is dependant on the heading change. However, if the flight path often comes close to itself, the spatial region method is expected to be more advantageous than the temporal region method.

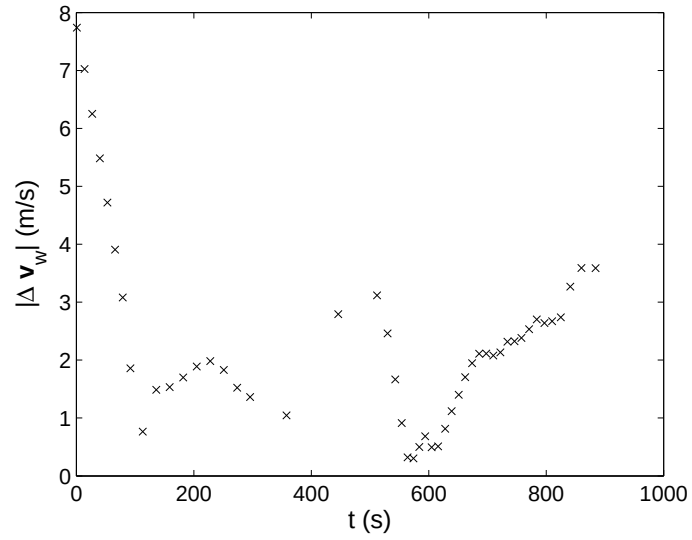

(a)

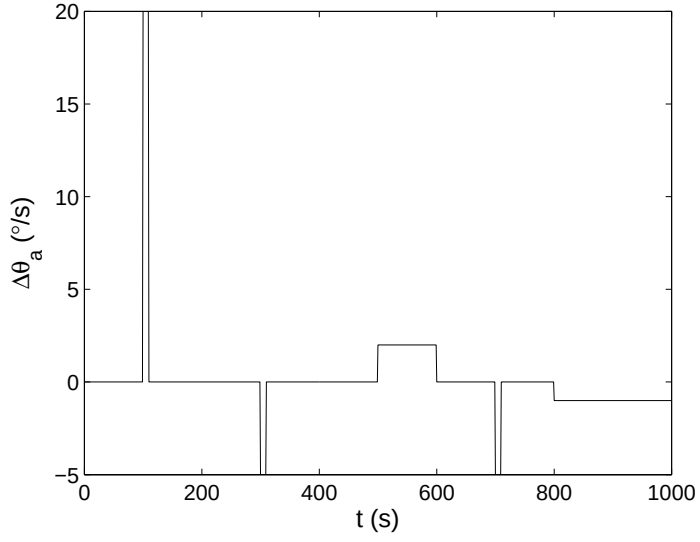

(b)

Figure 7.18 (a) Wind velocity error, and (b) heading difference for simulation 7.

7.5 3D simulation results

A 3D flight of length 1000 s was generated using the flight simulator described in Chapter 5. A 3D wind field was generated, with $v_{w0} = 25$ m/s, $\theta_{w0} = 0°$, $A = -0.5$ m/s/km, $B = 10°$/km, $C = 1$ m/s/km, $D = 3$ m/s, $\lambda = 10$ km, and $\phi = 30°$, as shown in Fig. 7.19(a) and (b). The DG505 polar for a wing load of 45 kg/m^2 was used to simulate the sink rate. The IAS and heading are shown in Fig. 7.19(c) and (d), respectively. The IAS was taken from a segment of Flight 3 (Section 3.4). This flight was used as there were frequent turning maneuvers during this flight. The IAS was converted to TAS using the standard atmosphere model. The output air path, ground path and altitude are shown in Fig. 7.20(a), (b) and (c), respectively. The ground position components are corrupted with Gaussian noise with a standard deviation of $\sqrt{2}$ m. The sailplane performs a number of circling maneuvers and the flight path crosses over several times. The wind velocity does not vary much for this flight, as the flight region is small.

The MAP estimator for the 3D horizontal wind velocity using the temporal region method was applied, with the parameters $N = 41$ s, $J = 23$, $\mu_a = -27$ m/s, $\sigma_a = 4$ m/s, $\sigma_g = 2$ m/s, $\sigma_{wh} = 5$ m/s/km, and $\sigma_{wv} = 10$ m/s/km. Note that σ_{wh} is half of σ_{wv} since the rate of change of the horizontal wind speed with horizontal position is half as the rate rate of change with vertical position. An initial estimate of the wind speed and direction of $(15$ m/s$, 10°)$ compared to the true value of $(25$ m/s$, 0°)$ was used. Once the horizontal wind velocities were estimated, they were used to calculate the true airspeed, which was then used to derive v_e and s, and the vertical wind speed was then calculated using (4.2). The estimated horizontal wind speed and direction, and the vertical wind speed are shown in Fig. 7.21(a), (b) and (c), respectively. The rms error in horizontal wind speed and direction and vertical wind speed are 2.2 m/s, $3.8°$ and 1.3 m/s, respectively. The results are reasonably good. The wind speed error, $|\Delta \mathbf{v}_w|$, and the heading change, $\Delta\theta_a$, are shown in Fig. 7.22(a) and (b), respectively. The heading varies during most of the flight, and the rate of change of heading is the large at 220, 420, 630, 922 s, which approximately correspond to the times at which low wind velocity errors occur.

The MAP estimator for the 3D horizontal wind velocity using the spatial region method was applied, with the parameters $r_0 = 400$ m, $h_0 = 100$ m, $J = 20$ (which is the whole flight), $\mu_a = -27$ m/s, $\sigma_a = 4$ m/s, $\sigma_g = 2$ m/s, $\sigma_{wh} = 5$ m/s/km, and $\sigma_{wv} = 10$ m/s/km. An initial estimate of wind speed and direction of $(15$ m/s$, 10°)$ compared to the true value of $(25$ m/s$, 0°)$ was used. After estimating the horizontal wind velocities, the vertical wind speed was estimated as described above. The estimated horizontal wind speed and direction, and vertical wind speed are shown in Fig. 7.23(a), (b) and (c), respectively. The rms error in the horizontal wind speed and direction and the vertical wind speed are 0.6 m/s, $2.6°$ and 1.0 m/s, respectively. The wind speed error, $|\Delta \mathbf{v}_w|$, and the heading change, $\Delta\theta_a$ are shown in Fig. 7.24(a) and (b), respectively. The wind velocity error has similar pattern to that in Fig. 7.22(a), which is low when the rate of change of heading is high. The spatial region method gave somewhat better results than the temporal method as anticipated. This is because in this simulation the wind velocity varies in space but not with time, and

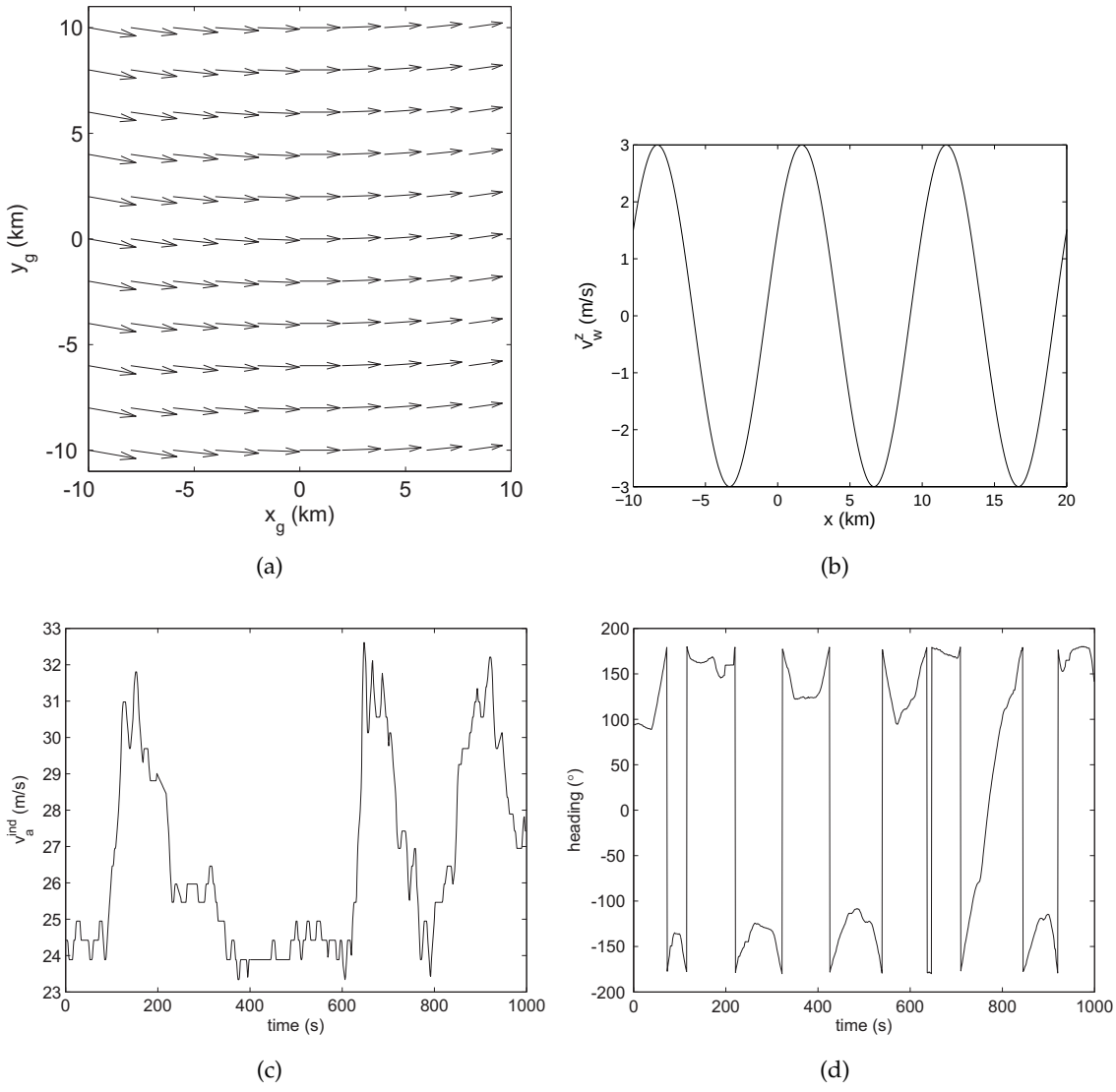

Figure 7.19 3D simulation: (a) Wind field vectors, (b) vertical wind speed versus x, (c) airspeed versus time, and (d) flight heading versus time.

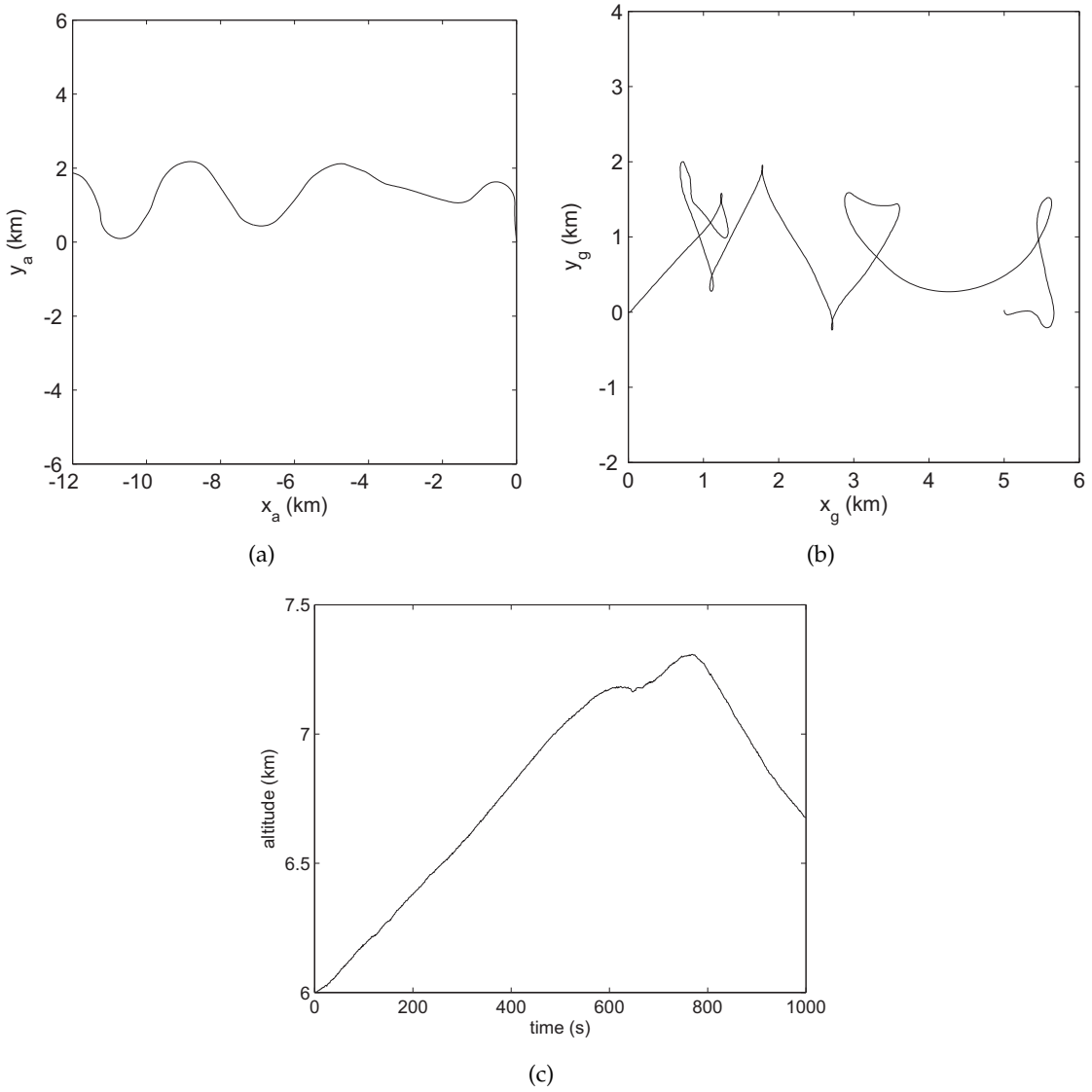

Figure 7.20 3D simulation: (a) Flight path relative to the air, (b) flight path relative to ground (with noise), and (c) flight altitude (with noise) versus time.

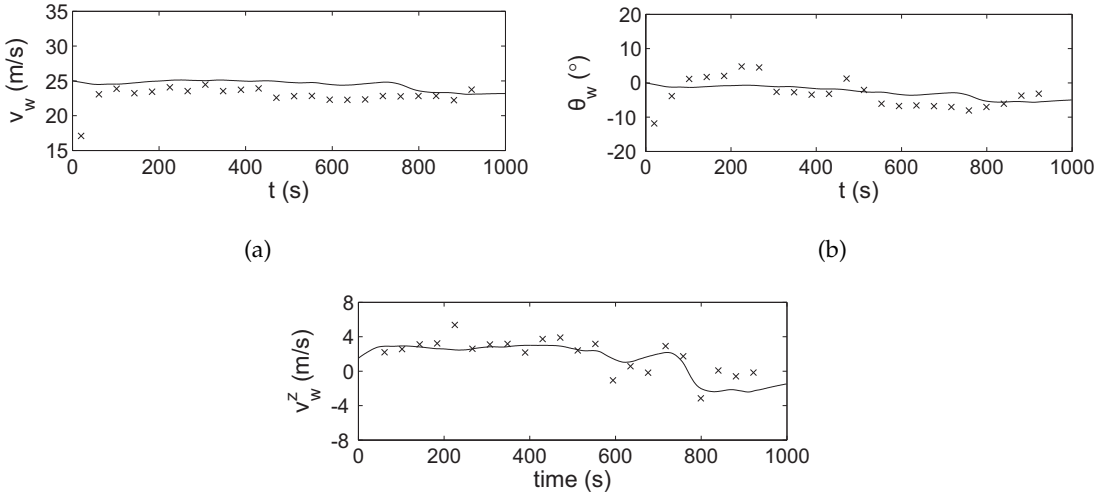

(a) (b) (c)

Figure 7.21 3D simulation: True (solid lines) and MAP estimates (crosses) of (a) horizontal wind speed, (b) horizontal wind direction, (c) vertical wind speed, and (d) rate of change of heading. The temporal region method was used.

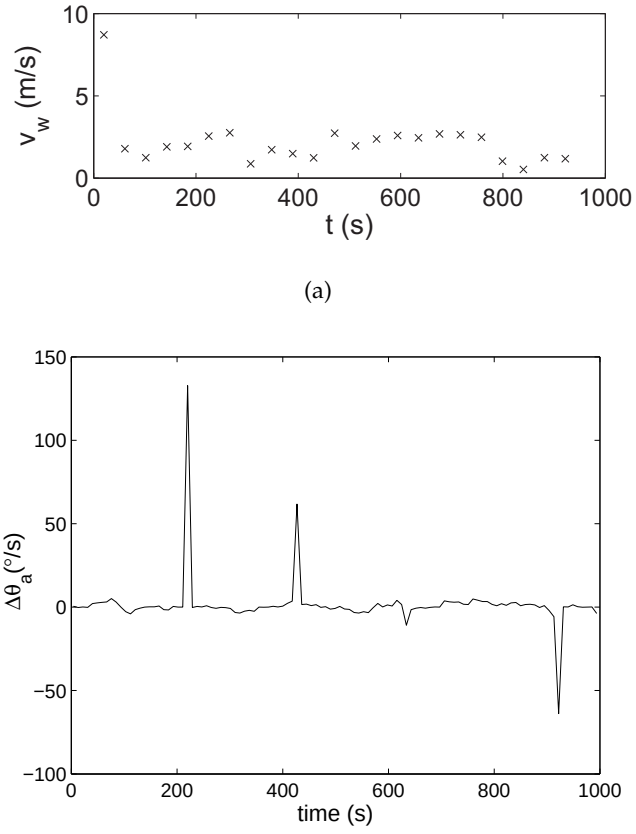

(a) (b)

Figure 7.22 3D simulation: (a) Wind velocity error, and (b) heading difference. The temporal region method was used.

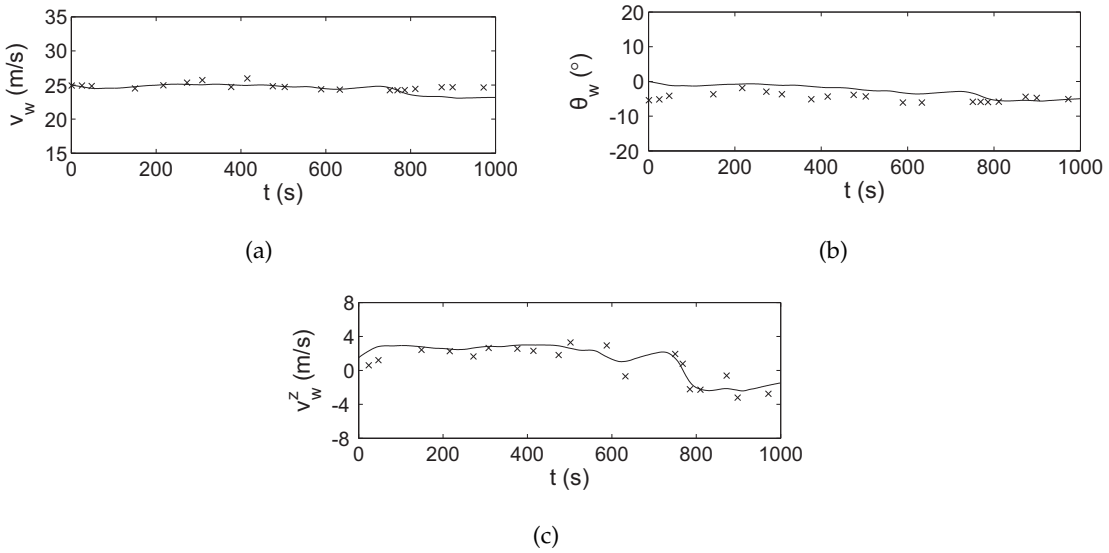

Figure 7.23 3D simulation: True (solid lines) and MAP estimates (crosses) of (a) horizontal wind speed, (b) horizontal wind direction, (c) vertical wind speed, and (d) rate of change of heading. The spatial region method was used.

the wind velocities at the locations where the flight path crosses are the same. For the spatial partition the flight path segments that cross over are included and constrained in the same region, while they may lie in different temporal regions.

The sensitivity of the results to the values of the prior distribution parameters, σ_{wh} and σ_{wv} is investigated by varying only these two parameters while maintaining the values of other parameters, and the results are summarised in Table 7.4. The results obtained with the correct values of σ_{wh} and σ_{wv} are shown in the first row. Doubling the parameters (second row) increases the error by only about 15%. Increasing them by a factor of 10 (third row) increases the error by almost 100%. Halving the parameters as shown in the last row increases the wind speed error by about 50%. Decreasing the parameters tends to over-constrain the estimates, preventing them from varying sufficiently. Overall, the estimates are relatively insensitive to the prior variances.

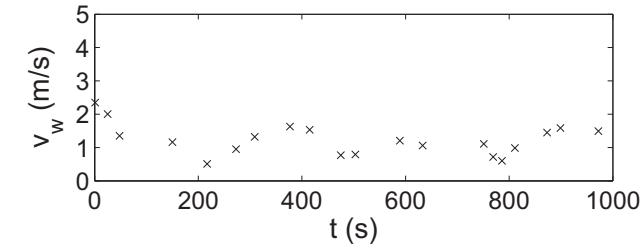

(a)

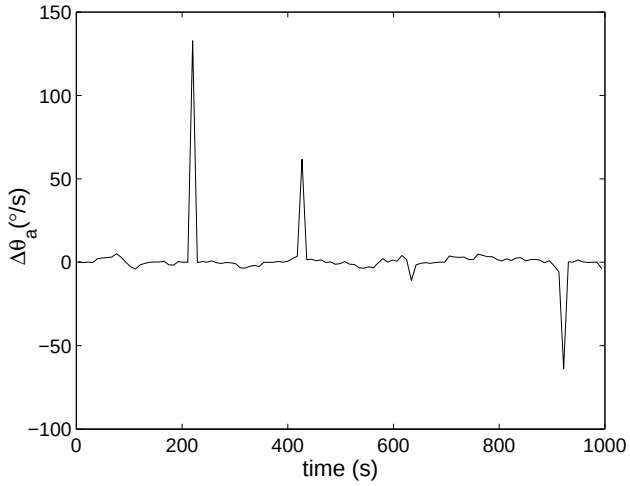

(b)

Figure 7.24 3D simulation: (a) Wind velocity error, and (b) heading difference. The spatial region method was used.

Table 7.4 Average rms wind speed and direction errors for different values of the prior parameters σ_{wh} and σ_{wv}.

Parameter			
σ_{wh} (m/s/km)	σ_{wv} (m/s/km)	Rms error in v_w (m/s)	Rms error in θ_w(°)
5	10	2.2	3.8
10	20	1.9	4.0
50	100	4.0	6.1
2.5	5	3.4	3.0

7.6 Experimental results

The MAP estimator was applied to the data from Flight 1 described in Section 3.2 using the temporal region method. The parameters used were $N = 41$, $J = 23$, $\sigma_{wh} = 10$ m/s/km, $\sigma_{wv} = 50$ m/s/km, $\mu_a = -27$ m/s, $\sigma_a = 4$ m/s and $\sigma_g = 2$ m/s. The parameters for the airspeed and ground velocity priors are chosen according to the instrument accuracy of the sailplane. Values of wind velocity prior variances were chosen such that the resulting wind field estimates approximately match those estimated using the ML method (Section 6.4.3). After estimating the horizontal wind velocities, the vertical wind speed was estimated as described in Section 2.3, and the results are shown in Fig. 7.25. The MAP estimates agree quite well with the estimates obtained using the heuristic method even though the latter used ground velocity and airspeed data. The average rms difference between the results obtained with the two methods are 3.8 m/s, 15° and 1.1 m/s for horizontal wind speed, wind direction, and vertical wind speed, respectively. The MAP estimates are interpolated over the flight time and collected into altitude bins 400 m thick and averaged, and are shown in Fig. 7.26 for altitudes above 2 km as well as the EAFB and DR radiosonde data. The estimates agree reasonably well with the radiosonde data. The wind direction estimates for the descending flight path are offset by about 50° compared to the values from the heuristic method. The reason for this is unknown.

The MAP estimator was then applied to the data from Flight 1 described in Section 3.2 using the spatial region method. The parameters used were $r_0 = 1000$ m, $d_0 = 200$ m, $J = 21$, $\sigma_{wh} = 10$ m/s/km, $\sigma_{wv} = 50$ m/s/km, $\mu_a = -27$ m/s, $\sigma_a = 4$ m/s and $\sigma_g = 2$ m/s. The region size is chosen so that the number of regions is close to that obtained with the temporal region method. The results are shown in Fig. 7.27. The MAP estimates agree quite well with estimates from the heuristic method. The average rms difference between the results obtained with the two methods are 5.7 m/s, 17°, and 1.1 m/s for horizontal wind speed, wind direction, and vertical wind speed, respectively. The agreement is not quite as good as for the temporal region method. The MAP estimates are interpolated over the flight time, and collected into altitude bins 400 m thick and averaged, and shown in Fig. 7.28 for altitudes above 2 km as well as the EAFB and DR radiosonde data. The estimates agree reasonably well with the radiosonde data, except that the wind direction for the descending flight is more erratic as noted above.

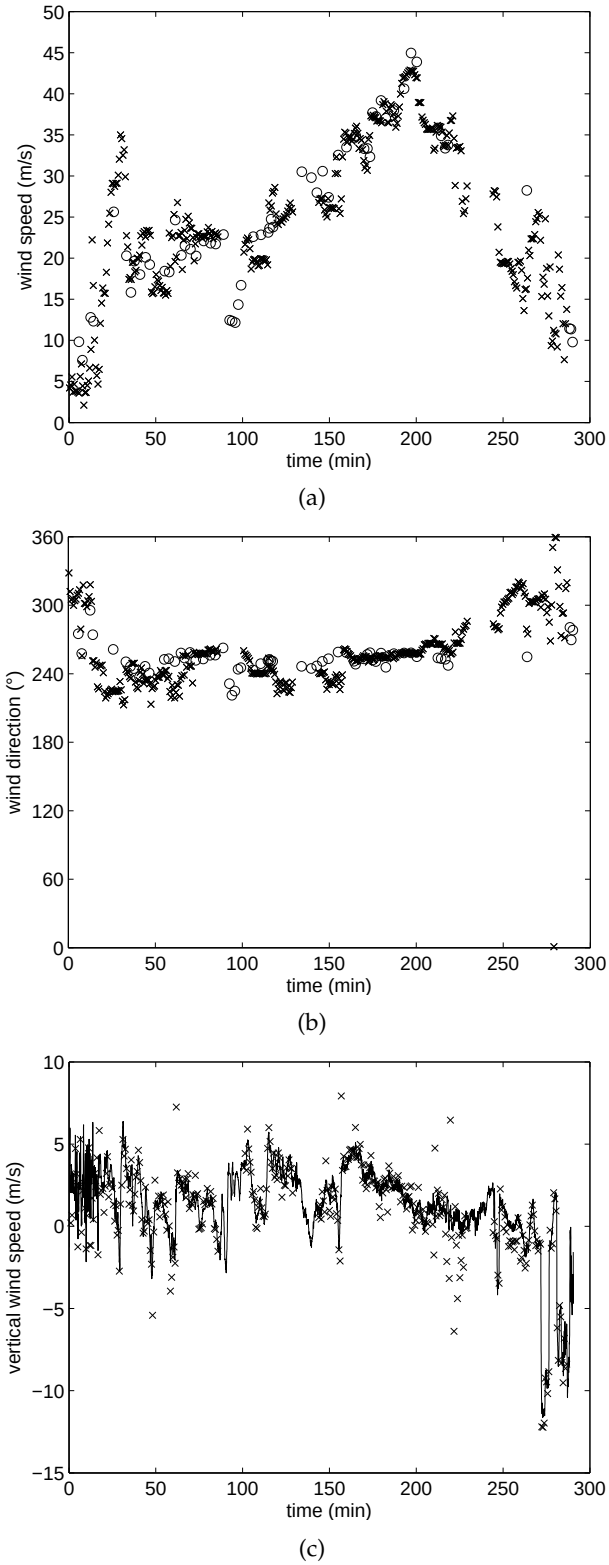

Figure 7.25 MAP estimates (crosses) of (a) horizontal wind speed, (b) wind direction and (c) vertical wind speed for Flight 1 using the temporal region method with ground velocity data, and estimates using the heuristic method with ground velocity and airspeed data described in Chapter 4 (horizontal wind speed and direction denoted by circles and vertical wind speed denoted by the solid line.

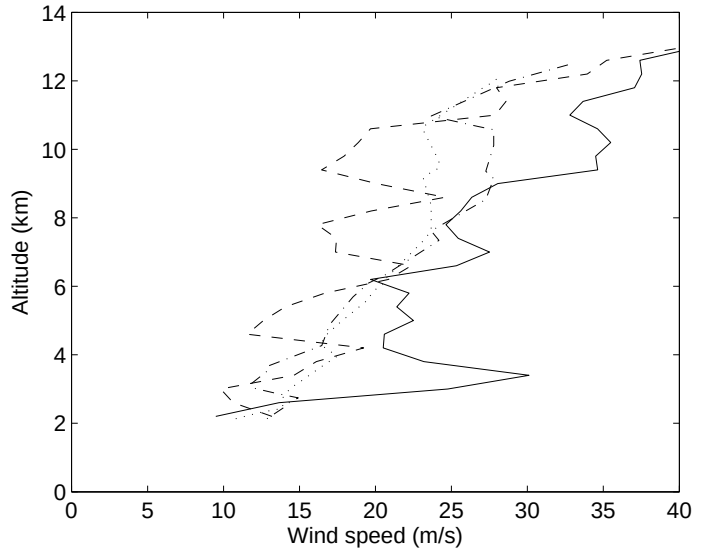

(a)

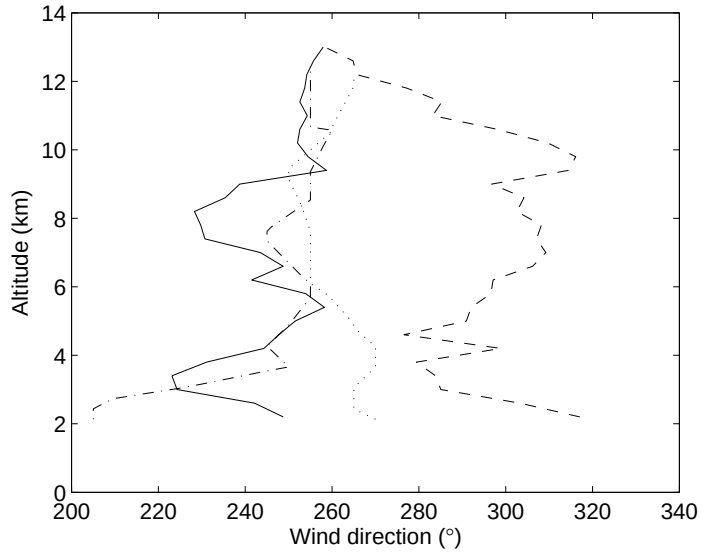

(b)

Figure 7.26 MAP estimates of (a) horizontal wind speed and (b) direction versus altitude, using the temporal region method with ground velocity data from Flight 1. The estimates are shown by the solid line for the ascending path, and by the dashed line for the descending path. The radiosonde soundings at EAFB is shown as the dotted line and that at DR by the dot-dashed line.

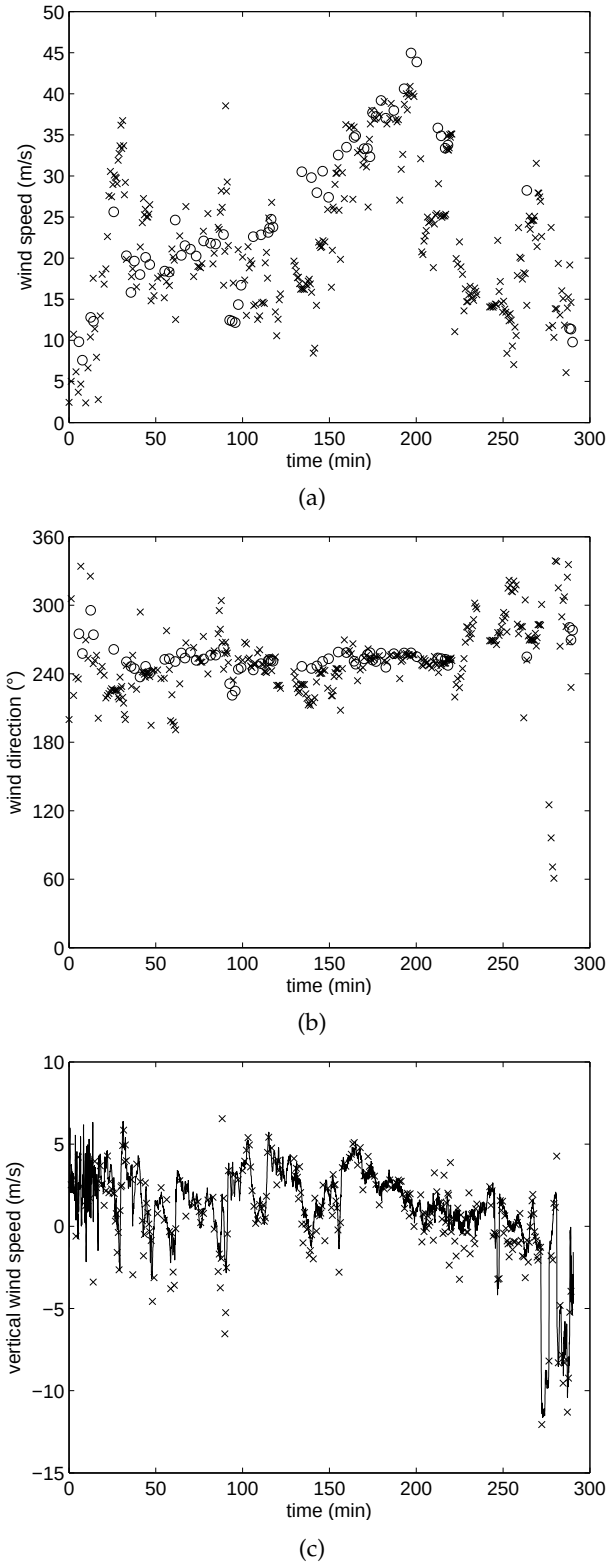

Figure 7.27 MAP estimates (crosses) of (a) horizontal wind speed, (b) wind direction and (c) vertical wind speed for Flight 1 using the spatial region method with the ground velocity data, and estimates using the heuristic method with ground velocity and airspeed data described in Chapter 4 (horizontal wind speed and direction denoted by circles and vertical wind speed denoted by the solid line.

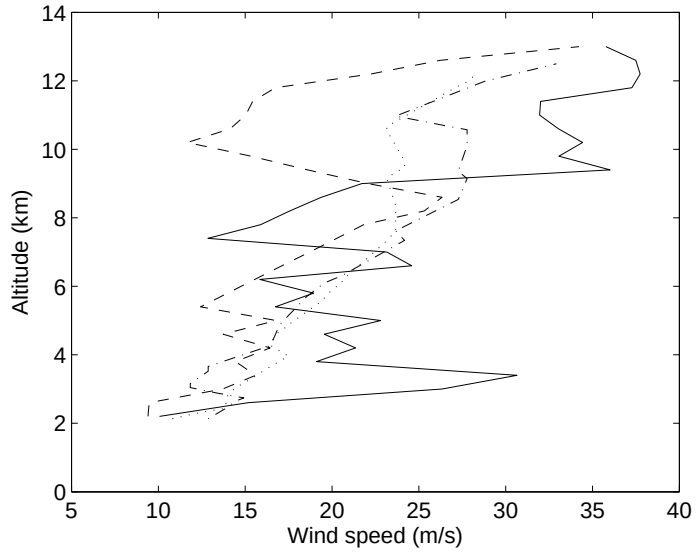

(a)

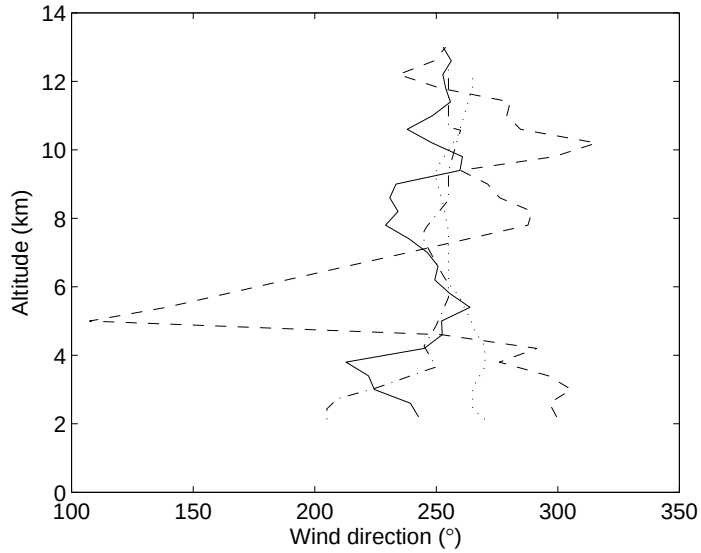

(b)

Figure 7.28 MAP estimates of (a) horizontal wind speed and (b) direction versus altitude, using the spatial region method with ground velocity data from Flight 1. The estimates are shown by the solid line for the ascending path, and by the dashed line for the descending path. The radiosonde soundings at EAFB is shown as the dotted line and that at DR by the dot-dashed line.

7.7 Discussion

In this chapter, methods for estimating the horizontal wind velocity from ground velocity data only were described. The problem is highly underdetermined and therefore reasonable airspeed and wind velocity priors were used to constrain the problem. MAP estimation methods were developed to incorporate this *a priori* information. Results from simulated flights showed that for a well-characterised sailplane the MAP methods are effective. The estimates are sensitive to noise when the heading is constant or changes slowly, as anticipated in Chapter 2. Various wind velocity priors were proposed, and these can be based on a temporal or spatial region. The performance of the two methods was similar for the stationary (time-invariant) wind field used in the simulations. The spatial region method is expected to give better results than the temporal region method for a stationary wind field if the flight path often comes close to itself as this increases the number of data and the likelihood of different headings in the regions. To accommodate time-varying wind fields, the wind velocity prior would need to be modified but this would not be difficult in practice. Selection of the estimator hyperparameters was based on known values for the simulations and heuristically for the experimental data, and this needs further investigation. Application to real flight data showed that the MAP methods give reasonably good results, given the paucity of data.

Chapter 8

Conclusions

In this thesis, novel methods have been described for using sailplanes as a sensor for measuring the 3D wind field structure in mountain lee waves. Available sailplane data considered include the GPS coordinates, GPS altitude, airspeed and heading. The wind velocities can be calculated directly from the ground velocities derived from the GPS coordinates, airspeed, and heading. In real flights however, the data is usually incomplete, and the problem becomes underdetermined. Three cases were considered: (1) If the heading of the sailplane is unknown, there exists a one-parameter family of solutions that lie on a circle. (2) If the airspeed is not measured, there is a one-parameter family of solutions for the wind velocities that lie on a straight line. (3) If only the GPS coordinates are recorded, there is a two-parameter family of solutions. The wind velocities in mountain lee waves vary slowly in space and time. This provides an important constraint and the ambiguities in cases (1) and (2) can be resolved if the wind field is assumed to be constant and data are measured at multiple times. The sensitivity of wind velocity estimates is studied in detail for these cases and a significant result is that the sensitivity reduces with increased differences in the sailplane heading for the multiple data. The problem is indeterminate for straight flight.

Based on the above characteristics, a heuristic method for calculating wind velocities from ground velocity and airspeed data was described in Chapter 4. The flight path is divided into a number of adjacent cylindrical regions and the data in each region are used to determine the wind velocities in that region, using a sensitivity analysis and clustering. The method was successfully applied to four sets of flight data.

Probability based methods are a powerful tool for solving inverse problems since they explicitly deal with uncertainties in the data, models and the solutions obtained. A maximum likelihood estimator was developed for cases (1) and (2) above as described in Chapter 6.

For case (3), the flight data do not provide sufficient information for estimating the wind velocity, even in a constant wind field. A Bayesian approach handles this kind of problem quite well by supplementing the incomplete data by incorporating prior densities for

other parameters. Chapter 7 described prior densities for the indicated airspeed, rate of change in heading, and the spatial variation of wind velocity. A MAP estimator was developed that gave good estimates of the wind velocity with reasonably good prior models, for simulated and experimental data.

The work completed here suggests a number of fruitful avenues for future research.

1. Estimation of hyperparameters requires more investigation.
2. The variability and applicability of the prior models for the air velocity described here could be investigated by collecting data for a wider range of flights and sailplanes.
3. The use of GPS and heading data could be further investigated as this can be provided by a simple instrument package that has no external sensors and does not interface with the flight system.
4. The Expectation-Maximum algorithm could be used for minimisation of the likelihood function, and multiple starting points can prevent the minimiser from being trapped in local minima.
5. The development of simple instrument package that provides the kind of data suitable for this kind of analysis would be useful.
6. There are large databases of simple flight data available for many flights. Analysis of this data, particularly for multiple flights in the same region, should provide a better mapping of a wave system.
7. A comparison of the results obtained here with those from atmospheric numerical models to compare wave characteristics would be useful.

Appendix A: IGC format

An IGC file is a formatted text file. Each line of characters begins with an upper-case letter which identifies the record type, and ends with Carriage Return Line Feed. The record type prefix may be one of the following:

- `A` - Flight recorder manufacturer and identification
- `B` - Fix (position)
- `C` - Task/declaration
- `D` - Differential GPS
- `E` - Event
- `F` - Constellation
- `G` - Security
- `H` - File header
- `I` - List of extension data included at end of each fix B record
- `J` - List of data included in each extension (`K`) Record
- `K` - Extension data
- `L` - Logbook/comments

The header of the file (records initiate with the letter `H`) contains important information on the flight, including sailplane type, logger type, pilot, date, GPS fix accuracy, etc. The header is followed by multiple-instance data lines, one for each GPS time-step.

The format of a line of the basic fix is as follows:

```
B HHMMSS DDMMmmm N(or S) DDDMMmmm E(or W) A(or V) PPPPP GGGGG
```

- `B` indicates that the type of data is fix (position).
- `HHMMSS` denotes (Coordinated Universal Time) UTC time in hours, minutes and seconds.
- `DDMMmmm N(or S)` is the latitude in degrees, minutes and decimal minutes, in which 'N' or 'S' stands for north or south, respectively.
- `DDDMMmmm E(or W)` are the longitude in degrees, minutes and decimal minutes, in which `E` or `W` stands for east or west, respectively.
- The next letter can be `A` for a 3D fix or `V` for a 2D fix or for no GPS data.
- `PPPPP` is the pressure altitude in meters.
- `GGGGG` is the GNSS altitude in meters.

Hence we can extract time, latitude, longitude, and altitude information from these IGC files. A example of an IGC file is shown below:

```
AGCS1IG
HFDTE290806
HFFXA100
HFPLTPILOT:STEVE FOSSETT
HFGTYGLIDERTYPE:DG505
HFGIDGLIDERID:N577SF
HFDTM100GPSDATUM:WGS84
HFRFWFIRMWAREVERSION:3.6
HFRHWHARDWAREVERSION:3.4
HFFTYFR TYPE:GARRECHT INGENIEURGESELLSCHAFT,VOLKSLOGGER 1.0
HFCIDCOMPETITIONID:SF
HFCCLCOMPETITIONCLASS:OPEN
I023638FXA3941ENL
LCONV-VER:4.24
C2908061330260000000000100
C4849638S04849638W
C0000000N00000000E
C0000000N00000000E
C0000000N00000000E
B1330265017026S07203163WV0030800000500004
B1330325017026S07203163WV0030800000500006
B1330385017026S07203160WA0030800190033004
B1330445017026S07203161WA0030800190033002
B1330505017026S07203161WA0030800190033002
B1330565017026S07203161WA0030800190033004
```

Bibliography

[1] R. P. Millane, R. G. Brown, E. Enevoldson, and J. E. Murray, "Estimating mountain wave windspeeds from sailplane flight data," in *Image Reconstruction from Incomplete Data III. Edited by P. J. Bones, M. A. Fiddy, and R. P. Millane. Proceedings of the SPIE*, vol. 5562, 2004, p. 218.

[2] NASA, *U.S. Standard Atmosphere*. U.S. Government Printing Office, Washington, D.C., 1976.

[3] D. G. Andrews, *An introduction to atmospheric physics*. Cambridge University Press, Cambridge, UK, 2000.

[4] R. B. Stull, *Meteorology for Scientists and Engineers*, 2nd ed. Brooks/Cole, 2000.

[5] S. H. Schneider, M. D. Mastrandrea, and T. L. Root, *Encyclopedia of climate and weather*. Oxford University Press, New York, 2011, vol. 1.

[6] E. E. Gossard and W. H. Hooke, *Waves in the atmosphere : atmospheric infrasound and gravity waves - their generation and propagation*. Elseview Scientific Publishing Company, Amsterdam, 1975.

[7] M. G. Wurtele, R. D. Sharman, and A. Datta, "Atmospheric lee waves," *Annu. Rev. Fluid Mech.*, vol. 28, pp. 429–476, 1996.

[8] C. D. Whiteman, *Mountain Meteorology: Fundamentals and Applications*. Oxford University Press, 2000.

[9] A. E. Gill, *Atmosphere-Ocean Dynamics*. Academic Press, 1982.

[10] K. Sato, "Vertical wind disturbances in the troposphere and lower stratosphere observed by the MU radar," *J. Atmos. Sci.*, vol. 47, pp. 2803–2817, 1990.

[11] J. C. Bird, S. R. Pal, A. I. Carswell, D. P. Donovan, G. L. Manney, J. M. Harris, and O. Uchino, "Observations of ozone structure in the arctic polar votex," *J. Geophys. Res.*, vol. 102, pp. 10 785–10 800, 1997.

[12] J. R. Holton, "The influence of gravity wave breaking on the general circulation of the middle atmosphere," *J. Atmos. Sci.*, vol. 40, pp. 186–201, 1983.

[13] A. S. Medvedev and G. P. Klaassen, "Vertical evolution of gravity wave spectra and the parameterization of associated wave drag," *J. Geophys. Res.*, vol. 100, pp. 25 841–25 853, 1995.

[14] J. D. Doyle and D. R. Durran, "The dynamics of mountain-wave induced rotors," *J. Atmos. Sci.*, vol. 59, pp. 186–201, 2002.

[15] S. B. Vosper, P. F. Sheridan, and A. R. Brown, "Flow separation and rotor information beneath two-dimensional trapped lee waves," *Quart. J. Roy. Meteorol. Soc.*, vol. 132, pp. 2415–2438, 2006.

[16] I. P. Chunchuzov, "The spectrum of high-frequency internal waves in the atmospheric waveguide," *J. Atmos. Sci.*, vol. 53, pp. 1798–1814, 1996.

[17] "NOAA's Geostationary Operational Environmental Satellite (GOES) data obtained from Comprehensive Large Array-data Stewardship System (CLASS)," [Available online at http://www.nsof.class.noaa.gov/].

[18] "NOAA's Polar Operational Environmental Satellite (POES) data obtained from Comprehensive Large Array-data Stewardship System (CLASS)," [Available online at http://www.nsof.class.noaa.gov/].

[19] T. P. Lane, M. J. Reeder, B. R. Morton, and T. L. Clark, "Observations and numerical modelling of mountain waves over the southern alps of new zealand," *Quart. J. Roy. Meteorol. Soc.*, vol. 126, pp. 2765–2788, 2000.

[20] J. L. Green, K. S. Gage, and T. E. V. Zandt, "Atmospheric measurements by VHF pulsed doppler radar," *IEEE Trans. Geosci. Electron.*, vol. 17, pp. 262–280, 1979.

[21] R. Ruster, J. Klostermeyer, and J. Rottger, "SOUSY VHF radar measurements in the lower and middle atmosphere," *IEEE Trans. Geosci. Remote Sens.*, pp. 1014–1025, 1986.

[22] I. P. Chunchuzov, W. Vachon, and X. Li, "Analysis and modelling of atmospheric gravity waves observed in RADARSAT SAR images," *Remote Sens. Environ.*, vol. 74, pp. 343–361, 2000.

[23] P. W. Vachon, O. M. Johannessen, and J. A. Johannessen, "An ERS-1 synthetic aperture radar imagery of atmospheric gravity waves," *J. Geophys. Res.*, vol. 97, pp. 14 249–14 257, 1994.

[24] P. W. Vachon, "ERS-1 SAR images of atmospheric gravity waves," *IEEE Trans. Geosci. Remote Sens.*, vol. 33, pp. 1014–1025, 1995.

[25] D. K. Lilly and P. J. Kennedy, "Observations of a stationary mountain wave and its associated momentum flux and energy dissipation," *J. Atmos. Sci.*, vol. 30, pp. 1135–1152, 1973.

[26] D. K. Lilly and P. F. Lester, "Waves and turbulence in the stratosphere," *J. Atmos. Sci.*, vol. 31, pp. 800–812, 1974.

[27] H. Volkert, C. Schär, and R. B. Smith, "Editorial: "MAP findings"," *Q. J. R. Meteorol. Soc.*, vol. 133, pp. 809–810, 2007.

[28] R. B. Smith, S. Skubis, J. D. Doyle, Q. Jiang, and S. A. Smith, "Alpine gravity waves: lessons from MAP regarding mountain wave generation and breaking," *Q. J. R. Meteorol. Soc.*, vol. 133, pp. 917–936, 2007.

[29] P. Bougeault, B. Benech, P. Bessemoulin, B. Carissimo, A. J. Clar, J. Pelon, M. Petitdidier, and E. Richard, "PYREX: A summary of findings," *Bull. Amer. Meteor. Soc.*, vol. 78, pp. 637–650, 1997.

[30] R. B. Smith, B. K. Woods, J. Jensen, W. A. Cooper, J. D. Doyle, Q. Jiang, and V. Grubišić, "Mountain waves entering the stratosphere," *J. Atmos. Sci.*, vol. 65, pp. 2543–2562, 2008.

[31] R. F. Whelan, *Exploring the Monster: Mountain Lee Waves: the Aerial Elevator*. Wind Canyon Books, 2000.

[32] S. Myschik and G. Sachs, "Wind measurement system using miniaturized navigation sensors for light aircraft and sailplanes," *Technical Soaring*, vol. 33, p. 26, 2006.

[33] "Mountain Wave Project,OSTIV," [http://www.mountain-wave-project.com].

[34] C. Lindemann, R. Heise, and W. Herold, "Lee waves in the andes region, mountain wave project (MWP) of OSTIV," *Technical Soaring*, vol. 32, pp. 93–96, 2008.

[35] A. Ultsch and R. Heise, "Data mining to distinguish wave vs. thermal climbs in soaring flight data," in *34th Annual Conference of the German Classification Society*, Karlsruhe, 2010.

[36] J. Dummann, "A report on glider pilot activities to document lee wave events in northern germany and their aims," *Technical Soaring*, vol. 33, pp. 109–116, 2009.

[37] R. F. Hertenstein and C. L. Martin, "Observations of internal rotor structure using an instrumented sailplane," *Technical Soaring*, vol. 32, p. 108114, 2008.

[38] C. J. Nappo, *An introduction to atmospheric gravity waves*. Academic Press, San Diego, 2002.

[39] R. S. Scorer, "Theory of waves in the lee of mountains," *Quart. J. Roy. Meterorol. Soc.*, vol. 75, pp. 41–56, 1949.

[40] Y.-L. Lin, *Mesoscale Dynamics*. Cambridge University Press, Cambridge, 2007.

[41] P. Queney, "The problem of air flow over mountains: A summary of theoretical results," *Bull. Amer. Meteor. Soc.*, vol. 29, pp. 16–26, 1948.

[42] R. S. Scorer, *Dynamics of Meteorology and Climate*. Wiley, 1997.

[43] R. B. Smith, "The influence of mountains on the atmosphere," *Adv. Geophys.*, vol. 21, pp. 87–230, 1979.

[44] D. R. Durran, "Another look at downslope windstorms. part i: The development of analogs to supercritical flow in an infinitely deep, continuously stratified fluid," *J. Atmos. Sci.*, vol. 43, pp. 2527–2543, 1986.

[45] P. G. Baines, *Topographic Effects in Stratified Flows*. Cambridge University Press, Cambridge, UK, 1995.

[46] S. D. Eckermann, J. Lindeman, D. Broutman, J. Ma, and Z. Boybeyi, "Momentum fluxes of gravity waves generated by variable froude number flow over three-dimensional obstacles," *J. Atmos. Sci.*, vol. 67, p. 2260, 2010.

[47] D. Piggott, *Gliding: A Hand Book on Soaring Flight*, 7th ed. A & C Black, 1997.

[48] H. Reichmann, *Cross-Country Soaring*, 7th ed. Soaing Society of America, 1993.

[49] J. Hoffren, "Quest for an improved explanation of lift," in *39th AIAA Aerospace Sciences Meeting & Exhibit*, Reno, NV, 2001.

[50] J. Katz and A. Plotkin, *Low-Speed Aerodynamics*, 2nd ed. Cambridge University Press, Cambridge, 2001.

[51] A. Miele, *Flight Mechanics*. Addison-Wesley, Reading, Massachusetts, 1962.

[52] *Federal Aviation Administration, Glider Flying Handbook*. Aviation Supplies and Academics, Inc., 2004.

[53] "Glaser-Dirks DG505 orion user manual," [http://www.dg-flugzeugbau.de/].

[54] A. Welch, L. Welch, and F. Irving, *New soaring pilot*, 3rd ed. John Murray Ltd, London, 1977.

[55] G. K. Batchelor, *An introduction to fluid dynamics*. Cambridge University Press, Cambridge, UK, 1999.

[56] W. M. Olson, *Aircraft performance flight testing. Technical Report AFFTC-TIH-99-02*. United States Air Force, Air Force Flight Test Center, Edwards AFB, CA, 2002.

[57] Naviter, "SeeYou Version 3.8," 2007, [Available online at http://www.seeyou.ws].

[58] A. Mohammad-Djafari, "From deterministic to probabilistic approaches to solve inverse problems," in *Proceedings of SPIE*, vol. 3459, 1998, pp. 2–11.

[59] W. Bogel and R. Baumann, "Test and calibration of the DLR falcon wind measuring system by maneuvers," *J. Atmos. Oceanic. Technol.*, vol. 8, pp. 5–18, 1991.

[60] D. Khelif, S. P. Burns, and C. A. Friehe, "Improved wind measurements on research aircraft," *J. Atmos. Oceanic. Technol.*, vol. 16, pp. 860–875, 1999.

[61] J. D. Doyle, H. Volkert, A. Dornbrack, K. P. Hoinka, and T. F. Hogan, "Aircraft measurements and numerical simulations of mountain waves over the central alps: A pre-MAP test case," *Quart. J. Roy. Meteorol. Soc.*, vol. 128, pp. 2175–2184, 2002.

[62] R. B. Smith, S. Skubis, J. D. Doyle, A. Broad, C. Kiemle, and H. Volkert, "Mountain waves over Mt.Blanc: Influence of a stagnant boundary layer," *J. Atmos. Sci.*, vol. 59, pp. 2073–2092, 2002.

[63] R. Wood, I. M. Stromberg, P. R. Jonas, and C. S. Mill, "Analysis of an air motion system on light aircraft for boundary layer research," *J. Atmos. Oceanic. Technol.*, vol. 14, pp. 960–968, 1997.

[64] G. J. Holland, P. J. Webster, J. A. Curry, G. Tyrell, D. Gauntlett, G. Brett, J. Becker, R. Hoag, and W. Vaglienti, "The aerosonde robotic aircraft: a new paradigm for environmental observations," *Bull. Amer. Meteor. Soc.*, vol. 82, pp. 889–901, 2001.

[65] A. van den Kroonenberg, T. Martin, M. Buschmann, J. Bange, and P. Vorsmann, "Measuring the wind vector using the autonomous mini aerial vehicle M^2AV," *J. Atmos. Oceanic. Technol.*, vol. 25, pp. 1969–1982, 2008.

[66] S. Mayer, G. Hattenberger, P. Brisset, M. o. Jonassen, and J.Reuder, "A 'no-flow-sensor' wind estimation algorithm for unmanned aerial systems," *Int. J. Micro Air Vehicles*, vol. 4, pp. 15–30, 2012.

[67] J. W. Langelaan, N. Alley, and J. Neidhoefer, "Wind field estimation for mini- and micro-unmanned aerial vehicles," *J Guidance, Control and Dynamics*, vol. 34, no. 4, pp. 1016–1030, 2010.

[68] N. R. J. Lawrance and S. Sukkarieh, "Autonomous exploration of a wind field with a gliding aircraft," *J Guidance, Control and Dynamics*, vol. 34, no. 3, pp. 719–733, 2011.

[69] G. Kocer, M. Mansour, N. Chokani, R. Abhari, and M. Müller, "Full-scale wind turbine near-wake measurements using an instrumented uninhabited aerial vehicle," *J. Solar Energy Engineering*, vol. 133, pp. 041 011–1–8, 2011.

[70] F. A. P. Lie and D. Gebre-Egziabher, "A synthetic airdata system," in *AIAA Guidance, Navigation, and Control Conference*, paper no. AIAA 2012-4704, Minneapolis, Minnesota, 2012.

[71] P. H. Dana, "Global positioning system overview, the geographer's craft project, department of geography, the university of colorado at boulder," 1999, [Available online at http://www.colorado.edu/geography/gcraft/contents.html].

[72] "The Perlan Project," [http://perlanproject.org/].

[73] E. H. Teets and E. J. Carter, "Atmospheric conditions of stratospheric mountain waves:soaring the perlan aircraft to 30 km," in *18th International Conference on Interactive Information and Processing Systems (IIPS) for Meteorology, Oceanography, and Hydrology*. Orlando, Florida: AMS, 2002.

[74] "Upper air soundings, Department of Atmospheric Science, University of Wyoming," data can be extracted from [http://weather.uwyo.edu/upperair/sounding.html].

[75] E. Kalnay *et al.*, "The NCEP/NCAR 40-year reanalysis project," *Bull. Amer. Meteor. Soc.*, vol. 77, pp. 437–470, 1996.

[76] F. Mesinger, G. DiMego, and E. Kalnay, "North American Regional Reanalysis," *Bull. Amer. Meteor. Soc.*, vol. 87, pp. 343–360, 2006.

[77] "NOAA/OAR/ESRL PSD NCEP Ranalysis Data," [Available online at http://www.esrl.noaa.gov/psd/].

[78] V. M. Richard, *Theory of Flght*. Dover, New York, 1959.

[79] R. P. Millane, G. D. Stirling, R. Brown, N. Zhang, V. L. Lo, E. Enevoldson, and J. E. Murray, "Estimating wind velocities in mountain lee waves using sailplane flight data," *Journal of Atmospheric and Oceanic Technology*, vol. 27, pp. 147–158, 2010.

[80] [http://www.leb.esalq.usp.br/disciplinas/Molin/leb447/Arquivos/GNSS/ArtigoAcuraciaGPSsemAutor.pdf].

[81] MathWorks, "Matlab for research," 1994-2011, [http://www.mathworks.com].

[82] C. G. Broyden, "The convergence of a class of double-rank minimization algorithms," *J. Inst. Math. Applic.*, vol. 6, pp. 76–90, 1970.

[83] R. Fletcher, "A new approach to variable metric algorithms," *Computer Journal*, vol. 13, pp. 317–322, 1970.

[84] S. Coles, *An Introduction to Statistical Modeling of Extreme Values*. Springer, London, 2001.

[85] P. Athanasios and P. S. Unnikrishna, *Probability, Random Variables, and Stochastic Processes*, 4th ed. McGraw-Hill, Boston, 2002.